University of Alberta

Interactions between Small Oil Droplets and Solid Surfaces in Aqueous Solutions

by

Yongan Gu ©

A thesis submitted to the Faculty of Graduate Studies and Research in partial fulfillment of the requirements for the degree of **Doctor of Philosophy**

Department of Mechanical Engineering

EDMONTON, ALBERTA

FALL 1999

National Library
of Canada

Acquisitions and
Bibliographic Services

395 Wellington Street
Ottawa ON K1A 0N4
Canada

Bibliothèque nationale
du Canada

Acquisitions et
services bibliographiques

395, rue Wellington
Ottawa ON K1A 0N4
Canada

Your file Votre référence

Our file Notre référence

The author has granted a non-exclusive licence allowing the National Library of Canada to reproduce, loan, distribute or sell copies of this thesis in microform, paper or electronic formats.

The author retains ownership of the copyright in this thesis. Neither the thesis nor substantial extracts from it may be printed or otherwise reproduced without the author's permission.

L'auteur a accordé une licence non exclusive permettant à la Bibliothèque nationale du Canada de reproduire, prêter, distribuer ou vendre des copies de cette thèse sous la forme de microfiche/film, de reproduction sur papier ou sur format électronique.

L'auteur conserve la propriété du droit d'auteur qui protège cette thèse. Ni la thèse ni des extraits substantiels de celle-ci ne doivent être imprimés ou autrement reproduits sans son autorisation.

0-612-46844-5

Canadä

University of Alberta

Library Release Form

Name of Author:	**Yongan Gu**
Title of Thesis:	**Interactions between Small Oil Droplets and Solid Surfaces in Aqueous Solutions**
Degree:	**Doctor of Philosophy**
Year this Degree Granted:	**1999**

Permission is hereby granted to the University of Alberta Library to reproduce single copies of this thesis and to lend or sell such copies for private, scholarly or scientific research purposes only.

The author reserves all other publication and other rights in association with the copyright in the thesis, and except as hereinbefore provided neither the thesis nor any substantial portion thereof may be printed or otherwise reproduced in any material form whatever without the author's prior written permission.

Signature: Yongan Gu

605B Michener Park Residence
Edmonton, AB T6H 5A1
CANADA

Dated: July 13, 1999

University of Alberta

Faculty of Graduate Studies and Research

The undersigned certify that they have read, and recommend to the Faculty of Graduate Studies and Research for acceptance, a thesis entitled **Interactions between Small Oil Droplets and Solid Surfaces in Aqueous Solutions** submitted by **Yongan Gu** in partial fulfillment of the requirements for the degree of **Doctor of Philosophy**.

Dong Li

Dr. Dongqing Li (Supervisor)

JD Dale

Dr. J. D. Dale

Dr. T. W. Forest

Dr. L. W. Kostiuk

LARRY KOSTIUK

for **Dr. Raj Rajagopalan**

Dr. T. Dabros

Dated: June 14, 1999

Abstract

Introduction of a fiber of appropriate material into an aqueous solution containing dispersed oil droplets may lead to deposition of small oil droplets onto the fiber surface, depending on their interactions. Such deposition process is governed by at least two types of colloidal interactions between the oil droplets and the fiber surfaces across the aqueous phase, based on the well-known Derjaguin-Landau-Verwey-Overbeek (DLVO) theory, and possibly external force fields as well. The colloidal interactions represent the van der Waals (vdW) and the electrical double layer (EDL) interactions. This thesis focuses on understanding and experimentally determining the colloidal interactions and the deposition process.

A general theoretical method is presented to determine the retarded vdW interaction between a spherical particle and a cylinder. The detailed numerical predictions indicate that the widely used flat plate approximation may seriously overestimate the vdW interaction for the sphere-cylinder system. An approximate integral solution is also obtained for the EDL interaction between a spherical particle and a cylindrical surface. This numerical solution shows that the curvature effect of cylinder on the EDL interaction can not be neglected at smaller separation distances.

In order to determine the Hamaker constant involved in the vdW interaction, a novel contact angle measurement technique has been developed. This experimental method determines the contact angle by analysis of the capillary profile around a cylinder (ACPAC). The contact angles as measured by the ACPAC technique agree very well with those measured by the Wilhelmy plate technique and the axisymmetric drop shape analysis (ADSA) technique for the sessile drop case, respectively. To determine the EDL

interaction, a new electrical suspension method is devised to measure the ζ-potentials of small liquid droplets dispersed in another immiscible liquid and the streaming potential technique is applied by using a parallel-plate microchannel to measure the ζ-potentials of glass surfaces in contact with an aqueous phase.

Both the analytical and numerical solutions of 1-D mass transfer equation have been obtained. The 2-D numerical model is also developed, in which both the colloidal interactions and the external force fields can be accounted for. In particular, the effects of the gravitational field and the electric field on the deposition process have been examined using the 2-D model. A systematic deposition experiment was conducted to examine the effects of the colloidal interactions on the deposition processes of silicone oil droplets onto two kinds of glass surfaces in a variety of aqueous solutions. The deposition data for the bare glass surface (hydrophilic) is in an excellent agreement with the numerical predictions of the 1-D model. However, the measured deposition rates for the FC725-precoated glass surface (hydrophobic) are found to be significantly higher than the numerical predictions. The latter differences are attributed to the attractive hydrophobic interaction.

Acknowledgements

The author wishes to acknowledge the following for their help in the preparation of this thesis.

- Dr. Dongqing Li for his supervision of this research.
- Dr. J. D. Dale and Dr. T. W. Forest for their guidance as part of the author's supervisory committee.
- Dr. J. H. Masliyah, Dr. K. Nandakumar, Dr. S. M. Kresta and Dr. H. Henein in Chemical Engineering Department for their valuable suggestions.
- Mr. Mark Ackerman, Mr. Craig Owens, Mr. Allan Muir, Mr. Albert Yuen and Mr. Terry Nord for their assistance in the experimental work.
- Helen, Gail, Doris, Liping and Shelly of Mechanical Engineering Department Office for all their general help.
- University of Alberta for awarding the Izaak Walton Killam Memorial Scholarship (May 1997-April 1999), Mechanical Engineering Department for providing the full-time Teaching Assistantship during the academic years (1994-1997), The Natural Sciences and Engineering Research Council of Canada and other industrial institutions.
- Moin Mala, Weilin Qu, Chun Yang, Sarah Arulanandam in Mechanical Engineering Department for their occasional help and useful discussions.
- To several colleagues on campus, Jean Zeng, Qizhu Ding, Zhongren Wang in Chemistry Department, Yu Li and Keith Anderson in Pharmaceutical Department, Dr. S. Basu, Dr. G. Zhou, Dr. Nianxi Yan in Chemical Engineering Department for their technical assistance.
- To the many individuals who have extended friendship and hospitality to our family during our stay in Edmonton. I always cheer for the Edmonton Oilers.
- My parents, for their support and inspiration throughout my entire education.
- My wife, Yue Song and my daughter, Annie Gu, for their unconditional love, support and patience during this research. Thank you for all of your sacrifices and for allowing me to pursue my dreams. I love you both very much.

Table of Contents

Chapter 1 **Introduction** 1

1.1 Motivation and Background 1

1.2 Literature Review 3

1.2.1 The DLVO Theory 4

1.2.2 Deposition Kinetics 6

1.3 Research Objectives 8

Chapter 2 **Mass Transport Equations** 12

2.1 Introduction 12

2.2 Colloidal Forces 13

2.3 One-dimensional (1-D) Mass Transport Equation 14

2.4 External Force Fields 15

2.4.1 Gravitational Field 16

2.4.2 Electric Field 16

2.5 Two-dimensional (2-D) Mass Transport Equation 17

2.6 Simplified 2-D Mass Transport Equation 20

Figures 23

Chapter 3 **The van der Waals (vdW) Interaction and the Electrical Double Layer (EDL) Interaction between a Spherical Particle and a Cylindrical Fiber** 24

3.1 The van der Waals (vdW) Interaction 24

3.2 Mathematical Formulations of the Unretarded vdW Interaction between a Spherical Particle and a Cylindrical Fiber 26

3.2.1 Molecule-Cylinder Interaction Potential 27

3.2.2 Sphere-Cylinder Interaction Potential 29

3.2.3 Analytical Solutions for the Sphere-Flat Plate vdW Interaction Potential 32

3.2.4 The vdW Interaction Force 33
3.3 Retarded van der Waals (vdW) Interaction 35
3.4 Retardation Effect and Curvature and Finite Size Effects 38
3.5 Determination of the Hamaker Constant A_{132} 41
3.5.1 Combining Relations 41
3.5.2 Relations between the Hamaker Constants and the Surface Energies 42
3.6 Equation of State for Interfacial Tensions of Solid-Liquid Systems 45
3.7 The Electrical Double Layer (EDL) Interaction 46
3.8 The HHF Expressions for the EDL Interaction between a Spherical Particle and a Flat Plate 49
3.9 The EDL Interaction between a Spherical Particle and a Cylindrical Fiber 54
3.9.1 Potential Distribution between Two Charged Flat Plates 54
3.9.2 Specific EDL Interaction Potential between Two Flat EDLs 54
3.9.3 Total EDL Interaction Potential and Force between a Spherical Particle and a Cylindrical Fiber 56
3.10 Numerical Results and Discussion 58
Figures 63

Chapter 4 A Novel Contact Angle Measurement Technique Based on Analysis of the Capillary Profile Around a Cylinder (ACPAC) 75
4.1 Introduction and Brief Literature Review 75
4.2 Mathematical Formulations of the ACPAC Technique for the ACRPAC Case 79
4.3 Computer Digital Image Techniques 84
4.4 Experimental Aspects of the ACRPAC Case 85
4.5 Experimental Results and Discussion of the ACRPAC Case 88
4.5.1 Contact Angle Measurements on Constant-Diameter Cylinders 88
4.5.2 Contact Angle Measurements on Conic Cylinders 89
4.6 Brief Introduction to the ACPAC Technique for the ACDPAC Case 92

4.6.1 Coordinate Transformation 93
4.6.2 Experimental Aspects of the ACDPAC Case 96
4.6.3 Experimental Results and Discussion of the ACDPAC Case 99
4.7 Hamaker Constants Determined from the Measured Surface Energies of the Fiber-Water-Oil Systems 101
4.8 Summary 106
Tables 110
Figures 115

Chapter 5 The ζ-Potential Measurements of Silicone Oil Droplets and Fiber Surfaces in Aqueous Solutions 121
5.1 The ζ-Potential Measurements of Silicone Oil Droplets Dispersed in Aqueous Solutions 121
5.2 Electrical Suspension Method 123
5.2.1 Principle 123
5.2.2 Electroosmotic Effects 126
5.2.3 Thermal Driven Convection Effect 128
5.2.4 Electrode Polarization Effect 130
5.2.5 Overall Measurement Error Analysis 130
5.3 Experimental Aspects of the ζ-Potential Measurements of Silicone Oil Droplets Dispersed in Aqueous Solutions 132
5.3.1 Apparatus 132
5.3.2 Preparation of the Silicone Oil-in-Water (O/W) Emulsions 132
5.3.3 Experimental Procedure 133
5.4 Experimental Results and Discussion 135
5.4.1 pH Effect 136
5.4.2 Electrolyte Effects 137
5.4.3 Effects of Ionic Surfactants 138
5.4.4 Summary 139
5.5 The ζ-Potential Measurements of Fiber Surfaces in Contact with Aqueous Solutions 140

5.6 Streaming Potential Technique 143
  5.6.1 The Origin of the Streaming Potential in Microchannel Flows 143
  5.6.2 Streaming Potential Equations 144
  5.6.3 Effect of Surface Conductance 147
  5.6.4 Determination of the ζ-Potential and the Surface Conductance λ_s 149
5.7 Experimental Aspects of the ζ-Potential Measurements of Glass Surfaces in Contact with Aqueous Solutions 151
  5.7.1 Experimental Set-up 151
  5.7.2 Preparation and Assembly of the Parallel-Plate Microchannels 152
  5.7.3 Streaming Potential Measurements 154
  5.7.4 Experimental Procedure 157
5.8 Experimental Results and Analyses 158
  5.8.1 Measurements of Surface Conductance Effect 160
  5.8.2 pH Effect 163
  5.8.3 Electrolyte Effects 165
  5.8.4 Effects of Ionic Surfactants 166
5.9 Determination of the EDL Interaction Parameters Dl, Da and κ^{-1} 167
Tables 169
Figures 172

Chapter 6 Numerical Solutions of Mass Transport Equations 184
6.1 1-D Mass Transport Equation 184
  6.1.1 Analytical Solution 184
  6.1.2 Numerical Solution 187
  6.1.3 The Colloidal Force and the Transforming Function 188
  6.1.4 1-D Numerical Results and Discussion 190
  6.1.5 Limitations of the 1-D Numerical Model 194
6.2 2-D Mass Transport Equation 197
  6.2.1 Boundary Conditions 199
  6.2.2 Calculation of $Sh(\phi)$ and $\overline{Sh}$ 200
  6.2.3 Transforming Functions 201

6.2.4 The Crank-Nicolson Method 203
6.2.5 Solution of the Finite Difference Equations (FDEs) 206
6.2.6 2-D Numerical Results and Discussion 209
Figures 213

Chapter 7 Experimental Results for Deposition Tests and Their Comparison with the Numerical Predictions 227
7.1 Introduction 227
7.2 Experimental 228
7.2.1 Materials 228
7.2.2 Preparation of the Silicone Oil-in-Water (O/W) Emulsions 230
7.2.3 Deposition Cell 231
7.2.4 Deposition Measurements 231
7.2.5 Determination of Sh 234
7.3 Deposition Experimental Results and Their Comparison with the Numerical Predictions 235
7.3.1 pH Effect 235
7.3.2 Electrolyte Effects 238
7.3.3 Effects of Ionic Surfactants 240
7.4 Hydrophobic Effect 243
Tables 249
Figures 251

Chapter 8 Conclusions and Recommendations 260
8.1 Major Academic Contributions 260
8.2 Future Research 263

References 266

List of Tables

4.1 Contact angles for four n-alkane liquids on the FC725-precoated constant-diameter cylinders, as measured by the ACPAC technique for the ACRPAC case and the Wilhelmy plate technique 110

4.2 Variation in the contact angle (θ) of decane on the FC725-precoated conic cylinder along its axial direction, with the local values of the radius (R_c) and the inclination angle (β) at the three-phase contact circle 110

4.3 The line tension (σ) and the contact angles (θ_∞) for four n-alkane liquids on the FC725-precoated solid surface, as derived from Equation (4.16) by using the contact angles measured on a conic cylinder 111

4.4 Contact angles for two silicone oil and pure DIUF water interfaces on the FC725-precoated glass fibers, as measured by the ACPAC technique for the ACDPAC case 111

4.5 Effect of the cationic surfactant, CTAB, on the contact angles of the silicone oil (A-type) and the DIUF water interfaces on the FC725-precoated glass fibers 112

4.6 Effect of the anionic surfactant, SDS, on the contact angles of the silicone oil (A-type) and the DIUF water interfaces on the FC725-precoated glass fibers 112

4.7 Effect of the anionic surfactant, SDS, on the contact angles of the silicone oil (B-type) and the DIUF water interfaces on the FC725-precoated glass fibers 112

4.8 Hamaker constants A_{owf} (or A_{132}) for the silicone oil droplet (phase 1, $\gamma_{ov}=26.10\pm0.14$ mJ/m^2) interacting with the bare glass fiber (phase 2, $\gamma_{fv}=71.56\pm0.39$ mJ/m^2) across aqueous solutions (medium 3 with varying surface tensions) 113

4.9 Hamaker constants A_{owf} (or A_{132}) for the silicone oil droplet (phase 1, $\gamma_{ov}=26.10\pm0.14$ mJ/m^2) interacting with the FC725-precoated glass fiber (phase 2, $\gamma_{fv}=13.87\pm0.51$ mJ/m^2) across aqueous solutions (medium 3 with varying surface tensions) 114

5.1 Values of the Henry correction factor $f_1(\kappa a)$ used in Equations (5.2) and (5.3) as a function of κa (Henry, 1931; Abramson et al., 1942; Hunter, 1981) 169

5.2 Temperature increase of the aqueous solution due to the Ohmic heating, as calculated from Equation (5.14) with the concentration of NaCl from 10^{-6} to 10^{-1} M and $E=1000$ V/m, $\Delta t=10$ s, and $C_v=1.0$ kcal/kg/°C and $\rho_w=998$ kg/m^3 169

5.3 Zeta-potential (ζ_p) of silicone oil droplets dispersed in aqueous solutions, zeta-potential (ζ_c) of the bare glass fiber surfaces in contact with aqueous solutions and their EDL interaction parameters (Dl, Da and κ^{-1}) across various aqueous solutions 170

5.4 Zeta-potential (ζ_p) of silicone oil droplets dispersed in aqueous solutions, zeta-potential (ζ_c) of the FC725-precoated glass fiber surfaces in contact with aqueous solutions and their EDL interaction parameters (Dl, Da and κ^{-1}) across various aqueous solutions 171

7.1 Dimensionless mass transfer rate Sh (Sherwood) numbers of silicone oil droplets onto the bare glass fiber surfaces in various aqueous solutions 249

7.2 Dimensionless mass transfer rate Sh (Sherwood) numbers of silicone oil droplets onto the FC725-precoated glass fiber surfaces in various aqueous solutions 250

List of Figures

2.1 A schematic diagram of oil droplet-fiber deposition cell 23

2.2 Cylindrical coordinate system (r,ϕ, z) used for deriving the general mass transport equation of oil droplet-fiber deposition problem 23

3.1a Schematic diagram of the van der Waals interaction between a molecule and a cylinder 63

3.1b The distance between a molecule at point O and a differential volume element at point P in a cylinder, where N is the projection point of the differential volume element P on the OMN plane, and oPN is in the cross-sectional plane (dotted line), which is normal to the OMN plane, $oP=\rho$, $oN=\rho\cos\phi$ and $PN=\rho\sin\phi$, $MN=z$, $OM=D+R+\rho\cos\phi$, $ON^2=z^2+(D+R+\rho\cos\phi)^2$, and $r^2=ON^2+PN^2=z^2+(D+R+\rho\cos\phi)^2+\rho^2\sin^2\phi$ 63

3.1c The total van der Waals interaction (Hamaker constant A_{132}) between a spherical particle (Phase 1) and a cylindrical solid (Phase 2) across an aqueous solution (Medium 3) 64

3.2 Comparison of the retarded and unretarded van der Waals forces between a spherical particle and a cylindrical collector 65

3.3 Comparison of the different retarded van der Waals force formulae for the sphere-cylinder and the sphere-plate systems 66

3.4 The effect of the curvature of the cylinder on the retarded vdW force between a sphere and an infinitely long cylinder ($B=\infty$) 67

3.5a The effect of the length of the cylinder on the retarded vdW force between a sphere and a cylinder for $A=1$ 68

3.5b The effect of the length of the cylinder on the retarded vdW force between a sphere and a cylinder for $A=10$ 69

3.5c The effect of the length of the cylinder on the retarded vdW force between a sphere and a cylinder for $A=100$ 70

3.6 (a) The front view of the two differential surface elements representing the electrical double layer (EDL) interaction between a spherical particle and a cylindrical fiber; (b) The top view of the differential surface element on the cylindrical fiber surface; (c) The side view of the differential surface element on the cylindrical fiber surface 71

3.7 The effect of the curvature of the cylinder on the EDL force between a spherical particle and an infinitely long cylindrical fiber (τ=10, Dl=+1000, Da=0) 72

3.8 The effect of $\tau=\kappa a_p$ on the EDL force between a spherical particle and an infinitely long cylindrical fiber (A=10, Dl=+1000, Da=0) 73

3.9 The effect of Da on the EDL force between a spherical particle and an infinitely long cylindrical fiber (A=10, τ=10, Dl=+1000) 74

4.1 Schematic diagram of the capillary rise profile around a conic cylinder for the ACRPAC case 115

4.2 Experimental set-up used to measure the contact angle using the ACPAC technique for the ACRPAC case 115

4.3 (a) Digital image of the capillary rise profile of hexadecane around the FC725-precoated conical cylinder at its tip (produced by a laser printer); (b) Digitized profile of the image shown in Figure 4.3a 116

4.4 (a) Digital image of the capillary rise profile of hexadecane around the FC725-precoated conical cylinder at its conic part (produced by a laser printer); (b) Digitized profile of the image shown in Figure 4.4a 117

4.5 The line tension (σ) and contact angles (θ_∞) derived from Equation (4.16) using the contact angles measured by the ACPAC technique for the ACRPAC case for the n-alkane liquids on the FC725-precoated conical glass cylinder 118

4.6 Schematic diagram of a capillary depression oil-water (O/W) interface around the FC725-precoated glass fiber 119

4.7 Experimental set-up for measuring the contact angle using the ACPAC technique for the ACDPAC case 119

4.8 (a, top) Digital image of the capillary depression profile of the silicone oil (A-type) and the pure DIUF water interface around the FC725-precoated glass fibre (produced by a laser printer); (b, middle) Digital image of the capillary "rise" profile of the silicone oil (A-type) and the pure DIUF water interface around the FC725 coated glass fibre after the video camera was purposely set upside down (produced by a laser printer); (c, bottom) Digitization of the image showed in Figure 4.8b 120

5.1 Experimental set-up for measuring the ζ-potential of the silicone oil droplets dispersed in aqueous solutions by using an electrical suspension method 172

5.2 The ζ-potential of the silicone oil (no. 1) droplets as a function of pH of the aqueous phase 173

5.3 The ζ-potential of the silicone oil (no. 1) droplets versus log concentration of two electrolytes with different valences 174

5.4 The ζ-potential of the silicone oil (no. 1) droplets versus log surfactant concentration of CTAB or SDS 175

5.5 Parallel-plate microchannel used in the streaming potential measurements 176

5.6 The linear relations of $\frac{\varepsilon_w \varepsilon_0 \Delta P_z}{\mu E_s \lambda_b}$ versus $\frac{1}{\delta}$ for the cases of $\lambda_s=0$ and $\lambda_s \neq 0$ for determining the ζ-potential at the solid-liquid interfaces and the surface conductivity λ_s from Equation (5.29), using the steaming potential technique 176

5.7 Schematic of experimental set-up for the streaming potential measurements of the parallel-plate microchannel 177

5.8 Experimental data of the streaming potential measurements and their linear curve fit using Equation (5.29) for the pure DIUF water 178

5.9 Experimental data of the streaming potential measurements and their linear curve fit using Equation (5.29) for the electrolyte solution of 10^{-3} M NaCl 179

5.10 Variations of the bulk conductivity (λ_b), the surface conductivity (λ_s) and the Dukhin number (Du) with log concentration of electrolyte NaCl 180

5.11 Variations of the ζ-potential of glass surfaces with pH of the aqueous phase 181

5.12 Variations of the ζ-potential of glass surfaces with log concentration of two electrolytes having different valences 182

5.13 Variations of the ζ-potential of glass surfaces with log concentration of two surfactants CTAB and SDS 183

6.1a Dimensionless droplet number concentration distribution (H in linear scale), $A_d=6.00$, $Dl=-1000$, $\tau=5$, $Sh=0.0645$ 213

6.1b Dimensionless droplet number concentration distribution (H in log scale), $A_d=6.00$, $Dl=-1000$, $\tau=5$, $Sh=0.0645$ 214

6.2a Dimensionless droplet number concentration distribution ($\tau=5$) 215

6.2b Variations of dimensionless mass transfer rate Sh with dimensionless deposition number A_d (τ=5) 216

6.3a Dimensionless droplet number concentration distribution (A_d=6.00, τ=5) 217

6.3b Variations of dimensionless mass transfer rate Sh with dimensionless EDL parameter Dl (A_d=6.00) 218

6.4a Dimensionless droplet number concentration distribution (A_d=6.00) 219

6.4b Variations of dimensionless mass transfer rate Sh with reduced radius od the oil droplet τ (A_d=6.00) 220

6.4c Variation of dimensionless mass transfer rate Sh with H_∞ used in the numerical simulations (A_d=6.00, Dl=+20, τ=10). The two dotted lines represent the limits of 10% deviation from the Sh_{cal}=0.0295 for H_∞=40 221

6.5 (a, left) The physical domain for the 2-D deposition problem; (b, middle) The transformed domain for the numerical simulation; (c, right) The finite difference stencil for the Crank-Nicolson scheme, where each multiplier, $a_{i,j}$, $b_{i,j}$, $c_{i,j}$, $d_{i,j}$, in Equation (6.25a) is placed beside its corresponding grid point(s) 222

6.6 Sh(ϕ) number versus ϕ in 2-D deposition case (A_d=6.00, Dl=0.0, Gr=0.50, Ef=-0.50, Sh_{ave}=1.4304) 223

6.7 Sh(ϕ) number versus ϕ in 2-D deposition case (A_d=6.00, Dl=0.0) 224

6.8a Dimensionless droplet number concentration distribution versus H and ϕ in 2-D deposition case (H in linear scale), A_d=6.00, Dl=0.0, Gr=0.05, Ef=-0.05, Sh_{ave}=0.1245 225

6.8b Dimensionless droplet number concentration distribution versus H and ϕ in 2-D deposition case (H in log scale), A_d=6.00, Dl=0.0, Gr=0.05, Ef=-0.05, Sh_{ave}=0.1245 226

7.1 Experimental set-up for the deposition measurements 251

7.2 (a, left) The deposition area under examination on the lateral surface of glass cylinder; (b, right) Magnified deposition area on the cylindrical surface 251

7.3 The snapshot of the silicone oil (No. 1) droplets on the bare glass bar in the pure DIUF water at t=15 min 252

7.4a Dimensionless mass transfer rate Sh (Sherwood) number as a function of pH of the aqueous phase 253

7.4b Total dimensionless interaction potential (vdW and EDL) between a silicone oil droplet and the bare glass fiber in the pure DIUF water (A_d=5.35, Dl=+48200, Da=+0.16, τ=10, Sh_{cal}=0.0153) 254

7.5a Dimensionless mass transfer rate Sh (Sherwood) number versus log concentration of two electrolytes with different valences (bare glass surface) 255

7.5b Dimensionless mass transfer rate Sh (Sherwood) number versus log concentration of two electrolytes with different valences (FC725-precoated glass surface) 256

7.6a Dimensionless mass transfer rate Sh (Sherwood) number versus log surfactant concentration of CTAB or SDS (bare glass surface) 257

7.6b Dimensionless mass transfer rate Sh (Sherwood) number versus log surfactant concentration of CTAB or SDS (FC725-precoated glass surface) 258

7.7 (a, upper) Digital image of silicone oil (No. 1) drop on the FC725-precoated glass slide in the pure DIUF water. The measured parameters are as follows: the contact angle $\theta=56.6^{\circ}$, the base radius of the sessile drop R_b=0.2729 cm and the drop volume V_o=0.0189 cm^3; (b, lower) Digital image of silicone oil (No. 1) drop on the bare glass slide in the pure DIUF water. The measured parameters are as follows: the contact angle $\theta=148.6^{\circ}$, the base radius of the sessile drop R_b=0.1234 cm and the drop volume V_o=0.0404 cm^3 259

Nomenclature

Notations

A	ratio of the radius of cylinder to the radius of oil droplet or particle, or cross-sectional area of two electrodes (m^2)
A_c	cross-sectional area of microchannel (m^2)
A_d	dimensionless adhesion number
A_{ij}	Hamaker constant for the interaction between phase i and phase j across vacuum (air) (J)
A_{132}, A_{owf}	Hamaker constant for the interaction between an oil droplet (phase 1) and a fiber (phase 2) across aqueous solution (medium 3) (J)
A_{ikj}	Hamaker constant for the interaction between phase i and phase j across medium k (J)
a, a_p	radius of oil droplet or particle (m)
$a_{i,j}$	constant as defined in Equations (6.25a) and (6.25b)
B	ratio of the length of cylinder to its radius
$B(\alpha)$	function of α as defined in Equation (6.14)
$b_{i,j}$	constant as defined in Equations (6.25a) and (6.25b)
C	potential coefficient defined in Equation (3.1) (J m^n/molecule^2), or constant as defined in Equation (5.15) (V^2/m^3), or dimensionless constant as defined in Equations (6.25a) and (6.25b)
C_1	constant as defined in Equation (6.2) (m^{-3})
C_2	constant as defined in Equation (6.5) (m^{-3})
$\overline{C}_2$	dimensionless constant as defined in Equation (6.9)
C_v	constant-volume specific heat capacity of aqueous phase (kcal/kg/^oC)
c	mole concentration (M or mole/l)
$c_{i,j}$	constant as defined in Equations (6.25a) and (6.25b)
$\underline{\underline{D}}$	droplet diffusion coefficient tensor (m^2/s)
D	separation distance between a particle and a cylinder (m), or dimensionless constant as defined in Equations (6.25a) and (6.25b)
D_0	interfacial contact separation distance, D_0=0.165 nm

d	separation distance (m)
d_i	normal distance of the measured point from the Laplacian curve (m)
$d_{i,j}$	constant as defined in Equations (6.25a) and (6.25b)
d_{rr}, $d_{\phi\phi}$	dimensionless components of droplet diffusion coefficient tensor
$\overline{d}$	dimensionless separation distance
Da	dimensionless EDL asymmetry parameter
Dl	dimensionless EDL parameter
Du	Dukhin numer
D_∞	droplet diffusion coefficient in the bulk (m^2/s)
E, $\underline{E}$	electric field strength or vector (V/m)
E	objective function as defined in Equation (4.12) (m)
E_s	streaming potential (V)
Ef	dimensionless electric field number
e	electron charge, 1.602×10^{-19} C
F, $\underline{F}$	force or force vector (N)
F_1, F_2	dimensionless universal hydrodynamic correction coefficients (UHCC)
$\overline{F}$	dimensionless force
$\overline{F}_1$	dimensionless vdW interaction force between a sphere and a finitely long cylinder
$\overline{F}_2$	dimensionless vdW interaction force between a sphere and an infinitely long cylinder
$\overline{F}_3, \overline{F}_4, \overline{F}_5$	dimensionless vdW interaction forces for the sphere-flat plate system
f(p)	dimensionless correction function as defined in Equation (3.19)
f	form factor as defined in Equation (5.26a) (m^{-1})
$f(H, \overline{\lambda})$	correction factor as defined in Equation (3.20)
$f_1(\kappa a)$	Henry function or correction factor as defined in Equations (5.2) and (5.3) and given in Table 5.1
f_1, f_4	dimensionless universal hydrodynamic correction coefficients (UHCC)

G	Gibbs free energy (J/m^2)
G(α)	function of α as defined in Equation (6.14)
g, $\underline{g}$	gravitational acceleration or vector (m/s^2)
g(H)	g(H)=H+1+A as defined in Equation (2.22)
$g_i(H,\phi)$, i=1-4	dimensionless functions as defined in Equation (2.22)
$G_i(\alpha,\beta)$, i=1-4	dimensionless function as defined in Equation (6.22)
Gr	dimensionless gravity number
H	dimensionless separation distance
h	capillary rise height (m)
h_0	relative capillary rise height (m)
I	unit tensor, or current (A)
$\underline{i}_r, \underline{i}_\phi, \underline{i}_z$	unit vectors in cylindrical-coordinate system
$\underline{j}$, j, J_0	droplet number flux vector or droplet number transfer rate (m^{-2} s^{-1})
K	total calculated points of the Laplacian curve
k	Boltzmann constant, 1.381x10^{-23} J/k
L	length of cylinder or microchannel (m)
l	separation distance between two electrodes, or the length observed along the axial direction of cylinder (m)
M	mole concentration (mole/l)
N	total measured points of the capillary profile
N(t)	number of the observed oil droplets on the fiber surface at time t
n	power as defined in Equation (3.1), n=6 for the Lifshitz-vdW potential
n	oil droplet number concentration (m^{-3})
n_i^0	number concentration of ions of type i in the bulk (m^{-3})
n_c, n_f, n_o, n_p	number density of molecules in cylinder, fiber, oil droplet and particle, respectively (m^{-3})
n_∞	oil droplet number concentration in the bulk (m^{-3})
$\bar{n}$	dimensionless oil droplet number concentration
P	perimeter (m) or pressure (N/m^2)

$\mathbf{P} = \dfrac{\varepsilon_c - \varepsilon_r}{\varepsilon_c + \varepsilon_r}$	dimensionless quantity as defined in Equation (2.14)
$p = \dfrac{2\pi r}{\lambda}$	reduced distance
P_w	wetted perimeter (m)
Q	Ohmic heating per unit time (J/s or W), or volume flux (m^3/s)
q	net charge on oil droplet (C)
q_e	electrostatic charge on per unit surface area of oil droplet (C/m^2)
R	radius of the three-phase contact circle, or radius of cylindrical fiber, or the principal radius (m), or electrical resistance (Ω or S^{-1})
r	radial cylindrical coordinate, or radius of circular capillary, or separation distance (m)
r_0	separation distance from the primary energy minimum (PEM) region (m)
r_∞	an "infinite" separation distance (m)
$\bar{r} = r/R$	dimensionless radial or separation distance
r^2	correlation coefficient
S	actual deposition area (m^2)
$\bar{s}$	dimensionless constant as defined [illegible] Equation (3.20)
Sh, Sh(ϕ)	Sherwood number
$\overline{Sh}$, Sh_{ave}	average Sherwood number along the azimuthal direction ϕ
T	absolute temperature (k)
t	time (s)
u	droplet velocity vector (s/m)
V	volume (m^3) or velocity (m/s)
V_1	vdW interaction potential between a sphere and a finitely long cylinder (J)
$\overline{V}_1$	dimensionless vdW interaction potential between a sphere and a finitely long cylinder
V_2	vdW interaction potential between a sphere and an infinitely long cylinder (J)

$\overline{V}_2$	dimensionless vdW interaction potential between a sphere and an infinitely long cylinder
$\overline{V}_3,\overline{V}_4,\overline{V}_5$	dimensionless vdW interaction potentials for the sphere-flat plate system
V_{eo}	electroosmotic velocity (m/s)
$V_z(y)$	z-directional velocity profile along y-direction (m/s)
v(r)	intermolecular vdW interaction potential (J/molecule^2)
v_1	vdW interaction potential between a molecule and a finitely long cylinder (J/molecule)
v_2	vdW interaction potential between a molecule and an infinitely long cylinder (J/molecule)
w	width of the observed strip (m)
W	width of rectangular cell or microchannel (m), or specific potential energy between planar surface (J/m^2)
X, x	x-coordinate (m)
Y, y, y_1	y-coordinate (m)
$\overline{y}$	dimensionless y-coordinate
z	axial coordinate or distance from the symmetric center in width direction (m), or valence
$\overline{z}$	dimensionless axial coordinate
z_i	valence of ion of type i

Greek Symbols

ε	dielectric constant (C/V/m or F/m)
ε_0	dielectric constant of vacuum, $\varepsilon_0=8.854\mathrm{x}10^{-12}$ C/V/m or F/m
ε_r	dimensionless or relative dielectric constant
λ	London characteristic wavelength or retardation parameter (m), or molar conductivity (m^2 S/mole)
λ_b	electrical conductivity in the bulk (S/m)
λ_s	specific surface conductivity (S)
$\overline{\lambda}$	dimensionless retardation parameter

δ	thickness of the microchannel (m)
σ	surface charge density (C/m^2), or line tension (J/m), or conductivity of aqueous phase in the bulk (Ω^{-1} m^{-1} or S/m)
γ	surface energy/tension or interfacial tension (J/m^2)
ρ	radial coordinate or local radius of curvature of the three-phase contact line (m), or density (kg/m^3)
$\rho(y)$	volume density of charge across the microchannel (C/m^3)
$\overline{\rho}$	dimensionless radial coordinate
ρ_o	density of oil phase (kg/m^3)
ρ_w	density of aqueous phase (kg/m^3)
$\Delta\rho=\rho_o-\rho_w$	density difference between the oil and aqueous phases (kg/m^3)
$\Delta\rho_0=\rho_w-\rho_o$	density difference between the aqueous and oil phases (kg/m^3)
$\Delta\rho=\rho_l-\rho_v$	density difference between the liquid and vapor phases (kg/m^3)
$\Delta\alpha$	mesh size for α variable
$\Delta\beta$	mesh size for β variable
$\Delta G=G_d-G_\infty$	difference of free energies of the EDLs separated by d and infinity (J)
Δh_m	measured capillary rise height (m)
ΔP	pressure drop, $\Delta P<0$ (N/m^2)
$\Delta P_z=-\Delta P$	pressure drop, $\Delta P_z>0$ (N/m^2)
ΔT	temperature increase (^{o}C)
Δt	time increment (s)
ΔV_0	electrical voltage applied across two electrodes (V)
α	dimensionless new variable as defined in Equations (6.13) and (6.21a)
β	local inclination angle (deg) or dimensionless new variable as defined in Equation (6.21b)
θ	contact angle or azimuthal angle (deg)
θ_1	supplementary contact angle (deg)
θ_∞	contact angle with no line tension effect (deg)
κ	Debye-Hückel parameter (m^{-1})

ζ	zeta-potential (V)
$\tau=\kappa a$	reduced radius of a particle or an oil droplet
μ	continuous phase viscosity (Pa s)
ψ	potential (J)
φ	tangential angle (deg)
ϕ	azimuthal coordinate (deg)
∇^2	Laplacian operator

Subscripts

0	in the primary energy minimum (PEM) region or on the solid surface
1	phase 1, or sphere 1, or the first principal radius
2	phase 2, or sphere 2, or the second principal radius
3	medium 3
ACPAC	ACPAC technique
actual	actual value
ADSA	ADSA technique
ave	average
b	buoyancy force or bulk
c	cylinder, or calculated, or conduction
cal	calculated value
col	colloidal force
d	at distance d, or drag force
e	electrical force
EDL	electrical double layer
exp	experimentally measured value
ext	external
f	fiber or electric field
fv	fiber-vapor interface
fw	fiber-water interface
g	gravitational
guess	guessing value

H	radial
i	ions of type i
i,j	grid point (i,j), i=0-imax, j=0-jmax
l	liquid
l0	reference position of liquid phase
lv	liquid-vapor interface
m	measured
max	maximum
min	minimum
o	oil
o0	reference position of oil phase
ov	oil-vapor interface
ow	oil-water interface
owf	oil droplet interacting with fiber across aqueous phase
p	particle
PEM	primary energy minimum
pred	predicted
r	radial
rr	radial
s	streaming or surface
sl	solid-liquid interface
sv	solid-vapor interface
t	total
v	vapor
v0	reference position of vapor phase
vdW	van der Waals
w	aqueous
w0	reference position of aqueous phase
Wilhelmy	Wilhelmy plate technique
wv	water-vapor interface
z	axial

α	in α direction or derivative with respect to α
$\alpha\alpha$	second-order derivative with respect to α
β	in β direction or derivative with respect to β
ϕ	azimuthal
$\phi\phi$	azimuthal
∞	in the bulk or infinity
+	cationic
-	anionic

Superscripts

0	in the bulk or reference value
Ret	retarded
+	valence equaling to +1
3+	valence equaling to +3

Chapter 1

Introduction

1.1 Motivation and Background

Introduction of a fiber into a liquid phase (e.g. water) containing dispersed droplets of another liquid phase (e.g. oil) may result in deposition of the oil droplets onto the fiber surface, depending on their interactions. A comprehensive study of such deposition phenomenon not only is of intrinsic interest in the field of colloid and interface science, but also has numerous direct and potential applications in industry.

Physically, the deposition process is governed by at least two types of colloidal forces and possibly external forces between the oil droplets through the aqueous phase and the fiber surface. According to the well-known Derjaguin-Landau-Verwey-Overbeek (DLVO) theory (Derjaguin and Landau, 1941; Verwey and Overbeek, 1948), here, the colloidal forces represent the van der Waals (vdW) and the electrical double layer (EDL) interaction forces. In colloid and interface sciences, theoretically, the vdW force can be quantitatively described by the van der Waals-Lifshitz theory (Lifshitz, 1956; Dzjalosinskij et al., 1961) or by semi-empirical approaches included in the acid-base theory (Fowkes and Patrick, 1967). The EDL force can be determined using the Derjaguin's theory (Derjaguin, 1934). The external forces can be the electrical force caused by the externally applied electric field through the liquid phase and the gravitational force exerted on the droplets (Adamczyk and van de Ven, 1981b).

The deposition process of liquid droplets onto a solid surface, both of which are immersed in another liquid, is involved in many industrial processes. The most significant applications are in petroleum, paper, fiber, textile and cosmetic industries. For example, how to efficiently separate oil droplets from the oil-in-water (O/W) emulsions, or the water droplets from water-in-oil (W/O) mixtures has been one of the critical problems for many years in the oil industry, especially in the oil sands and heavy oil industries (Masliyah, 1994). In the textile industry for finishing, silicone oils are usually padded onto a fabric from emulsion dispersions and then cured to form a durable elastometric coating which provides improved resistance to wrinkling or staining.

Chapter 1

Deposition of oils or polymers dispersed and stabilized with surfactants in aqueous medium is widely used in textile and paper industries to modify the binding and adhesive properties of fabrics and cellulose. On the other hand, removal of the dirty oil droplets attached to fabrics in textile detergency will solely depend on whether a proper surfactant solution capable of solubilizing the oils can be found (Carroll, 1988). Modification of the surface properties of solid substrates such as fibers by deposition of silicone and other oils from aqueous emulsions is also employed in textile and cosmetic industries (Carroll, 1988; Jachowicz and Berthiaume, 1989). In cosmetics, silicone oils are used as lubricating and/or hydrophobic agents in almost all hair and skin care formulations. The performance of these products is determined by the ability of the dispersed phase to interact with and adhere onto the keratinous fiber surface, by the total area coverage percentage and thickness distribution of the deposited silicone oil layer, and by the durability (i.e., resistance to detergents) of treatment (Jachowicz and Berthiaume, 1989; Berthiaume and Jachowicz, 1991; Jachowicz and Berthiaume, 1993).

In addition, deposition phenomenon of liquid droplets onto a solid surface is also frequently encountered in composite material and biomaterial engineering. For instance, interlaminar shear strength (ILSS) of fiber-reinforced plastic (FRP) is important in fiber composite material industry, and closely related to wetting of the fibers by the matrix polymer (Penn and Jutis, 1989; Ogawa and Ikeda, 1993; Drzal et al., 1994). Fiber assemblies are extensively used to filter a dispersed phase in emulsions, e.g., to purify contaminated water by filtration (Rajagopalan and Tien, 1979; Tien, 1989; Carroll, 1988). Another potential application of considerable interest is deposition of a liquid phase onto the surface of a bare optical fiber (Kawahara et al., 1983). When the deposited phase has a different refractive index from that of the fiber, light transmitted along the fiber will alter because the contact zones on the fiber act as optical windows. Based on the above mechanism, a variety of useful instruments can be developed. For instance, a new monitor was suggested by Kawahara et al. (1983) to detect and quantify oil pollutant concentrations in O/W mixtures. In the past decade, cellular deposition to solid surfaces has become a particularly popular subject because of its significance in many biotechnological and physiological applications (Stewart et al., 1989; Truskey and Pirone, 1990; Lahooti, et al., 1993; Ramsden et al., 1994; Ruardy et al., 1995).

1.2 Literature Review

Many theoretical, numerical and experimental studies of interactions between colloidal particles and solid substrates were accomplished and can be found in a proliferation of publications. In the past, the major focus was on either deposition of solid particles on solid substrates such as fibers, or the interaction between the particles themselves, i.e. liquid droplet coalescence, mutual coagulation of solid particles dispersed in liquid medium. The first kind of research topic, for example, is directly related to the surface treatment of pulp fibers used in papermaking (Alince, 1989; Alince et al., 1991; Alince and van de Ven, 1993) or engineering fibers used in fiber composites (Penn and Jutis, 1989), while the second is closely associated with the stability of colloidal emulsions (Okada and Akagi, 1987; Okada et al., 1990a; 1990b; Sanders et al., 1995; Deshiikan and Papadopoulos, 1995a; 1995b) or suspensions (Bochkarev et al., 1995). In contrast, few papers were devoted to elucidating the complex mechanism of interaction between liquid dispersions and solid substrates in aqueous solutions (Adamczyk and van de Ven, 1981b; Jachowicz and Berthiaume, 1989; Berthiaume and Jachowicz, 1991). There is an apparent lack of detailed technical information describing the interactions between a liquid droplet and a solid when both are submerged in various aqueous solutions. This fact may be partly caused by insufficient knowledge on the surface properties and the electrical properties of the liquid droplets dispersed in different emulsions. In practice, it is still practically difficult to accurately determine the vdW and EDL interaction forces. The unfortunate imbalance in emphasis results in the inevitable application of the theory of solid particle-solid surface interaction to liquid droplet-solid surface systems, though these two systems are rather different. As was described previously, a variety of industrial processes and applications rely inherently on a thorough understanding of the colloidal and external forces between a liquid droplet and a solid surface. Academically, it is not clear whether the existing DLVO theory, which was originally derived for describing coagulation of colloidal dispersions, is accurate enough or even suitable for describing the interactions between a liquid droplet and a solid surface.

A literature review will be given as follows on deposition of liquid droplets onto a solid surface submerged in another liquid, as well as its wide applications. A thorough literature search shows that there have been some preliminary attempts to understand the basic aspects governing the deposition and spreading kinetics of emulsion droplets onto a solid surface. Some main findings and existing problems in the literature will be summarized below in order to highlight why and how this thesis project is designed and what major research objectives are conceived in the present work.

1.2.1 The DLVO Theory

In terms of the DLVO theory of colloidal dispersions, there are two kinds of interaction forces between the colloidal particles and a solid surface, the vdW force and the EDL force. These two types of colloidal forces are discussed in many publications.

Generally speaking, there are essentially two methods to calculate the vdW interaction between approaching particles and a solid surface as a function of their separation distance (Gregory, 1981; Israelachvili, 1985). In the first, due largely to Hamaker (Hamaker, 1937), the interaction formula is derived by a pairwise summation of all the relevant intermolecular interactions. The second, more rigorous, method is based on the Lifshitz theory (Lifshitz, 1956; Parsegian, 1975) and depends entirely on their dielectric constants and refractive indices of the interacting media. It should be pointed out that, nevertheless, all the formulae for the vdW forces between large bodies of different shapes derived in terms of the Hamaker theory remain valid even within the Lifshitz's framework. The only thing that changes is the way in which the Hamaker constant is determined. Despite a number of shortcomings, the older Hamaker method continues to be quite widely used. This is mainly because of its great convenience and the fact that, for many practical systems, the Hamaker constants can be readily calculated by relating them properly to their surface and/or interfacial tensions.

It should be noted that, in the past, the computation of the vdW interaction between a spherical particle and a cylindrical surface was, however, usually performed under the assumption of a sphere interacting with an infinitely large flat plate (Adamczyk and van de Ven, 1981a; 1981b; Sanders, et al., 1995). Such a simple model neglects the possible large curvature and finite-size effects on the vdW interaction between a sphere and a finitely sized cylinder. In the literature, exact and approximate analytical expressions are available for the vdW interaction potentials between bodies of appropriate geometric combinations, such as two parallel flat plates, spheres, parallel cylinders, crossed cylinders, and a sphere and a flat plate (Israelachvili, 1985). Recently, Zeman and Wales (1981) and Papadopoulos and Kuo (1990) presented numerical methods to determine the vdW interaction energy for a spherical particle in a pore geometry. Bhattacharjee and Sharma (1995) obtained general and asymptotic analytical expressions for the same geometric configuration using the Hamaker microscopic approach. They all found that a commonly used simple model of a sphere interacting with a semi-infinitely large flat plate is reasonable only for very small particles close to the inner wall of a cylindrical pore, but in all other cases, it seriously underestimates the interaction energy. However, there is no similar work to consider the curvature and the finite-size effects on the vdW interaction between a sphere and a cylinder where the sphere is located outside of the cylinder. Theoretically, it is not clear how large an error will be caused by the sphere-flat plate approximation when it is used to calculate the vdW interaction between a spherical particle and a finitely sized (both the length and the radius) cylinder at an arbitrary separation distance. Therefore, a general theoretical method is required to obtain the accurate vdW interaction potential and force between a spherical particle and a cylinder without invoking the sphere-flat plate approximation.

On the other hand, the electrical double layer (EDL) interaction between an approaching sphere and a cylinder as a function of separation distance also plays an important role in the flow of colloidal emulsions or suspensions through a filter composed of many cylinders of fibers or other materials. This kind of interaction sometimes becomes essential to the problems of colloidal stability and particle deposition onto a cylindrical collector. In the past, similar to the case for the van der Waals (vdW) interaction, the computation of the EDL interaction between a spherical particle and a cylindrical surface, was, however, performed using the assumption of a sphere interacting with an infinitely large flat plate (Hogg, et al., 1966; Adamczyk and van de Ven, 1981b; Masliyah, 1994; Sanders et al., 1995). Regardless of possible large curvature effects that the cylindrical surface may cause, the flat plate approximation is often applied for simplicity. In the literature, the exact or approximate analytical expressions are available only for the EDL interaction potentials between two similar or dissimilar EDLs of appropriate geometric combinations, such as two parallel flat plates, two spheres, a sphere and a flat plate. When either radius of the two spheres is chosen to be infinity, the EDL interaction formula between two spheres becomes the widely used HHF (Hogg, Healy and Fuerstenau, 1966) expression for a sphere interacting with an infinitely large flat plate. It is obvious that the flat plate approximation always overestimates the EDL interaction between a sphere and a cylinder. However, a thorough literature search indicates that there has been no effort made yet to account for the curvature effect of the cylindrical EDL for this case. In fact, it has become common practice to employ the flat plate approximation for this geometry without any justification. It is not clear how large an error this approximation may cause when it is used to calculate the EDL interaction between a sphere and a cylinder at an arbitrary separation distance.

Recently, Miklavcic et al. (1994; 1995) performed some calculations of the EDL interaction between a charged spherical particle and a charged collector through a liquid medium. Nevertheless, the validity of their numerical data needs to be investigated.

In summary, a general theoretical method is needed to calculate the vdW and EDL interaction forces between a spherical particle and a cylinder without invoking the widely used sphere-flat plate approximation. Furthermore, the wettability of the solid-liquid-liquid systems and the ζ-potentials of oil droplets and the solid surface in an aqueous solution should be accurately measured in order to determine accurately the vdW and EDL forces, respectively.

1.2.2 Deposition Kinetics

So far a literature search has not yielded systematic studies covering the static deposition and slow spreading phenomena of small emulsion droplets onto a collector. In the literature, there are some papers focusing on cellular deposition onto solid surfaces and the subsequent spreading process (Stewart et al., 1989; Lahooti et al., 1993; Ruardy et al., 1995). These processes, nevertheless, are considerably different from those occurring in usual colloidal systems consisting of liquid droplets and solid surfaces in another liquid phase because of cell dimensions, its special properties and different liquid properties. Hence, these results may not be applicable to these emulsion systems.

Some experimental efforts to achieve fundamental understanding of the deposition kinetics of silicone oils from the O/W emulsions onto keratin fibers were made by Jachowicz and Berthiaume (Jachowicz and Berthiaume, 1989; Berthiaume and Jachowicz, 1991). Specifically, the effects of various factors such as type of oil, type of emulsifier, pH value, and presence of electrolyte on the deposition process were partially studied. They also explored to certain extent the contributions of other parameters including oil viscosity, emulsifier concentration and its ionic features to the deposition. However, their purely experimental work only allowed a less quantitative discussion of the overall deposition process. Secondly, they determined the amounts of the deposited silicone oils on fibers by the difference of oil droplet concentrations before and after deposition occurred, which were calculated from a calibration of solution turbidity versus oil droplet concentration. Generally, it is difficult to estimate the overall accuracy of such an indirect measurement method. Thirdly, they could not explain why the measured deposition was not decelerated or sometimes even accelerated by the repulsive EDL potential barrier created after an oil film on the fiber surface was formed. Neither quantitative comparison nor reasonable agreement was found between their experimental results and any theoretical or numerical predictions.

It becomes an obvious fact that thorough knowledge of the interactions of the liquid droplets through another liquid phase with a solid surface in static (or stationary) case in general is prerequisite to one's full understanding of the colloidal system. A comprehensive numerical model based on the complete mass transport governing equation of the deposition process should be developed. Then a complete mechanistic study of the static deposition occurring in different liquid phases has to be carried out to verify the numerical simulations based on the suggested model and to examine the validity of the DLVO theory.

In the past two decades, a number of publications were concentrated on the dynamic deposition kinetics of colloidal particles onto collectors of several typical shapes by using various numerical or experimental methods (Payatakes et al., 1974; Rajagopalan and Tien, 1977; Rajagopalan and Kim, 1981). With the progress in modern numerical simulation methods, such numerical solutions proliferated in recent years. They can be exemplified by the numerical results for deposition of colloidal particles onto cylindrical collectors (Adamczyk and van de Ven, 1981b). Numerical results are also available for the spherical collectors (Prieve and Ruckenstein, 1974), rotating-disk (Dabros et al., 1977; Dabors and Adamczyk, 1979) and parallel-plate and cylindrical channels (Adamczyk and van de Ven, 1981a). An excellent and comprehensive review paper on this topic was published by Adamczyk et al., 1983a. However, there remain some shortcomings with respect to these results. First of all, most of them had to employ certain assumptions in order to derive simple analytical relations for specific cases. Therefore, some of these theoretical results lack generality and may be valid only to a limited extent for practical applications. Secondly, the values of some important parameters used in these parametric studies were chosen and changed arbitrarily without any practical justifications. In these numerical simulations, it is common practice that each parameter is changed separately and thus its individual effect on the deposition kinetics is examined. In practice, it is an apparent fact that alternation of a factor might simultaneously cause appreciable changes on the values of several parameters. For instance, it is well known that changes on electrolyte type and concentration will definitely cause variations of several parameters such as the Hamaker constant, the zeta potentials of the solid-liquid-fluid system, in additional to the Debye-Hückel thickness. Finally, to date, there has not been relevant experimental data to verify most of these theoretical or numerical results. One exception is the good agreement reported between these predictions and experimental results for the dynamic deposition case in impinging jet flow (Dabros and van de Ven, 1983; 1987; Sanders et al., 1995).

1.3 Research Objectives

Based on the current status of the above research areas, this investigation is designed to fill the gap and establish a bridge between the theoretical model and the physics of deposition process. More specifically, this thesis will concentrate on understanding the deposition phenomenon of small oil droplets onto fiber surfaces in aqueous solutions. The main strategy employed in the project is to utilize proper experimental techniques to determine the relevant parameters required in the vdW and EDL interactions and then use the experimental deposition data to examine the numerical predictions based on the existing DLVO theory. Accordingly, this project is divided into three steps, which are then tackled chronologically.

1. Theoretical derivations of the vdW and EDL interactions between a spherical particle and a cylindrical fiber

Briefly, based on the Hamaker approach, a general method is developed to compute the retarded vdW interaction potential and force between a spherical particle and a cylinder (Gu and Li, 1998h). The effects of the relative dimensions of the sphere to the cylinder are examined by this general method. First, the unretarded vdW interaction potential between these two bodies is obtained by pairwise summation of all the relevant intermolecular interactions and evaluated by accurate multiple numerical integrals. The interaction potential is then modified to account for the retardation effect by incorporating a correction factor, which depends on the separation distance and the characteristic wavelength of the interactions. Since the spherical particles are small relative to the cylindrical collector, the correction factor for the sphere-plate interaction potential used in the well-known SHH equation (Suzuki, Ho and Higuchi, 1969) is used to calculate the retarded vdW force for the present case.

The curvature effect of the cylinder on the total EDL interaction is also studied in a similar fashion. The procedure used by Hogg, Healy and Fuerstenau (HHF) (1966) in deriving the EDL interaction potential between two spherical EDLs is followed. First, the EDL interaction potential between two differential surface elements, one on the spherical EDL and the other on the cylindrical EDL, is approximated by that between two parallel overlapping flat EDLs at the same separation distance. Then the Derjaguin's integration method (Derjaguin, 1934) is extended to evaluate the total EDL interaction potential between a spherical particle and a cylindrical collector. Hence, the effect of curvature of the cylinder on the total EDL interaction can be accounted for by the present configuration. Since the final solution is expressed by a two-dimensional integral equation that can not be integrated analytically, accurate numerical integration has to be sought. Eventually, the numerical predictions of the EDL interaction force for the sphere-cylinder system are compared with the analytical results of the EDL interaction force for the sphere-flat plate system at various separation distances. Consequently, the validity of the widely employed sphere-flat plate approximation can be assessed quantitatively.

2. Experimental determinations of the parameters involved in the vdW and EDL interactions between a spherical particle and a cylindrical fiber in a variety of aqueous solutions

After the curvature and finite size effects and the retardation effect on the vdW interaction are considered, the remaining task is to determine the Hamaker constant in the vdW force equation. By following the Hamaker method (Hamaker, 1937) and relating the Hamaker constant to the surface and interfacial tensions of the deposition system (Israelachvili, 1985), this constant can be determined experimentally. Currently, the surface tensions and interfacial tensions of liquid-fluid interface can be measured with satisfactory accuracy using existing advanced experimental techniques, such as the axisymmetric drop shape analysis (ADSA) technique developed by Neumann and co-workers (Rotenberg et al., 1983; Cheng et al., 1990; Li et al., 1992). Then in terms of the equation of state for interfacial tensions (Li and Neumann, 1992), the interfacial tensions of solid-fluid interface can be calculated from the relevant surface/interfacial tensions and contact angles of the solid-liquid-fluid systems, both of which can be measured by the ADSA technique. A new contact angle measurement technique is also developed in the course of this project. It can be used to accurately measure the contact angle by analysis of capillary profile around a cylinder (ACPAC) and will be described in detail in Chapter 4 (Gu et al., 1997a; Gu and Li, 1998a; 1998b).

The EDL interaction between a spherical particle and a flat collector can be well described by the general HHF expressions named after Hogg, Healy and Fuerstenau (1966). However, some effort is made in order to account for the curvature effect of the cylindrical collector on the resulting EDL interaction. The next tasks are to accurately measure the zeta-potentials (ζ_p) of oil droplets dispersed in a variety of aqueous solutions (Gu and Li, 1997b; 1997c; 1998c; 1998d; 1998g) and to accurately measure the zeta-potentials (ζ_c) of fiber surfaces in contact with varying aqueous phases (Gu, et al., 1999a). The Debye-Hückel constant (κ) also needs to be determined properly. These three quantities are directly involved in the EDL interaction expressions.

Once such experimentally determined colloidal forces (vdW and EDL forces) are available, the deposition kinetics can be predicted by substituting the interaction forces into the general mass transfer equations and numerically solving the differential equations.

3. Numerical simulations and experimental measurements of deposition kinetics

A thorough theoretical study on the deposition kinetics is carried out by numerically solving the mass transport equations for one-dimensional (1-D) and two-dimensional (2-D) cases. An experimental set-up is devised to implement a systematic investigation of the deposition processes of silicone oil droplets onto different fiber surfaces in a variety of aqueous solutions. With the numerical and experimental results (Gu and Li, 1999b), quantitative comparisons can be made and the existing DLVO theory can be justified. In particular, the effects of both surface properties of fiber material and liquid properties of the aqueous phases used on the deposition kinetics can be identified numerically and experimentally.

After going through the above numerical and experimental studies, the following principal research objectives are conceived to achieve a fundamental knowledge of the overall deposition processes of small oil droplets onto solid surfaces in aqueous emulsions: **1**. To derive the general formulas for calculating the vdW and EDL forces between a spherical particle and a cylindrical collector; **2**. To devise experimental techniques to determine the important parameters in vdW and EDL force equations, and thus to correctly predict overall deposition kinetics; **3.** To conduct systematic numerical and experimental studies on the fiber-oil-water deposition systems; and to compare the experimental results with the numerical predictions of deposition kinetics.

In order to state the contents of this project clearly, it is composed of the following four main parts: **1.** Introduction to the thesis research topic and the literature review of its current status (Chapter 1); followed by deriving the general mass transport equations which include the colloidal and possibly external forces (Chapter 2); **2.** Theoretical derivations (Chapter 3) and experimental determinations of the vdW interaction (Chapter 4) and the EDL interaction (Chapter 5) between a spherical particle and a cylindrical fiber in varying aqueous solutions; **3.** Numerical simulations of the mass transport equations for the 1-D and 2-D cases (Chapter 6), their comparison with the deposition test data and discussions (Chapter 7); and **4.** Summary of major conclusions and some suggestions on future research following this thesis research (Chapter 8).

Chapter 2

Mass Transport Equations

2.1 Introduction

When a fiber of suitable material is introduced into a deposition cell containing liquid phase (e.g. water) containing dispersed droplets of another liquid phase (e.g. oil), deposition and spreading of the oil droplets onto the fiber surface occur. The mass transfer of such Brownian oil droplets from the bulk oil-in-water (O/W) emulsions toward the fiber surface is governed by the continuity equation, which can be expressed in the following form:

$$\frac{\partial n}{\partial t} + \nabla \cdot \underline{j} = 0 \qquad (2.1)$$

where, n is oil droplet number volume concentration and t is time, $\underline{j}$ is droplet flux vector. Equation (2.1) is more generally called the mass transport equation. It is valid for a dilute mono-dispersion such that the interactions between the emulsion droplets themselves are negligible. In this study, the silicone oil was used as the only dispersed phase and all the oil-in-water (O/W) emulsions were made by suspending 0.25% (v/v) silicone oil in the aqueous solutions. The poly-disperse droplet effects are not present. Hence, the deposition process of the O/W emulsion droplets onto a cylindrical surface can be described by Equation (2.1). For a steady state, the first term in Equation (2.1) drops off, i.e., $\frac{\partial n}{\partial t} = 0$, the general mass transport equation becomes:

$$\nabla \cdot \underline{j} = 0 \qquad (2.2)$$

Further, the droplet flux vector, $\underline{j}$, can be decomposed into three contributions, fluid convection, Brownian diffusion, and migration effect under various force fields as follows:

$$\underline{j} = \underline{u}n - \underline{\underline{D}} \cdot \nabla n + \underline{\underline{D}} \cdot \underline{F}_t \frac{n}{\mathbf{k}T} \qquad (2.3)$$

where $\underline{u}$ is the droplet velocity, $\underline{\underline{D}}$ is droplet diffusion coefficient tensor, $\underline{F_t}$ is the total forces acting on the oil droplets, **k** is the Boltzmann constant and T is the absolute temperature. Generally, $\underline{F_t}$ is composed of the colloidal forces and the external forces,

$$\underline{F_t} = \underline{F_{col}} + \underline{F_{ext}} \quad , \tag{2.4}$$

For a static deposition process, i.e., there is no appreciable bulk convection flow of the O/W emulsions, then $\underline{u}=\underline{0}$. Thus, there are no hydrodynamic forces and torque acting on oil droplet. The mass transfer Equation (2.2) becomes:

$$\nabla \cdot \underline{j} = \nabla \cdot [-\underline{\underline{D}} \cdot \nabla n + \underline{\underline{D}} \cdot (\underline{F_{col}} + \underline{F_{ext}}) \frac{n}{\mathbf{k}T}] = 0 \tag{2.5}$$

It can be seen from the above equation that, for the steady static deposition case, the deposition process is controlled by the gradient of oil droplet number concentration near the fiber, and the colloidal and external forces acting on the droplets. Here a further restriction is that the droplet velocity induced by the action of the colloidal forces and the external forces at the position far from the fiber surface must be so small that the undisturbed emulsion phase can be assumed stationary. Thus the bulk migration effect is negligible and the above mass transport equation is applicable.

2.2 Colloidal Forces

There are two kinds of the colloidal forces involved in the mass transfer process: the van der Waals (vdW) interaction force and the force caused by two overlapped electrical double layers (EDLs). The latter is simply called the EDL force. Thus,

$$\underline{F_{col}} = \underline{F_{vdW}} + \underline{F_{EDL}} \tag{2.6}$$

Their specific expressions and accurate determinations will be given in details in Chapter 3, respectively. It is noted that these two forces always act between the oil droplet and the fiber in the radial direction. The interactions between droplets themselves are assumed to be negligible for diluted emulsions. They can be inward or outward, depending on whether they are attractive or repulsive. Their magnitudes are dependent only on the separation distance between the oil droplet and the fiber surface. For the deposition cell illustrated in Figure 2.1, due to the axisymmetry in the system, a cylindrical coordinate system (r, ϕ, z) is chosen and shown in Figure 2.2. Then the total colloidal force acts along the chosen radial direction only, i.e.,

$$\underline{F_{col}} = F_{col}(r)\underline{i_r} \tag{2.7}$$

where, $F_{col}(r)$ is module of the total colloidal force $\underline{F_{col}}$ and $\underline{i_r}$ is a unit vector that points outwards along the radial direction.

2.3 One-dimensional (1-D) Mass Transport Equation

In order to derive a one-dimensional (1-D) mass transport equation, three assumptions are made as follows. First, for a dilute mono-dispersion such as the O/W emulsions studied in this work, the silicone oil droplets are assumed to be much smaller than the glass fibers. For the case of small particles with the sizes in the range of 0.1-10 μm (Adamczyk and van de Ven, 1981b; van de Ven, 1989) and a large collector (Masliyah, 1994; Sanders et al., 1995), the interactions between the oil emulsion droplets themselves can be negligible. Secondly, the effect of the presence of the cylinder on the droplet diffusion coefficient is neglected. Thirdly, there are no external forces involved in the deposition systems. As will be shown in Section 2.5, if the first assumption is kept but the remaining two assumptions are discarded, the deposition process can be described by a two-dimensional (2-D) mass transport equation. Physically, the first two assumptions mean that the droplet diffusion coefficient is not affected by the presence of surrounding droplets and solid surface. Therefore, it becomes independent of position and orientation of one droplet relative to another or cylinder, i.e.,

$$\underline{\underline{D}} = D_\infty \underline{\underline{I}} \tag{2.8}$$

where, $\underline{\underline{I}}$ is a unit tensor and D_∞ is the droplet diffusion coefficient in the bulk emulsions and is given by the well-known Stokes-Einstein equation for a dilute dispersion:

$$D_\infty = \frac{\mathbf{k}T}{6\pi\mu a} \tag{2.9}$$

where, μ is viscosity of the bulk emulsion and *a* is the radius of an oil droplet. Strictly speaking, Equation (2.9) is valid for an infinite dilution only. The detailed discussion on the various forms of the diffusion coefficient as influenced by the approximity of other particles can be found elsewhere (van de Ven, 1989).

The third assumption indicates that only colloidal forces need to be considered. Then for the static deposition case, the droplet flux vector in Equation (2.3) becomes:

$$\underline{j} = -D_\infty \nabla n + D_\infty \underline{F_{col}} \frac{n}{\mathbf{k}T}$$

Further substituting the above expression into Equation (2.5) gives the mass diffusion equation:

$$\nabla \cdot \underline{j} = D_\infty[-\nabla^2 n + \frac{1}{\mathbf{k}T}\nabla \cdot (n\underline{F_{col}})] = 0 \qquad (2.10)$$

As shown above, $\underline{F_{col}} = F_{col}(r)\underline{i_r}$ and thus n=n(r), i.e., the droplet number concentration only changes along the radial direction in the cylindrical coordinate system (r, ϕ, z) in Figure 2.2. Equation (2.10) can be rewritten as:

$$\frac{1}{r}\frac{d}{dr}[-r\frac{dn(r)}{dr} + \frac{rn(r)F_{col}(r)}{\mathbf{k}T}] = 0 \qquad (2.11)$$

Equation (2.11) is a second-order ordinary differential equation, which is valid for the static deposition case without the external forces. In this case, Equation (2.5) reduces to the one-dimensional (1-D) mass transport equation as shown by Equation (2.11). Detailed derivations of the analytical and numerical solutions of the 1-D mass transport equation will be described in Chapter 6.

2.4 External Force Fields

All the above derivations are obtained in the absence of external forces. Since the colloidal forces are oriented only in the radial direction and their magnitudes depend only on the gap width between the oil droplet and the fiber surface, the general mass transport Equation (2.2) reduces to a one-dimensional second-order ordinary differential equation, i.e., Equation (2.11). Nevertheless, if the external force fields are present, the local mass transfer rate will depend not only on the magnitudes of these fields but also on their orientation relative to the fiber surface. However, the deposition of droplets in arbitrarily oriented external fields can not be readily analyzed numerically because the usually adopted "symmetry" boundary conditions, i.e., $\frac{\partial n}{\partial \phi}\Big|_{\phi=0,\pi} = 0$, are not satisfied. Hence, only the external forces that are vertically directed either downward or upward will be investigated, assuming that the fiber is placed horizontally inside the deposition cell. Under this restriction, the external forces do not depend on the z coordinate. In additional to universally existing colloidal forces, the deposition process is also studied in the presence of the two frequently encountered external force fields.

2.4.1 Gravitational Field

A net gravity and buoyancy force $\underline{F_g}$ on a spherical droplet can be expressed by the following formula:

$$\underline{F_g} = \frac{4}{3}\pi a^3 \Delta\rho \underline{g}$$

where $\Delta\rho=\rho_o-\rho_w$ is the density difference between the oil and aqueous phases, and $\underline{g}$ is the gravitational acceleration vector. Depending on the density difference, the net gravitational force, $\underline{F_g}$, can be either upward ($\rho_o<\rho_w$) or downward ($\rho_o>\rho_w$). It is worthwhile mentioning that, if $\Delta\rho$ is small or the fiber is purposely placed vertically, the gravitational field will not affect the deposition process of oil droplets onto the fiber surface.

Referring to the cylindrical coordinate system (r, ϕ, z) depicted in Figure 2.2, $\underline{F_g}$ can be easily decomposed into two components, one is perpendicular and the other is tangent to the collector surface,

$$\underline{F_g} = \frac{4}{3}\pi a^3 \Delta\rho g(-\cos\phi \underline{i_r} + \sin\phi \underline{i_\phi}) \tag{2.12}$$

where, ϕ is the azimuthal coordinate and $\underline{i_\phi}$ is a unit vector along the azimuthal direction.

2.4.2 Electric Field

It has long been experimentally observed that oil droplets dispersed in an aqueous emulsion are usually charged to some extent. If an external electric filed of intensity $\underline{E}$ (directed either downward or upward) is applied intentionally, there are electrical forces acting on these charged droplets whose magnitude is determined by the equation

$$\underline{F_f} = q\underline{E} = \pm q|\underline{E}|(-\cos\phi \underline{i_r} + \sin\phi \underline{i_\phi}) \tag{2.13}$$

where q is a net charge on the oil droplet, $|\underline{E}|$ represents the magnitude of the electric field vector, $\underline{E}$, and the "±" signs represent the cases in which the electric filed is applied downward (+) or upward (-). If the influence of the fiber surface on the externally applied electric field is considered, the electrical force becomes (Adamczyk and van de Ven, 1981b)

$$\underline{F_f} = \pm q|\underline{E}|[-(1+P\bar{r}^{-2})\cos\phi\,\underline{i_r} + (1-P\bar{r}^{-2})\sin\phi\,\underline{i_\phi}] \tag{2.14}$$

where, $\bar{r} = \frac{r}{R}$, r is the radial coordinate and R is the radius of fiber, $P = \frac{\varepsilon_c - \varepsilon_r}{\varepsilon_c + \varepsilon_r}$, ε_c and ε_r are the dimensionless dielectric constants of the cylinder and the aqueous medium respectively. In case $P \approx 0$ ($\varepsilon_c \approx \varepsilon_r$) or the oil droplet is located far away from the fiber surface ($\bar{r} \gg 1$), Equation (2.14) will reduce to Equation (2.13) that takes no account of the intrusion of the fiber body into the applied electric field. For the thin non-conducting fibers studied here, their effect on the externally applied electric field is negligible.

Combining $\underline{F_g}$ in Equation (2.12) and $\underline{E_f}$ in Equation (2.13) together, the sum of the external forces is equal to:

$$\underline{F_{ext}} = (\frac{4}{3}\pi a^3 \Delta\rho g \pm q|\underline{E}|)(-\cos\phi\,\underline{i_r} + \sin\phi\,\underline{i_\phi}) = F_{ext,r}(\phi)\underline{i_r} + F_{ext,\phi}(\phi)\underline{i_\phi} \tag{2.15}$$

It can be seen from the above expression that, in fact, the two external forces act together on an oil droplet as a joint external force. They either strengthen or counteract each other, depending on the directions they exert on the droplet. It is also noted that the total external force depends only on the orientation of the droplet relative to the cylindrical collector, regardless of its separation distance from the fiber surface. This is because these two external force fields are both conservative.

2.5 Two-dimensional (2-D) Mass Transport Equation

In the previous sections, it has been mentioned that the total colloidal force acts along the radial direction only and its magnitude depends only on the separation distance between the oil droplet and the collector surface. On the other hand, the total external force of the gravitational field and the electric field force depends only on the orientation of the droplet relative to the cylindrical collector, regardless of its separation distance from the fiber surface. Therefore, the deposition predictions in the presence of the colloidal forces and external forces become a two-dimensional boundary value problem.

If the O/W emulsion is still assumed to be dilute mono-dispersion such that the interactions between the oil emulsion droplets can be negligible and the droplet diffusion coefficient becomes independent of position and orientation of one droplet relative to another. However, the droplet diffusion coefficient tensor depends on its relative position to the fiber surface if the presence of the collector surface is taken account. Using the correction method developed by van de Ven (1989) and Masliyah (1994) for the sphere-flat plate geometry, the diffusion coefficient tensor for the present case can be approximated as (Sanders et al., 1995):

$$\underline{\underline{D}} = D_{\infty} \begin{pmatrix} d_{rr} & 0 \\ 0 & d_{\phi\phi} \end{pmatrix} \tag{2.16}$$

where $D_{rr}(r)=D_{\infty}d_{rr}= D_{\infty}f_1(r)$ and $D_{\phi\phi}(r)=D_{\infty}d_{\phi\phi}= D_{\infty}f_4(r)$. The parameters $f_1(r)$ and $f_4(r)$ in the above expressions represent the universal hydrodynamic correction coefficients (UHCC), where f_1 was developed by Brenner (1961) and f_4 was given by Goldman et al. (1967a; b). These two coefficients account for the deviation of the actual droplet diffusion coefficient from D_{∞} that is determined from the Stokes-Einstein Equation (2.9), because of the presence of the collector surface. Their values were given in tabular form by the above researchers, respectively. In order to incorporate their values, as functions of dimensionless separation distance of oil droplets from the collector surface, directly into the subsequent numerical calculations, it is advantageous to curve fit each of the UHCC functions so that they can be represented by analytical expressions. The results of these curve fits were given by Masliyah (1994) and are listed as follows:

$$f_1(H) = 1.00 - 0.3990\exp(-0.14869H) - 0.6010\exp(-1.2015H^{0.92667}) \tag{2.17a}$$

$$f_4(H) = 1.00 - 1.23122\exp(-0.2734H) + 0.8189\exp(-0.1750H^{1.2643}) \tag{2.17b}$$

where, H is the dimensionless gap width between the oil droplet and the fiber surface, $H = \dfrac{r - R - a}{a}$.

When Equation (2.16) is substituted into the general droplet flux formula, Equation (2.3), for the static deposition case, i.e., $\underline{u}=\underline{0}$, the following explicit expressions for j_r and j_ϕ can be obtained:

$$j_r = -D_\infty f_1(r)\frac{\partial n}{\partial r} + D_\infty f_1(r) F_r(r,\phi)\frac{n}{\mathrm{k}T} \tag{2.18a}$$

$$j_\phi = -D_\infty \frac{f_4(r)}{r}\frac{\partial n}{\partial \phi} + D_\infty f_4(r) F_\phi(\phi)\frac{n}{\mathrm{k}T} \tag{2.18b}$$

where $F_r(r, \phi)$ and $F_\phi(\phi)$ are the components of all the colloidal and external forces acting on an oil droplet in the radial and azimuthal directions, respectively,

$$F_r(r,\phi) = F_{col}(r) + F_{ext,r}(\phi) = F_{col}(r) - (\frac{4}{3}\pi a^3 \Delta\rho g \pm q|\underline{E}|)\cos\phi \tag{2.19a}$$

$$F_\phi(\phi) = F_{ext,\phi}(\phi) = (\frac{4}{3}\pi a^3 \Delta\rho g \pm q|\underline{E}|)\sin\phi \tag{2.19b}$$

Noting that $j_z=0$ in the present case. Again referring to the chosen cylindrical coordinate system (r, ϕ, z), the general mass transport Equation (2.2), can be explicitly expressed as:

$$\nabla \cdot \underline{j} = \frac{1}{r}\frac{\partial}{\partial r}(r j_r) + \frac{1}{r}\frac{\partial j_\phi}{\partial \phi} = 0 \tag{2.20}$$

By bringing Equations (2.18-2.19) into the above equation and introducing the following dimensionless variables and parameters:

$$\overline{n} = \frac{n}{n_\infty};\ H = \frac{r-R-a}{a};\ \overline{F}_{col}(H) = \frac{F_{col}(r)}{\frac{\mathrm{k}T}{a}};\ A = \frac{R}{a}, \tag{2.21}$$

where n_∞ is the oil droplet volume concentration in the bulk emulsion at an "infinite" distance $r=r_\infty$ from the fiber surface, it can be derived that:

$$\frac{\partial^2 \overline{n}}{\partial H^2} + g_1(H,\phi)\frac{\partial \overline{n}}{\partial H} - g_2(H,\phi)\frac{\partial \overline{n}}{\partial \phi} - g_3(H,\phi)\overline{n} + g_4(H)\frac{\partial^2 \overline{n}}{\partial \phi^2} = 0 \tag{2.22}$$

where:

$$g_1(H,\phi) = \frac{d}{dH}\{\ln[f_1(H)g(H)]\} - \overline{F}_H(H,\phi)\ ,$$

$$g_2(H,\phi) = \frac{f_4(H)\overline{F}_\phi(\phi)}{f_1(H)g(H)},$$

$$g_3(H,\phi)=\overline{F}_H(H,\phi)\frac{d}{dH}\{\ln[f_1(H)g(H)]\}+\frac{d\overline{F}_{col}(H)}{dH}+\frac{f_4(H)}{f_1(H)}\frac{(Gr\pm Ef)\cos\phi}{g(H)},$$

$$g_4(H)=\frac{f_4(H)}{f_1(H)g^2(H)},$$

$$g(H)=H+1+A,$$

$\overline{F}_H(H,\phi)=\dfrac{F_r(r,\phi)}{\dfrac{\mathbf{k}T}{a}}=\overline{F}_{col}(H)-(Gr\pm Ef)\cos\phi$ is the component of the total dimensionless force in $\underline{i_H}$ direction,

$\overline{F}_\phi(\phi)=\dfrac{F_\phi(\phi)}{\dfrac{\mathbf{k}T}{a}}=(Gr\pm Ef)\sin\phi$ is the component of the total dimensionless force in $\underline{i_\phi}$ direction,

$\overline{F}_{col}(H)=\dfrac{F_{col}(r)}{\dfrac{\mathbf{k}T}{a}}$ is the total dimensionless colloidal force that has a component in $\underline{i_H}$ direction only,

$Gr=\dfrac{\frac{4}{3}\pi a^3(\rho_o-\rho_w)g}{\dfrac{\mathbf{k}T}{a}}$ is the dimensionless gravity number,

and $Ef=\dfrac{q|E|}{\dfrac{\mathbf{k}T}{a}}$ is the dimensionless electric field number.

Equation (2.22) as it stands is a linear homogeneous elliptic (Note: $g_4(H)\geq 0$) second-order 2-D partial differential equation (PDE) whose solution might be achieved only by using proper numerical methods. As expected, it can be shown that this 2nd-order PDE will reduce to the 1-D mass transfer Equation (2.11) if one sets Gr=Ef=0 and $f_1(H)=f_4(H)=1$.

2.6 Simplified 2-D Mass Transport Equation

Mathematically, Equation (2.22) represents an elliptic 2nd-order 2-DS PDE which is very difficult to solve, even by use of sophisticated numerical methods (Adamczyk and van de Ven, 1981b). Therefore, as stated before, this study will only deal with the external forces that are perpendicular to the axis of the fiber cylinder. Under this restriction, the coefficient of the angular diffusion term $\frac{\partial^2 \bar{n}}{\partial \phi^2}$ in the PDE, i.e., $g_4(H) = \frac{f_4(H)}{f_1(H) g^2(H)} \approx \frac{1}{(H+1+A)^2}$, which depends on H and A only, is usually negligible since in most practical cases $A \gg 1$. Thus, if this term is neglected, the elliptical PDE becomes a parabolic 2nd-order PDE whose numerical solution can be pursued relatively easily,

$$\frac{\partial^2 \bar{n}}{\partial H^2} + g_1(H,\phi)\frac{\partial \bar{n}}{\partial H} - g_2(H,\phi)\frac{\partial \bar{n}}{\partial \phi} - g_3(H,\phi)\bar{n} = 0 \qquad (2.23)$$

The same strategy was utilized by Adamczyk and van de Ven (1981b) to simply their elliptical PDE. However, it should be emphasized that the whole term, $g_4(H)\frac{\partial^2 \bar{n}}{\partial \phi^2}$, is omitted solely because A^{-2} in the multiplier $g_4(H)$ is small. Such omission does not imply $\frac{\partial^2 \bar{n}}{\partial \phi^2} \approx 0$. In other word, $\bar{n}$ should not be considered to be a linear function of ϕ.

As will be presented in details in Chapter 6, Equation (2.23) together with proper boundary conditions can be numerically solved by using the well-known implicit Crank-Nicolson method (Hoffman, 1992). This numerical method is two-level, single-step, second-order, six-point, unconditionally stable and convergent. In the literature, Adamczyk and van de Ven (1981a; 1981b) have successfully applied the Crank-Nicolson method to solving the mass transport equations in the case of parallel-plate and cylindrical channels. Nevertheless, some efforts should be made in order to improve the accuracy and flexibility of this method. This is because Equation (2.23) is characterized by a rapid change (stiff problem) of coefficients at small separation distances due to the presence of terms describing the colloidal forces. It is also expected that the dimensionless variable H changes a few orders and that ϕ ranges from 0 to π. In this study, two special transforming functions are implemented to enable a continuous changing of the mesh sizes in the new radial coordinate and the new azimuthal coordinate, respectively.

Since the Crank-Nicolson approximation method is unconditionally stable, the new mesh sizes do not affect the stability of numerical solution and thus are chosen purely based on accuracy requirements. The accuracy of the numerical solutions is then checked by varying the mesh sizes respectively and only results which are insensitive to these changes (i.e., exhibiting relative differences less than 0.01%) are considered accurate. The specific transforming functions and the numerical procedures and results, as well as their direct comparison with the experimental results and discussion will be presented in details in Chapter 6 and Chapter 7 respectively.

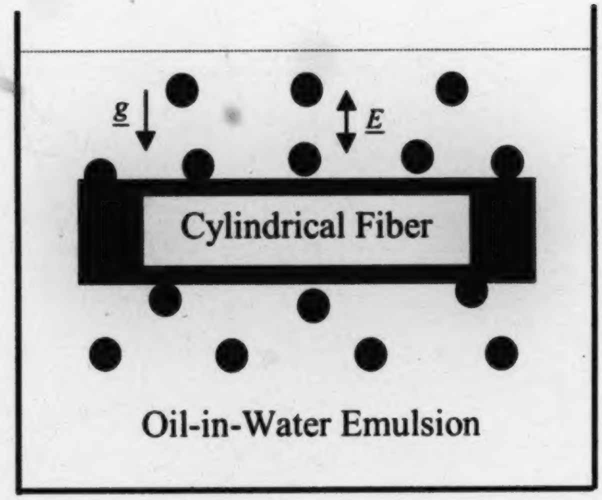
g
E
Cylindrical Fiber
Oil-in-Water Emulsion

Figure 2.1 A schematic diagram of oil droplet-fiber deposition cell

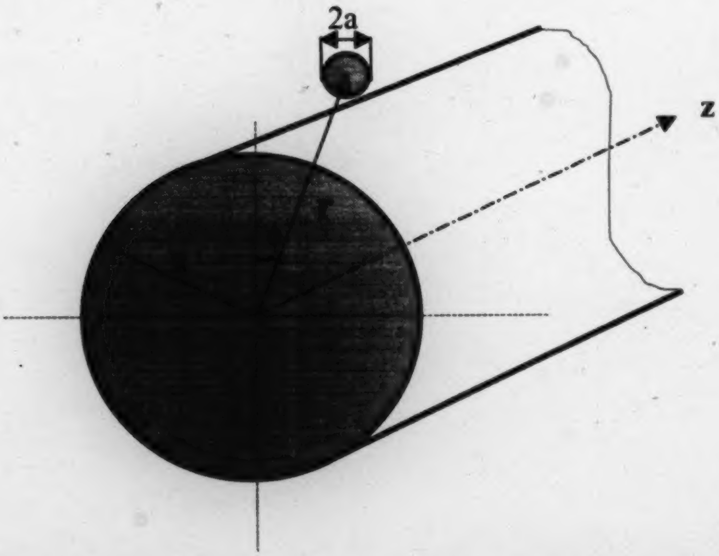

Figure 2.2 Cylindrical coordinate system (r,ϕ, z) used for deriving the general mass transport equation of oil droplet-fiber deposition problem

Chapter 3

The van der Waals (vdW) Interaction and the Electrical Double Layer (EDL) Interaction between a Spherical Particle and a Cylindrical Fiber

3.1 The van der Waals (vdW) Interaction

The van der Waals (vdW) interaction between a colloidal particle and a solid surface as a function of separation distance is important in studying the flow of colloidal emulsions or suspensions and macromolecular solutions through porous media or a filter composed of fiber materials. This kind of interaction also plays an essential role in problems of colloidal stability and particle deposition onto a solid collector (Adamczyk and van de Ven, 1981a; 1981b; Jachowicz and Berthiaume, 1989; Berthiaume and Jachowicz, 1991). In the past, there are numerous publications focusing on the vdW interaction (see Chapter 1 for details). However, there remain several issues that warrant further investigating. First, the computation of the vdW interaction between a spherical particle and a cylindrical surface was usually performed under the assumption of a sphere interacting with an infinitely large flat plate (Adamczyk and van de Ven, 1981a; 1981b). Such a simple model completely ignores the possible large curvature and finite-size effects of the cylindrical collector on the vdW interaction between a sphere and a finitely sized cylinder. Secondly, owing to the electromagnetic nature of the interaction, the actual vdW interaction between two interacting macroscopic bodies is reduced at large distances because the time of the electric field propagation from one body to another body and back is such that the fluctuating electric moments become slightly out of phase. The reduction of the vdW interaction due to the finite speed of light is often called the retardation effect (Israelachvili, 1985; Bhattacharjee and Sharma, 1995). Thirdly, it is rather difficult to determine the Hamaker constant experimentally and thus to calculate the vdW interaction accurately for many practical applications.

In this chapter, a general method will be presented to compute the unretarded vdW interaction potential and force between a spherical particle and a cylinder (Gu and

Li, 1998h). Therefore, the effects of the curvature and the length of the cylinder on the vdW interaction can be explored quantitatively. However, it is noted that, in this study, the spherical particles or the oil droplets are assumed to be rigid such that their deformation effects on the vdW interaction are not included in the curvature effects. Then the interaction potential is modified to account for the retardation effect by incorporating a correction factor, which depends on the separation distance and the characteristic wavelength of the interaction. Next, for the practical deposition systems, their unknown Hamaker constants can be related to the known ones, which are obtained directly from the relevant surface and/or interfacial tensions. At present, the surface tensions and interfacial tensions of liquid-fluid interfaces can be measured with satisfactory accuracy by using some existing advanced experimental techniques, such as the axisymmetric drop shape analysis (ADSA) technique developed by Neumann and co-workers (Rotenberg et al., 1983; Cheng et al., 1990; Li et al., 1992). According to the equation of state for interfacial tensions (Li and Neumann, 1990a; 1992a), the interfacial tensions of solid-fluid interfaces can be determined from the relevant surface/interfacial tensions and contact angles of the solid-liquid-fluid systems, both of which can be measured by the ADSA technique. However, it has long been noted that the ADSA technique and most other widely used contact angle measurement techniques require a flat solid surface. Hence, they cannot be utilized to measure contact angles on curved surfaces, such as a cylindrical fiber surface, though the determination of contact angles or wettability on fibre is of practical importance in composite materials, textile and cosmetic industries. In the course of this work, a new contact angle measurement technique has been developed (Gu et al., 1997a; Gu and Li, 1998a; 1998b). This method can be used to accurately measure the contact angle of a liquid-fluid interface by analyzing the capillary profile around a cylinder (ACPAC). As will be described separately in details in the next chapter, the ACPAC technique is a powerful alternative tool to the existing ADSA technique for accurate measurements of contact angles of any liquid-fluid interfaces on cylindrical surface. It will be particularly useful in studying the wetting, spreading and deposition processes of a liquid drop on fiber surfaces. A general user-oriented computer program code to implement this technique is also developed.

3.2 Mathematical Formulations of the Unretarded vdW Interaction between a Spherical Particle and a Cylindrical Fiber

In the literature, exact and approximate analytical expressions are available only for the vdW interaction potentials between bodies of appropriate geometric combinations, such as two parallel flat plates, spheres, infinitely long parallel cylinders, infinitely long crossed cylinders, and a sphere and an infinitely large flat plate (Israelachvili, 1985). Recently, Zeman and Wales (1981) and Papadopoulos and Kuo (1990) presented numerical methods to determine the vdW interaction energy for a spherical particle in a pore geometry. Bhattacharjee and Sharma (1995) obtained asymptotic analytical expressions for the same geometric configuration using the Hamaker microscopic approach. They all found that a commonly used simple model of a sphere interacting with a semi-infinitely large flat plate is reasonable only for very small particles close to the inner wall of a cylindrical pore. But in all other cases, it seriously underestimates the interaction energy.

However, there is no similar effort made yet to consider the curvature and the finite-size effects on the vdW interaction between a sphere and a cylinder for the case in which the sphere is located outside of the cylinder. In such a case, it has become a common practice to employ the sphere-flat plate approximation without any justification. Theoretically, it is not clear how large an error will be created by this approximation when it is used to calculate the vdW interaction between a spherical particle and a finitely sized (both the length and the radius) cylinder at an arbitrary separation distance.

There are two practical methods to determine the vdW interaction between approaching bodies as a function of their separation distance. The first, referred to as the Hamaker approach (Hamaker, 1937), determines the vdW interaction of two macroscopic bodies by carrying out the so-called Hamaker-type integration of all the intermolecular interactions. The second approach, based on the Lifshitz theory (Lifshitz, 1956; Parsegian, 1975), is more rigorous and gives the vdW interaction energy as a function of macroscopic electrodynamic properties of the interacting media, such as their dielectric permittivities and their refractive indexes (Israelachvili, 1985). In practice, the Hamaker approach is much more widely used mainly because of its simplicity and applicability.

In this section, a general theoretical method is presented to obtain the vdW interaction potential and force between a spherical particle and a cylinder without invoking the sphere-flat plate approximation. Based on the well-known Hamaker approach and pairwise summation of all the relevant intermolecular interactions (Hamaker, 1937; Israelachvili, 1985), this method determines the vdW interaction from evaluation of total four multidimensional integrals. As will be seen later, the integrand after the first analytical integration becomes so cumbersome that it is impossible to derive any meaningful asymptotic analytical expressions for any situations of interest. Therefore, accurate numerical integration is performed for the remaining three integrals.

Specifically, on the bases of the Hamaker approach and pairwise additivity, the total vdW interaction potential is evaluated by integrating the pair interaction potential between two molecules, one in the sphere and the other in the cylinder. Therefore, the first step is to obtain the interaction potential between a molecule in the sphere and the whole cylinder. Then the total interaction potential between the sphere and the cylinder can be evaluated by integrating the molecule-cylinder interaction potential over all the differential volume elements in the sphere, i.e. performing the Hamaker-type integration for the configuration.

3.2.1 Molecule-Cylinder Interaction Potential

Generally, the unretarded pair potential between two interacting molecules separated by a distance r can be assumed to be of the power-law form:

$$v(r) = -\frac{C}{r^n}, \tag{3.1}$$

where C is their potential coefficient and n depends on the specific potential model used for the inter-molecular potential. For the van der Waals (vdW) interaction discussed here, C is the Lifshitz-vdW potential coefficient and n=6 (Israelachvili, 1985; Bhattacharjee and Sharma, 1995). As will be seen later, C is directly related to the well-known Hamaker constant. Then, with the further assumption of the pairwise additivity, the vdW interaction potential of a molecule and a solid cylinder, as schematically shown in Figure 3.1a, is the sum of its interactions with all the molecules in the cylinder of radius R and length L. For an infinitesimal differential volume element of cross-sectional area ρdϕdρ and vertical height dz, the element volume is ρdϕdρdz, and the total number of molecules in the element is n_cρdϕdρdz, where n_c is the number density of molecules in the cylinder. Referring to Figure 3.1b, geometrically, the distance between the molecule and the differential volume element is equal to,

$$r = [z^2 + (D + R + \rho\cos\phi)^2 + \rho^2 \sin^2\phi]^{\frac{1}{2}}$$

By choosing the cylindrical coordinate system (ρ, ϕ, z) and noting the symmetries in the z and ϕ directions, the total vdW interaction potential between the molecule and the cylinder at a separation distance D away from the cylinder surface is, using Equation (3.1)

$$v_1(D,R,L) = -4Cn_c \int_0^{\pi} \{\int_0^{R} (\int_0^{\frac{L}{2}} \frac{dz}{[z^2 + (D + R + \rho\cos\phi)^2 + \rho^2 \sin^2\phi]^3}) \rho d\rho\} d\phi \quad (3.2)$$

In order to generalize these integrals, three nondimensional parameters are introduced as follows:

$A = \frac{R}{a}$, the ratio of the cylinder radius to the sphere radius,

$B = \frac{L}{R}$, the ratio of the cylinder length to its radius, therefore, $\frac{L}{a} = AB$,

$H = \frac{D}{a}$, the dimensionless separation distance.

Correspondingly, the integration variables are nondimensionalized as follows:

$\bar{z} = \frac{z}{a}$ and $\bar{\rho} = \frac{\rho}{a}$.

Substituting these nondimensional parameters and new integration variables into Equation (3.2) gives:

$$v_1(H,A,B) = -\frac{4Cn_c}{a^3} \int_0^{\pi} d\phi \int_0^{A} \bar{\rho} d\bar{\rho} \int_0^{\frac{AB}{2}} \frac{d\bar{z}}{[\bar{z}^2 + (H + A + \bar{\rho}\cos\phi)^2 + \bar{\rho}^2 \sin^2\phi]^3} \quad (3.3)$$

It is also noted that the proper choice of the integration sequence may result in a simple analytical expression for the subsequent integrals. In the present case, the integration with respect to $\bar{z}$ is simpler and thus is chosen first. After some mathematical manipulations regarding the integration over the $\bar{z}$ direction, Equation (3.3) becomes:

$$v_1(H,A,B) = -\frac{4Cn_c}{a^3}\int_0^{\pi} d\phi \int_0^{A} p_1(\phi,\bar{\rho},H,A,B)\bar{\rho}\,d\bar{\rho}, \qquad (3.4)$$

where,

$$\begin{aligned} p_1(\phi,\bar{\rho},H,A,B) = {} & \frac{2AB}{[(H+A+\bar{\rho}\cos\phi)^2+\bar{\rho}^2\sin^2\phi]\{A^2B^2+4[(H+A+\bar{\rho}\cos\phi)^2+\bar{\rho}^2\sin^2\phi]\}^2} \\ & + \frac{3AB}{4[(H+A+\bar{\rho}\cos\phi)^2+\bar{\rho}^2\sin^2\phi]^2\{A^2B^2+4[(H+A+\bar{\rho}\cos\phi)^2+\bar{\rho}^2\sin^2\phi]\}} \\ & + \frac{3}{8[(H+A+\bar{\rho}\cos\phi)^2+\bar{\rho}^2\sin^2\phi]^{\frac{5}{2}}}\arctan\left\{\frac{AB}{2[(H+A+\bar{\rho}\cos\phi)^2+\bar{\rho}^2\sin^2\phi]^{\frac{1}{2}}}\right\} \end{aligned}$$

Here, in the function $p_1(\phi,\bar{\rho},H,A,B)$, H is the nondimensional separation distance but at this stage it is irrelevant to these integrals; whereas A and B are the nondimensional parameters which depend merely on the dimensions of the sphere and the cylinder as defined previously. As seen from Equation (3.4), ϕ and $\bar{\rho}$ are the remaining integration variables. However, the complicated integrals in Equation (3.4) have to be performed numerically. Equation (3.4) is a general integral equation for calculating the vdW interaction potential between a molecule and a cylinder of a finite nondimensional radius, A, and a finite nondimensional length, AB, at a nondimensional separation distance, H. If the cylinder is sufficiently long, i.e. $B=\frac{L}{R} \gg 1$, then the first two terms in the function, $p_1(\phi,\bar{\rho},H,A,B)$, become negligible. In the extreme case for an infinitely long cylinder, $B=\infty$, Equation (3.4) can be simplified as:

$$v_2(H,A) = -\frac{3\pi Cn_c}{4a^3}\int_0^{\pi} d\phi \int_0^{A} \frac{\bar{\rho}\,d\bar{\rho}}{[(H+A+\bar{\rho}\cos\phi)^2+\bar{\rho}^2\sin^2\phi]^{\frac{5}{2}}} \qquad (3.5)$$

3.2.2 Sphere-Cylinder Interaction Potential

The next step is to calculate the total vdW interaction potential between a sphere and a cylinder. First of all, as shown in Figure 3.1c, the interaction between an infinitesimal differential circular disk of cross-sectional area πx^2 and thickness dy in the sphere and the cylinder is considered. From the elementary geometry, it is known that

$$x^2 = a^2 - (a - y)^2 = (2a - y)y$$

Thus, the volume of the circular element disk is $\pi x^2 dy = \pi(2a-y)ydy$, and the number of molecules in this differential volume element is $n_p\pi(2a-y)ydy$, where n_p is the number density of molecules in the spherical particle. Since all these molecules in the thin disk are at the same separation distance (D+y) away from the cylinder surface, the overall vdW interaction potential between this element and the cylinder is $v_1(D+y,R,L)\,n_p\pi(2a-y)ydy$, where $v_1(D,R,L)$ is given in Equation (3.2). Further employing the previously defined nondimensional parameters, the function, $p_1(\phi,\overline{\rho},H,A,B)$, and $\overline{y} = \frac{y}{a}$, the total vdW interaction potential between the sphere and the cylinder is equal to:

$$V_1(H,A,B) = -4\pi C n_p n_c \int_0^2 [\int_0^{\pi} d\phi \int_0^{A} p_1(\phi,\overline{\rho},H+\overline{y},A,B)\overline{\rho}d\overline{\rho}](2-\overline{y})\overline{y}d\overline{y} \qquad (3.6)$$

The Hamaker constant for interaction between two bulk bodies is defined as (Israelachvili, 1985):

$$A_{12} = \pi^2 C n_p n_c, \qquad (3.7)$$

where A_{12} is the Hamaker constant for the interaction between phase '1' (say, spherical particle) and phase '2' (the cylindrical collector) in vacuum. Here, n_1 and n_2 are the densities of phase 1 and phase 2, respectively, in number of molecules per unit volume. The parameter C is the interaction energy parameter specified in Equation (3.1) for van der Walls interaction between a molecule of phase 1 and a molecule of phase 2. For obtaining the Hamaker constant A_{132}, namely, the Hamaker constant for interaction between '1' and '2' through medium '3' (the aqueous phase, in the present case), combining relations outlined in Section 3.5.1 are used. Using the Hamaker constant to nondimensionalize V_1(H,A,B) in Equation (3.6) yields

$$\overline{V}_1(H,A,B) = \frac{V_1(H,A,B)}{A_{12}}, \qquad (3.8a)$$

$$\overline{V}_{vdw1}(H,A,B)=\frac{V_1(H,A,B)}{\mathrm{k}T}=\frac{A_{12}}{\mathrm{k}T}\overline{V}_1(H,A,B), \tag{3.8b}$$

where,

$$\overline{V}_1(H,A,B)=-\frac{4}{\pi}\int_0^2[\int_0^\pi d\phi\int_0^A p_1(\phi,\overline{\rho},H+\overline{y},A,B)\overline{\rho}d\overline{\rho}](2-\overline{y})\overline{y}d\overline{y} \tag{3.9a}$$

$$\overline{V}_{vdw1}(H,A,B)=-\frac{4A_{12}}{\pi \mathrm{k}T}\int_0^2[\int_0^\pi d\phi\int_0^A p_1(\phi,\overline{\rho},H+\overline{y},A,B)\overline{\rho}d\overline{\rho}](2-\overline{y})\overline{y}d\overline{y} \tag{3.9b}$$

In accordance with the definition of the total dimensionless colloidal force, $\overline{F}_{col}(H)=\frac{F_{col}(H)}{\frac{\mathrm{k}T}{a}}$, given in Section 2.5, another nondimensional vdW interaction potential, expressed by $\overline{V}_{vdw1}(H,A,B)=\frac{V_1(H,A,B)}{\mathrm{k}T}$, is also defined in Equation (3.8b) and its formula is also given in Equation (3.9b) for comparison. Nevertheless, such defined dimensionless vdW potential will not be further referred for the following two reasons. First, as shown in the above equations, these two nondimensional vdW potentials are based on different references and thus differ only by a dimensionless multiplier, $\frac{A_{12}}{\mathrm{k}T}$. Secondly, at this stage, the vdW potential nondimensionlized by A_{12}, i.e., $\overline{V}_1(H,A,B)=\frac{V_1(H,A,B)}{A_{12}}$, is preferred because A_{12} is unknown. How to determine the Hamaker constant, A_{12}, will be described later in Section 3.5. The vdW potential nondimensionlized by kT will be used in Chapter 6 in order to be consistent with usual definition of the dimensionless adhesion number, $A_d=\frac{A_{12}}{6\mathrm{k}T}$ (Adamczyk and van de Ven, 1981b; Sanders et al., 1995).

Similarly, the total nondimensional vdW interaction potential between a sphere and an infinitely long cylinder (B=∞) can be written as, using Equation (3.5),

$$\overline{V}_2(H,A)=\frac{V_2(H,A)}{A_{12}}, \tag{3.10}$$

where,

$$\overline{V}_2(H,A) = -\frac{3}{4}\int_0^2 \{\int_0^\pi d\phi \int_0^A \frac{\overline{\rho}d\overline{\rho}}{[(H+\overline{y}+A+\overline{\rho}\cos\phi)^2+\overline{\rho}^2\sin^2\phi]^{\frac{5}{2}}}\}(2-\overline{y})\overline{y}d\overline{y} \tag{3.11}$$

Later on, these two nondimensional total interaction potential functions for a sphere and a cylinder in two cases, $\overline{V}_1(H,A,B)$ and $\overline{V}_2(H,A)$, will be compared with those between a sphere and a flat plate.

3.2.3 Analytical Solutions for the Sphere-Flat Plate vdW Interaction Potential

With the molecule-flat plate interaction potential obtained by integrating the molecule-molecule pair potential, Israelachvili (1985) derived the sphere-flat plate vdW interaction potential, which, in the nomenclature used here, can be expressed by

$$\overline{V}_3(H) = -\frac{1}{6}\int_0^2 \frac{(2-\overline{y})\overline{y}d\overline{y}}{(H+\overline{y})^3} \tag{3.12}$$

The exact analytical solution for $\overline{V}_3(H)$ can be obtained by performing the above integration:

$$\overline{V}_3(H) = -\frac{1}{6}[\frac{1}{H}+\frac{1}{H+2}-\ln(\frac{H+2}{H})] \tag{3.13}$$

If the third term on the right-hand side of Equation (3.13) is expanded in a Taylor's series by using

$$\ln x = 2[\frac{x-1}{x+1}+\frac{1}{3}(\frac{x-1}{x+1})^3+\frac{1}{5}(\frac{x-1}{x+1})^5+\cdots], \qquad (x>0)$$

and choosing $x = \frac{H+2}{H}$, then an excellent approximation to Equation (3.13) over all the range of H can be achieved by truncating the $\ln x$ expansion up to the third order and substituting the resultant expression into Equation (3.13),

$$\overline{V}_3(H) \approx -\frac{2H^2+3H+3}{9H(H+1)^3(H+2)} \qquad \text{(all H values)} \tag{3.14}$$

Mathematically, it can be readily proved that Equation (3.14) will approach the following two limiting solutions:

$$\overline{V}_4(H) = -\frac{1}{6H}, \qquad (H \ll 1) \tag{3.15}$$

for small separation distances and

$$\overline{V}_5(H) = -\frac{2}{9H^3}, \qquad (H \gg 1) \qquad (3.16)$$

for large separation distances, respectively. These two asymptotic expressions are also given by Israelachvili (1985).

3.2.4 The vdW Interaction Force

After the vdW interaction potential formulae are derived, the vdW interaction forces can be easily related to the vdW interaction potentials by the following relation:

$$F(D) = -\frac{dV(D)}{dD}$$

Accordingly, two different dimensionless vdW interaction forces can be defined as:

$$\overline{F}(H) = \frac{F(D)}{\frac{A_{12}}{a}} = -\frac{d\overline{V}(H)}{dH} \qquad (3.17a)$$

$$\overline{F}_{vdW}(H) = \frac{F(D)}{\frac{kT}{a}} = \frac{A_{12}}{kT}\overline{F}(H) \qquad (3.17b)$$

As was mentioned previously, $\overline{F}_{vdW}(H)$ defined in Equation (3.17b) is the dimensionless vdW interaction force defined in Section 2.5. By differentiating the dimensionless vdW interaction potentials expressed by Equations (3.9a), (3.11), (3.13), (3.15) and (3.16) with respect to H and then bringing the resultant equations into Equation (3.17a), respectively, the dimensionless vdW interaction forces for different cases can be summarized as follows:

$$\overline{F}(H) = \begin{cases} \overline{F}_1(H,A,B) & \text{(between a sphere and a finitely long cylinder)} \\ \overline{F}_2(H,A) & \text{(between a sphere and an infinitely long cylinder)} \\ \left.\begin{array}{ll} \overline{F}_3(H) & \text{(all H values)} \\ \overline{F}_4(H) & \text{(small H values)} \\ \overline{F}_5(H) & \text{(large H values)} \end{array}\right\} & \text{(between a sphere and a flat plate)} \end{cases} \qquad (3.18)$$

where:

$$\overline{F}_1(H,A,B) = -\frac{d\overline{V}_1(H,A,B)}{dH} = \frac{4}{\pi}\int_0^2 [\int_0^\pi d\phi \int_0^A f_1(\phi,\overline{\rho},H+\overline{y},A,B)\overline{\rho}d\overline{\rho}](2-\overline{y})\overline{y}d\overline{y}$$

$$f_1(\phi,\bar{\rho},H,A,B)=\frac{\partial p_1(\phi,\bar{\rho},H,A,B)}{\partial H}=$$

$$-\frac{10AB(H+A+\bar{\rho}\cos\phi)}{[(H+A+\bar{\rho}\cos\phi)^2+\bar{\rho}^2\sin^2\phi]^2\{A^2B^2+4[(H+A+\bar{\rho}\cos\phi)^2+\bar{\rho}^2\sin^2\phi]\}^2}$$

$$-\frac{32AB(H+A+\bar{\rho}\cos\phi)}{[(H+A+\bar{\rho}\cos\phi)^2+\bar{\rho}^2\sin^2\phi]\{A^2B^2+4[(H+A+\bar{\rho}\cos\phi)^2+\bar{\rho}^2\sin^2\phi]\}^3}$$

$$-\frac{15AB(H+A+\bar{\rho}\cos\phi)}{4[(H+A+\bar{\rho}\cos\phi)^2+\bar{\rho}^2\sin^2\phi]^3\{A^2B^2+4[(H+A+\bar{\rho}\cos\phi)^2+\bar{\rho}^2\sin^2\phi]\}}$$

$$-\frac{15(H+A+\bar{\rho}\cos\phi)}{8[(H+A+\bar{\rho}\cos\phi)^2+\bar{\rho}^2\sin^2\phi]^{\frac{7}{2}}}\arctan\{\frac{AB}{2[(H+A+\bar{\rho}\cos\phi)^2+\bar{\rho}^2\sin^2\phi]^{\frac{1}{2}}}\}$$

$$\bar{F}_2(H,A)=-\frac{d\bar{V}_2(H,A)}{dH}=-\frac{15}{4}\int_0^2\{\int_0^\pi d\phi\int_0^A\frac{(H+\bar{y}+A+\bar{\rho}\cos\phi)\bar{\rho}d\bar{\rho}}{[(H+\bar{y}+A+\bar{\rho}\cos\phi)^2+\bar{\rho}^2\sin^2\phi]^{\frac{7}{2}}}\}(2-\bar{y})\bar{y}d\bar{y}$$

$$\bar{F}_3(H)=-\frac{d\bar{V}_3(H)}{dH}=-\frac{2}{3H^2(H+2)^2}$$

$$\bar{F}_4(H)=-\frac{d\bar{V}_4(H)}{dH}=-\frac{1}{6H^2}$$

$$\bar{F}_5(H)=-\frac{d\bar{V}_5(H)}{dH}=-\frac{2}{3H^4}$$

For comparison, the analytical solutions for the vdW interaction forces between a sphere and a flat plate are also included in Equation (3.18). As expected, the exact solution for this case, $\bar{F}_3(H)$, will approach the asymptotic solutions, $\bar{F}_4(H)$ for H«1, and $\bar{F}_5(H)$ for H»1, respectively. It is seen from the equations for $\bar{V}_1 \sim \bar{V}_5$ and $\bar{F}_1 \sim \bar{F}_5$ that these ten functions are all dependent on the nondimensional separation distance H, some of which are also dependent on the nondimensional geometric parameters A and B. Furthermore, the vdW interaction potential $\bar{V}(H)$ and force $\bar{F}(H)$, which are nondimensionlized by A_{12} and $\frac{A_{12}}{a}$, respectively, are always negatively valued at any separation distances.

To evaluate the exact nondimensional vdW interaction potential and force between a sphere and a cylinder at any arbitrary nondimensional separation distances, H, the integral equations for $\bar{V}_1(H,A,B)$ and $\bar{F}_1(H,A,B)$, $\bar{V}_2(H,A)$ and $\bar{F}_2(H,A)$ are numerically integrated by using a second-order trapezoid rule method (Hoffman, 1992). More specifically, since these integrands are found to be extremely stiff functions, the adaptive integration technique is also applied. The minimum integration step size for each integration variable is chosen properly in order to satisfy a pre-specified error criterion. The overall accuracy of the three remaining integrals with respect to $\overline{\rho}$, ϕ, and $\overline{y}$ is improved by evenly taking a smaller step size for each integration variable until the numerical results exhibit relative difference less than 0.01% between the two successive integration steps.

3.3 Retarded van der Waals (vdW) Interaction

So far all the above expressions for the vdW interaction potentials and forces are derived based on an implicit assumption that the speed of light is infinite. Thus they are often referred to as the unretarded vdW potentials and forces. Owing to the electromagnetic nature of the interaction, the actual vdW potential between two interacting macroscopic bodies is reduced at large separation distances because the time of the electric field propagation from one body to another body and back is such that the fluctuating electric moments become slightly out of phase. The reduction of the vdW interaction due to the finite speed of light is called the retardation effect (Israelachvili, 1985; Bhattacharjee and Sharma, 1995). Such effect may become very pronounced for macroscopic bodies at separation distances larger than about 5 nm (Nir and Vassilieff, 1988). For fairly large particles (1 μm or greater), omission of the retardation has been proved to lead to a serious overestimate of the vdW interaction (Gregory, 1981). However, in practice, a full treatment of the retardation effect presents a rather intractable task for complex geometries (Israelachvili, 1985; Nir and Vassilieff, 1988), and is thus rarely pursued.

Unlike the Lifshitz approach, the original Hamaker approach does not include the retardation effect. Nevertheless, as was suggested by Gregory (1981), in principle, this approach can be modified to account for the retardation by multiplying the unretarded intermolecular vdW interaction potential given in Equation (3.1) by a correction factor:

$$v(r) = -\frac{C}{r^6} f(p), \tag{3.19}$$

where the correction function, $f(p)$, depends on the reduced distance only, $p = \frac{2\pi r}{\lambda}$, and λ is the "London characteristic wavelength" of the interaction and is often assumed to be about 100 nm (Gregory, 1981; Dabros and van de Ven, 1983; Masliyah, 1994). Nonetheless, a difficulty with this correction method arises from the lack of a convenient single formula for $f(p)$ over the entire range of separation distances (Casimir and Polder, 1948; Overbeek, 1952; Schenkel and Kitchener, 1960; Gregory, 1981). Alternatively, after making a complete comparison, Gregory (1981) suggested several simple approximations for retarded vdW interaction between plates, between spheres, and between a sphere and a plate. Furthermore, Gregory (1981) concluded that introducing the simpler approximations for retarded interactions, such as an appropriate correction factor, gives even better agreement with exact predictions.

In this study, all the expressions derived heretofore are only for the unretarded interactions, i.e. the zero-frequency component of the vdW interactions. Therefore, a proper correction to the retardation effect is warranted in order to account for the nonzero frequency components of the vdW interactions. Following the approach of Gregory (1981), this is attempted by incorporating a correction factor, which is a function of the separation distance, H, and the "London characteristic wavelength" of the interaction, λ, into these unretarded vdW interaction equations. It should be noted that, at larger distances, when the retardation correction becomes significant, the vdW interaction itself becomes insignificant compared with other forces such as hydrodynamic force and the electrical double layer (EDL) force (Hoffmann and Stein, 1992).

Since the spherical particles are usually so much smaller than the cylinder, as a first-order approximation, the existing correction factor for the sphere-plate interaction potential may be the most suitable one to account for the retardation effect on the sphere-cylinder system. This correction factor is given by (Suzuki, Ho and Higuchi, 1969; Gregory, 1981; Adamczyk and van de Ven, 1981b; Masliyah, 1994):

$$f(H,\bar{\lambda}) = \frac{\bar{\lambda}}{\bar{\lambda} + \bar{s}H}, \tag{3.20}$$

where, $\bar{\lambda} = \dfrac{\lambda}{a}$ is the dimensionless retardation parameter and $\bar{s}$ is a constant equal to 11.116 (Suzuki, Ho and Higuchi, 1969) or 14.0 (Gregory, 1981). Multiplying the non-dimensional unretarded vdW interaction potentials by $f(H,\bar{\lambda})$ yields the approximate nondimensional retarded vdW interaction potentials, i.e.,

$$\bar{V}_i^{Ret}(H) = (\frac{\bar{\lambda}}{\bar{\lambda}+\bar{s}H})\bar{V}_i(H) \qquad (i = 1 \sim 5) \qquad (3.21)$$

Accordingly, the non-dimensional retarded vdW forces can be found by differentiating Equation (3.21) with respect to H:

$$\bar{F}_i^{Ret}(H) = -\frac{d\bar{V}_i^{Ret}(H)}{dH} = (\frac{\bar{\lambda}}{\bar{\lambda}+\bar{s}H})\bar{F}_i(H) + \frac{\overline{\lambda s}}{(\bar{\lambda}+\bar{s}H)^2}\bar{V}_i(H) \qquad (i = 1 \sim 5) \qquad (3.22)$$

Equations (3.21) and (3.22) can be directly employed to correct the unretarded vdW interaction potentials and forces between a sphere and a cylinder, $\bar{V}_1(H,A,B)$ and $\bar{V}_2(H,A)$, $\bar{F}_1(H,A,B)$ and $\bar{F}_2(H,A)$ given in Equations (3.9a), (3.11), and (3.18), respectively. For the sphere-flat plate system, the analytical expressions for retarded vdW potentials and forces in different cases can be easily derived as follows, using Equations (3.13), (3.15), (3.16) and (3.18), respectively,

$$\left\{\begin{array}{c}
\bar{V}_3^{Ret}(H) = -\frac{1}{6}(\frac{\bar{\lambda}}{\bar{\lambda}+\bar{s}H})[\frac{1}{H} + \frac{1}{H+2} - \ln(\frac{H+2}{H})] \\
\bar{V}_4^{Ret}(H) = -\frac{1}{6H}(\frac{\bar{\lambda}}{\bar{\lambda}+\bar{s}H}) \\
\bar{V}_5^{Ret}(H) = -\frac{2}{9H^3}(\frac{\bar{\lambda}}{\bar{\lambda}+\bar{s}H}) \\
\text{and} \\
\bar{F}_3^{Ret}(H) = -(\frac{\bar{\lambda}}{\bar{\lambda}+\bar{s}H})\frac{2}{3H^2(H+2)^2} - \frac{1}{6}\frac{\overline{\lambda s}}{(\bar{\lambda}+\bar{s}H)^2}[\frac{1}{H} + \frac{1}{H+2} - \ln(\frac{H+2}{H})] \\
\bar{F}_4^{Ret}(H) = -\frac{\bar{\lambda}(\bar{\lambda}+2\bar{s}H)}{6H^2(\bar{\lambda}+\bar{s}H)^2} \\
\bar{F}_5^{Ret}(H) = -\frac{2\bar{\lambda}(3\bar{\lambda}+4\bar{s}H)}{9H^4(\bar{\lambda}+\bar{s}H)^2}
\end{array}\right. \qquad (3.23)$$

In the above equation, if $\bar{s}$ in $\overline{V}_4^{Ret}(H)$ is taken to be 11.116, this expression will be identical to the so-called SHH expression, due to Suzuki, Ho and Higuchi (1969). Such SHH expression for the retarded vdW interaction force, $\overline{F}_4^{Ret}(H)$, has been employed by others to determine the retarded vdW interaction force between a sphere and a flat plate (Adamczyk and van de Ven, 1981b; Sanders et al., 1995).

3.4 Retardation Effect and Curvature and Finite Size Effects

The general theoretical method described above can determine the van der Waals interaction potential and force between a spherical particle and a cylinder at any separation distances. Equations (3.9a), (3.10) and (3.18) give the nondimensional unretarded vdW potentials and forces as functions of dimensionless geometric parameters, A and B, for a cylinder of finite dimensions, or A only for an infinitely long cylinder. Here, A is defined as the ratio of the radius of the cylinder to the radius of the sphere, and B is defined as the ratio of the length of the cylinder to its radius. Thus B depends only on the dimensions of the cylinder itself. In the numerical computations, the nondimensional separation distance, H, is chosen to vary from 0.001 to 100. As will be discussed in Chapter 6, such a range for H includes all the interesting cases of significant interactions. The typical values for A and B are chosen as 1, 10 and 100. Two orders of change in A and B cover practically all situations as well. Particular attention is given to the vdW interactions in the following three rather different ranges of H, i.e., H«1 (H≈0.001~0.1), H≈1 (H≈0.1~10) and H»1 (H≈10~100).

Such calculated unretarded vdW interaction potentials are modified to take account of the retardation effect by introducing a correction factor, $f(H,\bar{\lambda})$, given in Equation (3.20). In $f(H,\bar{\lambda})$, the "London characteristic wavelength", λ, and the constant, $\bar{s}$, are taken to be 10^{-7} m (Suzuki, Ho and Higuchi, 1969; Gregory, 1981) and 11.116 (Suzuki, Ho and Higuchi, 1969), respectively. A typical value of the dimensionless retardation parameter, $\bar{\lambda}$, is chosen as 0.01, i.e. a≈10μm, in the present numerical simulations. As was indicated by Adamczyk and van de Ven (1981b), the dimensionless retardation parameter when changed within the limits of 0.1~1.0 affected the deposition rates of the Brownian particles onto cylindrical collectors by only 0.5%. The detailed numerical results will be discussed and compared with those based on the flat plate approximation.

Figure 3.2 shows the variations of the unretarded (empty symbols and dotted lines) and the retarded (solid symbols and solid lines) vdW forces, $\overline{F}_1(H,A,B)$ and $\overline{F}_1^{Ret}(H,A,B)$ between a sphere and a finitely sized cylinder (A=1 and B=1) and $\overline{F}_2(H,A)$ and $\overline{F}_2^{Ret}(H,A)$, between a sphere and an infinitely long cylinder (A=1 and B=∞) with the nondimensional separation distance, H. It is seen from the log-scale plot that the vdW interactions decay by approximately twenty orders of magnitude as the nondimensional separation distance, H, changes by five orders from 0.001 to 100. At the two extremes, either H«1 (H≈0.001~0.1) or H»1 (H≈10~100), the vdW interactions decrease approximately linearly as H increases, but with considerably different slopes. Between these two limiting cases, there is an obvious transition region for the vdW interactions near H≈1 (H≈0.1~10). These facts suggest that it is actually difficult to find a single simple formula for the vdW interaction force between a sphere and a cylinder over the entire range of the separation distances as considered here.

Figure 3.2 also clearly shows that, at small separation distances, H«1 (H≈0.001~0.1), the retardation effect is negligible. However, when H≥0.1, the difference between the unretarded and retarded vdW interactions becomes much more pronounced as the sphere and the cylinder are separated by a large distance. Hence, complete neglect of the retardation effect results in unacceptably overestimated vdW interactions at larger separation distances. Fortunately, the vdW interactions themselves become much weaker at larger separation distances. As a matter of fact, at such large separation distances, other driving forces such as the hydrodynamic force and the EDL force might become dominant (Hoffmann and Stein, 1992).

The comparison of the vdW forces for the sphere-cylinder systems (A=1, B=1, and A=1, B=∞) and for the sphere-flat plate system is presented in Figure 3.3. At H«1, the vdW forces between a sphere and a cylinder, whether the cylinder is finitely or infinitely long, are essentially the same as those calculated from the flat plate approximation. Nevertheless, when H≥1, the vdW forces for the sphere-cylinder systems deviate significantly from that for the sphere-flat plate system. It becomes obvious that, at large separation distances, the flat plate approximation and its asymptotic solution $\overline{F}_5^{Ret}(H)$ for H»1 give a serious overestimation of the vdW interactions for the sphere-cylinder systems. Furthermore, as expected, at H»1, the vdW interaction force between a sphere and an infinitely long cylinder (B=∞) is stronger than that between a sphere and a finitely long cylinder (B=1). Figure 3.3 also indicates that the asymptotic expression $\overline{F}_4^{Ret}(H)$ is an excellent approximation to the exact vdW force between a sphere and a flat plate at H«1, whereas $\overline{F}_5^{Ret}(H)$ is a good approximation to the exact solution of the sphere-flat plate model at H»1. At the intermediate separation distances, H≈1, however, both of them slightly overestimate the vdW interaction between a sphere and a flat plate. Thus, at H≈1, neither of them can be justifiably used to substitute the exact solution $\overline{F}_3^{Ret}(H)$ given in Equation (3.23).

Figure 3.4 shows the curvature effect of the cylinder, represented by the dimensionless geometric parameter, A, on the vdW force between a sphere and an infinitely long cylinder (B=∞). It is found that the curvature of cylinder has a strong influence on the vdW force at H>1, especially when A is small. Only when A≥10, the vdW force for the sphere-cylinder system approaches its limiting case, the exact solution for the sphere-flat plate system.

The length effect of cylinder, expressed by the dimensionless geometric parameter, B, on the vdW force between a sphere and a finitely sized cylinder is shown in Figure 3.5a for A=1, Figure 3.5b for A=10 and Figure 3.5c for A=100, respectively. Clearly, at large separation distances (H>1), the vdW force decreases as B (the cylinder length) decreases. It is also noticed that B has an appreciable effect only when A≤10 and H>1, as shown in Figures 3.5a and 3.5b. Figure 3.5c shows that, when A=100, the vdW force between a sphere and a cylinder can be well estimated by the flat plate approximation at any separation distances. Physically, this fact indicates that the retarded vdW interaction between a small spherical particle and a very thick cylinder can be adequately approximated by using $\overline{F}_3^{Ret}(H)$ in Equation (3.23) over the range of H=0.001~100.

3.5 Determination of the Hamaker Constant A_{132}

The previous sections deal with the vdW interaction potential $\overline{V}(H)$ and force $\overline{F}(H)$ nondimensionlized by A_{12} and $\frac{A_{12}}{a}$, respectively. However, when the numerical solutions (Chapter 6) of the general mass transport equation (Chapter 2) are pursued, it is required to determine the Hamaker constant in order to quantify the effect of the vdW interactions on the deposition processes of fiber-oil-water systems. For the fiber-oil-water deposition systems, the well-known Hamaker constant (see Section 3.2.2) can be defined as (Israelachvili, 1985):

$$A_{of} = \pi^2 C n_o n_f, \tag{3.24}$$

where subscript *o* identifies the oil phase and subscript *f* the fiber.

Since the number densities of molecules of most materials are unknown, it becomes hardly possible to determine their Hamaker constants directly from Equation (3.24). On the other hand, in principle, on the basis of the Lifshitz theory (Lifshitz, 1956; Parsegian, 1975; Israelachvili, 1985), the Hamaker constants can be easily related to the static dielectric constants and the refractive indexes of the media involved. However, it is also very difficult to accurately measure these electrodynamic properties of the interacting media under a variety of practical conditions. Alternatively, in the present study, it is attempted to obtain the unknown Hamaker constants in terms of those, which can be determined directly from the known surface energies γ of solids and liquids. For an interface formed between a liquid and its vapor, γ is usually referred to as its surface tension, whereas for an interface formed between a liquid and a fluid or between a solid and a fluid, γ is strictly referred to as the interfacial tension.

3.5.1 Combining Relations

The combining relations or combining laws are frequently used for the cases in which the exact value of the unknown Hamaker constant either is difficult to determine or can not be found directly in the literature but it can be related to known ones by the combining laws. A glance at Equation (3.24) indicates that A_{132} can be related to A_{131} and A_{232} via:

$$A_{132} = \pm\sqrt{|A_{131}A_{232}|} \tag{3.25}$$

where A_{132} is the Hamaker constant for the interaction between phase 1 (spherical oil droplet) and phase 2 (cylindrical fiber) across medium 3 (aqueous phase), as shown in Figure 3.1c. The "±" sign is to be chosen such that positive A_{132} is for the attractive vdW interaction force and negative A_{132} stands for the repulsive vdW interaction force. For the fiber-oil-water deposition system, A_{131} represents the Hamaker constant for two oil droplets interacting across water medium and A_{232} represents the Hamaker constant for two fiber surfaces interacting across water medium. Therefore, it is seen from its definition that A_{132} depends on the physical properties of the oil droplet and the fiber surface and the aqueous solution separating them in terms of A_{131} and A_{232}. Furthermore, these two Hamaker constants can be related to the following Hamaker constants (Israelachvili, 1972):

$$\begin{cases} A_{131} = A_{313} \approx A_{11} + A_{33} - 2A_{13} \\ A_{232} = A_{323} \approx A_{22} + A_{33} - 2A_{23} \end{cases} \tag{3.26}$$

where, A_{ij} is Hamaker constant for media i and j interacting across vacuum (air), i, j=1, 2, 3. Substituting Equation (3.26) into Equation (3.25) gives:

$$A_{owf} \approx \pm\sqrt{|(A_{oo} + A_{ww} - 2A_{ow})(A_{ff} + A_{ww} - 2A_{fw})|} \tag{3.27}$$

Here, for convenience, the subscripts, 1, 2 and 3 for the Hamaker constants are replaced by the subscripts, o, f and w, which represent the oil phase, the fiber phase and the water medium respectively.

3.5.2 Relations between the Hamaker Constants and the Surface Energies

It has been proved that the unretarded van der Waals interaction potential between two planar surfaces at a distance D apart is equal to $-\frac{A_{11}}{12\pi D^2}$ for per unit area (Israelachvili, 1985). Further, the specific potential energy W(D) of the two planar surface at a distance D apart may be written as (Israelachvili, 1985):

$$W(D) = \frac{A_{11}}{12\pi}\left(\frac{1}{D_0^2} - \frac{1}{D^2}\right) \quad \text{per unit area} \tag{3.28}$$

where, D_0 is the separation distance at which the two surfaces are actually in contact, i.e., at $D=D_0$, $W(D_0)=0$. D_0 is sometimes also called either the interfacial contact separation distance or a "cut-off" distance. Physically, the surface energy γ can be defined as either the energy required to create a new surface of unit area or half the energy needed to separate two surfaces from contact ($D=D_0$) to infinity ($D=\infty$). Hence, the first term on the right-hand side of Equation (3.28) is equal to the total surface energy 2γ of the two identical surfaces, each of which has a unit surface area. The specific potential energy $W(\infty)$ for the two identical isolated surfaces can thus be related to the surface energy by:

$$W(\infty) = \frac{A_{11}}{12\pi D_0^2} = 2\gamma \tag{3.29a}$$

or

$$A_{11} = 24\pi D_0^2\gamma \tag{3.29b}$$

With the known Hamaker constants, Israelachvili (1985) gives the predicted surface energies of a variety of compounds using the above equation with the same cut-off separation distance of $D_0=0.165$ nm. It is shown that $D_0=0.165$ nm yields values for γ in such good agreement with those measured, even for very different liquids and solids. Only for highly polar H-bonding liquids, such as methanol, glycol and water, does Equation (3.29b) always underestimate their surface energies determined from the known Hamaker constants or overestimate their Hamaker constants determined from the measured surface energies. Furthermore, it has been concluded that, taking the cut-off separation distance D_0 as a "universal constant" ($D_0=0.165$ nm), Equation (3.29b) can be used to determine the unknown Hamaker constants from the measured surface energies or vice verse for non-H-bonding solids and liquids (Israelachvili, 1985). Therefore, in this study, the unknown Hamaker constants for silicone oil (close to dodecane and hexadecane) and the glass fiber surface (close to mica) can be determined from the measured surface energies using Equation (3.29b) with $D_0=0.165$ nm. Strictly speaking, it is not suggested to use Equation (3.29b) to relate the Hamaker constant with the surface energies for highly polar H-bonding liquids such as the aqueous solutions tested in this work. However, on the one hand, the Hamaker constants for the oil-water-fiber systems studied here can not be found in the literature. On the other hand, as will be described in the next section and Chapter 4 in detail, all the relevant surface energies of the oil-water-fiber systems can be measured properly. Hence, Equation (3.29b) is still used to determine the individual Hamaker constants on the right side of Equation (3.27). In Section 4.7, it will be shown that such determined overall Hamaker constants A_{owf} (see Tables 4.8 and 4.9 for details) for the oil-water-fiber systems are in a reasonable range in comparison with those published values for oils (dodecane and hexadecane), mica and metals (Ag, Au and Cu) interacting across water (Israelachvili, 1985).

For the present deposition system, using Equation (3.29b) to rewrite Equation (3.27) yields:

$$A_{owf} \approx +24\pi D_0^2 \sqrt{|(\gamma_{ov}+\gamma_{wv}-2\gamma_{ow})(\gamma_{fv}+\gamma_{wv}-2\gamma_{fw})|} \tag{3.30}$$

where, γ_{ov}, γ_{wv} and γ_{ow} represent the surface tensions of the oil-vapor and the water-vapor interfaces and the interfacial tension of the oil-water interface, while γ_{fv} and γ_{fw} are the surface tension of the fiber-vapor interface and the interfacial tension of the fiber-water interface, correspondingly. As will be mentioned in Chapter 7, it is found from the deposition tests that, in this study, deposition of the oil droplets onto the fiber surface always occurs to some extent, regardless of the liquid properties of the aqueous solutions and the polarity characteristics of the EDL interaction. This experimental observation requires that the vdW interaction be always attractive in this study. Accordingly, the "+" sign is chosen in Equation (3.30) in order for A_{owf} to be always positive. It should be noted that, in principle, the vdW interaction between any two different phases across a medium rather than vacuum (air) can be either attractive ($A_{132}>0$) or repulsive ($A_{132}<0$), depending on the static dielectric constants and the refractive indexes of the three media involved (see Equations (11.13a,b) for details, Israelachvili, 1985).

As indicated by Equations (3.26) and (3.27), in this study, the combining laws were employed to relate the overall Hamaker constant A_{owf} to the Hamaker constants for the media i and j interacting across vacuum (air) to A_{ij}, i,j=1, 2, 3. In principle, it is not recommended to use Equation (3.30) for non-pure aqueous systems. Nevertheless, it will be shown in Chapter 4 in detail that, the surface energies, γ_{wv} and γ_{ow}, always decrease if the pH value of the aqueous phase deviates from the equilibrium value (pH=6.50) or if an electrolyte/ionic surfactant is added into the aqueous phase (see Tables 4.8 and 4.9). Based on the above discussion on the interfacial contact separation distance D_0, it can be inferred that the Hamaker constants calculated for the non-pure aqueous phases, such as the aqueous solutions with different pHs, or electrolyte/ionic surfactant solutions, should at least have the same accuracy as that for the pure water-oil-fiber system. Furthermore, in order to avoid dealing with very complicated aqueous solutions, in this study, the effects of pH value, electrolyte and ionic surfactant on the deposition of the oil droplets onto the fiber surfaces were studied individually. Each aqueous solution was prepared by adding a different chemical each time into the pure DIUF water.

It is well known that the surface energies of any liquid-fluid interfaces can be experimentally measured, e.g., based on its deformation under the gravitational field. For instance, the surface energies of the liquid-fluid interfaces, γ_{ov}, γ_{wv} and γ_{ow} required in Equation (3.30), can be measured easily and accurately by using the axisymmetric drop shape analysis (ADSA) technique for the pendant drop case. The detailed technical descriptions on the ADSA technique were given by Neumann and co-workers (Rotenberg et al., 1983; Cheng et al., 1990; Li et al., 1992). However, the surface energy of any solid-fluid interfaces, such as γ_{fv} and γ_{fw} required in Equation (3.30), can not be measured directly because rigid solid surface prevents any deformation of the solid-fluid interfaces. Thus an indirect method has to be sought.

3.6 Equation of State for Interfacial Tensions of Solid-Liquid Systems

The equation of state for interfacial tensions of solid-liquid systems is probably the most widely used method to determine the surface energies of the solid-fluid interfaces from the directly measured surface energies of the liquid-fluid interfaces and the contact angle (wettability) of the solid-liquid-fluid system (Li and Neumann, 1990a; 1992a). For the fiber-oil-water system considered here, this equation can be written as:

$$\cos\theta = -1 + 2\sqrt{\frac{\gamma_{fv}}{\gamma_{wv}}}e^{-0.0001247(\gamma_{wv}-\gamma_{fv})^2} \tag{3.31a}$$

where, θ is the contact angle of water drop formed on the fiber surface. This angle represents the wettability of the water-vapor interface on the fiber surface. In Equation (3.31a), γ_{wv} and θ for fiber-water-vapor system can be accurately measured by using the ADSA technique for the flat fiber surfaces. Once the values of γ_{wv} and θ are measured, the fiber surface tension γ_{fv} can be calculated from the equation of state for the solid-water-vapor system by iteration. Furthermore, the interfacial tension of the fiber-water interfaces, γ_{fw}, can be determined from the following classical Young equation:

$$\gamma_{wv}\cos\theta = \gamma_{fv} - \gamma_{fw} \tag{3.31b}$$

Nevertheless, it has long been noted that the sophisticated ADSA technique for the sessile drop case can be used to measure the wettability (θ) of any liquid-fluid interface on a flat solid surface only. Hence, a new contact angle measurement technique has to be devised in order to measure the contact angles on curved surfaces, such as cylindrical fiber surfaces studied here. In this study, a novel contact angle measurement technique is developed during the course of this thesis research. It determines the contact angle of a solid-liquid-fluid system by analyzing the capillary profile around a cylinder (ACPAC) and will be described in detail in Chapter 4.

3.7 The Electrical Double Layer (EDL) Interaction

According to the well-known DLVO theory (Derjaguin and Landau, 1941; Verwey and Overbeek, 1948), the colloidal interaction force required in the general mass transport Equation (2.4) consists of the van der Waals (vdW) and the electrical double layer (EDL) interaction forces. In additional to the vdW interaction, the electrical double layer (EDL) interaction between an approaching spherical particle and a cylindrical surface as a function of separation distance also plays an important role in the flow of colloidal emulsions or suspensions through a filter composed of many cylinders of fibers or other materials. This kind of interaction sometimes becomes essential to the problems of colloidal stability and particle deposition onto a cylindrical collector. In the past, similar to the case for the vdW interaction, the computation of the EDL interaction between a spherical particle and a cylindrical surface was, however, performed using the assumption of a sphere interacting with an infinitely large flat plate (Hogg, Healy and Fuerstenau (HHF), 1966; Adamczyk and van de Ven, 1981b; Masliyah, 1994; Sanders et al., 1995). Regardless of possible large curvature effect that the cylindrical surface may have, the sphere-flat plate approximation is often used without justification because of its simplicity.

In the literature, the exact or approximate analytical expressions are available only for the EDL interaction potentials between two similar or dissimilar EDLs of appropriate geometric configurations, such as those between two parallel flat plates and between two spheres. Then by letting either radius of the two spheres be infinity, the EDL interaction potential between the two spheres (HHF, 1966) will become the EDL interaction potential between a sphere and a flat plate. However, it is an obvious fact that the sphere-flat plate approximation always overestimates the EDL interaction between a spherical particle and a cylindrical surface. A thorough literature search indicates that there has not been effort made yet to account for the curvature effect of the cylindrical EDL for this case. In fact, one has no option but to employ the sphere-flat plate approximation for the sphere-cylinder configuration. At present, it is not quite clear how large an error this approximation may cause when it is used to calculate the EDL interaction between a sphere and a cylinder at an arbitrary separation distance.

Irrespective of the methods used to determine the EDL interaction between any two EDLs, usually, its determination requires the exact information about the potential distribution between these two interacting EDLs. Obviously, the potential distribution between the two approaching EDLs differs considerably from each individual potential distribution around each EDL when it is far away from the other. The potential distribution between the two interacting EDLs strongly depends on the extent to which they are overlapped. As will be shown later, with invoking the well-known Debye-Hückel (D-H) approximation, i.e., taking potential as small in magnitude, it is easy to derive an analytical expression for the potential distribution between two overlapped flat EDLs. In fact, mathematically, the D-H approximation enables the Poisson-Boltzmann (P-B) equation to become a linear 2nd-order ordinary differential equation (ODE). Thus the potential distribution between the approaching flat EDLs simply equals to the addition of each potential distribution around each EDL. It is also relatively easy to obtain the general formula for the EDL interaction potential between the two flat EDLs once the potential distribution between them is obtained under the D-H approximation.

The general analytical solution of the potential distribution around a single spherical or cylindrical EDL is available if the Debye-Hückel approximation is invoked (Hunter, 1981). However, for these kinds of geometrical combinations, the governing P-B equation of the potential distribution is extremely difficult to be solved even numerically because of their geometrical complexities. Therefore, it becomes practically impossible in the present case to directly derive an exact EDL interaction potential between a spherical EDL and a cylindrical EDL. Alternatively, in a later section, an attempt is made to obtain an approximate integral solution of the EDL interaction potential between a spherical EDL and a cylindrical EDL. In this study, the same procedure used by HHF (1966) in deriving the EDL interaction potential between two spherical EDLs will be followed. First, the EDL interaction potential between two differential surface elements, one on the spherical EDL and the other on the cylindrical EDL, is approximated by that between two parallel overlapped flat EDLs at the same separation distance. Then the Derjaguin's integration method (Derjaguin, 1934) is extended to evaluate the total EDL interaction potential between a spherical particle and a cylindrical surface. Hence, the effect of curvature of the cylinder on the total EDL interaction can be accounted for the present configuration. Since the final solution is expressed by a two-dimensional integral equation that can not be integrated analytically, accurate numerical integration has to be pursued. Eventually, the numerical predictions of the EDL interaction force for the sphere-cylinder system are compared with the analytical results of the EDL interaction force for the sphere-flat plate system at various separation distances. Consequently, the validity of the widely employed sphere-flat plate approximation can be assessed quantitatively.

In the subsequent sections, after a brief review on the HHF expressions for the sphere-sphere and extended sphere-flat plate configurations, first, an approximate integral solution for the EDL interaction between a spherical particle and a cylinder will be presented. Based on this numerical solution, the effects of the curvature of the cylindrical surface on the EDL interaction can be studied. It is worthwhile noting that, similar to the case for the vdW interaction, in this study, the spherical particle or the oil droplet is assumed to be rigid such that its deformation effects on the EDL interaction are not considered. The numerical predictions of the EDL interaction force between a sphere and a cylinder are then compared with the analytical solution for the EDL interaction force between a sphere and a flat plate at rather different separation distances. Finally, the validity of the widely employed sphere-flat plate approximation will be examined.

3.8 The HHF Expressions for the EDL Interaction between a Spherical Particle and a Flat Plate

It has long been observed in numerous experiments that, when dispersed in a liquid solution, a colloidal particle may be charged and thus surrounded by the ions of opposite polarity from the bulk solution. The overall arrangement of the electric charge on the particle, together with the balancing charge in the bulk phase, is often referred to as the electrical double layer (EDL) of the particle. Generally, the EDL can be well characterized by its strength and polarity, ζ, the zeta-potential, and its thickness, κ^{-1}, the Debye-Hückel reciprocal length parameter. The parameter κ is very important in colloid science and is usually referred to as the Debye-Hückel parameter named after these two workers. It can be expressed as follows (Hunter, 1981):

$$\kappa = \left(\frac{e^2 \sum n_i^0 z_i^2}{\varepsilon_r \varepsilon_0 \mathbf{k} T}\right)^{1/2}, \tag{3.32}$$

where, e is the electron charge (e=1.602×10^{-19} C, in this thesis, all the fundamental physical constants are quoted from Weast et al., 1989); n_i^0 is the number of ions of type *i* per unit volume (number density or concentration) in the bulk solution and z_i is the valence of ion of type *i*, ε_r is the dimensionless dielectric constant or relative dielectric permittivity of the solution ($\varepsilon_r \approx 80$ for water at T=295.15 K) and ε_0 is the permittivity of vacuum ($\varepsilon_0 = 8.854\times10^{-12}$ CV^{-1}m^{-1} or Fm^{-1}), **k** is the Boltzmann constant (**k**=1.381×10^{-23} J K^{-1}) and T is the absolute temperature (at room temperature, 22°C, T=295.15 K). It is seen from Equation (3.32) that the EDL thickness, κ^{-1}, mainly depends on the ionic properties (z_i) and concentrations (n_i^0) of the dispersing medium.

According to the Gouy-Chapman theory (Gouy, 1910; Chapman, 1913) for a diffuse electrical double layer around a colloidal particle, the potential distribution at any point in the system is governed by the Poisson-Boltzmann (P-B) equation (Hunter, 1981):

$$\nabla^2 \psi = \frac{2n^0 ze}{\varepsilon_r \varepsilon_0} \sinh\left(\frac{ze\psi}{\mathbf{k}T}\right), \tag{3.33}$$

where, ψ is the potential and ∇^2 is the Laplacian operator. At this point, it should be pointed out that Equation (3.33) is the simplified P-B equation for the case where the supporting electrolyte is symmetric, i.e., in the bulk solution, the cations and anions have the same valence. Thus, $n_+^0 = n_-^0 = n^0$ and $z_+ = -z_- = z$, where n^0 is the ion number density of the bulk phase and z is the valence of ions and the counterions. In reality, it turns out to be possible to treat most electrolytes as though they were symmetric for the reasons clearly stated by Hunter (1981, see Section 2.3.1.3). If the colloidal particle is far from another interface (or another EDL), its potential distribution can be easily determined by solving the P-B equation either analytically (with invoking the D-H approximation) or numerically (without invoking the D-H approximation). The boundary conditions for the P-B equation are that, at the particle surface, the potential is equal to the zeta-potential ζ_p of the particle and that, in the bulk phase at infinity, the potential vanishes. However, if the particle approaches another interface or vice verse, for instance, another EDL is in the vicinity, the original EDLs surrounding these two interfaces will become overlapped and thus will interact each other. This leads to the so-called EDL interaction. When these two EDLs approach each other, the potential distribution between the two EDLs will be modified and thus differ from that around each single EDL, though in either case the potential distribution is still governed by the same P-B equation, Equation (3.33). Apparently, the determination of the EDL interaction between the two overlapped EDLs requires the specific information regarding the modified potential distribution. Such modified potential distribution depends on their separation distances, their geometrical sizes and configurations, and their ζ-potentials and thickness as well. Furthermore, since the above physical properties of the two EDLs strongly depend on the ionic properties and concentrations of the bulk medium between the two interacting EDLs, such EDL interaction certainly depends on the liquid properties as well.

Verwey and Overbeek (1948) solved Equation (3.33) graphically for the potential distribution as a function of separation distance between two infinite plates subject to the boundary conditions that the surface potentials of the two plates are equal, i.e., for similar particles. Derjaguin (1954) obtained similar solutions for the more general case of different particles, having surface potentials that differ in both sign and magnitude. However, all these solutions are extremely unwieldy. Later on, a simplified analytical solution was achieved by Hogg, Healy and Fuerstenau (1966), which is usually called HHF expression or formula named after them. In the literature, the HHF formula is widely used to provide a general relation expressing the EDL interaction potential between the electrical double layers surrounding any two similar or dissimilar colloidal particles, which is expressed as follows:

$$V_R(D) = \frac{2\pi\varepsilon_r\varepsilon_0 a_1 a_2 \zeta_1 \zeta_2}{(a_1 + a_2)}\{\ln[\frac{1+\exp(-\kappa D)}{1-\exp(-\kappa D)}] + \frac{(\zeta_1^2 + \zeta_2^2)}{2\zeta_1\zeta_2}\ln[1-\exp(-2\kappa D)]\}, \quad (3.34a)$$

where, $V_R(D)$ is the interaction potential between the two EDLs on the two particles; a_1 and a_2, ζ_1 and ζ_2 are the radii of the two particles and the zeta-potentials of their EDLs, respectively; and D is their separation distance. With Equation (3.34a), the HHF expression for the EDL interaction potential between a particle and a flat plate can be readily derived by letting the radius of one particle be $a_1=a_p$ and the other's be infinity, $a_2=\infty$, in the equation,

$$V_1(H) = 2\pi\varepsilon_r\varepsilon_0 a_p \zeta_p \zeta_c \{\ln[\frac{1+\exp(-\tau H)}{1-\exp(-\tau H)}] + \frac{(\zeta_p^2 + \zeta_c^2)}{2\zeta_p\zeta_c}\ln[1-\exp(-2\tau H)]\}, \quad (3.34b)$$

where, $V_1(H)$ is the interaction potential between the EDL on the particle and the EDL on the flat plate; ζ_p and ζ_c are the zeta-potentials of the EDLs on the particle and on the flat plate collector, respectively; $\tau = \kappa a_p$ is the ratio of the radius of the particle to the EDL thickness, sometimes simply called the reduced radius of the particle; $H=D/a_p$ is the dimensionless separation distance.

Since the detailed derivations of Equation (3.34a) were presented by Hogg, Healy and Fuerstenau (1966), here, only the applicability of Equation (3.34a), and of course Equation (3.34b) as well, will be addressed briefly. In principle, the relationship expressed by the Equation (3.34a) only holds exactly for values of ζ_1 and/or ζ_2 of less than 25 mV (i.e. $\left|\frac{e\zeta}{\mathrm{k}T}\right| < 1.0$) and for the liquid conditions such that the thickness of the EDLs, κ^{-1}, is small compared with the particle sizes, a_1 and a_2, i.e. $\tau_1 = \kappa a_1 \gg 1$, and $\tau_2 = \kappa a_2 \gg 1$. Theoretically, the first requirement is necessary condition for the use of the well-known D-H approximation because these two workers used the same approximation in their theory of strong electrolytes, i.e. taking ψ as small in magnitude. Consideration is confined to the case where the potential is always small ($|\psi|$<25 mV) and the electrolyte is symmetric. Under these conditions, a mathematical linearization approximation, $\sinh(\frac{ze\psi}{kT}) \approx \frac{ze\psi}{kT}$, can be applied. Therefore, the HHF expressions represented by Equations (3.34a,b) are based on the linear approximation. For the liquid solution containing symmetric electrolyte and small potentials, Equations (3.32) and (3.33) reduce to:

$$\kappa = (\frac{2e^2 n^0 z^2}{\varepsilon_r \varepsilon_0 kT})^{1/2}, \tag{3.35a}$$

and

$$\nabla^2 \psi = \kappa^2 \psi \tag{3.35b}$$

Thus, using the D-H approximation, an analytical solution of Equation (3.35b) can be found not only for a single flat, or spherical, or cylindrical EDL (Hunter, 1981), but also for two overlapped flat EDLs (Hogg, Healy and Fuerstenau, 1966). The second assumption, i.e. $\tau_1 = \kappa a_1 \gg 1$, and $\tau_2 = \kappa a_2 \gg 1$, is required in order to use the Derjaguin's integration method to obtain the total EDL interaction potential between two spherical particles from that between two differential flat surface elements. However, as was shown by HHF (1966), Equation (3.34a) is a good approximation for ζ_1 and ζ_2 up to less than 50~60 mV. In addition, Verwey and Overbeek (1948) showed that the Derjaguin's integration method gives a good approximation for the EDL interaction provided that $\tau_1>10$ and $\tau_2>10$, and that the approximation is not too bad for $\tau_1>5$ and $\tau_2>5$. In summary, Equation (3.34b) should be a good expression for calculating the EDL interaction potential between a particle and a flat collector as long as ζ_p and $\zeta_c \le 60$ mV and the reduced radius of the particle $\tau = \kappa a_p > 5$.

Using kT to nondimensionalize the EDL interaction potential $V_1(H)$ between a particle and a flat plate in Equation (3.34b) yields:

$$\overline{V}_1(H) = \frac{V_1(H)}{kT} = \frac{Dl}{2}\{\ln[\frac{1+\exp(-\tau H)}{1-\exp(-\tau H)}] + (Da+1)\ln[1-\exp(-2\tau H)]\}, \tag{3.36}$$

where,

$$Dl = \frac{4\pi\varepsilon_r \varepsilon_0 a_p \zeta_p \zeta_c}{kT} \tag{3.37a}$$

$$Da = \frac{(\zeta_p - \zeta_c)^2}{2\zeta_p \zeta_c} \tag{3.37b}$$

$$\tau = \kappa a_p \tag{3.37c}$$

Dl is the dimensionless EDL parameter, and Da is the dimensionless EDL asymmetry parameter. The latter represents the portion of the EDL interaction attributable to the difference between the ζ-potential of the spherical particle and that of the flat collector. $\tau = \kappa a_p$, as defined previously, is the ratio of the radius of the particle to the EDL thickness and sometimes it is also simply called the reduced radius of the particle. The dimensionless EDL interaction force between a particle and a flat plate can be readily derived from the above dimensionless EDL interaction potential by using the following relation:

$$\overline{F}_I(H) = \frac{F_I(H)}{\frac{kT}{a_p}} = -\frac{d\overline{V}_I(H)}{dH} = Dl \cdot \tau\left[\frac{\exp(-\tau H)}{1+\exp(-\tau H)} - Da\frac{\exp(-2\tau H)}{1-\exp(-2\tau H)}\right] \tag{3.38}$$

It is seen from Equations (3.36) and (3.38) that the dimensionless EDL interaction between a particle and a flat collector depends only on the dimensionless separation distance H, and the dimensionless physical parameters of the EDLs, Dl, Da and $\tau = \kappa a_p$ given in Equations (3.37a,b,c). Two of these three parameters, Dl (through ε_r) and τ (through κ) are functions of the liquid properties of the bulk medium separating the two EDLs. As will be shown in Chapter 5, Dl and Da (through ζ_p and ζ_c) strongly depend on the liquid properties as well. All the above $V_R(D)$, $V_I(H)$, $\overline{V}_I(H)$ and $\overline{F}_I(H)$ expressions given in Equations (3.34a), (3.34b), (3.36) and (3.38) are often simply called HHF expressions. In Section 3.10, the HHF expression for the EDL interaction force between a spherical particle and a flat collector, Equation (3.38), will be used as an asymptotic analytical solution to compare with the numerical results of the EDL interaction force between a spherical particle and a cylindrical collector.

3.9 The EDL Interaction between a Spherical Particle and a Cylindrical Fiber

3.9.1 Potential Distribution between Two Charged Flat Plates

If a spherical particle and a cylindrical collector are close enough and thus their EDLs start to overlap, the potential distribution between two differential surface elements, one on the spherical EDL and the other on the cylindrical EDL, can be approximated by that between two differential surface elements on two parallel flat plates. In the Cartesian coordinate system, Equation (3.35b) can be expressed as:

$$\frac{d^2\psi}{dx^2} = \kappa^2\psi, \tag{3.39}$$

since the potential varies only in the separation direction, x, as shown in Figure 3.6a. The analytical solution of Equation (3.39) satisfying the following two boundary conditions on the both surfaces:

$$\begin{cases} \psi(x)\big|_{x=0} = \zeta_p \\ \psi(x)\big|_{x=d} = \zeta_c \end{cases} \tag{3.40}$$

can be derived and expressed as follows:

$$\psi(x) = \zeta_p \cosh \kappa x + \left(\frac{\zeta_c - \zeta_p \cosh \kappa d}{\sinh \kappa d}\right)\sinh \kappa x \quad (0 \le x \le d) \tag{3.41}$$

Equation (3.41) describes the potential distribution as a function of separation distance x ($0 \le x \le d$) between the two differential surface elements shown in Figure 3.6a, one on a spherical particle surface (x=0) of the zeta potential ζ_p and the other on a cylinder surface (x=d) of the zeta potential ζ_c.

3.9.2 Specific EDL Interaction Potential between Two Flat EDLs

The EDL interaction potential of per unit surface area between two flat EDLs, v(d), can be simply called the specific EDL interaction potential. Thermodynamically, v(d) is equal to the change in the Gibbs free energy of the EDL system when the two differential surface elements are brought closer from infinity to a specific separation distance d. Thus,

$$v(d) = \Delta G = G_d - G_\infty, \tag{3.42}$$

where G_d and G_∞ are the corresponding Gibbs free energies of the EDL system when the two elements are separated by distances of *d* and infinity respectively. For a single EDL when it is in the thermal equilibrium (dT=0) and mechanical equilibrium (dP=0) with the surrounding aqueous solution, Verwey and Overbeek (1948) have shown that its Gibbs free energy is given by:

$$G = -\frac{1}{2}\sigma\zeta, \quad \text{(for small constant } \zeta\text{)} \tag{3.43a}$$

where σ is the surface charge density. It is noted that Equation (3.43a) is valid for an individual EDL whose ζ-potential can be assumed to be constant (Type I EDLs named by Verwey and Overbeek, 1948) and small so as to satisfy the D-H approximation (Verwey and Overbeek, 1948). Therefore, G_d, the Gibbs free energy of the present EDL system, is equal to the sum of the free energies of the two separate EDLs, i.e.,

$$G_d = -\frac{1}{2}(\sigma_p\zeta_p + \sigma_c\zeta_c), \tag{3.43b}$$

where σ_p and σ_c are the surface charge densities of the EDLs on the spherical surface element and the cylindrical surface element respectively.

Physically, from the electric charge balance condition when a flat element of EDL is in an equilibrium state with a bulk solution, its surface charge density can be related to its surface potential gradient by (Verwey and Overbeek, 1948; Hunter, 1981):

$$\sigma = \pm\varepsilon_r\varepsilon_0\left(\frac{d\psi}{dx}\right)\Big|_{\text{at each surface}}$$

Hence, differentiating Equation (3.41) with respect to x and evaluating the resultant equation at x=0 and x=d respectively yield:

$$\sigma_p = -\varepsilon_r\varepsilon_0\left(\frac{d\psi}{dx}\right)\Big|_{x=0} = -\varepsilon_r\varepsilon_0\kappa(\zeta_c \operatorname{cosech}\kappa d - \zeta_p \coth\kappa d) \tag{3.44a}$$

and

$$\sigma_c = +\varepsilon_r\varepsilon_0\left(\frac{d\psi}{dx}\right)\Big|_{x=d} = +\varepsilon_r\varepsilon_0\kappa(\zeta_c \coth\kappa d - \zeta_p \operatorname{cosech}\kappa d) \tag{3.44b}$$

Substituting the above two expressions for σ_p and σ_c into Equation (3.43b) produces:

$$G_d = \frac{\varepsilon_r\varepsilon_0\kappa}{2}[2\zeta_p\zeta_c \operatorname{cosech}\kappa d - (\zeta_p^2 + \zeta_c^2)\coth\kappa d] \tag{3.45a}$$

As the separation distance of the flat EDLs becomes infinity, i.e., d = ∞, Equation (3.45a) becomes:

$$G_{\infty} = -\frac{\varepsilon_r \varepsilon_0 \kappa}{2}(\zeta_p^2 + \zeta_c^2) \tag{3.45b}$$

Thus bringing Equations (3.45a) and (3.45b) into Equation (3.42) and rearranging it gives

$$v(d) = \varepsilon_r \varepsilon_0 \kappa \zeta_p \zeta_c [\operatorname{cosech} \kappa d + \frac{\zeta_p^2 + \zeta_c^2}{2\zeta_p \zeta_c}(1 - \coth \kappa d)] \tag{3.46}$$

Equation (3.46) expresses the specific EDL (per unit surface area) interaction potential of two flat EDLs as a function of their separation distance, d, their ζ-potentials, ζ_p and ζ_c, as well as the dimensionless dielectric constant, ε_r and the Debye-Hückel parameter, κ. It is worthwhile reiterating that the ionic properties and concentrations of the liquid medium separating the two flat EDLs will affect the specific EDL interaction potential through ε_r and κ, even though the ζ-potentials were assumed to be independent of the liquid properties.

3.9.3 Total EDL Interaction Potential and Force between a Spherical Particle and a Cylindrical Fiber

In the derivation of Equation (3.34a), HHF (1966) employed the Derjaguin's integration method that has been used in many publications. Derjaguin (1934; 1939) considers that provided that the thickness of the EDLs is small compared with the particle size, the interaction between EDLs on two spherical particles may be assumed to be made up of contributions from infinitesimally small parallel rings, each of which can be considered as a flat plate. With the above derived specific EDL interaction potential between two parallel flat EDLs, v(d), given in Equation (3.46), in this study, the Derjaguin's integration method is extended to evaluate the total interaction potential between an EDL on a spherical particle and the other EDL on a cylindrical collector. As schematically shown in Figure 3.6a, the differential surface element chosen on the spherical particle has surface area of ydθdy at separation distance, d, from the corresponding differential surface element on the cylindrical fiber. Thus, the total interaction potential between the two EDLs can be expressed as follows, noting the axisymmetry involved in the coordinate system,

$$V_2(D) = 4\int_0^{\frac{\pi}{2}}\Big[\int_0^{a_p} v(d)ydy\Big]d\theta, \tag{3.47}$$

where D is the separation distance between the particle and the cylinder. Referring to Figures 3.6a-c for details, the following geometrical relations can be readily established:

$$d = D + a_p - \sqrt{a_p^2 - y^2} + L - l,$$

$$L = R - \sqrt{R^2 - y^2},$$

$$l = \sqrt{R^2 - y^2\sin^2\theta} - \sqrt{R^2 - y^2}.$$

Therefore,

$$d = D + a_p - \sqrt{a_p^2 - y^2} + R - \sqrt{R^2 - y^2\sin^2\theta} \tag{3.48}$$

Substituting Equation (3.46) into Equation (3.47) yields

$$V_2(D) = 4\varepsilon_r\varepsilon_0\kappa\zeta_p\zeta_c\int_0^{\frac{\pi}{2}}\Big\{\int_0^{a_p}\Big[\operatorname{cosech}\kappa d + \frac{\zeta_p^2 + \zeta_c^2}{2\zeta_p\zeta_c}(1 - \coth\kappa d)\Big]ydy\Big\}d\theta \tag{3.49}$$

where d is a function of both y and θ variables, i.e. $d=d(H,y,\theta)$ given in Equation (3.48), here H can be considered as a parameter, which at this point is nothing with respect to the integration in the above integral equation. Further using the previously defined dimensionless parameters and nondimensionalizing the both sides of Equation (3.49) by kT produce:

$$\overline{V}_2(H) = \frac{1}{\pi}Dl\cdot\tau\int_0^{\frac{\pi}{2}}\Big[\int_0^1 p_2(H,\overline{y},\theta)\overline{y}d\overline{y}\Big]d\theta, \tag{3.50}$$

where,

$$p_2(H,\overline{y},\theta) = \operatorname{cosech}\tau\overline{d} + (Da+1)(1 - \coth\tau\overline{d}),$$

$$\overline{d} = \frac{d}{a_p} = H + 1 - \sqrt{1 - \overline{y}^2} + A - \sqrt{A^2 - \overline{y}^2\sin^2\theta}$$

$$\overline{y} = \frac{y}{a_p}$$

Similar to the definition given in Section 3.2.1, $A = \frac{R}{a_p}$ is equal to the ratio of the cylinder radius to the sphere radius. Thus, the dimensionless EDL interaction force can be derived by directly differentiating Equation (3.50) with respect to H:

$$\overline{F}_2(H) = \frac{F_2(H)}{\frac{\mathbf{k}T}{a_p}} = -\frac{d\overline{V}_2(H)}{dH} = \frac{1}{\pi} Dl \cdot \tau \int_0^{\frac{\pi}{2}} [\int_0^1 f_2(H, \overline{y}, \theta)\overline{y} d\overline{y}] d\theta, \tag{3.51}$$

where,

$$f_2(H, \overline{y}, \theta) = -\frac{\partial p_2(H, \overline{y}, \theta)}{\partial H} = \tau[\coth \tau\overline{d} \cos ech \tau\overline{d} - (Da + 1)(\cos ech \tau\overline{d})^2]$$

3.10 Numerical Results and Discussion

Based on the Debye-Hückel approximation and the Derjaguin's integration method, the general solutions of the EDL interaction between a spherical particle and a cylindrical fiber are obtained and expressed in Equation (3.50) for the dimensionless EDL interaction potential and in Equation (3.51) for the dimensionless EDL interaction force. These two integral equations can be integrated only numerically. This is performed by using a second-order trapezoid rule method (Hoffman, 1992). The adaptive integration technique is applied and the minimum integration step size for each integration variable is chosen properly in order to satisfy a pre-specified accuracy criterion. In the numerical calculations, the overall accuracy of the two remaining integrals with respect to $\overline{y}$ and θ is improved by evenly reducing the step size of each integral variable until the numerical results exhibit the relative difference less than 0.01% between the two successive integration steps. The numerical predictions are carried out for the following chosen values of the relevant parameters: A=1, 10, 100, τ=5, 10, 100, Dl=+1000, and Da=0, 0.25, 0.50, 0.75, which should cover the most practical situations of interest. Since the dimensionless EDL force is proportional to the dimensionless EDL parameter, Dl, as shown by Equations (3.38) and (3.51), the direct influence of the EDL parameter on the EDL interaction is thus not examined here. It is worthwhile mentioning that, in this numerical study, only the repulsive EDL interaction forces are examined, i.e.

ζ_p and ζ_c have the same polarity. This is because, physically, the repulsive (Dl>0 and Da>0) EDL interaction potentials and the attractive (Dl<0 and Da<0) EDL interactions (forces and potentials) should follow similar trends. The detailed numerical results will be obtained for the nondimensional repulsive EDL interaction force between a spherical particle and a cylindrical fiber, using Equation (3.51). These results will be further compared with the analytical solutions expressed by the HHF expression, Equation (3.38) for the nondimensional EDL interaction force between a spherical particle and a flat plate under the same conditions (τ, Dl and Da). Particular attentions are focused on the EDL interaction forces for these two configurations in the following three rather different ranges of the dimensionless separation distances H, i.e., H«1 (H≈0.001~0.1), H≈1 (H≈0.1~10) and H»1 (H≈10~100).

The curvature effect of the cylindrical fiber, represented by the dimensionless geometric parameter, $A=R/a_p$, on the dimensionless EDL force is shown in Figure 3.7. This figure clearly indicates the strong curvature effect of cylinder on the EDL force between a sphere and an infinitely long cylindrical fiber from H=0.001 to H≈1 above which the EDL interaction quickly diminishes. Hence, the curvature effect on the calculated EDL interaction force can not be neglected at the smaller separation distances. Even for A=100, there is still a noticeable difference (more than 10%) of the EDL forces between the sphere-cylinder and the sphere-flat plate configurations. Therefore, below H≈1, the flat plate approximation, i.e. the HHF expression for the sphere-flat plate system given in Equation (3.38), will considerably overestimate the EDL interaction between a sphere and a cylinder.

Figure 3.8 shows the effect of $\tau = \kappa a_p$, the ratio of the radius of the particle to the EDL thickness, on the EDL forces for the sphere-cylinder configuration and the sphere-flat plate system. Again it is seen from the figure that the flat plate approximation overestimates the EDL interaction between a spherical particle and a cylindrical fiber for A=10. Clearly, at small separation distances, i.e. H«1 (H≈0.001~0.1), the EDL force is nearly proportional to τ as predicted by Equations (3.38) and (3.51). However, around H≈1 (H≈0.1~10), the EDL forces for larger values of τ decrease more quickly and become even smaller than those for smaller values of τ. Furthermore, for rather larger separation distances, H»1 (H≈10~100), as expected, all the EDL forces are small and negligible. Here, some proper understanding of the EDL interaction is required in order to explain the predictions shown in this plot. Physically, the EDL interaction between the two approaching EDLs depends not only on the extent (the dimensionless separation distance H) to which these two EDLs are overlapped, but also on the specific potential distribution between them. The latter is strongly affected by their potential gradients on the solid surfaces and particularly represented by τ, see Equations (3.44a) and (3.44b) for details.

Two systems can be compared with each other, in which the radii of the spheres are same but their Debye-Hückel parameters (κ) are quite different, still assuming that all the other parameters such as A, Dl and Da are identical. For instance, there are two solutions, one has higher electrolyte concentration than the other. Thus their reduced radii of the particles, $\tau = \kappa a_p$, are rather different. From Equation (3.32), it is known that the medium containing higher electrolyte concentration has a larger $\tau = \kappa a_p$. It can also be seen from Equations (3.43) through (3.46) that the slopes of potential on the solid surfaces (or the surface charge densities) are greater if κ is larger. Hence, at same smaller separation distances H, the EDL interaction will strongly depend on the potential gradients only as long as the two EDLs can sufficiently interact with each other (adequately overlapping). Furthermore, the larger the $\tau = \kappa a_p$ is, the stronger the EDL interaction will be between these two EDLs. At this point, it becomes feasible to approximately determine the upper limit of the separation distances below which the above variation tendency of the EDL interaction with $\tau = \kappa a_p$ remains valid. Mathematically, the separation distance for an adequate overlapping between the two approaching EDLs can be estimated as below. By solving Equation (3.35b), Hunter (1981) has shown that the potential distribution remains appreciable (say about 25% of its surface potential) at separation distances up to about $1.5\kappa^{-1}$ from a flat plate surface. Thus the maximum separation distance between the EDLs should be around $D=3.0\kappa^{-1}$ in order for them to interact with each other appreciably. Correspondingly, the upper limit of the dimensionless separation distance is equal to:

$$H_{max} = \frac{D}{a_p} = \frac{3}{\kappa a_p} = \frac{3}{\tau} \tag{3.52}$$

If $H > H_{max}$, the EDL interaction between the two EDLs of the system having larger $\tau = \kappa a_p$ will decrease much more quickly and become even smaller because they can not effectively interact with each other. Based on Equation (3.52), H_{max} is equal to 0.03 for $\tau=100$ and 0.3 for $\tau=10$. The above inference is well supported by the numerical predictions given in Figure 3.8. More specifically, when $H>0.03$, the EDL force for $\tau=10$ becomes stronger than that for $\tau=100$. At $H>0.3$, the EDL force for $\tau=5$ is stronger than that for $\tau=10$ as well.

Finally, the effect of the dimensionless EDL asymmetry parameter, Da, (see Equation (3.37b) for its definition), on the EDL interaction is also studied. The detailed numerical results at the different values of Da=0, 0.25, 0.50 and 0.75 are plotted in Figure 3.9 for the EDL forces of the sphere-cylinder configuration and sphere-flat plate configurations. This figure, as well as Figures (3.7) and (3.8), shows that the EDL forces are always repulsive (positive) as long as Da=0. Physically, a repulsive EDL interaction always exists between two EDLs whose ζ-potentials are the same in magnitude and polarity, i.e. for symmetric EDLs ($\zeta_p=\zeta_c$).

However, it is unexpected to find that, at smaller separation distances, the EDL interaction can become attractive (negative) between the asymmetric EDLs (Da>0), even though their ζ-potentials have the same polarity. Here, Da>0 means that the ζ-potentials on the EDLs differ in strength, i.e., $\zeta_p \neq \zeta_c$, but have the same polarity. One possible interpretation is furnished as follows. The following discussion is focused on the case in which both ζ_p and ζ_c are positive for simplicity, though a similar argument holds valid for the case in which both ζ_p and ζ_c are negative. Generally, the potential distribution around a positively charged EDL ($\zeta>0$) is established such that the potential is equal to its ζ-potential of the EDL at the interface and gradually reduces to zero as the separation distance from the EDL increases. Thus if the ζ-potentials on two EDLs are the same (Da=0), the potential distribution between these two EDLs is established such that the potential reaches the minimum at the middle point between them. It is seen from Equations (3.44a, b) that the surface charge densities on the both EDLs, σ_p and σ_c, are positive (noting that $(\frac{d\psi}{dx})|_{x=0} < 0$ and $(\frac{d\psi}{dx})|_{x=d} > 0$ in this case) and have the same polarity as their ζ-potentials (refer to Figure 3.6a for the configuration and coordinate system). Consequently, their EDL interaction is always repulsive, see Figure 3.9 for the results of Da=0. Nevertheless, if the ζ-potential on an EDL is larger than that on the other side (larger Da) and if the two EDLs are at much smaller separation distances (H<0.3 in Figure 3.9), the potential distribution between them may be quite different. In this case, the potential distribution will be established such that the potential closer to the EDL having larger ζ-potential decreases while the potential closer to the other EDL having smaller ζ-potential has to increase in order to have a continuous potential profile. Again referring to Equations (3.44a, b), the surface charge density on the EDL having larger ζ-potential will be positive while the surface charge density on the other EDL having smaller ζ-potential will be negative. Therefore, the total EDL interaction may become attractive (negative). However, at larger separations, the potential distribution between the two interacting EDLs resumes a shape resembling that between two EDLs whose ζ-potentials are same and thus the EDL interaction becomes repulsive again as shown in Figure 3.9. At even larger separations, the EDL interaction vanishes. All the calculations for Da≠0 given in the figure follow the similar pattern. In addition, this figure indicates that the larger Da is, the stronger the attractive EDL interaction at H«1 (H≈0.001~0.1) but the weaker the repulsive EDL interaction at H≈1 (H≈0.1~10) and H»1 (H≈10~100).

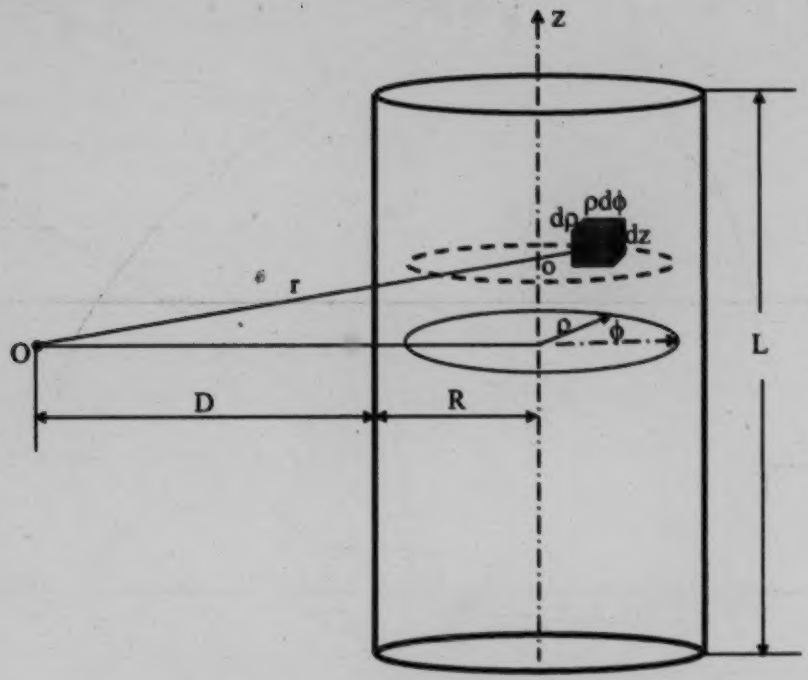

Figure 3.1a Schematic diagram of the van der Waals interaction between a molecule and a cylinder

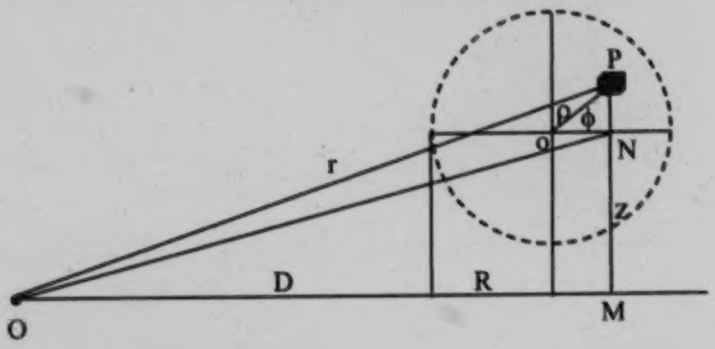

Figure 3.1b The distance between a molecule at point O and a differential volume element at point P in a cylinder, where N is the projection point of the differential volume element P on the OMN plane, and oPN is in the cross-sectional plane (dotted line), which is normal to the OMN plane, oP=ρ, oN=$\rho\cos\phi$ and PN=$\rho\sin\phi$, MN=z, OM=D+R+$\rho\cos\phi$, $ON^2=z^2+(D+R+\rho\cos\phi)^2$, and $r^2=ON^2+PN^2=z^2+(D+R+\rho\cos\phi)^2+\rho^2\sin^2\phi$

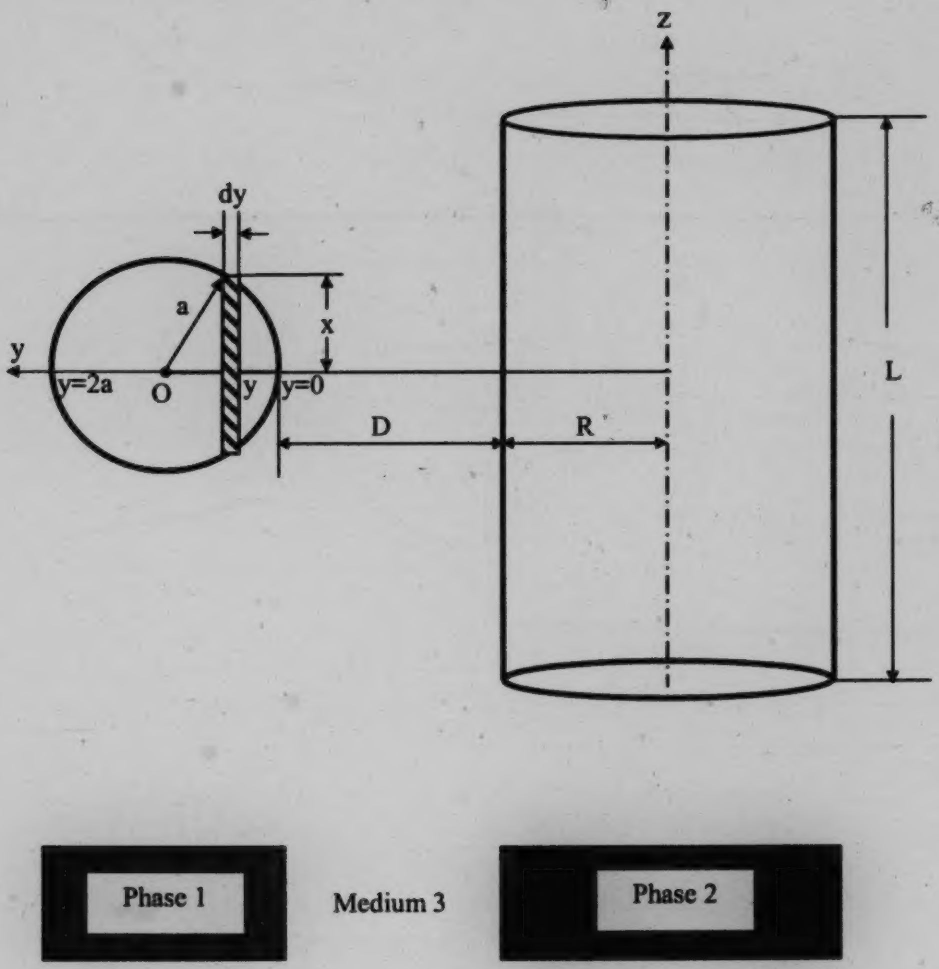
z
dy
a
x
y
y=2a
O
y
y=0
D
R
L
Phase 1
Medium 3
Phase 2

Figure 3.1c The total van der Waals interaction (Hamaker constant A_{132}) between a spherical particle (Phase 1) and a cylindrical solid (Phase 2) across an aqueous solution (Medium 3)

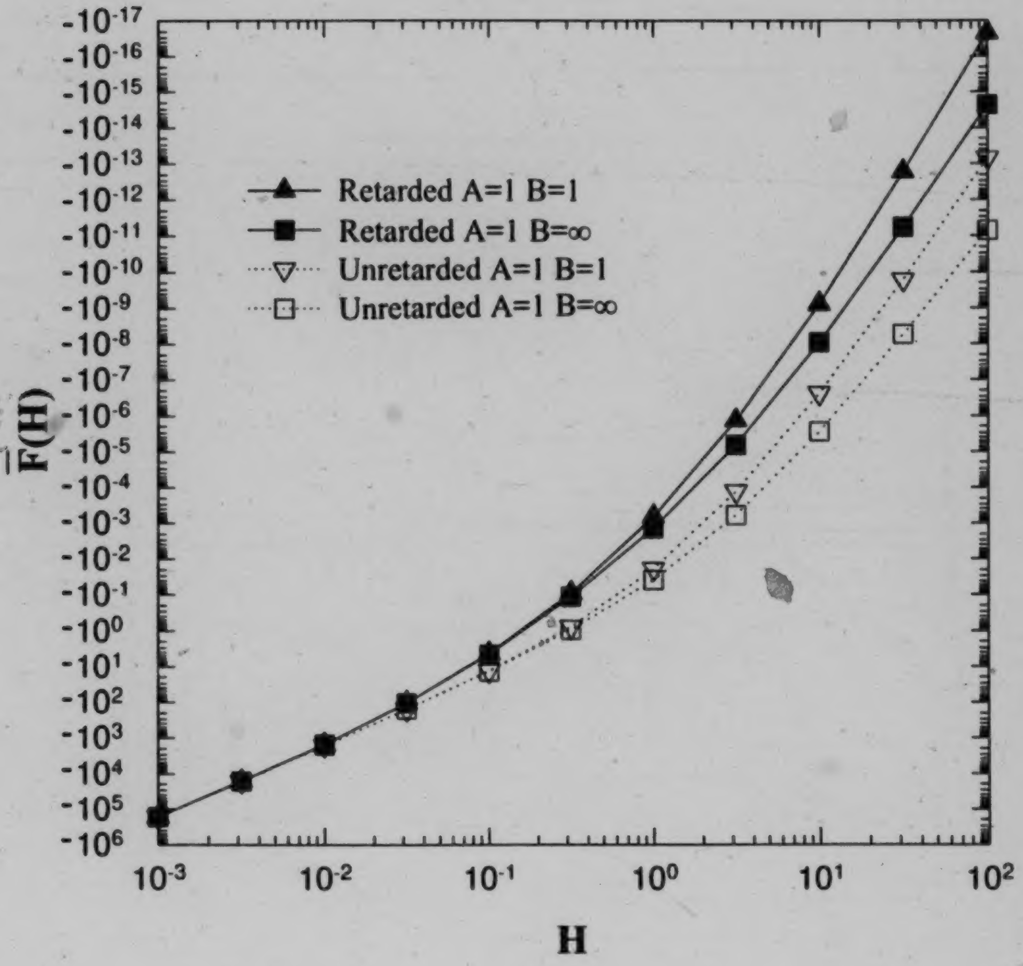

Figure 3.2 Comparison of the retarded and unretarded van der Waals forces between a spherical particle and a cylindrical collector

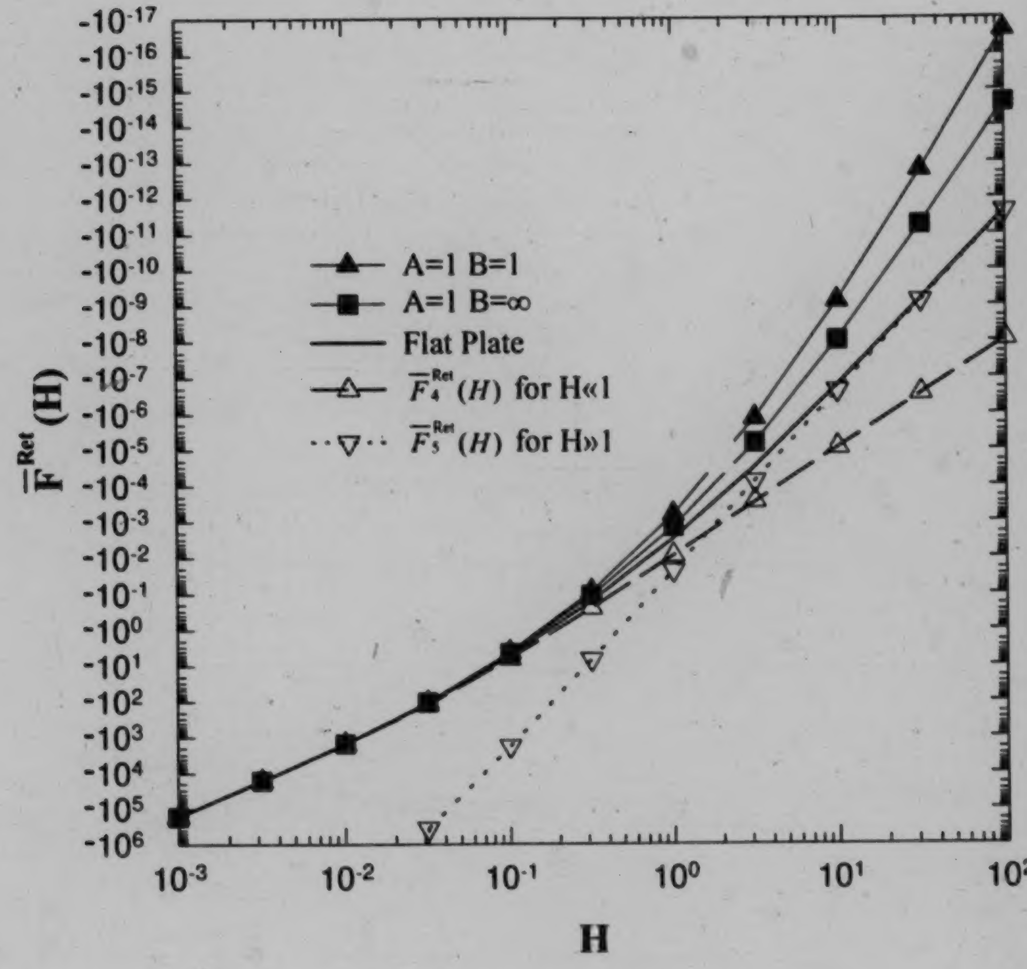

Figure 3.3 Comparison of the different retarded van der Waals force formulae for the sphere-cylinder and the sphere-flat plate systems

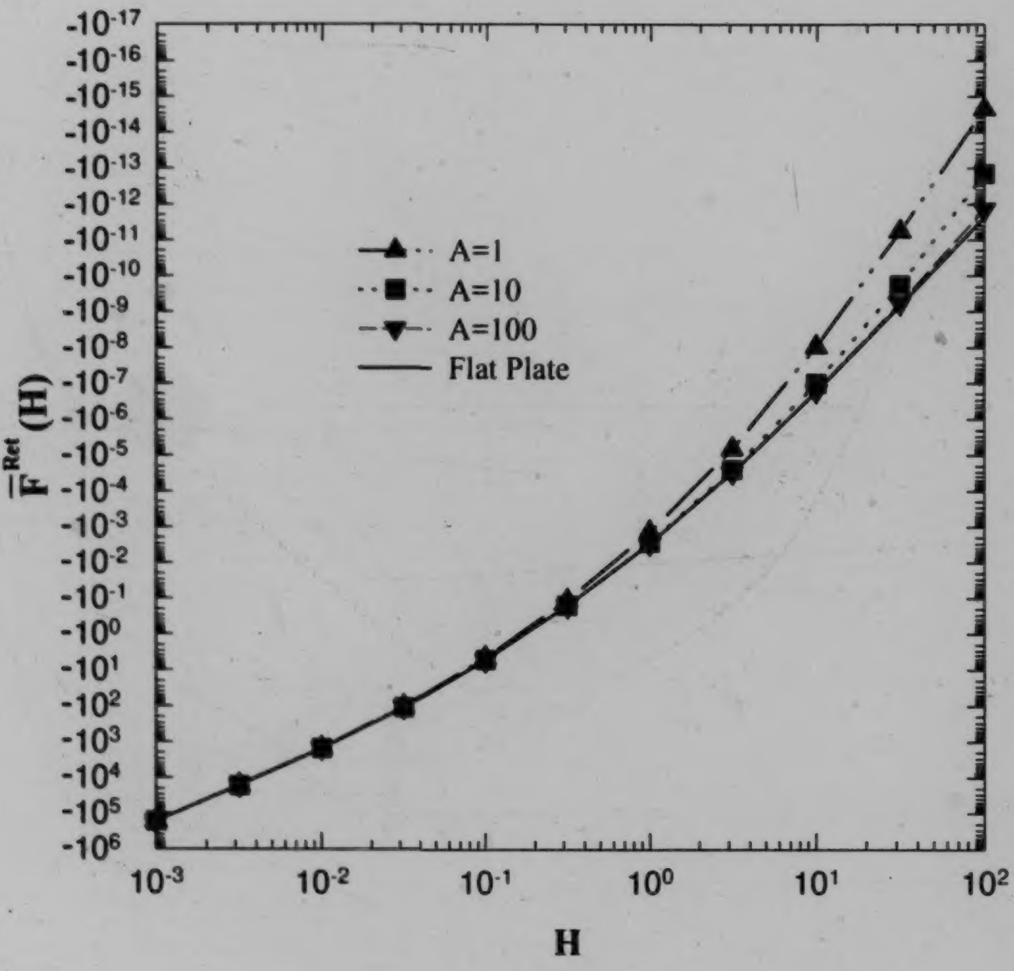

Figure 3.4 The effect of the curvature of the cylinder on the retarded vdW force between a sphere and an infinitely long cylinder (B=∞)

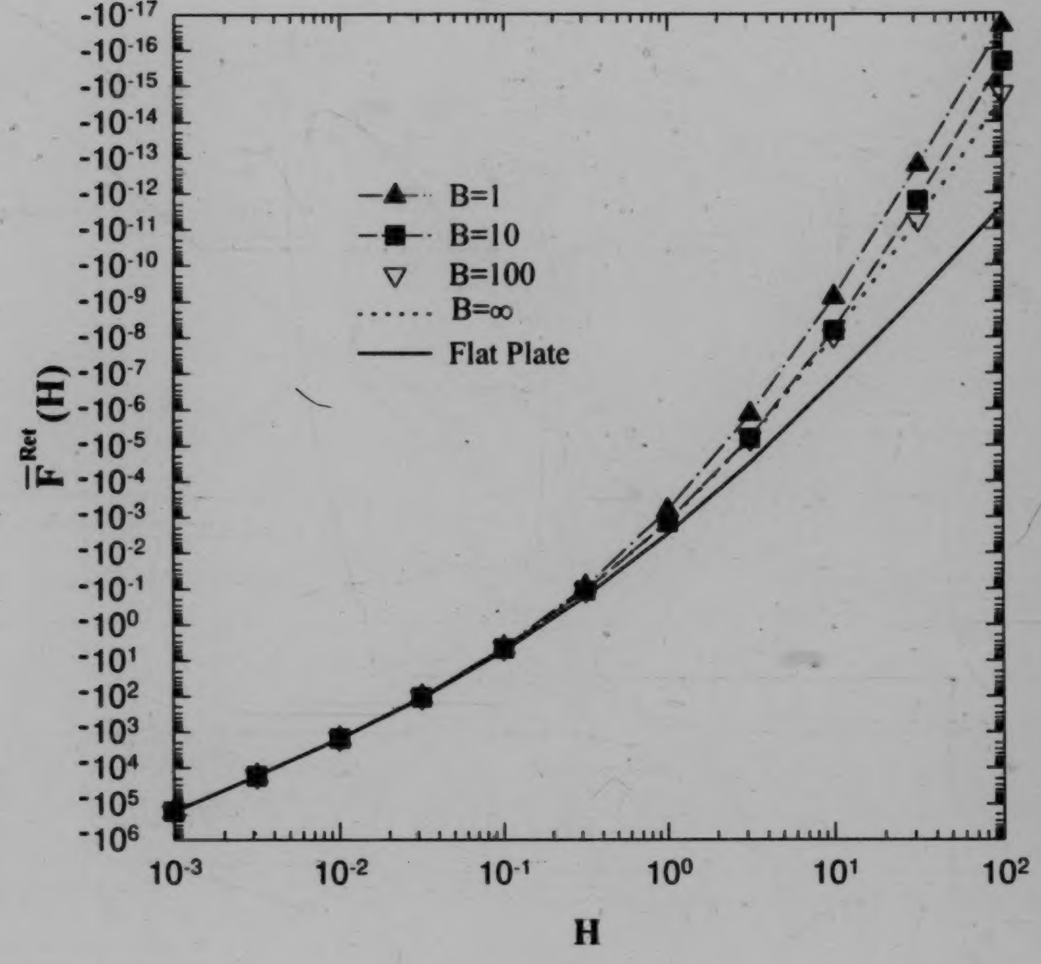

Figure 3.5a The effect of the length of the cylinder on the retarded vdW force between a sphere and a cylinder for A=1

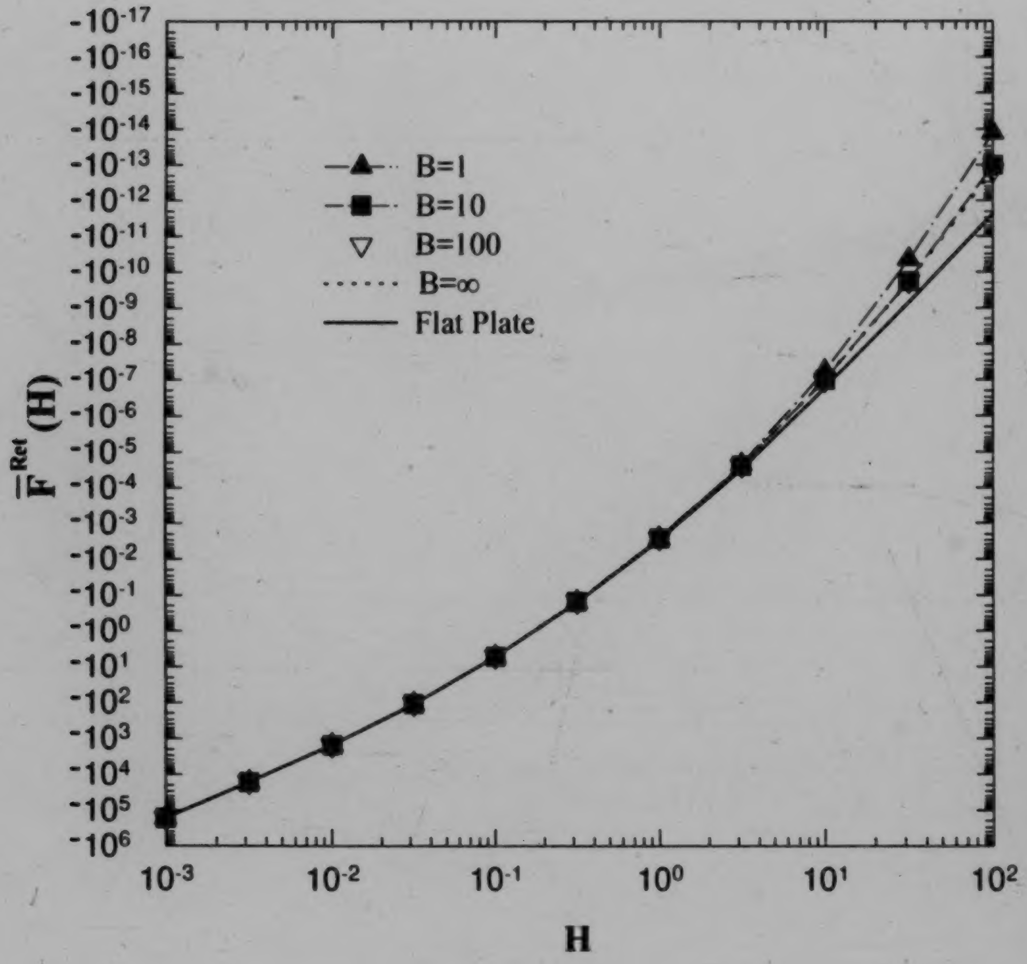

Figure 3.5b The effect of the length of the cylinder on the retarded vdW force between a sphere and a cylinder for A=10

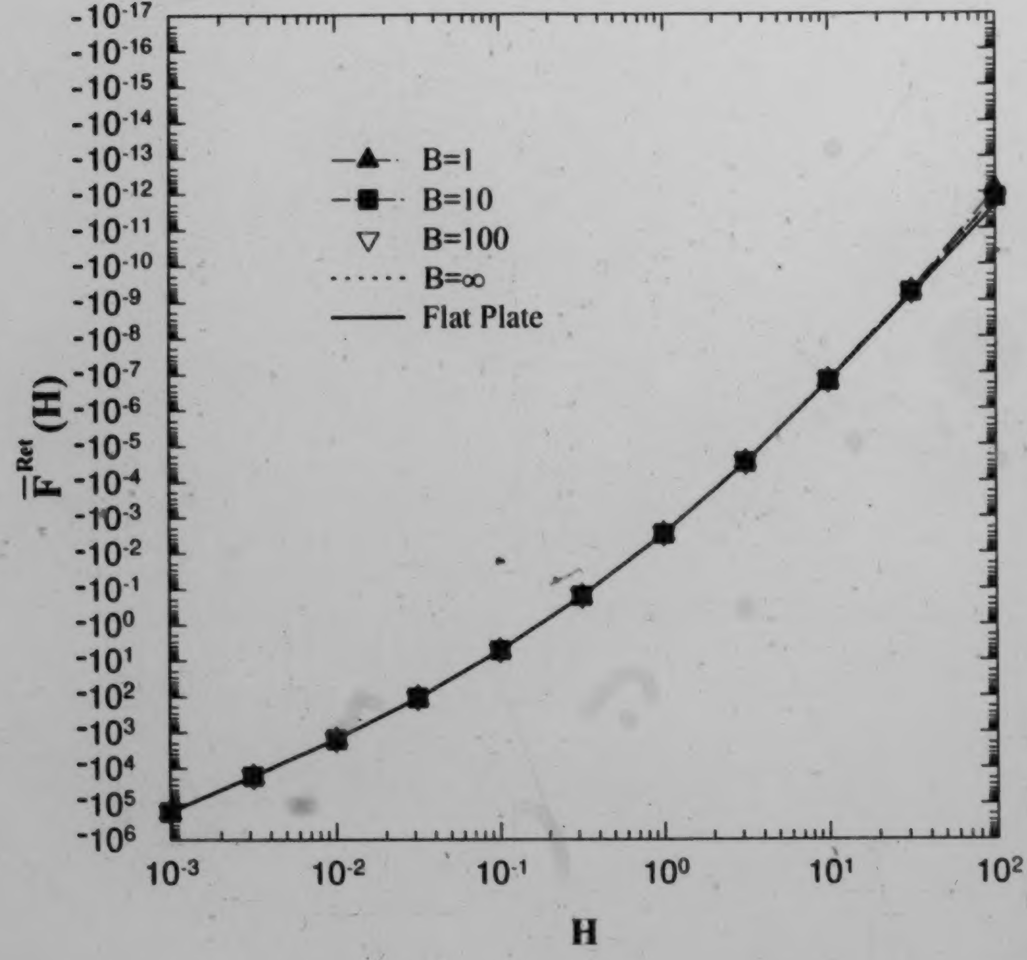

Figure 3.5c The effect of the length of the cylinder on the retarded vdW force between a sphere and a cylinder for A=100

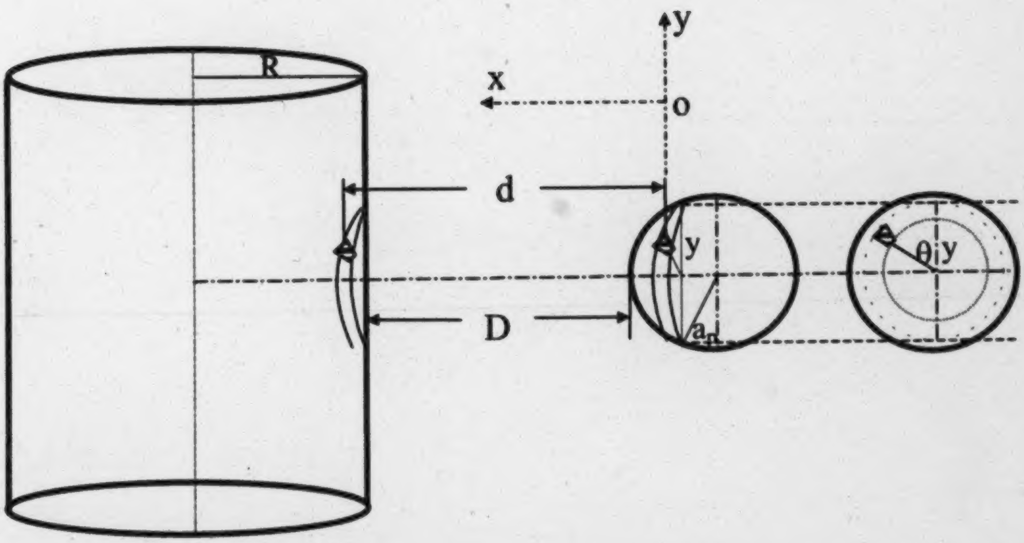

Figure 3.6a The front view of the two differential surface elements representing the electrical double layer (EDL) interaction between a spherical particle and a cylindrical fiber

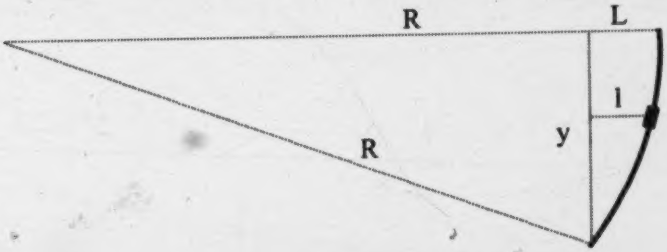

Figure 3.6b The top view of the differential surface element on the cylindrical fiber surface

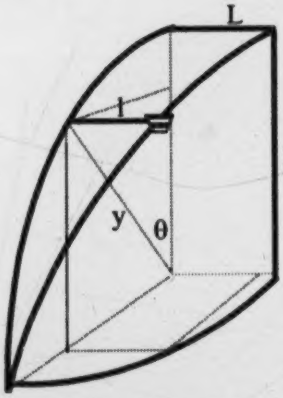

Figure 3.6c The side view of the differential surface element on the cylindrical fiber surface

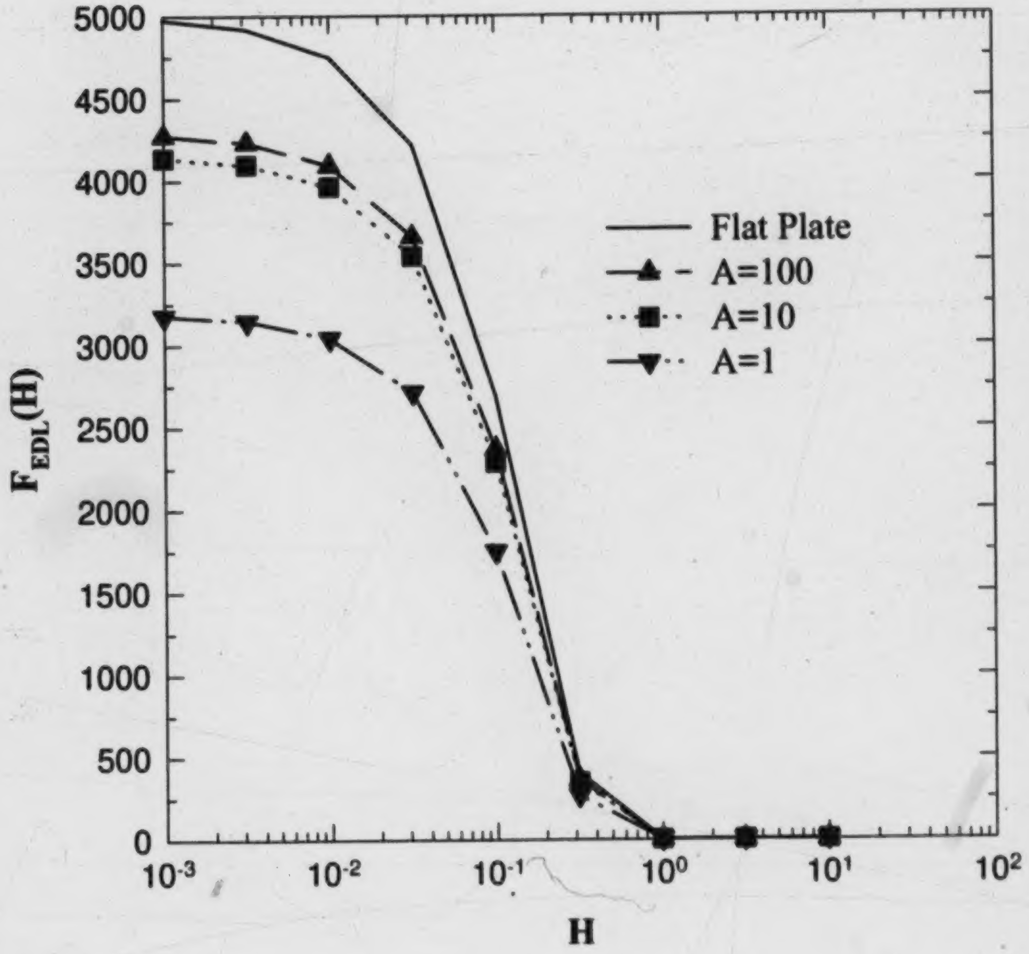

Figure 3.7 The effect of the curvature of the cylinder on the EDL force between a spherical particle and an infinitely long cylindrical fiber (τ=10, Dl=+1000, Da=0)

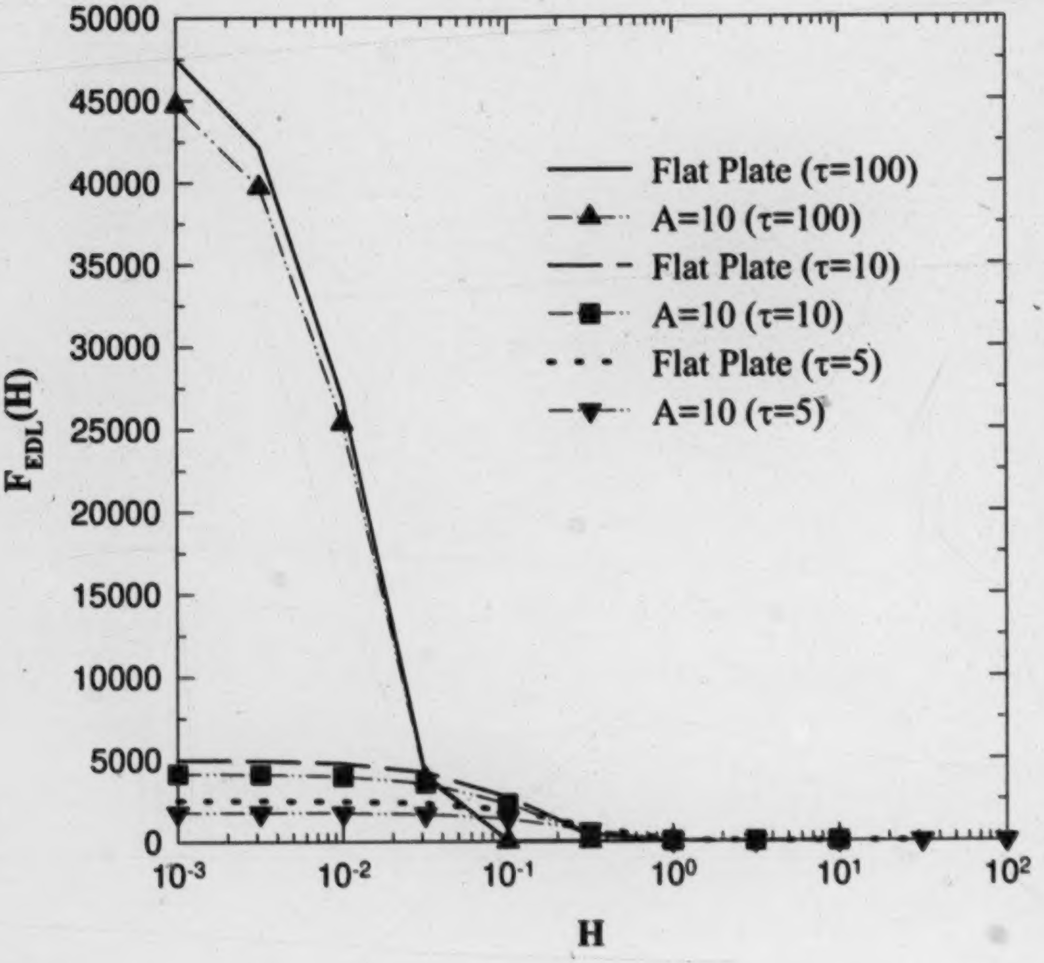

Figure 3.8 The effect of $\tau=\kappa a_p$ on the EDL force between a spherical particle and an infinitely long cylindrical fiber (A=10, Dl=+1000, Da=0)

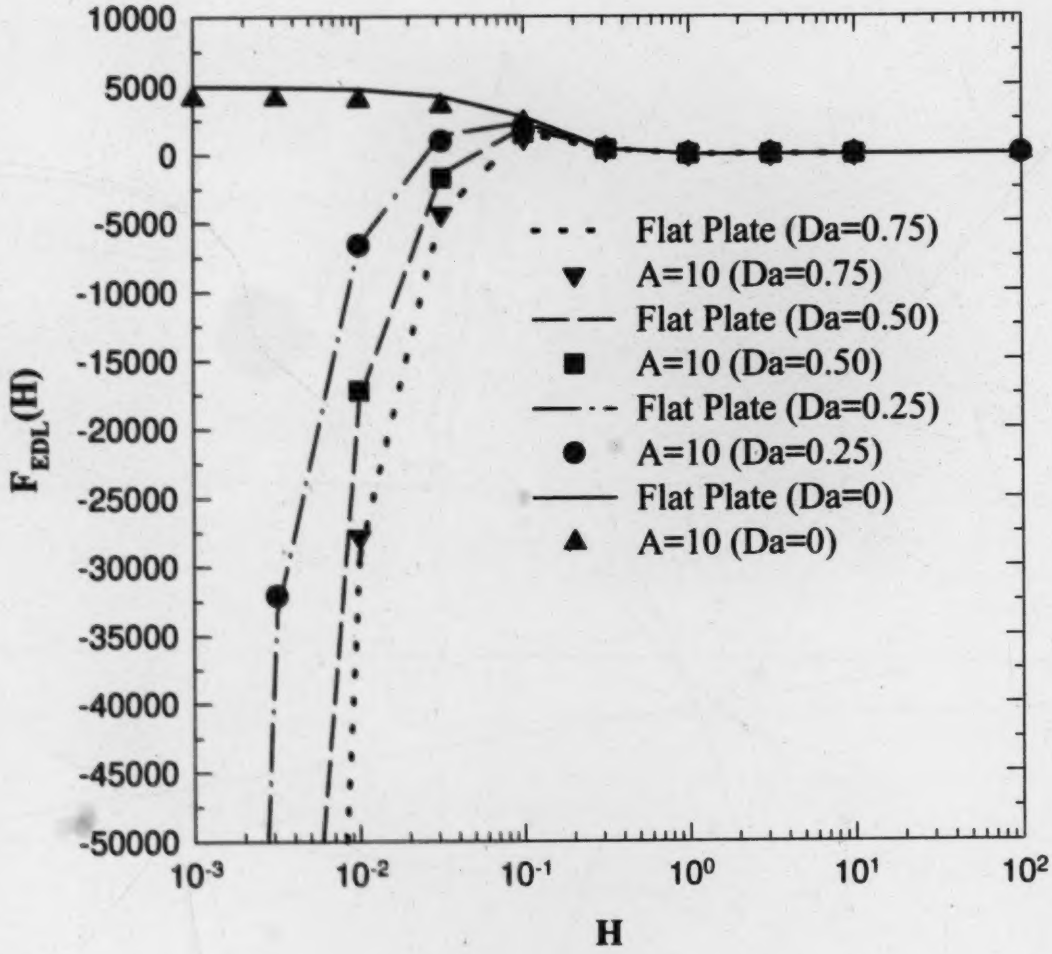

Figure 3.9 The effect of *Da* on the EDL force between a spherical particle and an infinitely long cylindrical fiber (A=10, τ=10, Dl=+1000)

Chapter 4

A Novel Contact Angle Measurement Technique Based on Analysis of the Capillary Profile Around a Cylinder (ACPAC)

4.1 Introduction and Brief Literature Review

The contact angle is an important quantity in many areas of applied science and engineering. Physically, the contact angle of a liquid on a solid provides a basis for studying the interaction between the two phases. Changes in the angle reflect changes in net interactions across their interface and changes of compositions and environmental conditions of bulk phases forming the interface. It is well known that the studies of wettability, deposition, adsorption and flotation require knowledge of the contact angle (Adamson, 1982; Neumann et al., 1983a; 1983b; Chen, 1988; Padday, 1968; 1992; Good, 1992). Measurement of contact angle can also be used to determine the solid surface tensions (Li and Neumann, 1990a; 1992a) and study thin-liquid film phenomena (Marmur, 1992; Toshev and Platikanov, 1992; Li and Neumann, 1992b) and line tension effects (Good and Koo, 1979; Gaydos and Neumann, 1987; Yekta-Fard and Ponter, 1988; Wallace and Schürch, 1990; Li and Neumann, 1990b; Duncan et al., 1995; Li, 1996; Gu et al., 1996; Gu and Li, 1998i).

There have been many experimental techniques available for contact angle measurements. Review of these methods can be found in a number of references (Ambwani and Fort, 1979; Neumann and Good, 1979; Wu, 1982; Adamson, 1982; Neumann et al., 1983b; Padday, 1968; 1992; Good, 1992). Of all the methods employed to measure contact angles, the direct measurement from the sessile drops is probably the most popular approach. The measurement is performed by using a telescope equipped with a goniometer eyepiece. The contact angle is determined by aligning a tangent with the drop profile at the point of the three-phase contact circle on the solid surface. In addition to its experimental simplicity, the sessile drop method requires only small quantities of liquid and solid surface. However, there are some difficulties remaining with the simple sessile drop method whenever high accuracy and consistency are needed. A precision of ±2° is usually claimed. Alignment of the tangent is subjective and depends on the experience of the operator. In recent years, a sophisticated sessile drop method, the Axisymmetric Drop Shape Analysis (ADSA) technique (Rotenberg et al., 1983; Cheng et al., 1990; Li et al., 1992) was developed to determine the contact angles and the interfacial tensions simultaneously. The accuracy of the ADSA technique is about 0.1° for contact angle measurements and 0.05 mJ/m^2 for the interfacial tension measurements. However, it has long been found that, in the sessile drop method, the measured contact angles are dependent on the drop size, a phenomenon often referred to as the drop size dependence of contact angles or the line tension effect (Li, 1996; Gu et al., 1996; Gu and Li, 1998i). For example, the measured contact angles can decrease as much as 3-10° as the base radius of the sessile drop on the solid substrate changes, say, from 1 to 5 mm (Gaydos and Neumann, 1987; Li and Neumann, 1990b; Duncan et al., 1995; Li, 1996). Therefore, the sessile drop method can not be used to directly measure the contact angles, θ_∞, which is the contact angle of an infinitely large drop with no line tension effect. A concise discussion on the line tension effect and its determination from the measured contact angles will be given later.

The Wilhelmy plate technique (Neumann, 1974; Neumann and Good, 1979; Adamson, 1982; Budziak and Neumann, 1990) is an alternative method in which the contact angle is determined by measuring the height of capillary rise at a vertical flat plate. In this method, the contact angle is determined from the height of capillary rise at a vertical plate, according to:

$$\sin\theta_\infty = 1 - \frac{\Delta\rho g h^2}{2\gamma_{lv}} \tag{4.1}$$

where $\Delta\rho=\rho_l-\rho_v$ is the density difference between the liquid phase and the vapour phase; g is the gravitational acceleration; γ_{lv} is the surface tension of the liquid(l)-vapour(v) interface; h is the capillary rise height and θ_∞ is the contact angle of the capillary rise profile on the vertical plate. The best precision of contact angles obtained by this technique is about ±0.1°. The Wilhelmy plate method can avoid the line tension effect on contact angles, as the three-phase contact line in this case is a straight line.

However, it has long been noted that the sessile drop method, exemplified by the ADSA technique, the Wilhelmy plate method and most other widely used contact angle measurement techniques require a flat solid surface. They cannot be utilized to measure contact angles on curved surfaces, such as a cylindrical fiber surface. However, the determination of contact angles or wettability on fiber is of practical importance in composite materials, textile and cosmetic industries. The Wilhelmy-Gravitational method is probably the only existing technique suitable for this kind of measurement. In this method, a fiber hanging on an electrobalance is immersed partially into a testing liquid. The contact angle is determined by measuring the force, F, which is required to balance the fiber according to the following equation (Neumann and Good, 1979):

$$F = P\gamma_{lv}\cos\theta - V\Delta\rho g \qquad (4.2)$$

where P is perimeter of the fiber; V is the liquid volume displaced by the fiber, or the volume of the fiber immersed in the liquid. The major limitation of this method is that the accurate values of P, γ_{lv}, V and $\Delta\rho$ have to be known. For non-porous fibers with a smooth surface such as a glass fiber, P and V can be measured and remain constant during the experiment. Thus the reproducibility of contact angle results may be satisfactory in this case. Nevertheless, fibers usually do not have constant diameters, i.e., their perimeters change along their axial directions. Furthermore, for a porous fiber, the perimeter and the volume of the fiber will change during the measurement because of the penetration of liquid into the fiber and hence the fiber's shape changes (swelling). The contact angle results therefore are generally difficult to reproduce by using the Wilhelmy-Gravitational method.

In the course of this thesis research project, a new contact angle measurement technique has been developed (Gu et al., 1997a; Gu and Li, 1998a; 1998b). This method can be used to measure accurately the contact angle of a liquid-fluid interface by analysis of the capillary profile around a cylinder (ACPAC). As will be described in details in the present chapter, the ACPAC technique is a powerful alternative tool to the existing ADSA technique for accurate measurements of contact angles of any liquid-fluid interfaces on cylindrical surfaces.

The ACPAC method is first used to determine the contact angles by analysis of the capillary rise profile around a cylinder (ACRPAC), which is referred to as simply ACRPAC case hereafter (Gu et al., 1997a). In this method, the precise image of a partial capillary profile of the liquid around a conic or constant-diameter cylinder was acquired and digitized by applying computer image processing and analysis techniques. Then the contact angle of the capillary profile on the cylinder was determined by numerically minimizing the deviation between the physically observed (the digitized) capillary profile and the theoretically predicted curve. The latter is the curve representing a solution of the Laplace equation of capillarity. The accuracy of the measured contact angles is approximately 0.1°. Besides local gravity, densities of liquid and vapour phases and the liquid-vapour surface tension, the only input data is the digitized partial capillary profile. The contact angles determined by the ACPAC technique are insensitive to reasonable uncertainties involved in these input data. This method was used to measure the contact angles of four n-alkane liquids around cylindrical glass fibers coated with the FC725 material. The results are in good agreement with those obtained by using the Wilhelmy plate method. This new method was then applied to study the dependence of contact angles on the geometry of the conic glass cylinders, which was interpreted as the line tension effect. In particular, the contact angle in the case without the line tension effect, θ_∞, can be measured directly by the present method. Using computer digital image analysis techniques, the ACPAC technique is fully automatic, objective and accurate. It is a useful tool in studying the wetting, spreading and deposition processes of a liquid drop on fiber surfaces. It will be particularly suitable for precise measurement of the contact angles of a liquid on fibers with some roughness. A general user-oriented computer code to implement the ACPAC technique is also developed.

In the following sections, first, the numerical solution is presented for the differential equation governing the shape of the capillary rise profile around a conic cylinder in the presence of gravity. Then the objective function is defined as a measure of the deviation of the calculated Laplacian curve from the measured capillary rise profile. This function is the average of the 'normal' distances between the measured points and the calculated curve. The optimization of the objective function is achieved by using the contact angle as one of the adjustable parameters. A computational scheme is developed to determine the contact angle. Next, computer digital image acquisition and digitization techniques and the detailed experimental set-up and procedure are described respectively. Finally, the measured contact angles on constant-diameter and conic cylinders as well as their application to determination of the line tension of four n-alkane liquids on the FC725 solid surface are given and discussed. Comparisons are also made of the experimental data with those obtained from both the sessile drop method by using the ADSA technique and the Wilhelmy plate technique.

The ACPAC technique for the ACRPAC case is then modified and extended to measure such a contact angle formed between an oil-water interface and a fiber surface by analysis of the capillary depression profile around a cylinder (ACDPAC). A brief introduction to the ACPAC technique for the ACDPAC case will be presented in Section 4.6. Once the wettability of the fiber-water-oil system is measured properly using the ACPAC technique, the contact angle can be substituted into Equation (3.31a) to determine γ_{fv} and further to determine γ_{fw} from Equation (3.31b) given in Section 3.6. If γ_{fv}, γ_{fw} and the other surface energies are known, the Hamaker constant can be determined from Equation (3.30) given in Section 3.5.2. The detailed results of the Hamaker constants determined from the measured surface energies for a variety of fiber-water-oil systems will be presented in Section 4.7.

4.2 Mathematical Formulations of the ACPAC Technique for the ACRPAC Case

When a conic cylinder is vertically inserted into a pool of liquid, the latter may climb up the cylinder above the undisturbed surface of the liquid. As illustrated in Figure 4.1, the liquid-vapour interface will form a contact angle with the surface of the conic cylinder. For a moderately curved liquid-vapour interface, the pressure difference across the curved interface is described by the classical Laplace equation of capillarity:

$$\Delta P = P_l - P_v = \gamma_{lv}\left(\frac{1}{R_1} + \frac{1}{R_2}\right) \tag{4.3}$$

where, ΔP is the pressure difference across a liquid-vapour interface; P_l and P_v are the pressures on the liquid side and on the vapour side of the interface, respectively; γ_{lv} is the surface tension of the liquid(l)-vapour(v) interface; R_1 and R_2 are the principal radii of curvature of the interface. In the absence of external forces other than gravity, the pressure difference is a linear function of the elevation. For an arbitrary point P(x,y) on the liquid-vapour interface, the pressures in Equation (4.3) can be further expressed as:

$$P_l = P_{l0} - \rho_l g y \tag{4.4a}$$

and

$$P_v = P_{v0} - \rho_v g y \tag{4.4b}$$

where, ρ_l and ρ_v are the densities of the liquid phase and vapour phase respectively; y is the local capillary rise height of point P(x,y) on the interface above the horizontal undisturbed surface of the liquid; P_{l0} and P_{v0} are the reference pressures of the liquid phase and the vapour phase, chosen at the vicinity of the undisturbed surface of the liquid. If the ratio of the radius of the conic cylinder to the radius of the pool is sufficiently small, the difference between the two reference pressures, ΔP_0, will be zero by applying Equation (4.3) at y=0, i.e., on the undisturbed flat liquid-vapour interface, and noticing $R_1^0=R_2^0=\infty$:

$$\Delta P_0 = P_{l0} - P_{v0} = 0 \tag{4.4c}$$

where R_1^0 and R_2^0 are the principal radii of curvature of the undisturbed liquid-vapour interface very far from the cylinder axis. Substituting Equations (4.4a,b,c) into Equation (4.3) and rewriting it give

$$\gamma_{lv}\left(\frac{1}{R_1}+\frac{1}{R_2}\right) = -\Delta\rho g y \tag{4.5}$$

where $\Delta\rho=\rho_l-\rho_v$ is the density difference between the liquid phase and the vapour phase. For the system illustrated in Figure 4.1, the x-y coordinate system is chosen as follows: the y axis is the axis of the conic cylinder; the x axis is along the horizontal undisturbed liquid-vapour interface and normal to the y axis. The Laplace equation of capillarity, Equation (4.5), can be rewritten as:

$$\frac{\dfrac{d^2y}{dx^2}}{\left[1+\left(\dfrac{dy}{dx}\right)^2\right]^{3/2}} + \frac{\dfrac{dy}{dx}}{x\left[1+\left(\dfrac{dy}{dx}\right)^2\right]^{1/2}} = \frac{\Delta\rho g y}{\gamma_{lv}} \tag{4.6}$$

Equation (4.6) is a second-order ordinary differential equation that requires two boundary conditions. The convenient choice of the boundary conditions is the capillary rise height and the contact angle on the conic surface. At the three-phase contact circle on the conic cylinder, the capillary rise height, h, the tangential angle, ϕ, and the contact angle, θ, of the liquid-vapour interface constitute the relevant boundary conditions:

$$y|_{x=R_c} = h \tag{4.7a}$$

$$\frac{dy}{dx}\Big|_{x=R_c} = -\tan\varphi = -\tan(180^0 - \beta - \theta) = \tan(\beta + \theta) \tag{4.7b}$$

where R_c is the local radius and β is the local inclination angle of the conic cylinder. Another choice of boundary conditions on the undisturbed surface of the liquid at infinity is:

$$y|_{x=\infty} = 0 \tag{4.8a}$$

$$\frac{dy}{dx}|_{x=\infty} = 0 \tag{4.8b}$$

Obviously, such boundary conditions can not be implemented in the practical computations.

By substituting y_1=y and y_2=dy/dx into Equation (4.6), it can be transformed into:

$$\frac{dy_1}{dx} = y_2 \tag{4.9a}$$

$$\frac{dy_2}{dx} = [\frac{\Delta\rho g y_1}{\gamma_{lv}} - \frac{y_2}{x(1+y_2^2)^{1/2}}]\ (1+y_2^2)^{3/2} \tag{4.9b}$$

Consequently, the boundary conditions, Equations (4.7a,b) or Equations (4.8a,b) associated with Equation (4.6) can be changed into the corresponding initial conditions:

$$y_1|_{x=R_c} = h \tag{4.10a}$$

$$y_2|_{x=R_c} = \tan(\beta+\theta) \tag{4.10b}$$

or

$$y_1|_{x=\infty} = 0 \tag{4.11a}$$

$$y_2|_{x=\infty} = 0 \tag{4.11b}$$

Equations (4.9a,b) with the initial conditions, Equations (4.10a,b), form a set of first-order non-linear ordinary differential equations for y_1 (i.e., y) and y_2 (i.e., dy/dx) as functions of the independent variable x. For given R_c, β, θ, h and $\Delta\rho g/\gamma_{lv}$, which depend on the shape of the conic cylinder and the properties of the liquid tested, the complete shape of the axisymmetric capillary rise profile y=y(x) can be easily obtained by numerically integrating differential Equations (4.9a,b) simultaneously with the initial conditions, Equations (4.10a,b). In this study, the 4th-order Runge-Kutta technique is used to solve the differential equation system, which was successfully used to predict the equilibrium shapes of axisymmetric liquid solder menisci previously (Gu and Li, 1997d). For the steep part of the liquid-vapour profile where |dy/dx| is greater than 1.0, the differential equation system will be automatically switched to another set of first-order ordinary differential equations for x_1

(i.e., x) and x_2 (i.e., dx/dy) as functions of the independent variable y. This can be done by using y as an independent variable and substituting:

$$\frac{dy}{dx} = \frac{1}{\frac{dx}{dy}}$$

$$\frac{d^2 y}{dx^2} = -\frac{1}{(\frac{dx}{dy})^3} \frac{d^2 x}{dy^2}$$

into Equation (4.6). The detailed mathematical transformations of the differential equations as well as their initial conditions are straightforward, and are thus not included here. In this way it is ensured that variation of the dependent variable in each step be definitely less than the calculating step of the independent variable during numerical calculation of capillary rise profile. The latter can be chosen properly.

Like the ADSA technique (Rotenberg et al., 1983; Cheng et al., 1990; Li et al., 1992), the ACPAC technique determines the contact angles from the shapes of the liquid-vapour interfaces, i.e., from the capillary profiles on a conic or constant-diameter cylinder. The strategy employed is to define an objective function which is a measure of the discrepancy between the physically observed capillary profile and the theoretically calculated curve, i.e., a curve satisfying the Laplace equation of capillarity. Then the objective function is minimized numerically by using the contact angle as one of the adjustable parameters.

Let x_{mi} and y_{mi} (i=1, 2, ..., N) be a set of experimentally measured coordinates which describe the measured liquid-vapour interface, and x_{cj} and y_{cj} (j=1, 2, ..., K, choosing $x_{cK} > x_{mN}$) be another set of the coordinates of a calculated Laplacian curve. In this paper, the objective function, E, is defined as:

$$E = \frac{\sum_{i=1}^{N} |d_i|}{N} \tag{4.12}$$

where d_i is the "normal" distance from each measured point (x_{mi}, y_{mi}) to the calculated capillary profile (i=1, 2, ..., N). According to the above definition, physically, the objective function is the average of the "normal" distances between the measured points and the theoretical Laplacian curve. Hence, the value of the objective function depends only on the shape of the calculated Laplacian curve once the real capillary profile is measured, i.e., x_{mi} and y_{mi} (i=1, 2, …, N) are given.

In order to construct a theoretical Laplacian curve by solving Equations (4.9a,b) with the initial conditions Equations (4.10a,b), some parameters, such as the local gravity, g, the density difference between the liquid and the vapour phases, $\Delta\rho$, and the liquid-vapour surface tension, γ_{lv}, have to be known. As will be discussed in the next section, for a given conic cylinder, Δh_m, R_c and β can be readily determined from the physically observed capillary profile, where Δh_m is the measured relative elevation of the position of the three-phase contact circle on the cylinder to the position of the lower edge of the acquired partial capillary rise profile. In the experiments, only partial capillary profile could be acquired because of the contradiction between the image resolution and the scope of the microscope and video camera system. The calculated capillary profile around the conic cylinder in this study shows that the liquid-vapour interface could extend to a quite large range. Thus it becomes practically impossible to acquire the complete capillary rise profile with sufficient image resolution. If h_0 represents the capillary rise height at the lower edge of the measured partial capillary rise profile relative to the undisturbed liquid surface, then the absolute height of the capillary rise, h, at the conic cylinder is equal to:

$$h = h_0 + \Delta h_m \tag{4.13a}$$

Therefore, once $\Delta\rho g/\gamma_{lv}$, Δh_m, R_c and β are known, the calculated Laplacian curve will depend merely on the values of θ and h_0. Consequently, the objective function depends only on the two parameters, θ and h_0, i.e.,

$$E = E(\theta, h_0) \tag{4.13b}$$

In the present optimization scheme, θ and h_0 are used as the adjustable parameters to find the best fit of the theoretical Laplacian curve to the digitized liquid-vapour interface. Once the objective function is minimized, the corresponding θ is the measured contact angle. For a given conic cylinder and a tested liquid, hence, only a set of discrete coordinates of the physically observed capillary rise profile is required as input data. The output of the optimization scheme will provide the values of the contact angle, θ, and the capillary rise height, h (or h_0), as well as the calculated capillary rise profile corresponding to the minimum objective function E_{min}.

4.3 Computer Digital Image Techniques

A block diagram of the apparatus used in the present experiments is shown in Figure 4.2. A coated glass cylinder is inserted into a shallow dish slightly overfilled with the tested liquid and they were placed between the light source and the microscope. A Cohu 4910 CCD monochrome camera was mounted on a Leica Wild M3B microscope. The video signal of the capillary profile was transmitted to a videopix digital video processor which performed the frame grabbing and digitization of the image to 640 x 480 pixels with 256 grey levels, where zero represents black and 255 represents white. A Sun Sparc10 computer was used to acquire the image from the videopix and perform the image analysis, computation and digitization.

All experimental digital images were automatically stored in the computer memory. The basics of digital image acquisition process are as follows. A video source, such as a video camera attached to a microscope, produces an analog video signal containing image data. This signal is transmitted to the image processor. The analog signal is converted to a digital signal containing the image data in the form of digital picture elements, or pixels. The digital pixel data are then stored in frame memory one frame at a time, with each pixel occupying one frame memory location. Once the image is stored in frame memory, it may be accessed for display or other additional computer processing. Display circuitry transforms the pixels stored in frame memory back into an analog signal for display on a video monitor. The number of pixels that are transferred to or from frame memory in one frame time defines the display resolution of the frame memory.

Two typical images (produced by a laser printer) of the partial capillary rise profiles of hexadecane-vapour (air) interface, one around the bottom tip part and another around the conic part of a conic cylinder, are shown in Figures 4.3a and 4.4a (produced by a laser printer), respectively. For each image, using a standard grid image as a calibration to correct possible optical distortion, a special computer image processing and analysis program was used to digitize the image automatically with sub-pixel resolution. Then the computer program will determine the conic cylinder profile and the profile of liquid-vapour interface. The output of this program are two sets of discrete coordinates, x and y in mm, of the profile of the cylinder surface and the capillary rise profile of the tested liquid on the left and the right sides, respectively. The digitized plots of the above two images, as seen in Figures.

4.3a and 4.4a, are given in Figures 4.3b and 4.4b, respectively. These plots clearly indicate the profiles of the cylinder surface and the hexadecane-vapour interfaces on the both sides. By implementing the spline curve fitting, the accuracy of the digitized profiles is about 1.0 μm, at x40 magnification.

With the digitized profiles of each image, the local radius R_c of the three-phase contact circle is half of the horizontal difference between the three-phase contact points on the left side and on the right side. The relative elevation between the three-phase contact circle and the lower edge of the partial capillary rise profile covered by the image, Δh_m, as defined before, is merely their vertical difference. The local slope of the solid surface profile, i.e., $\tan\beta$, at the position of the three-phase contact circle can be easily calculated by applying a polynomial curve fit to the measured profile of the solid surface.

4.4 Experimental Aspects of the ACRPAC Case

The liquids used in the present contact angle measurements are decane, dodecane, tetradecane, and hexadecane (Aldrich Chemical Company, Inc., 99% pure). These liquids are chosen in order to satisfy the following general requirements: they have low vapour pressure or a high boiling temperature so as to minimize evaporation; they are chemically stable and not excessively toxic; they will form finite contact angles on the solid surface used in this study. In addition, the contact angles, θ_∞, and line tensions, σ, of these liquids on a similar solid surface, FC721, are available in the literature (Li and Neumann, 1990b; Duncan et al., 1995; Li, 1996).

In the present work, the solid surface used in the experiments is FC725 (a fluorochemical surfactant coating material, 3M Product) coated on very smooth glass cylinders. Two types of glass cylinders were used in this work: constant-diameter cylinders and conic (varying diameter) cylinders. As illustrated in Figure 4.1, the local radius, R_c, of the conic cylinder changes smoothly from approximately 0.14 mm at the tip to 1.0 mm (or 1.5, 2.5 mm) on its upper cylindrical part. The local inclination angle, β, defined as the angle between the gradient of the cylinder profile and the horizontal level, decreases from 90° near the tip, reaches the minimum about 60° on the conic part, and finally increases to 90° again on the upper cylindrical part. The FC725 surface was prepared by a dip-coating method as described below. First, the cylinder was slowly and vertically dipped into a small bottle filled with the FC725 coating material. The bottle was placed on a disk floating in a beaker of water. The position of the floating disk, and hence the level of the coating liquid, was then lowered very slowly by draining the water in the beaker at a controlled rate. Thus, a uniform and smooth FC725 coating was left on the cylinder. Finally, the coated cylinder was suspended vertically and dried in air before use in the experiment.

The quality of the FC725 surfaces was carefully examined in this study. First, it was known from the 3M Product Selection Guide that this fluorochemical surfactant coating material is very stable, even in many extremely aggressive chemical environments. The FC725 coating material is insoluble to organic liquids such as n-alkanes used in this study. Second, the average roughness of the dip-coated FC725 surfaces, measured by the Tencor Surface Profilometer (TSP), is less than 0.0250 μm. Lastly, the contact angle hysteresis has been measured by using the following procedures. To avoid the line tension effects, the contact angle measurements were done on the FC725 coated glass cylinders of constant radius (i.e., $\beta=90^{\circ}$). Initially, the coated cylinder was slowly inserted vertically into the liquid to a certain depth. Thirty seconds was given to allow the three-phase contact line and the liquid meniscus to reach equilibrium. Then an image of the capillary rise profile around the cylinder was taken. The cylinder was further inserted into the liquid so that the three-phase contact line reached a new position, and a new image was taken after 30 seconds; and so on. Five advancing contact angles were measured from successive digital images, each at a different vertical position downwards along the cylinder. Afterwards, five receding contact angles were measured in a similar way by moving the cylinder upwards. For a given liquid, the above measurements were repeated for three separate cylinders. For all liquids tested in this work, the contact angle hysteresis is almost the same, ranging from 5-7°. For example, for the FC725-tetradecane system, the average advancing contact angle is 65.3° and the average receding contact angle is 58.4°. Although the solid surfaces used in this work are very smooth, these surfaces may still have a very small percentage of heterogeneity, probably due to impurities of the coating material and dust in the air. This might be the cause of the observed contact angle hysteresis. It has been shown by Li and Neumann (1992c) that the advancing contact angle on a smooth but heterogeneous surface represents the equilibrium properties of the dominant material of the surface, while the receding contact angle reflects the property of the impurity of the surface. Hence, the contact angles mentioned thereafter will be the advancing contact angles only.

Measurements of capillary rise profile around a conic cylinder in this study were carried out according to the following procedure. For each liquid, three conic cylinders of different sizes were used in the measurement. First, the tip part of the conic cylinder was inserted into the liquid and the image of the capillary rise profile around that part was taken. Then the conic cylinder was moved downwards very gently to change the position of the three-phase contact circle on the conic cylinder. Once the capillary rise profile around the conic cylinder was formed and stable, another image was taken at the new position and the experiment continued until the profile reached the upper cylindrical part. Contact angle measurements for constant-diameter cylinders were carried out in a similar fashion. The entire experimental set-up was placed on a vibration-free table. All measurements were conducted at room temperature, 22°C.

For comparison, the ADSA and the Wilhelmy plate techniques were also utilized to measure contact angles of the same solid-liquid systems. Glass slides (7.5 cm x 2.5 cm) used in these measurements were coated with the FC725 material by using the dip-coating method as described above. In the first experiment, the contact angle of a sessile drop on a FC725 coated glass slide was measured by applying the ADSA technique. Secondly, the Wilhelmy plate technique was employed to determine the contact angle without line tension effect, θ_∞, at the vertical glass slide. Once the capillary rise height, h, was measured, the contact angle was calculated from Equation (4.1). The measurement procedures in the present study are summarized as follows. A vertical glass slide coated with the FC725 was dipped into a shallow dish slightly overfilled with the tested liquid. They were put between a light source and a goniometer. The dish is wide enough to ensure that the liquid surface is horizontal in the region far from the glass slide. A goniometer was installed on a three-dimensional translation stage with a vertical resolution of 1.0 μm. The stage was mounted on a separate stand so as to insulate mechanical vibrations created by its movement. Using the goniometer and the translation stage, the height of capillary rise is determined by measuring the positions of the three-phase contact line on the coated glass slide and the position of the horizontal liquid surface. For an individual measurement of h, a total of ten readings of the position of the horizontal liquid surface and the position of the three-phase contact line were taken.

4.5 Experimental Results and Discussion of the ACRPAC Case

4.5.1 Contact Angle Measurements on Constant-Diameter Cylinders

Experiments were conducted to test the ACPAC technique for the ACRPAC case. As a first application, the contact angles on the FC725 coated constant-diameter cylinders for the four n-alkane liquids: decane, dodecane, tetradecane and hexadecane, were measured. To examine the possible effect of the cylinder size on the measured contact angles, three cylinders of different sizes (R_c=1.0, 1.5 and 2.5 mm) were used for each liquid. Ten images were taken at different positions of each cylinder. The consistency of the measured contact angles for three different cylinders indicates that there is no appreciable effect of the cylinder size on the results. Physically, these measured contact angles are the advancing contact angles without line tension effect, $\theta_{\infty ACRPAC}$, since the constant-diameter cylinders are vertically positioned, i.e., $\beta=90^\circ$, as will be seen from Equation (4.16). According to the classical Young Equation (4.14b), these contact angles depend only on the interfacial tensions of the solid-liquid-vapour interfaces in the system.

Table 4.1 shows the average contact angle value (at the 95% confidence level) of each liquid measured by the ACPAC method for the ACRPAC case. For comparison, the contact angles, $\theta_{\infty Wilhelmy}$, (at the 95% confidence level) of each liquid obtained from the Wilhelmy plate technique are also listed in Table 4.1. An excellent agreement is found between the contact angles measured by these two techniques. However, it is noted that the measured contact angles have a maximum variation of about $\pm0.5^\circ$ around the mean values. This is due to the practical difficulty in aligning either the cylinder or the slide truly vertically in the measurements. Experimental results indicate that the slight inclination of the cylinder or the slide could cause a rather large difference in the measured contact angles between the left and the right sides. The maximum variation at the 95% confidence level is only about $\pm0.1^\circ$ if the measured contact angles from one side are averaged. Therefore, the accuracy of the measured contact angles by the ACPAC technique is approximately 0.1°.

4.5.2 Contact Angle Measurements on Conic Cylinders

The contact angles on the FC725 coated conic cylinders for the four n-alkane liquids were also measured by the ACPAC technique for the ACRPAC case. As an example, Table 4.2 shows the changing contact angles of decane on the FC725 solid surface at the different positions of a conic cylinder from its lower tip part to its upper cylindrical part. The contact angles on the conic part are approximately 3-4° larger than those on the cylindrical part. This phenomenon can be interpreted in terms of the so-called line tension effect. Hence, a direct application of the present experimental technique is to determine line tension by measuring the contact angles at the different positions of a conic cylinder.

In surface thermodynamics, line tension in a three-phase equilibrium system can be either defined as the free energy per unit length of a three-phase contact line (Gibbs, 1961; Boruvka and Neumann, 1977) or understood as the force operating in a one-dimensional three-phase contact line and tending to minimize its length. For a sessile drop on an ideal solid surface, the mechanical equilibrium condition at any point along the three-phase contact circle can be expressed by the modified Young equation (Boruvka and Neumann, 1977):

$$\cos\theta = \cos\theta_{\infty} - \frac{\sigma}{\gamma_{lv}} \cdot \frac{1}{R} \qquad (4.14a)$$

and

$$\cos\theta_{\infty} = \frac{\gamma_{sv} - \gamma_{sl}}{\gamma_{lv}} \qquad (4.14b)$$

where γ_{lv}, γ_{sv} and γ_{sl} are the interfacial tensions of the liquid-vapour interface, the solid-vapour interface and the solid-liquid interface, respectively; R is the radius of the three-phase contact circle; θ is the advancing contact angle corresponding to a finite contact radius, R; θ_{∞} is the contact angle corresponding to an infinitely large drop, i.e., $R = \infty$; and σ is the line tension. The well-known classical Young Equation (4.14b) indicates that θ_{∞} is constant for a given solid-liquid-vapour system. The modified Young Equation (4.14a) relates the line tension to contact angle and the radius of a three-phase contact circle. Thus, line tension can be determined by measuring the contact angle dependence on the drop size. As defined in Equation (4.14a), the slope of the $\cos\theta$ versus $1/R$ straight line is $(-\sigma/\gamma_{lv})$. If the slope and the liquid surface tension are known, then the line tension can be determined.

Recently, Lin and Li (1994) have incorporated the local inclination angle, β, of an inclined solid surface or a solid surface of revolution in the form of $\cos\beta$ into the line tension term in Equation (4.14a). They derived another form of the modified Young equation for the case where the three-phase line is in contact with an inclined solid surface:

$$\cos\theta = \cos\theta_\infty - \frac{\sigma}{\gamma_{lv}} \cdot \frac{\cos\beta}{\rho} \tag{4.15}$$

where ρ is the local radius of curvature of the three-phase contact line. Equation (4.15) clearly shows the influence of the local inclination angle, β, on the curvature ($1/\rho$) dependence of contact angles due to the line tension effect. For an ideal solid surface of revolution, such as a cone or cylinder, the three-phase contact line is a circle because of its axisymmetry and ρ becomes a constant, R_c, the local radius of the contact circle on the solid surface. Therefore, Equation (4.15) can be simplified as:

$$\cos\theta = \cos\theta_\infty - \frac{\sigma}{\gamma_{lv}} \cdot \frac{\cos\beta}{R_c} \tag{4.16}$$

Equation (4.16) will reduce to Equation (4.14a) if $\beta = 0°$, i.e., if $\cos\beta = 1$, which corresponds to a horizontal planar solid surface. It will become the classical Young Equation (4.14b), if $\beta = 90°$, i.e. $\cos\beta = 0$ and $\theta = \theta_\infty$, which corresponds to either a vertical cylinder with a constant radius as discussed in the previous case or a vertical flat plate as used in the Wilhelmy plate technique (Neumann, 1974; Neumann and Good, 1979; Adamson, 1982; Budziak and Neumann, 1990). In such a case, the line tension term is absent from Equation (4.16). Therefore, θ_∞ should be defined more exactly as the contact angle without line tension effect. However, the linear relationship between $\cos\theta$ and ($\cos\beta/R_c$) for a given solid-liquid system predicted by Equation (4.16) has yet to be confirmed experimentally.

It should be noted that the advancing contact angle measured on a real surface is the Young contact angle, i.e., which can be used in the Young equation (Neumann and Good, 1972). Since the conditions required in deriving Equation (4.16) are the same as those required in deriving the classical Young equation, the advancing contact angles can also be used in Equation (4.16). It has also been shown elsewhere (Neumann and Good, 1972; Li and Neumann, 1992c) that the advancing contact angle represents the equilibrium property of the dominant material of a smooth but non-homogeneous surface. Thus, the line tensions calculated from the advancing contact angles represent the property of the dominant material, the FC725, in the present case.

By employing the present experimental technique, the quantities in Equation (4.16), such as the radius of the three-phase contact circle, R_c, the inclination angle, β, and the contact angle, θ, can be measured directly. Therefore, the remaining tasks are to bring the measured R_c, β and θ into the modified Young Equation (4.16) and then to plot the data in terms of $\cos\theta$ versus $\cos\beta/R_c$. The line tension, σ, and the contact angle, θ_∞, can be readily determined since the gradient and the intercept of the linearly fitted line to these data are $-\sigma/\gamma_{lv}$ and $\cos\theta_\infty$, respectively.

The experimental data obtained in this work and their corresponding linear lines fitted using Equation (4.16) for the four liquids on the FC725 surface are shown in Figure 4.5. The correlation coefficients r^2 for these fitted linear functions are all above 0.83. Therefore, the linear relationship between $\cos\theta$ and $\cos\beta/R_c$ as predicted by Equation (4.16) is statistically supported by these data. The line tensions, σ, and the contact angles, θ_∞, for the four n-alkanes on the FC725 surface were obtained from the plots in Figure 4.5 and summarized in Table 4.3. These line tension values agree well with those reported in the literature for similar systems (Gaydos and Neumann, 1987; Li and Neumann, 1990b; Duncan et al., 1995). In order to examine the validity of the contact angle, θ_∞, and line tension, σ, derived from the measured contact angles around a conic cylinder, comparative experiments were done. For each liquid on the FC725 coated glass slides, contact angles, θ_{ADSA}, of sessile drops with a contact radius R of 3 mm were measured by using the ADSA technique. The results are listed in the last column of Table 4.3. In addition, the predicted contact angles, θ_{pred}, by using Equation (4.16) with R=3 mm, the derived θ_∞ and σ values are listed in the same table. For all four liquids, these two contact angles are in excellent agreement within the experimental error.

As discussed before, the contact angle without line tension effect, θ_∞, would correspond to the contact angle of an infinitely large drop in the sessile drop method. In the sessile drop method, θ_∞ can only be evaluated (Gaydos and Neumann, 1987; Li and Neumann, 1990b; Duncan et al., 1995) by extrapolating the fitted line of $\cos\theta$ versus 1/R to the vertical axis (i.e., 1/R=0), because in practice it is impossible to generate an infinitely large drop. For the conic cylinder-liquid systems, however, both the local radius, R_c, of the three-phase contact circle and the local inclination angle, β, of the solid surface can be changed simultaneously. The quantity $\cos\beta/R_c$ in Equation (4.16) covers a wider range, in this study approximately from -1.00 to 10.00 cm^{-1}. More importantly, the point of $\cos\beta/R_c=0$ is also included in the range. At this point, $\cos\theta$ becomes $\cos\theta_\infty$ and the line tension effect term is absent from the equation. Hence, the contact angle without line tension effect, θ_∞, which is derived from the contact angles measured by the ACPAC technique for the ACRPAC case, is more reliable. In fact, this conclusion is also supported by the excellent consistency between the θ_∞ values derived from Equation (4.16) (Table 4.3) and those measured directly by either the ACPAC method for the constant-diameter cylinders or the Wilhelmy plate technique (Table 4.1).

4.6 Brief Introduction to the ACPAC Technique for the ACDPAC case

Many applications in cosmetic and textile industries require the knowledge of contact angles formed by an oil-water interface on a fiber surface. However, when a hydrophobic fiber is inserted into a beaker filled with a layer of water at the bottom and a layer of oil at the top (assuming that the oil phase is lighter than the water phase), the oil-water interface forms a depressed meniscus around the fiber. Therefore, this section will focus on the measurement of such a contact angle formed between a depressed oil-water interface and a cylindrical fiber surface (Gu and Li, 1998a). The ACPAC technique for the previous ACRPAC case is modified and extended to determine the contact angles by analysis of the capillary depression profile around a cylinder (ACDPAC). Mathematically, calculation of the capillary depression profile around a cylinder can be transformed into the prediction of the previous capillary rise profile by using appropriate coordinate transformation. In the measurements, an image of the capillary depression profile of the oil-water interface is taken as an image of the capillary rise profile by purposely setting the video camera upside down. Thus the contact angle can be determined by using the approach similar to the ACRPAC case. As an application, the contact angles of two different oil-water interfaces on the cylindrical glass fibers coated with the FC725 material are measured by using the ACPAC technique for the ACDPAC case. In addition, this method has been applied to study the effects of two typical ionic surfactants, cetyltrimethylammonium bromide (CTAB) and sodium dodecyl sulphate (SDS), on the wettability of the oil-water interfaces. The oil phase are two dimethyl siloxane liquids, silicone oil A and silicone oil B.

4.6.1 Coordinate Transformation

When a solid cylinder is vertically inserted through a horizontal liquid-fluid interface formed between the upper fluid phase and the lower liquid phase in a beaker, the interface will either climb up the cylinder above the undisturbed liquid-fluid interface or deform downward around the cylinder. The overall shape of the capillary profile depends on the surface/interfacial tension and the wettability of the liquid-fluid interface on the solid surface. The determination of the contact angles in the capillary rise case for a liquid-vapour interface around a fiber has been dealt with in the previous sections (Gu et al., 1997a). The focus in this part is to determine the contact angles in the capillary depression case for a liquid-liquid interface around a cylinder. As illustrated in Figure 4.6, a depressed oil-water (O/W) interface will form an obtuse contact angle on the cylinder surface. For such a moderately curved O/W interface, its equilibrium shape is governed by the classical Laplace equation of capillarity, similar to Equation (4.3):

$$\Delta P = P_w - P_o = \gamma_{ow}\left(\frac{1}{R_1} + \frac{1}{R_2}\right) \tag{4.17}$$

where γ_{ow} is the interfacial tension of the O/W interface. As shown in Figure 4.6, the X-Y coordinate system was chosen as follows: the Y axis coincides with the axis of the cylinder, and the X axis is along the horizontal undisturbed O/W interface and normal to the Y axis. In the absence of external forces other than gravity, the pressure difference is a linear function of the elevation. For an arbitrarily chosen point P(X,Y) on the O/W interface as marked in Figure 4.6, the pressures in Equation (4.17) can be expressed as:

$$P_w = P_{w0} - \rho_w g Y \tag{4.18a}$$

and

$$P_o = P_{o0} - \rho_o g Y \tag{4.18b}$$

where, ρ_w and ρ_o are the densities of the water phase and the oil phase respectively; Y is negative and represents the local capillary depression depth of the point P(X, Y) below the horizontal O/W interface; and P_{w0} and P_{o0} are the reference pressures of the water and the oil phases, respectively, chosen at the vicinity of the undisturbed O/W interface. Note that the difference between the two reference pressures, ΔP_0, will be equal to zero by applying Equation (4.17) at Y=0. Substituting Equations (4.18a,b) into Equation (4.17) and rearranging gives:

$$\gamma_{ow}\left(\frac{1}{R_1}+\frac{1}{R_2}\right)=-\Delta\rho_0 gY \tag{4.19}$$

where $\Delta\rho_0 = \rho_w-\rho_o$ is the density difference between the aqueous and the oil phases. Therefore, in the X-Y coordinate system, the Laplace equation of capillarity, Equation (4.19), can be rewritten as:

$$\frac{\dfrac{d^2Y}{dX^2}}{[1+(\dfrac{dY}{dX})^2]^{\frac{3}{2}}}+\frac{\dfrac{dY}{dX}}{X[1+(\dfrac{dY}{dX})^2]^{\frac{1}{2}}}=-\frac{\Delta\rho_0 gY}{\gamma_{ow}} \tag{4.20}$$

Equation (4.20) is a second-order ordinary differential equation that requires two boundary conditions. The convenient choice of the boundary conditions is either at the solid surface or on the undisturbed horizontal O/W interface. At the three-phase contact circle on the cylinder, the capillary depression depth on the cylinder, h, and the contact angle, θ, of the O/W interface constitute the relevant boundary conditions at the solid surface:

$$Y\big|_{X=R_c}=-h \tag{4.21a}$$

and

$$\frac{dY}{dX}\Big|_{X=R_c}=\tan(\theta-90^o)=-\cot(\theta) \tag{4.21b}$$

where R_c is the constant radius of the cylinder. Another choice of the boundary conditions is on the undisturbed flat O/W interface at infinity, where

$$Y\big|_{X=\infty}=0 \tag{4.22a}$$

and

$$\frac{dY}{dX}\Big|_{X=\infty}=0 \tag{4.22b}$$

It is an apparent fact that in practice the above two boundary conditions at infinity can not be used.

Mathematically, calculation of the capillary depression profile in the present case can be readily transformed into the prediction of the capillary rise problem that has been properly solved previously. Let x = X, y = -Y and bring them into Equation (4.20), one can obtain:

$$\frac{\frac{d^2y}{dx^2}}{[1+(\frac{dy}{dx})^2]^{\frac{3}{2}}}+\frac{\frac{dy}{dx}}{x[1+(\frac{dy}{dx})^2]^{\frac{1}{2}}}=\frac{\Delta\rho gy}{\gamma_{ow}} \tag{4.23}$$

Note here that $\Delta\rho = -\Delta\rho_0 = \rho_o - \rho_w$ is the density difference between the oil and the aqueous phases. Physically, such a switch of the density difference can be readily understood by considering the fact that the gravitational acceleration, g, will become positive in the reversed x-y coordinate system (see Figure 4.6). The boundary conditions expressed by Equations (4.21a,b) can be transformed into the corresponding boundary conditions for Equation (4.23) as follows:

$$y\Big|_{x=R_c}=h \tag{4.24a}$$

and

$$\frac{dy}{dx}\Big|_{x=R_c}=\cot(\theta)=\cot(180^o-\theta_1)=\tan(90^o+\theta_1) \tag{4.24b}$$

Here, h becomes the capillary rise height on the cylinder and $\theta_l=180^o-\theta$ is the supplementary contact angle on the oil side.

Equation (4.23) with its boundary conditions Equations (4.24a,b) are essentially the same as Equation (4.6) with its boundary conditions Equations (4.7a,b), except that in the present case $\beta=90^o$, γ_{lv} is replaced by γ_{ow} and θ is substituted by θ_l. They can be further transformed into two first-order ordinary differential equations in conjunction with their corresponding initial conditions by using the variable substitution method. Furthermore, these two resultant equations can be solved numerically by using, e.g., the 4th-order Runge-Kutta technique. Thus, for each set of given values of R_c, θ_l, h and $\Delta\rho g/\gamma_{ow}$, which depend on the size of the cylinder and the properties of the solid-liquid-fluid system tested, one can obtain an accurate shape of the transformed capillary rise profile, y=y(x), or the corresponding actual capillary depression profile, Y(X)=-y(X). The detailed variable substitution approach and complete mathematical transformation procedures were presented previously and thus are not included here.

After the above manipulations, the ACPAC technique for the ACRPAC case can be directly used to determine the supplementary contact angle θ_1 by analysis of the capillary depression profile around a cylinder (ACDPAC). It should be noted that, as one of the input data, $\Delta\rho$ is the density difference between the oil phase and the aqueous phase in the reversed x-y coordinate system. Hence, here $\Delta\rho = -\Delta\rho_0 = \rho_o-\rho_w$ is negative if the oil phases tested are lighter than the aqueous counterparts. Similar to the ADSA technique, the ACPAC technique for the ACDPAC case determines the supplementary contact angle by the shape analysis of the capillary depression profile on the cylinder. An objective function is defined as the discrepancy between a physically observed capillary "rise" profile and a theoretically predicted one. Acquisition and digitization processes of the physical profile are the same as those for the ACRPAC case. The theoretical profile is a curve satisfying the Laplace equation of capillarity. The objective function is then minimized numerically by using the supplementary contact angle as one of the adjustable parameters.

4.6.2 Experimental Aspects of the ACDPAC Case

A block diagram of the experimental apparatus used in the ACDPAC case is shown in Figure 4.7. In the set-up, a pre-coated glass cylinder was inserted through the O/W interface formed between the upper oil phase and the lower aqueous phase in a test beaker. A square beaker of 40x40x40 mm^3 was used for optical consideration. Because the glass fiber was coated with the hydrophobic FC725 material, the O/W interface was deformed downward and a capillary depression profile around the cylinder was formed. The test beaker was placed between a light source and a microscope. In order to use the previously developed ACPAC technique for the ACRPAC case, the video camera system was intentionally set upside down in all measurements. Thus, it is seen from Figure 4.7 that the actual capillary depression profile becomes a capillary "rise" profile, which is displayed on-line on the computer monitor. Such a capillary "rise" profile was acquired and processed by the computer digital image system.

All experimental digital images were automatically stored in the computer memory and could be retrieved, processed and analyzed after the experiment was completed. The basic aspects of the digital image acquisition and digitization process and much more experimental details about the digital image technique were described previously in Section

4.3. Figures 4.8a and 4.8b show two typical digital images of the partial O/W interfaces around the FC725-precoated glass fiber. Specifically, Figure 4.8a was taken before the camera was set upside down, whereas Figure 4.8b was taken after the setting. Thus, Figure 4.8a is the actual capillary depression profile formed by the interface between the silicone oil A and the deionized ultra-filtered (DIUF) pure water. Figure 4.8b shows the corresponding capillary "rise" profile obtained by reversing the camera position. In these digital images, the central black block represents the glass fiber and the remaining black space represents the oil phase, while the two white parts on the both sides of the solid surface represent the aqueous phase.

For such oil-water profile images, a standard grid image was used to calibrate the image and correct possible optical distortion. A special computer image processing and analyzing program was then implemented to digitize the image automatically with a sub-pixel resolution. The computer program can determine the profiles of the glass fiber and the O/W interface. The output data of the digitization process are two sets of discrete coordinates, x and y, representing the profiles of the glass fiber surface and the O/W interface around the fiber, respectively. The digitized plot of the image seen in Figure 4.8b is given in Figure 4.8c. This figure clearly indicates the profiles of the fiber surface and the profiles of the O/W interface between the silicone oil and the DIUF water on the left-hand and the right-hand sides. By implementing the spline curve fitting, the accuracy of the digitized profiles is about 1.0 μm, at 40 times magnification. With the digitized profiles of the capillary rise image, the radius of the cylinder, R_c, is half the horizontal difference between the three-phase contact points on the left- and right-hand sides. As seen from Figures (4.8b,c), the elevation of the three-phase contact circle on the glass fiber relative to the lower edge of the partial capillary "rise" profile covered by the image, Δh_m, is equal to their vertical difference. Therefore, x_{mi} and y_{mi} (i=1, 2, N), R_c and Δh_m, which are all required in the optimization scheme, are obtained by applying the computer digital image techniques.

The oil phases used in the present contact angle measurements were silicone oil (A-type) with kinematic viscosity of ν_A = 2 Centistokes and silicone oil (B-type) with kinematic viscosity of ν_B = 5 Centistokes (Dow Corning 200 Series Fluids). These pure oil liquids were chosen as the oil phases in order to satisfy the following general requirements. They have low vapour pressures or high boiling temperatures, in order to minimize possible adsorption and evaporation effects. Moreover, they are chemically stable and not excessively toxic.

The aqueous phases were either the pure deionized ultra-filtered (DIUF) water (Fisher Scientific, Canada) or ionic surfactant solutions. The pure DIUF water has a density of ρ_w = 998 kg/m^3 and a liquid-air surface tension of γ_{wv} = 72.66 mJ/m^2 at 22°C. Two typical ionic surfactants were used: the cationic surfactant cetyltrimethylammonium bromide, CTAB, and the anionic surfactant sodium dodecyl sulphate, SDS (Aldrich, 95% pure). Their critical micelle concentrations (CMC) in water, determined from their surface tension-concentration curves, were reported to be about 9.2x10^{-4} M for CTAB (Czerniawski, 1966) and 8.1x10^{-3} M for SDS (Stalidis et al., 1990) at 25°C. The ionic surfactant solutions were prepared by adding one of the two ionic surfactants, either CTAB or SDS, at a different concentration each time into the pure DIUF water. Usually a period of more than 12 h was allowed for the chosen surfactant to become completely dissolved and evenly distributed in the ionic surfactant solution.

In this study, the glass cylinder of R_c=1.5 mm was coated with a fluorochemical surfactant coating material, FC725 (3M Product). The FC725 solid surface was prepared using a dip-coating method and the quality of the FC725 surfaces was carefully examined following the procedures as described in details in Section 4.4.

After the aqueous phase was prepared, the oil-water interface was formed according to the following steps. First, the square glass beaker was half filled with the test aqueous phase. Then the oil phase was gently added by using a syringe until the beaker was almost full. Due to their density difference, the upper oil phase was layered above the lower aqueous phase. The O/W interface in the centre of the beaker was a horizontal flat surface. When a FC725 coated glass fiber was inserted through the O/W interface in the centre of the beaker, a capillary depression meniscus was formed around the fiber. However, a capillary rise O/W interface was formed on the walls of the beaker because of high-energy glass surfaces. This configuration made it possible to observe the capillary depression profile from the outside of the beaker by using the video camera. Usually, the O/W interface was aged for at least two hours before the FC725 coated glass fiber was introduced. Thus, the possible adsorption of the dissociated ions in the pure DIUF water or the ionic surfactant solution onto the O/W interface could reach an equilibrium state, as indicated by other researchers (Shinoda et al., 1963; Ives, 1984; Saulnier et al., 1996).

Measurements of the capillary rise O/W profile around a glass fiber coated with the FC725 were carried out according to the following procedure. First, after a flat O/W interface was formed, the FC725-precoated cylinder was positioned in the centre of the beaker and gradually inserted through the O/W interface. The capillary depression O/W profile was formed around the fiber because of the hydrophobic FC725 surface. It was observed that the initial non-equilibrium contact angle of the O/W interface varies with time up to several minutes, though the glass fiber is kept stationary. Hence, in this study, the image of the capillary profile around the cylinder was taken 10 min after each movement of the glass fiber in order to measure the static or the equilibrium contact angles. Then the glass fiber was gently moved downward by using a three-dimensional translation stage with a vertical resolution of 1.0 μm. The position of the three-phase contact circle on the fiber was thus changed. Again the image was taken at this new position after 10 min to ensure that the contact angle reached the equilibrium value. The experiment continued until a total of ten digital images at ten different positions were recorded. All measurements were conducted at 22°C.

4.6.3 Experimental Results and Discussion of the ACDPAC Case

The contact angles on the FC725-precoated glass fibers were measured for two silicone oil-pure DIUF water systems (silicone oil A-type and silicone oil B-type). Table 4.4 lists the mean values of the supplementary contact angles, θ_1, and the true contact angles, θ, for the two O/W interfaces. Some surface properties of the oil phases and the O/W interfaces are also included in the table, where γ_{ov} and γ_{ow} are the oil-air surface tension and the O/W interfacial tensions, respectively. They were measured by the pendant drop method using the ADSA technique (Rotenberg et al., 1983; Cheng et al., 1990; Li et al., 1992). Any value following the "±" sign represents the standard deviation of the mean value over ten trials. It is noted that the maximum variation of the measured supplementary contact angles, θ_1, or the true contact angles, θ, is about ±0.4° around the mean values. As was discussed previously (Gu et al., 1997a), this error is solely attributed to the inability to align the cylinder truly vertically in the actual experiments.

The standard variance is only approximately 0.1° if the average is taken over the measured contact angles from one side of the glass fiber only. It is seen from Table 4.4 that, for the two silicone oil liquid, their surface tensions, γ_{ov}, and interfacial tensions against the pure DIUF water, γ_{ow}, increase as their densities increase. Consequently, their O/W interfaces have slightly larger contact angles and become more non-wetting on the FC725 surface.

The contact angles of the silicone oil and the ionic surfactant solution interfaces on the FC725-precoated fiber were also determined by using the ACPAC technique for the ACDPAC case. Table 4.5 gives the measured contact angles of the silicone oil (A-type) and the DIUF water interfaces on the FC725-precoated glass fiber at different cationic surfactant concentrations of CTAB from 10^{-5}~10^{-3}M. The corresponding surface tensions of the aqueous surfactant solutions against the air, γ_{wv}, and the O/W interfacial tensions, γ_{ow}, at these surfactant concentrations are measured by the pendant drop method using the ADSA technique. As expected, both γ_{wv} and γ_{ow} decrease greatly when the surfactant concentration increases. The maximum CTAB concentration tested is equal to 10^{-3} M, very close to its CMC, 9.2×10^{-4} M, in water at 25°C (Czerniawski, 1966). Accordingly, the contact angles of the O/W interfaces are reduced by nearly 8° as CTAB concentration approaches its CMC. With the increase in CTAB concentration, the O/W interfaces become more wetting than the silicone oil and the pure DIUF water interfaces.

Similar results of the silicone oil A-type and the DIUF water interfaces on the FC725-precoated glass fiber are presented in Table 4.6 for different anionic surfactant concentrations of SDS from 10^{-4}~10^{-2} M. This table also clearly shows the wetting effect of the anionic surfactant on the O/W interfaces when it is added into the aqueous phase. This test terminates as SDS concentration is near its CMC, 8.1×10^{-3} M, in water at 25°C (Stalidis et al., 1990). Compared with the measured results for CTAB, SDS at about one order of magnitude higher surfactant concentration has the similar wetting ability to CTAB, regardless of their different ionic features. Near their CMCs, their γ_{wv}, γ_{ow} and the contact angles of the O/W interfaces are almost the same.

The wetting ability of SDS on the O/W interfaces was also investigated using the ACPAC technique for the ACDPAC case for the silicone oil (B-type). Table 4.7 presents the contact angles of the silicone oil B and the DIUF water interfaces on the FC725-precoated glass fiber measured by using the ACPAC technique for the ACDPAC case. These results follow the same general trends as described above. Since silicone oil (B-type) is denser and more viscous, its O/W interfacial tensions, γ_{ow}, and the measured contact angles, θ, are also greater than those for silicone oil (A-type) at the same SDS concentration given in Table 4.6. It is found that, at the CMC of SDS, the contact angle of the silicone oil (B-type) and the DIUF water interface is only approximately 5^{o} smaller than that for the silicone oil B and the pure DIUF water interface. Therefore, SDS has less pronounced wetting effect on the silicone oil (B-type)-DIUF water interfaces than on the silicone oil (A-type)-DIUF water interfaces.

All of the above experimental results indicate that the ACPAC technique is an appropriate experimental method to study the wetting effect of any surfactants dissolved in the aqueous solution on the liquid-fluid interface around a curved solid surface.

4.7 Hamaker Constants Determined from the Measured Surface Energies of the Fiber-Water-Oil Systems

As was derived and expressed by Equation (3.30) in Section 3.5.2, the Hamaker constant can be related to the surface energies by the following equation:

$$A_{owf} \approx +24\pi D_0^2 \sqrt{|(\gamma_{ov} + \gamma_{wv} - 2\gamma_{ow})(\gamma_{fv} + \gamma_{wv} - 2\gamma_{fw})|} \tag{4.25}$$

where D_0 is the separation distance at which the two surfaces are actually in contact. It is sometimes also called either the interfacial contact separation distance or a "cut-off" distance. It has been shown that the cut-off separation distance D_0 can be treated as a "universal constant" (D_0=0.165 nm) for very different liquids and solids (Israelachvili, 1985). In Equation (4.25), γ_{ov}, γ_{wv} and γ_{ow} represent the surface tensions of the oil-vapor and the water-vapor interfaces and the interfacial tension of the oil-water interface, which can be measured directly by using the ADSA technique for the pendant drop case. In addition, γ_{fv} and γ_{fw} are the surface tension of the fiber-vapor interface and the interfacial tension of the fiber-water interface and can not be measured directly. In terms of the equation of state for interfacial tensions of solid-liquid systems, however, they can be determined from the measured surface energies of the liquid-fluid interfaces and the contact angle (wettability) of the solid-liquid-fluid system (Li and Neumann, 1990a; 1992a). The equation of state for interfacial tensions of the present fiber-water-oil system can be written as:

$$\cos\theta = -1 + 2\sqrt{\frac{\gamma_{fv}}{\gamma_{wv}}}e^{-0.0001247(\gamma_{wv}-\gamma_{fv})^2} \tag{4.26a}$$

where, θ is the contact angle of water drop formed on the fiber surface.

In Equation (4.26a), γ_{wv} can be measured by using the ADSA technique for the pendant drop case. The pure DIUF water-air surface tension is equal to $\gamma_{wv} = 72.66 \pm 0.31$ mJ/m^2 at 22°C. For the flat fiber surface, θ can be accurately measured by using the ADSA technique for the sessile drop case. For the cylindrical fiber, however, as was discussed in details in the previous sections, θ can be measured by using the ACPAC technique. Once the values of γ_{wv} and θ are measured, the fiber surface tension γ_{fv} can be calculated from the equation of state for the solid-water-vapor system by iteration. Furthermore, the interfacial tension of the fiber-water interface, γ_{fw}, can be determined from the classical Young equation:

$$\gamma_{wv}\cos\theta = \gamma_{fv} - \gamma_{fw} \tag{4.26b}$$

Therefore, eventually, all the relevant surface energies required in Equation (4.25) can be determined and thus the Hamaker constant can be determined from the equation by choosing $D_0 = 0.165$ nm.

In this thesis study, two kinds of fiber surfaces were used: the bare glass fiber is a typical hydrophilic surface and the FC725-precoated one represents a hydrophobic surface. Their solid surface tensions, γ_{fv}, and the interfacial tensions with the water, γ_{fw}, can be determined using the equation of state for interfacial tensions, Equation (4.26a), and the classical Young equation for fiber-water systems, Equation (4.26b), respectively. The contact angle θ of the pure DIUF water-vapor interface is about $10.1^\circ \pm 1.7^\circ$ on the bare glass surface and $115.6^\circ \pm 0.9^\circ$ on the FC725-precoated fiber surface respectively. Therefore, γ_{fv} is found to be 71.56 ± 0.39 mJ/m^2 for the bare glass fiber surface and 13.87 ± 0.51 mJ/m^2 for the FC725-precoated fiber surface by substituting the values of γ_{wv} and θ into Equation (4.26a).

It should be pointed out that, ideally, the contact angle between the pure DIUF water and a clean glass surface should be equal to zero since clean glass is a typical surface of high hydrophilicity. In this work, the above contact angle ($\theta=10.1^{\circ}\pm1.7^{\circ}$) of the pure DIUF water on the bare glass surface was measured using the ADSA technique for the sessile drop case. This small non-zero contact angle may be due to a very small percentage of the bare glass surface covered by possible impurities (or remaining traces) of Acetone and dust from the air when it was washed with the cleaning agent and then dried in air. In addition, this contact angle may not be accurate because, in principle, it is not recommended to use the ADSA technique to measure any contact angles smaller than 25°. Hence, the surface energy ($\gamma_{fv}=71.56\pm0.39$ mJ/m^2) for the bare glass surface determined by substituting the measured values of γ_{wv} and θ into Equation (4.26a) may not be accurate. In fact, unlike the liquid surface energy, the solid surface energy can not be measured directly. In the literature, Fisher (1948) estimated the solid surface tensions of several solid surfaces from the other surface tension measurements. The surface tension of glass was reported to be about 150-300 mJ/m^2. However, the exact surface energy of clean glass is unknown. Thus, in this study, the above surface energy for the bare glass surface was still used in determining γ_{fw} from Equation (4.26b). Furthermore, in conjunction with the other surface energies, such determined γ_{fv} and γ_{fw} were then used in Equation (4.25) to calculate the Hamaker constant A_{owf} for the oil-pure water-bare glass fiber system.

A sensitivity analysis was conducted to study the influence of the surface energy γ_{fv} on the model predictions. If the surface energy γ_{fv} for the bare glass is purposely chosen as 71.56, 100.00, 150.00 and 200.00 mJ/m^2, the corresponding Hamaker constants A_{owf} (or A_{132} in Table 4.8) calculated from Equation (4.25) are found to be 13.07, 14.31, 16.25, and $17.98\text{x}10^{-20}$ J. Accordingly, the dimensionless adhesion numbers $A_d=\dfrac{A_{132}}{6\mathbf{k}T}$ are equal to 5.35, 5.85, 6.64 and 7.36, respectively. The Hamaker constant A_{owf} or the dimensionless adhesion number A_d for the oil-pure water-bare glass system increases only by approximately 38% as the surface energy γ_{fv} of the bare glass increases by nearly three times. The other dimensionless parameters required in the 1-D model (see Chapter 6) are selected as follows: A=10, Dl=+10, Da=0 and $\tau=5$. A parametric study with respect to

A_d (reflecting γ_{fv} as well) was carried out for the case in which the vdW force becomes an important driving force in the deposition of oil droplet onto the bare glass surface (see Figures 6.2a,b for details). The final numerical results of the dimensionless mass transfer rate Sh are found to be 0.0471, 0.0475, 0.0481 and 0.0486, if A_d is chosen as 5.35, 5.85, 6.64 and 7.36, which corresponds γ_{fv}=71.56, 100.00, 150.00 and 200.00 mJ/m^2 for the bare glass respectively. The Sh number of the oil-water-glass system increases only by approximately 3% if the surface energy γ_{fv} for the bare glass increases by nearly three times. Therefore, it can be concluded from the above sensitivity analysis that use of the surface energy of γ_{fv}=71.56 mJ/m^2 for the bare glass surface has no appreciable effect on the final numerical results (i.e. Sh number) of the model predictions.

Silicone oil No. 1 with density of ρ_o = 1050 kg/m^3 and viscosity of μ_o = 172.7 mPa s (Aldrich Chemical Co.) was chosen as the dispersed oil phase in the deposition tests. Its small density difference from the aqueous phase makes it particularly suitable for this experimental study. The silicone oil-air surface tension is equal to γ_{ov} = 26.10 ± 0.14 mJ/m^2 at 22°C. The aqueous phases were either the pure deionized ultra-filtered (DIUF) water (Fisher Scientific, Canada) or other aqueous solutions made with the DIUF water. The pure DIUF water has a density of ρ_w = 998 kg/m^3 and a liquid-air surface tension of γ_{wv} = 72.66 ± 0.31 mJ/m^2 at 22°C. Moreover, it has an initial conductivity of 1.21x10^{-4} S/m and an equilibrium pH of about 6.5. The interfacial tension for pure water-oil interface is equal to γ_{ow} = 35.31 ± 0.44 mJ/m^2. In additional to the pure DIUF water, three kinds of aqueous solutions were tested as follows: the aqueous solutions with different pH values, the electrolyte solutions at different concentration and the ionic surfactant solutions. The pH value of the DIUF water solution was adjusted to a desired value with NaOH or HCl. The aqueous solutions containing electrolytes were prepared by adding one of the following two typical electrolytes at a different concentration each time into the pure DIUF water: NaCl, $AlCl_3$. When making surfactant solutions, two widely used ionic surfactants were used: the cationic surfactant cetyltrimethylammonium bromide (CTAB) and the anionic surfactant sodium dodecyl sulphate (SDS). The ionic surfactant solutions were prepared by adding one of the two ionic surfactants at a different concentration each time into the pure DIUF water. Usually a period of more than 12 h was given for all the chemicals to be completely dissociated and uniformly distributed in the aqueous solution.

At this point, it is worthwhile emphasizing that γ_{wv}, γ_{ow} and γ_{fw} are strongly dependent on the aqueous phase used in the test, although γ_{fv} and γ_{ov} are the surface tensions of the fiber surface and the oil phase and are thus independent of the aqueous solution tested. Hence, for a given fiber-water-oil deposition system, once all the relevant surface energies required in Equation (4.25) are known, the Hamaker constant for the fiber interacting with the oil droplet across the aqueous medium A_{owf} can be calculated directly from the equation (choosing D_0 = 0.165 nm, Israelachvili, 1985). Such calculated Hamaker constants for the bare glass fiber interacting with the silicone oil droplet across different aqueous media are listed in Table 4.8. Similarly, Table 4.9 gives the Hamaker constant values for the FC725-precoated glass fiber interacting with the silicone oil droplet across different aqueous media.

Some important information and tendency can be easily identified from Tables 4.8 and 4.9, which will be useful in correlating the numerical predictions (see Chapter 6) and the deposition test data (see Chapter 7) to the surface properties of the fiber-water-oil systems. In additional to the Hamaker constant, a dimensionless parameter is often used to describe the strength of the vdW interaction and defined as below:

$$A_d = \frac{A_{132}}{6\mathbf{k}T} \tag{4.27}$$

where, A_d is often referred to as the dimensionless adhesion number, where the Boltzmann constant $\mathbf{k}$ = $1.381\text{x}10^{-23}$ J/k (All the fundamental physical constants are quoted from Weast et al., 1989) and T = 295.15 K. For each Hamaker constant, its corresponding value of A_d is also listed in Tables 4.8 and 4.9 for reference. First of all, it is found that the Hamaker constants A_{owf} for the silicone oil droplet interacting with the two typical glass fibers across a variety of aqueous media changes from $0.40\text{x}10^{-20}$ J to $13.07\text{x}10^{-20}$ J (A_d = 0.16-5.35). Although the Hamaker constants for the oil-water-fiber systems studied here can not be found elsewhere, the Hamaker constants for two identical media (e.g., oil, mica, metals) interacting across another medium (e.g., water) are available in the literature (Hough and White, 1980; Parsegian and Weiss, 1981; Israelachvili, 1985). Typically, the Hamaker constants for oils (dodecane and hexadecane), mica and metals (Ag, Au and Cu) interacting across water are about 0.36-$0.49\text{x}10^{-20}$ J, $2.0\text{x}10^{-20}$ J and 30-$40\text{x}10^{-20}$ J, respectively (Israelachvili, 1985). In this study, the silicone oil has a surface tension of γ_{ov} = 26.10 mJ/m^2 at 22°C, which is between the surface tension of dodecane γ_{ov} = 25.44 mJ/m^2 and that of hexadecane γ_{ov} = 27.76 mJ/m^2 at 22°C (see Table 4.1). It is also estimated that the vdW interaction for glass fibers interacting across water medium should be slighter stronger than (and closer to) that for micas but much weaker than that for metals interacting across water phase. Therefore, the Hamaker constant listed in Tables 4.8 and 4.9 are in a reasonable range as expected.

In addition, these two tables clearly indicate that the Hamaker constants for the bare glass fibers given in Table 4.8 are larger than those for the FC725-precoated glass fibers given in Table 4.9. This is because the bare glass fiber surfaces have higher surface energy (γ_{fv} = 71.56 mJ/m^2 at 22°C) and thus are hydrophilic, while the FC725-precoated glass fiber surfaces have much lower surface energy (γ_{fv} = 13.87 mJ/m^2 at 22°C) and thus are hydrophobic. More specifically, Table 4.8 shows that, for the bare glass fiber surfaces, their Hamaker constants decrease as the pH value deviates from the equilibrium value (pH=6.50) of the DIUF water. However, for the FC725-precoated fiber surfaces, their Hamaker constants decrease almost monotonically from 2.40x10^{-20} J to 0.40x10^{-20} J when the corresponding pH value increases from 2.68 to 10.32. For the bare glass fiber surfaces, their Hamaker constants slightly increase with addition of electrolytes such as NaCl or $AlCl_3$ into the DIUF water. Nevertheless, addition of either ionic surfactants, CTAB and SDS, will substantially reduce the Hamaker constants for the bare glass fiber surfaces, regardless of ionic feature of the surfactant added. These last two patterns are completely reversed for the FC725-precoated fiber surfaces. All above changes in the Hamaker constants are attributed to the variations of the surface energies of the fiber-water-oil systems with the liquid properties of the aqueous media, specifically, γ_{wv}, γ_{ow} and γ_{fw}.

4.8 Summary

In order to determine the vdW interaction described in Chapter 3, the Hamaker constant is related to the surface energies of the deposition system by using the combining rules. All the surface energies of the liquid-fluid interfaces can be readily measured by using, for example, the ADSA technique for the pendant drop case.

Nevertheless, the surface energies of the solid-fluid interfaces can not be measured directly. The equation of state for interfacial tensions of solid-liquid systems is used to determine the surface energies of the solid-fluid interfaces from the surface energies of the liquid-fluid interfaces and the contact angle of the solid-liquid-fluid system. Since the ADSA can measure the contact angle of any liquid-fluid interfaces formed on a flat solid surface only, in this chapter, a new contact angle measurement technique is presented to measure the contact angles on cylindrical fiber surface. The novel method determines the contact angles by analysis of the capillary profile around a cylinder (ACPAC). There are two specific application cases, one is by analysis of the capillary rise profile around a cylinder (ACRPAC) and the other is by analysis of the capillary depression profile around a cylinder (ACDPAC).

In the ACPAC technique, computer image processing and analysis techniques are used to obtain the profiles of the cylinder and the liquid-vapour interface around the cylinder. The contact angle is determined by numerically minimizing the discrepancy between the physically observed liquid-vapour interface and the theoretical predicted capillary rise profile, i.e., the curve representing a solution of the Laplace equation of capillarity. The input requirements are the density difference between the liquid and the vapour phases, the liquid-vapour surface tension and the local gravity. The present technique has been successfully tested to measure the contact angles of capillary rise profiles around a constant-diameter or conic cylinder. The measured contact angles agree very well with those measured by the Wilhelmy plate technique or the ADSA technique for the sessile drop case, respectively.

In addition, the ACPAC technique for the ACRPAC case can be modified and extended to measure the contact angle of a liquid-liquid interface by analysis of the capillary depression profile around a cylinder (ACDPAC). The wettability of several oil-water interfaces is studied by using the method. For silicone oil and pure DIUF water interfaces, they have slightly larger contact angles as their interfacial tensions increase. Cationic surfactant CTAB dissolved in the aqueous phase was tested to have nearly the same wetting effect as the anionic surfactant SDS if SDS concentration is one order of magnitude higher, regardless of their different ionic properties. All these results show that the ACPAC technique is a powerful tool for accurate measurements of contact angles of any liquid-

liquid interfaces on fiber surfaces. It can be used to measure the contact angles between a liquid-vapour interface, or a liquid-liquid interface and a constant-diameter or conic cylinder. It should be pointed out that most natural and artificial fibers encountered in textile, cosmetic and composite material industries are rough and porous. Their shapes may deviate considerably from those of constant-diameter cylinders. Thus, the ACPAC methods will be particularly useful for studying the wetting phenomena associated with a liquid-vapour interface, or an oil-water interface on these fiber surfaces.

Based on the modern computer digital image processing and analysis techniques, the ACPAC technique is fully automatic, objective and accurate. This technique is an excellent alternative tool for accurate measurements of contact angles on fibers. It will be particularly useful in studies of wetting, spreading and deposition processes of a liquid on fiber surfaces. It is anticipated that the novel contact angle measurement technique can be used to explore the effects of other factors on the wettability of various solid-liquid-fluid systems, such as time, temperature, pressure and humidity, and the other liquid properties. A general user-oriented computer code for implementing the techniques is now available.

With both the sophisticated ADSA technique and the newly devised ACPAC technique, all the relevant surface energies can be determined for a fiber-water-oil deposition system. Therefore, the Hamaker constant for the fiber interacting with the oil droplet across an aqueous medium A_{owf} can be calculated from Equation (4.25). Such determined Hamaker constant depends solely on the surface energies of the fiber-water-oil system under investigation. In comparison with the values of the Hamaker constants available in the literature (Israelachvili, 1985), the values of the Hamaker constants given in Tables 4.8 and 4.9 for the silicone oil droplets interacting with two different fiber surfaces across various aqueous media are in an expected range. In particular, the Hamaker constants are found to be about 10^{-19} to 10^{-20} J for the high-energy bare glass fiber surfaces and 10^{-20}-10^{-21} J for the low-energy FC725-precoated glass fiber surfaces. Changes in the Hamaker constants of the fiber-water-oil systems are caused by the variations of the surface energies of the fiber-water-oil systems, specifically, γ_{ov}, γ_{wv}, γ_{ow} γ_{fv} and γ_{fw}. It is noticed from Tables 4.8 and 4.9 that the Hamaker constant changes about by one order for each fiber surface. Hence, it is expected that the vdW force will influence the deposition results to an appreciable extent if it is one of the dominant factors involved in the deposition process.

However, precaution should be taken in attempting to interpret the deposition test data since both the vdW and the EDL interactions will affect the deposition process. As will be shown in the next chapter (see Tables 5.3 and 5.4 for details), actually, the EDL interaction switches its sign (from repulsive to attractive or vice verse) and changes about two orders (Dl = 10^3-10^5) as the aqueous medium changes. Another fact worthwhile mentioning here is that, from the experimental point of view, it is hardly possible to purposely and considerably modify the vdW interaction without causing substantial variation of the EDL interaction. Therefore, it is practically difficult to examine the sole effect of the vdW interaction in experiments. Nonetheless, it is much easier to greatly modify the EDL interaction while the vdW interaction remains almost unchanged. As will be shown in the next chapter, for example, the EDL interaction will vary significantly and even switch its sign as the electrolyte concentration in an aqueous phase and its valence are varied. As seen from Tables 4.8 and 4.9, the vdW interaction only changes to a limited extent when the electrolyte, NaCl or $AlCl_3$, is added into the aqueous medium. Thus the important role of the EDL interaction in deposition tests can be readily identified.

By going through such lengthy theoretical derivations and experimental endeavors (see the ζ-potential measurements in Chapter 5 as well), at this stage, the effects of the physical properties of the fiber-water-oil system on the vdW interaction can be quantified. More importantly, it is possible to quantitatively identify the important role of the vdW interaction that might play in the actual deposition process. After the ζ-potential values of the fiber-water-oil systems are measured properly and further discussion on the EDL interaction is elaborated in Chapter 5, the joint effects of the vdW interaction and the EDL interaction on a specific deposition process will be numerically investigated in Chapter 6. These numerical predictions will be further compared with the detailed deposition test data in Chapter 7.

Table 4.1 Contact angles for four n-alkane liquids on the FC72-precoated constant-diameter cylinders, as measured by the ACPAC technique for the ACRPAC case and the Wilhelmy plate technique

Solid-Liquid System	γ_{lv} (mJ/m^2)	$\theta_{\infty ACPAC}$ (°)	$\theta_{\infty Wilhelmy}$ (°)
FC725-Decane	23.43	58.7±0.4	58.9±0.5
FC725-Dodecane	25.44	63.7±0.4	63.3±0.5
FC725-Tetradecane	26.55	65.8±0.5	65.4±0.5
FC725-Hexadecane	27.76	69.8±0.4	69.2±0.5

Table 4.2 Variation in the contact angle (θ) of decane on the FC725-precoated conic cylinder along its axial direction, with the local values of the radius (R_c) and the inclination angle (β) at the three-phase contact circle

Image no.	R_c (mm)	β (°)	θ (°)
1	0.1937	86.7	59.5
2	0.1997	85.1	62.4
3	0.2363	82.6	62.5
4	0.2607	82.2	62.0
5	0.3539	70.3	63.2
6	0.4240	68.5	62.3
7	0.4378	67.4	63.6
8	0.8614	70.4	60.0
9	1.0234	88.5	59.3
10	1.0313	88.7	59.0

Table 4.3 The line tensions (σ) and the contact angles (θ_∞) for four n-alkane liquids on the FC725-precoated solid surface, as derived from Equation (4.16) by using the contact angles measured on a conic cylinder

Solid-Liquid	γ_{lv} (mJ/m^2)	σ (μJ/m)	Correl. [a]	θ_∞ (°)	θ_{pred} (°) (R=3 mm)	θ_{ADSA} (°) (R≈3 mm)
FC725-Decane	23.43	1.7	0.85	58.5	60.2	59.9
FC725-Dodecane	25.44	2.1	0.87	63.6	65.8	66.3
FC725-Tetradecane	26.55	3.3	0.84	65.4	68.0	68.2
FC725-Hexadecane	27.76	3.7	0.83	69.5	71.4	71.2

[a] The Correlation coefficient of the linear curve fitting.

Table 4.4 Contact angles for two silicone oil and pure DIUF water interfaces on the FC725-precoated glass fibres, as measured by the ACPAC technique for the ACDPAC case

Oil Phase	ρ_o (kg/m^3)	γ_{ov} (mJ/m^2)	γ_{ow} (mJ/m^2)	θ_1 (°)	θ (°)
Silicone Oil (A)	862	17.64±0.04	39.14±0.35	38.0±0.4	142.0
Silicone Oil (B)	919	19.13±0.04	41.51±0.41	35.5±0.3	144.5

Table 4.5 Effect of the cationic surfactant, CTAB, on the contact angles of the silicone oil (A-type) and the DIUF water interfaces on the FC725-precoated glass fibres

CTAB Concentration (M)	γ_{wv} (mJ/m^2)	γ_{ow} (mJ/m^2)	θ_1 (°)	θ (°)
10^{-3}	36.80±0.18	9.21±0.09	45.6±0.3	134.4
10^{-4}	50.00±0.28	26.27±0.25	41.8±0.2	138.2
10^{-5}	61.94±0.02	38.12±0.21	39.1±0.2	140.9
0	72.66±0.12	39.14±0.35	38.0±0.4	142.0

Table 4.6 Effect of the anionic surfactant, SDS, on the contact angle of the silicone oil (A-type) and the DIUF water interfaces on the FC725-precoated glass fibres

SDS Concentration (M)	γ_{wv} (mJ/m^2)	γ_{ow} (mJ/m^2)	θ_1 (°)	θ (°)
10^{-2}	37.96±0.08	9.76±0.07	45.7±0.2	134.3
10^{-3}	60.62±0.29	35.70±0.36	39.1±0.2	140.9
10^{-4}	71.85±0.26	39.09±0.28	38.9±0.1	141.1
0	72.66±0.12	39.14±0.35	38.0±0.4	142.0

Table 4.7 Effect of the anionic surfactant, SDS, on the contact angle of the silicone oil (B-type) and the DIUF water interfaces on the FC725-precoated glass fibres

SDS Concentration (M)	γ_{wv} (mJ/m^2)	γ_{ow} (mJ/m^2)	θ_1 (°)	θ (°)
10^{-2}	37.96±0.08	11.05±0.11	40.7±0.1	139.3
10^{-3}	60.62±0.29	36.30±0.13	36.4±0.1	143.6
10^{-4}	71.85±0.26	40.23±0.29	36.2±0.1	143.8
0	72.66±0.12	41.51±0.41	35.5±0.3	144.5

Table 4.8 Hamaker constants A_{owf} (or A_{132}) for the silicone oil droplet (phase 1, γ_{ov}=26.10±0.14 mJ/m^2) interacting with the bare glass fiber (phase2, γ_{fv}=71.56±0.39 mJ/m^2) across aqueous solutions (medium 3 with varying surface tensions)

Aqueous Medium	γ_{wv} (mJ/m^2)	γ_{ow} (mJ/m^2)	θ (°)	γ_{fw} [a] (mJ/m^2)	A_{132} [b] (10^{-20} J)	A_d [c]
DIUF Water	72.66±0.31	35.31±0.44	10.1±1.7	0.03	13.07	5.35
pH=2.68	68.70±0.12	30.75±0.43	57.7±1.1	34.85	9.95	4.07
pH=3.52	70.76±0.10	32.84±0.52	55.8±1.2	31.79	10.17	4.16
pH=4.20	72.40±0.07	34.80±0.51	56.8±1.0	31.92	9.88	4.04
pH=6.50	72.66±0.31	35.31±0.44	10.1±1.7	0.03	13.07	5.35
pH=7.20	70.78±0.10	31.89±0.15	40.5±1.4	17.74	12.21	4.99
pH=8.93	70.43±0.22	30.84±0.15	42.7±2.1	19.80	12.26	5.01
pH=10.32	70.16±0.23	31.03±0.09	44.7±1.8	21.69	11.90	4.87
10^{-6} M NaCl	71.89±0.37	32.69±0.22	62.7±1.9	38.59	9.54	3.90
10^{-5} M NaCl	68.81±0.28	30.82±0.07	56.2±1.3	33.28	10.17	4.16
10^{-4} M NaCl	66.83±0.34	30.60±0.09	51.7±1.0	30.14	10.22	4.18
10^{-3} M NaCl	66.22±0.27	30.16±0.20	45.8±1.3	25.40	10.83	4.43
10^{-6} M $AlCl_3$	69.07±0.36	32.57±0.46	72.4±2.3	50.67	7.05	2.88
10^{-5} M $AlCl_3$	68.73±0.25	31.65±0.18	61.0±1.6	38.24	9.49	3.88
10^{-4} M $AlCl_3$	68.20±0.35	31.60±0.41	61.3±1.6	38.33	9.31	3.81
10^{-3} M $AlCl_3$	66.94±0.19	31.12±0.18	47.1±1.2	25.99	10.60	4.33
10^{-6} M CTAB	68.24±0.25	31.79±0.41	55.5±1.9	32.91	9.79	4.00
10^{-5} M CTAB	61.94±0.18	30.27±0.24	53.1 ±1.6	34.37	8.66	3.54
10^{-4} M CTAB	50.00±0.21	21.77±0.38	53.3±1.3	41.68	7.24	2.96
10^{-3} M CTAB	36.80±0.20	6.55±0.13	70.8±1.4	59.46	4.71	1.92
10^{-6} M SDS	72.44±0.10	34.81±0.18	44.2±0.7	19.63	11.30	4.62
10^{-5} M SDS	72.00±0.12	34.65±0.13	44.0±0.6	19.77	11.24	4.60
10^{-4} M SDS	71.85±0.26	31.74±0.12	51.0±0.7	26.34	10.41	4.26
10^{-3} M SDS	60.62±0.29	30.46±0.35	53.1±1.9	35.16	8.20	3.35
10^{-2} M SDS	37.96±0.08	6.11±0.15	42.8±0.6	43.71	6.95	2.84

[a] γ_{fw} is determined from Equation (4.26b) with the measured values of γ_{fv}, γ_{wv} and θ.

[b] A_{132} is determined from Equation (4.25) with all the measured values of the surface energies, γ_{ov}, γ_{wv}, γ_{ow}, γ_{fv} and γ_{fw}, and the chosen value of D_0=0.165 nm (Israelachvili, 1985).

[c] $A_d = \dfrac{A_{132}}{6kT}$ is referred to as the dimensionless adhesion number, where the Boltzmann constant k=1.381x10^{-23} J K^{-1} and T=295.15 K.

Table 4.9 Hamaker constants A_{owf} (or A_{132}) for the silicone oil droplet (phase 1, γ_{ov}=26.10±0.14 mJ/m^2) interacting with the FC725-precoated glass fiber (phase2, γ_{fv}=13.87±0.51 mJ/m^2) across aqueous solutions (medium 3 with varying surface tensions)

Aqueous Medium	γ_{wv} (mJ/m^2)	γ_{ow} (mJ/m^2)	θ (°)	γ_{fw} [a] (mJ/m^2)	A_{132} [b] (10^{-20} J)	A_d [c]
DIUF Water	72.66±0.31	35.31±0.44	115.6±0.9	45.27	2.18	0.89
pH=2.68	68.70±0.12	30.75±0.43	115.4±0.5	43.34	2.40	0.98
pH=3.52	70.76±0.10	32.84±0.52	115.3±1.2	44.11	2.17	0.89
pH=4.20	72.40±0.07	34.80±0.51	115.5±0.5	45.04	2.15	0.88
pH=6.50	72.66±0.31	35.31±0.44	115.6±0.9	45.27	2.18	0.89
pH=7.20	70.78±0.10	31.89±0.15	114.7±1.0	43.45	1.77	0.72
pH=8.93	70.43±0.22	30.84±0.15	113.3±0.4	41.73	1.11	0.45
pH=10.32	70.16±0.23	31.03±0.09	113.6±0.6	41.96	0.40	0.16
10^{-6} M NaCl	71.89±0.37	32.69±0.22	115.2±0.6	44.48	2.10	0.86
10^{-5} M NaCl	68.81±0.28	30.82±0.07	114.8±0.5	42.73	1.97	0.81
10^{-4} M NaCl	66.83±0.34	30.60±0.09	114.2±1.2	41.27	1.57	0.64
10^{-3} M NaCl	66.22±0.27	30.16±0.20	113.5±0.9	40.28	0.80	0.33
10^{-6} M $AlCl_3$	69.07±0.36	32.57±0.46	114.6±0.3	42.62	1.71	0.70
10^{-5} M $AlCl_3$	68.73±0.25	31.65±0.18	114.4±1.0	42.26	1.60	0.65
10^{-4} M $AlCl_3$	68.20±0.35	31.60±0.41	114.2±0.8	41.83	1.44	0.59
10^{-3} M $AlCl_3$	66.94±0.19	31.12±0.18	113.6±0.6	40.67	0.83	0.34
10^{-6} M CTAB	68.24±0.25	31.79±0.41	115.6±0.9	43.36	2.44	1.00
10^{-5} M CTAB	61.94±0.18	30.27±0.24	109.3±0.8	34.34	2.87	1.18
10^{-4} M CTAB	50.00±0.21	21.77±0.38	103.0±0.7	25.12	4.32	1.77
10^{-3} M CTAB	36.80±0.20	6.55±0.13	91.2±0.5	14.64	6.70	2.74
10^{-6} M SDS	72.44±0.10	34.81±0.18	115.8±0.8	45.17	2.22	0.91
10^{-5} M SDS	72.00±0.12	34.65±0.13	111.7±0.4	40.49	2.44	1.00
10^{-4} M SDS	71.85±0.26	31.74±0.12	111.5±1.1	40.20	3.34	1.14
10^{-3} M SDS	60.62±0.29	30.46±0.35	107.0±0.9	31.59	3.51	1.43
10^{-2} M SDS	37.96±0.08	6.11±0.15	93.6±0.9	16.25	6.50	2.66

[a] γ_{fw} is determined from Equation (4.26b) with the measured values of γ_{fv}, γ_{wv} and θ.

[b] A_{132} is determined from Equation (4.25) with all the measured values of the surface energies, γ_{ov}, γ_{wv}, γ_{ow}, γ_{fv} and γ_{fw}, and the chosen value of D_0=0.165 nm (Israelachvili, 1985).

[c] $A_d = \dfrac{A_{132}}{6kT}$ is referred to as the dimensionless adhesion number, where the Boltzmann constant k=1.381x10^{-23} J K^{-1} and T=295.15 K.

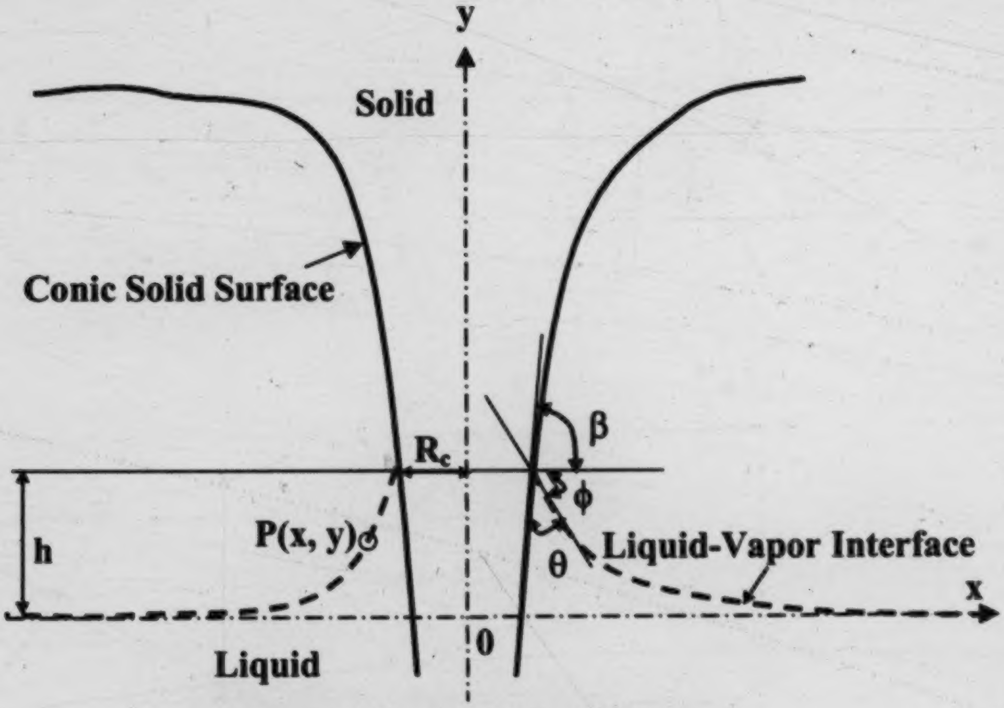
y
Solid
Conic Solid Surface
β
R_c
ϕ
h
P(x, y)
Liquid-Vapor Interface
θ
x
0
Liquid

Figure 4.1 Schematic diagram of the capillary rise profile around a conic cylinder for the ACRPAC case

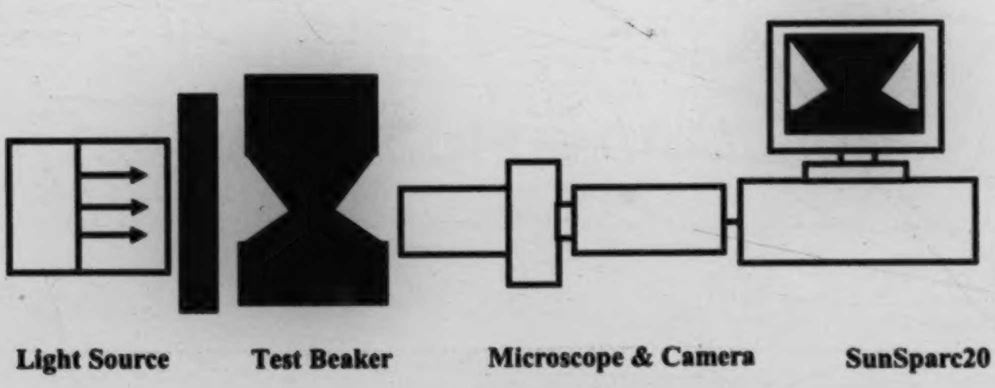
Light Source
Test Beaker
Microscope & Camera
SunSparc20

Figure 4.2 Experimental set-up used to measure the contact angle using the ACPAC technique for the ACRPAC case

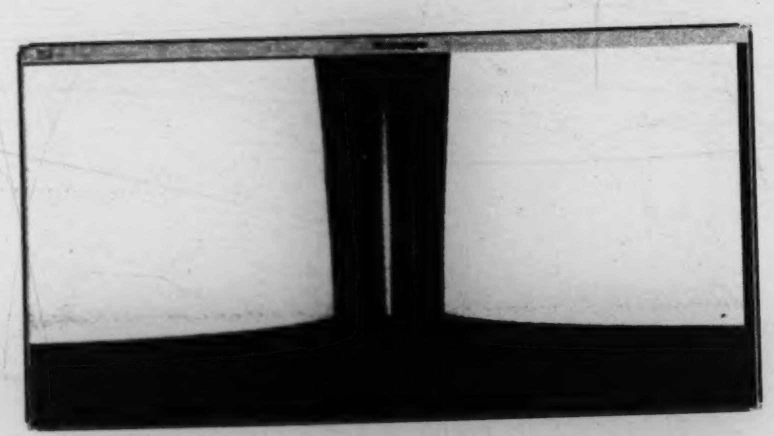

Figure 4.3a Digital image of the capillary rise profile of hexadecane around the FC725-precoated conical cylinder at its tip part (produced by a laser printer)

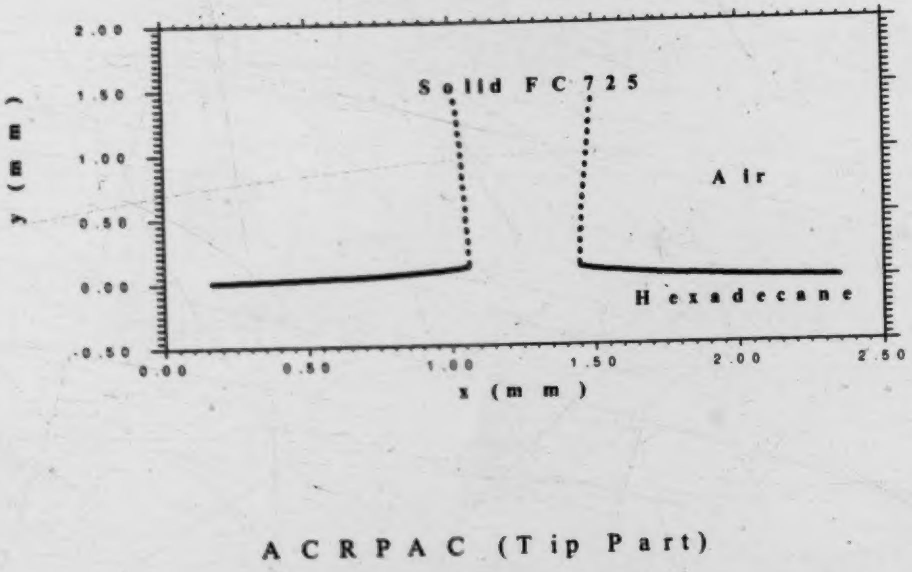

Figure 4.3b Digitized profile of the image shown in Figure 4.3a

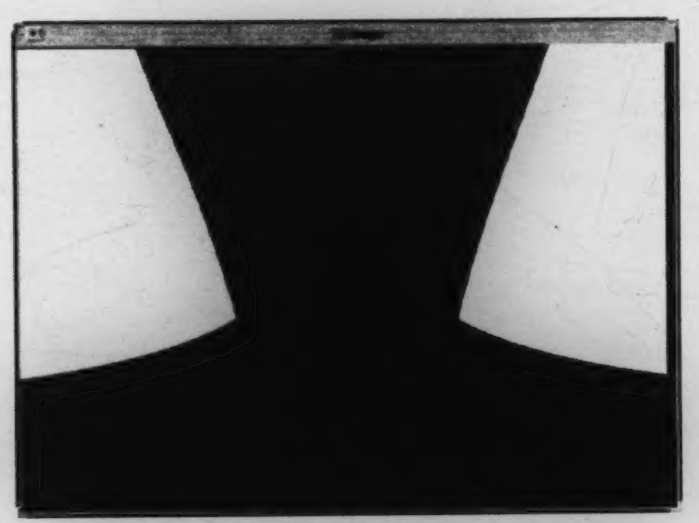

Figure 4.4a Digital image of the capillary rise profile of hexadecane around the FC725-precoated conical cylinder at its conic part (produced by a laser printer)

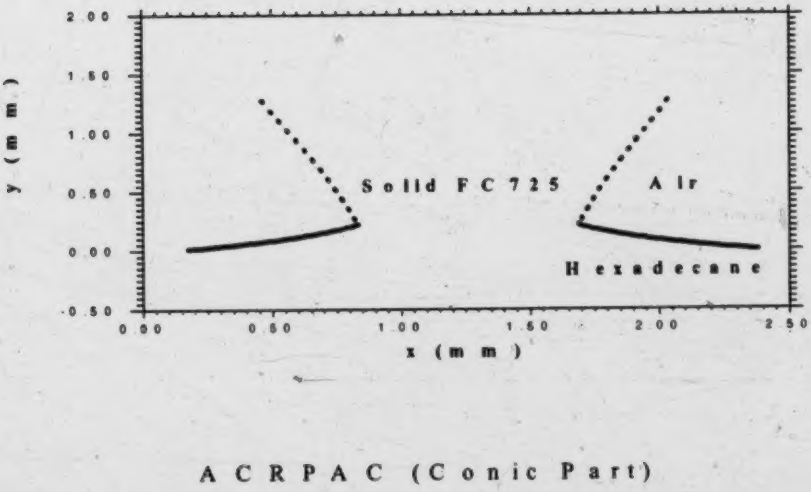

Figure 4.4b Digitized profile of the image shown in Figure 4.4a

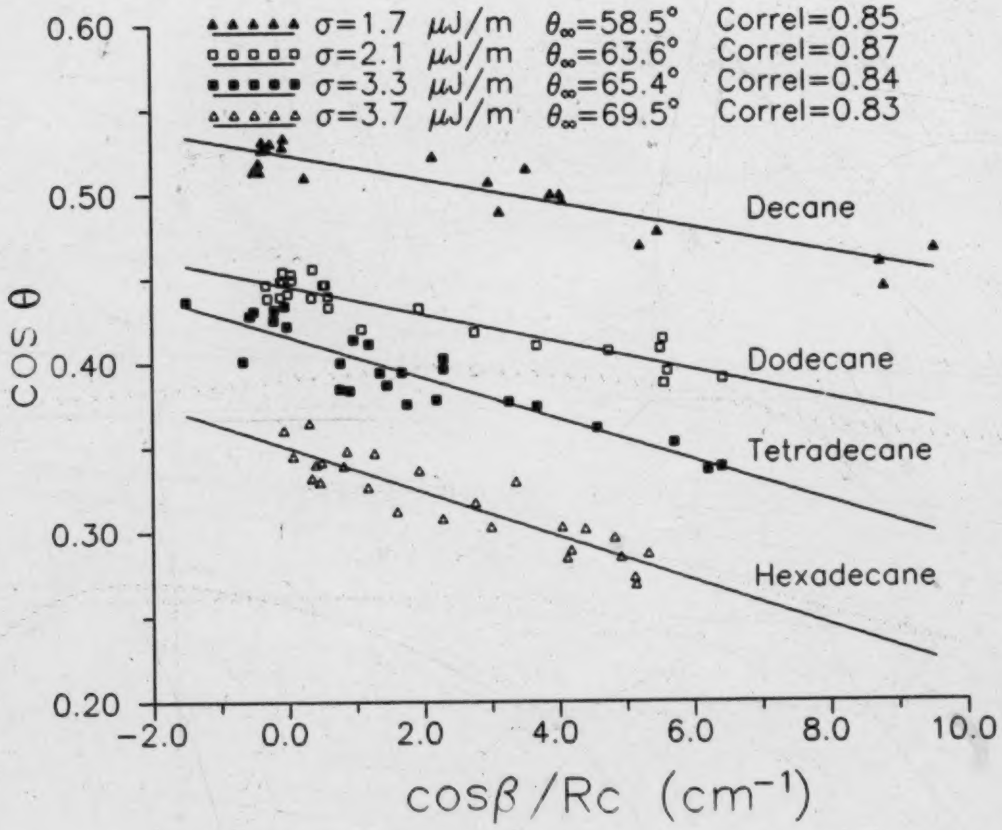

Figure 4.5 The line tension (σ) and contact angles (θ∞) derived from Equation (4.16) using the contact angles measured by the ACPAC technique for the ACRPAC case for the n-alkane liquids on the FC725-precoated conical glass cylinder

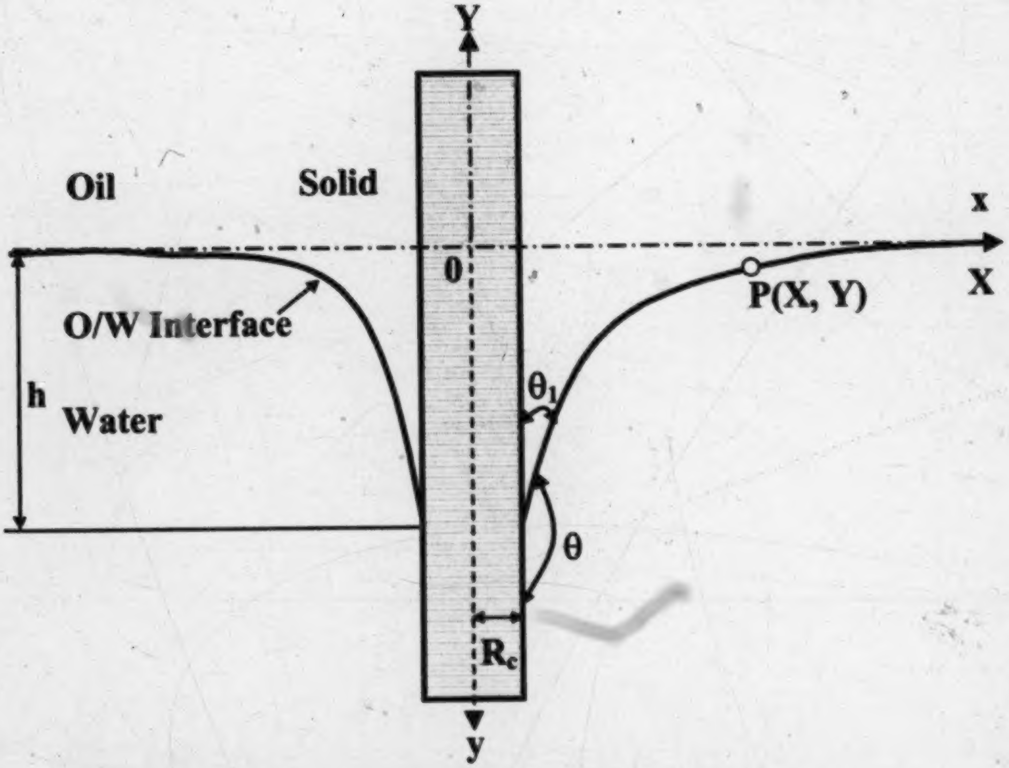
Y
Oil
Solid
x
0
X
P(X, Y)
O/W Interface
h
Water
θ1
θ
Rc
y

Figure 4.6 Schematic diagram of a capillary depression oil-water (O/W) interface around the FC725-precoated glass fiber

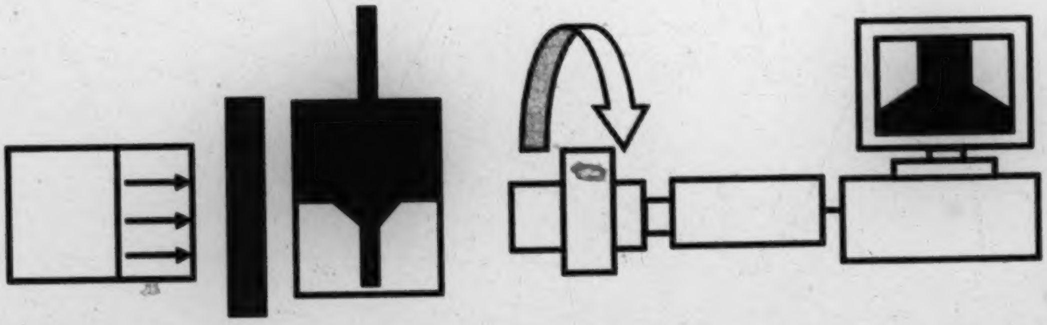
Light Source
Test Beaker
Microscope & Camera
SunSparc20

Figure 4.7 Experimental set-up for measuring the contact angle using the ACPAC technique for the ACDPAC case

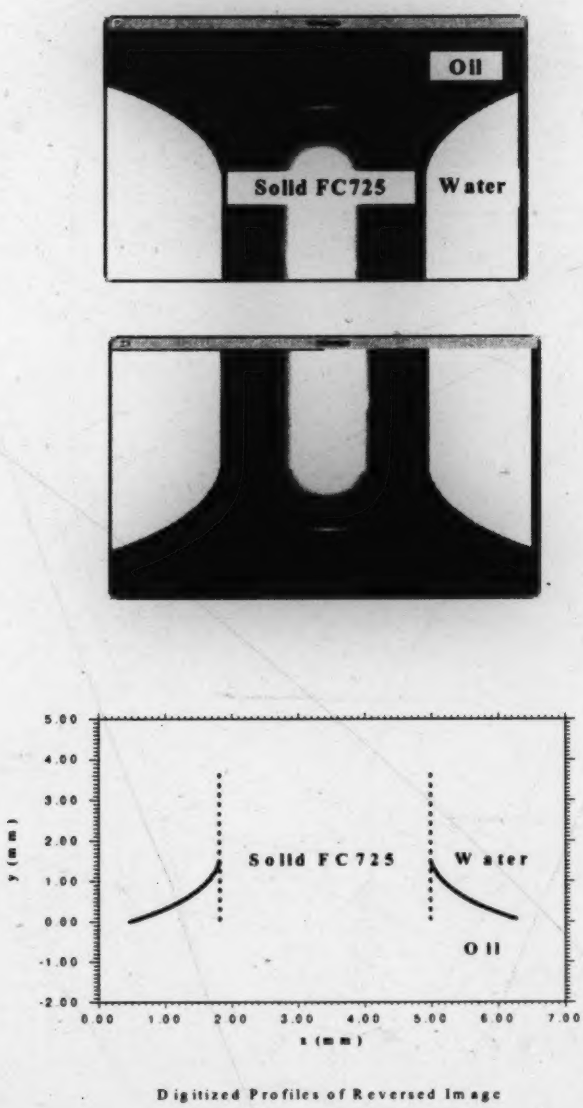

Figure 4.8a (top) Digital image of the capillary depression profile of the silicone oil (A-type) and the pure DIUF water interface around the FC725-precoated glass fibre (produced by a laser printer); Figure 4.8b (middle) Digital image of the capillary "rise" profile of the silicone oil (A-type) and the pure DIUF water interface around the FC725 coated glass fibre after the video camera was purposely set upside down (produced by a laser printer); Figure 4.8c (bottom) Digitization of the image showed in Figure 4.8b

Chapter 5

The ζ-Potential Measurements of Silicone Oil Droplets and Fiber Surfaces in Aqueous Solutions

This chapter will focus on measuring the ζ-potentials of silicone oil droplets and fiber surfaces, both of which are immersed in a variety of aqueous solutions. Specifically, from Sections 5.1 through 5.4, an electrical suspension method is developed to measure the ζ-potential of small liquid droplets dispersed in another immiscible liquid. It is then utilized to determine the ζ-potential of the silicone oil droplets dispersed in various aqueous solutions. Sections 5.5 through 5.8 will deal with the ζ-potential measurements of fiber surfaces in contact with the same kinds of aqueous phases. The conventional streaming potential technique is used but more attention is focused on understanding and evaluating the solid surface conductance phenomenon and ultimately correcting its effect on the measured ζ-potential. Using the experimental technique, the ζ-potential values of two kinds of fiber surfaces are measured when each is in contact with different aqueous solutions. After the ζ-potentials of both silicone oil droplets and fiber surfaces in various aqueous solutions are determined experimentally, three important parameters can be calculated, which are used to characterize the EDL interaction between the silicone oil droplets and the fiber surfaces across the aqueous media (see Section 5.9).

5.1 The ζ-Potential Measurements of Silicone Oil Droplets Dispersed in Aqueous Solutions

When it is dispersed in an immiscible aqueous solution, a small oil droplet may be charged and surrounded by the ions of the opposite sign from the solution. The arrangement of the electric charge on the oil droplet, together with the balancing charge in the solution, is called the electrical double layer (EDL) of the droplet (Hunter, 1981; Adamson, 1982). The electric charge residing at the liquid-liquid interface is of great importance in many colloidal and interfacial phenomena, such as in the studies of interactions between various colloidal droplets and solid substrates, i.e. deposition phenomena (Adamczyk and van de Ven, 1981b;

Adamczyk et al., 1983; Alince, 1989; Alince et al., 1991; Alince and van de Ven, 1993, Jachowicz and Berthiaume, 1989; Berthiaume and Jachowicz, 1991), and the interactions between the droplets themselves, i.e. liquid droplet coalescence (Okada and Akagi, 1987; Deshiikan and Papadopoulos, 1995a; 1995b; Sanders et al., 1995). The electric charges on liquid droplets are directly related to a variety of emulsification, demulsification and micelle formation processes.

The oil-in-water (O/W) emulsions are encountered in various industrial applications and commercial products. The electrokinetic properties, especially the electrokinetic or zeta potential, of the oil droplets dispersed in various aqueous solutions are of fundamental importance in colloid and interface sciences. The determination of the ζ-potential has been a traditional tool for characterizing the surface properties and stability of the colloidal systems (Hunter, 1981; Jachowicz and Berthiaume, 1989). The ζ-potential of oil droplets dispersed in different aqueous phases is an important quantity in a number of technological processes, such as emulsion flotation, oil agglomeration, emulsification and micelle formation, demulsification, as well as removal of the dispersed contaminants such as oils from waste waters. In the past, there have been some attempts to determine the ζ-potential of oil droplets dispersed in aqueous phases. Among the existing methods, the electrophoresis (and microelectrophoresis) technique is probably the most widely used method for colloidal emulsions and suspensions. Specifically, the electrophoresis technique was successfully used to measure the ζ-potential of some oil droplets dispersed in different aqueous solutions (Jachowicz and Berthiaume, 1989; Sanders et al., 1995; Deshiikan and Papadopoulos, 1995a; 1995b; Stachurski and Michalek, 1996), or in several ionic surfactant solutions (Bethiaume and Jachowicz, 1991; Stalidis et al., 1990; Avranas and Stalidis, 1991). In particular, it was shown (Bethiaume and Jachowicz, 1991; Stalidis et al., 1990; Avranas and Stalidis, 1991) that the electrical characteristics on the emulsion droplets can be easily modified by adsorbing surfactant onto the liquid-liquid interfaces and thus related to the surfactant adsorption process. Measurements of the ζ-potential or the electric charge on the liquid droplets dispersed in ionic surfactant solutions are of practical importance because the ionic surfactants are extensively used in many industrial processes and commercial products. Moreover, the adsorption phenomena of cationic and anionic surfactants onto emulsion droplets are of special interest because these two surface-active agents are basically different from each other with regard to their ionic features.

Basically, using the electrophoresis technique, the ζ-potential of the O/W emulsion droplets is determined by measuring the electrophoretic mobility of the oil droplets under an externally applied static electric field according to the Helmholtz-Smoluchowski equation for spherical droplets (Hunter, 1981). Since the electrophoresis technique is widely used and well documented in the literature (Hunter, 1981), its principle and technical details will not be reiterated in this thesis. Several commercial electrophoresis apparatuses are widely used, such as Rank Brothers (Sanders et al., 1995), Malvern Zetasizer (Sanders et al., 1995) and Pen Ken Laser Zee Meter (Jachowicz and Berthiaume, 1989; Berthiaume and Jachowicz, 1991). However, some electrophorometers are too expensive and their maintenance and operation are a difficult task in some cases. In addition, the electrophoresis technique requires a complicated procedure to measure the electrophoretic mobilities only at the so-called "stationary levels" (Hunter, 1981; Stalidis et al., 1990; Avranas and Stalidis, 1991). Furthermore, this technique is also restricted in its applicability by the special requirements of the dilution of the colloids, the optical properties and size range of the colloidal particles.

The objective of the present work is to devise a novel and simple experimental method to directly measure the ζ-potential of liquid droplets dispersed in another immiscible liquid. This method is then used to study the effects of varying pH value and the valence and the concentration of electrolytes on the measured ζ-potential of the silicone oil droplets dispersed in a variety of aqueous solutions (Gu and Li, 1997b; 1998c). Using this new experimental technique, the contribution of the ionic surfactants to the measured ζ-potential is also investigated (Gu and Li, 1998c; 1998d). These factors are anticipated to influence not only the magnitude but also the polarity of the ζ-potential.

5.2 Electrical Suspension Method

5.2.1 Principle

When an oil phase with a density greater than the continuous phase is dispersed in an aqueous solution, the oil droplets will move downward. The small oil droplets will soon reach the so-called terminal velocities if only the gravity force, the buoyancy force, and the viscous drag force act on them. However, it has been observed in numerous experiments for a long time that such dispersed oil droplets may be charged and thus surrounded by the ions of opposite sign from the aqueous solution. The arrangement of the electric charge on the oil droplet together with the balancing charge in the continuous phase is often referred to as the electrical double layer (EDL). Because of the presence of the EDL around an oil droplet, the above forces may be balanced by applying an electrical force on the oil droplet. This electrical force can be produced by an externally imposed electric field. Thus the motion of the oil droplet may be stopped with the droplet ultimately suspended in the aqueous phase. The ζ-potential of the oil droplet can be determined by using such an electrical suspension method since the electrical force is directly related to the ζ-potential.

An oil droplet moving at its terminal velocity in an aqueous solution can be gradually slowed down and eventually kept stationary by applying a suitable electric field. The polarity and the strength of the electric field depend on the polarity and the magnitude, respectively, of the ζ-potential of the oil droplet. While the oil droplet is held in such a stationary state, the viscous drag force vanishes and all the remaining forces acting on it must be balanced, i.e.

$$F_g - F_b = F_e \tag{5.1}$$

where, $F_g = \frac{4}{3}\pi a^3 \rho_o g$ is the gravitational force and $F_b = \frac{4}{3}\pi a^3 \rho_w g$ is the buoyancy force, since the small stationary oil droplet can be justifiably assumed to be spherical (Panton, 1984), a is the radius of the oil droplet, ρ_o is the density of the oil phase and ρ_w is the density of the aqueous phase, and g is the gravitational acceleration. F_e is the electrical force on the oil droplet produced by the externally applied electric field, which can be related to the to-be-determined ζ-potential as follows (Babchin et al., 1989; Sawatzky and Babchin, 1993):

$$F_e = 4\pi a \varepsilon_r \varepsilon_0 \zeta E f_1(\kappa a) \tag{5.2}$$

where, ε_r is the relative dielectric permittivity or the dimensionless dielectric constant of the aqueous solution and ε_0 is the dielectric permittivity of free space, ζ is the zeta or electrokinetic potential. In Equation (5.2), $E=\Delta V_0/l$ is the static uniform electric field strength, and here ΔV_0 is the electrical voltage applied across two electrodes and l is separation distance between the electrodes. As defined in Equation (3.32), κ is the Debye-

Hückel constant, which characterizes the extent of the EDL and mainly depends on the ionic properties of the aqueous phase. The reciprocal of this constant, κ^{-1}, represents the EDL thickness. The function $f_1(\kappa a)$ required in the above equation is the well-known Henry function or the Henry correction factor. It takes account of the well-known electrophoretic retardation effect and typical values of the Henry function of $f_1(\kappa a)$ as a function of κa can be found in the literature (Hunter, 1981), which are listed in Table 5.1 for quick reference. By substituting F_g and F_b as well as F_e in Equation (5.2) into Equation (5.1), the ζ-potential can be expressed as

$$\zeta = \frac{a^2 \Delta\rho g}{3\varepsilon_r \varepsilon_0 (\Delta V_0 / l) f_1(\kappa a)} \tag{5.3}$$

where, $\Delta\rho=\rho_o-\rho_w$, the density difference between the oil and the aqueous phases. In this study, the average size of dispersed oil droplets is about a=10 μm, i.e. $\kappa a \gg 1$. Since the EDL is much thinner than the size of the oil droplets (Hunter, 1981), i.e. $\kappa a \sim \infty$, the Henry function $f_1(\kappa a)$ approaches $\frac{3}{2}$ (see Table 5.1). In this case, an approximation expression of the ζ-potential can be obtained by replacing the Henry function $f_1(\kappa a)$ in Equation (5.3) with $\frac{3}{2}$:

$$\zeta = \frac{2a^2 \Delta\rho g}{9\varepsilon_r \varepsilon_0 (\Delta V_0 / l)} \tag{5.4}$$

It should be noted at this point that Equation (5.4) is valid for almost all the aqueous solutions tested in this work, except for the pure DIUF water. When the pure water is used as a dispersing medium, the thickness of the EDL, κ^{-1}, may be as large as approximately 1.0 μm at 25°C (Hunter, 1981; also see Table 5.3 or 5.4). Accordingly, values of κa range approximately from 10 to 20 as the sizes (radius a) of oil droplets changes from 10 to 20 μm. In this case, Table 5.1 should be referred to find a value of the Henry function of $f_1(\kappa a)$ for each oil droplet, i.e. each κa where $\kappa^{-1} \approx 1.0$ μm. Thus Equation (5.3) should be used to determine the ζ-potential of the silicone oil droplets dispersed in the pure water.

To calculate the ζ-potential from either Equation (5.3) for any value of κa or Equation (5.4) for the case of $\kappa a \gg 1$, only the values of *a* and ΔV_0 for each oil droplet have to be measured directly and individually since the other parameters in the equations are known. Therefore, in practice, it is much easier to implement the electrical suspension method. Nevertheless, prior to proceeding to the thorough descriptions of the experimental conditions and the detailed discussion on the experimental results, it is essential at this point to carefully examine several well-known effects that may be involved in this experimental study. Some precautions have to be taken in order to minimize or, ideally, to eliminate their possible influence on the measured results of ζ-potential. Several relevant effects will be addressed in detail in the following paragraphs.

5.2.2 Electroosmotic Effects

The electroosmotic effect has long been recognized and extensively discussed by a number of researchers (Hunter, 1981; Graciaa et al., 1995; Sirois and Millar, 1973; Collins et al., 1978; Okada and Akagi, 1987). There might be two kinds of the electroosmotic flows involved in the present electrical suspension method, one is at the walls of glass cell in which the O/W emulsion is held and the other is around each O/W emulsion droplet.

Physically, the origin of the electroosmotic flux is due to the surface charge at any glass fiber-water interface and the EDL in the aqueous phase immediately adjacent to the interface. The electroosmosis occurs near the walls of glass beaker whenever an electric field is applied. It has been reported that the electroosmotic effect may have substantial influence on the ζ-potential of air bubbles obtained from the electrophoretic mobility measurements. For example, some authors even showed that failure to take account of the effect could affect not only the magnitude, but also the polarity of the ζ-potential of air bubbles inferred from the measurements of the spinning tube electrophorometer (Bach and Gilman, 1938; Gilman and Bach, 1938). Nevertheless, the electroosmosis has not been addressed in most electrophoretic mobility measurements of the O/W emulsion droplets. This is probably because the O/W emulsion droplets have much greater inertia than the air bubbles and thus the electroosmotic effect on their motions is not appreciable.

Technically, the electroosmotic flux may be minimized or eliminated either by neutralizing the surface charge of the test cell or by creating a highly viscous layer that impedes the aqueous motion in the region near the cell walls. For instance, coating an appropriate polymeric material on the solid surface has been proven to be a promising approach as described by Graciaa et al. (1995). In the experiment, measuring the electrophoretic mobility only at the so-called "stationary levels", i.e. there is no bulk flow at these positions, is another widely used effective method to get rid of the effect (Hunter, 1981). Recently, this method has been successfully employed to measure the electrophoretic mobility of both hydrocarbon oil droplets and small air bubbles (Stalidis et al., 1990; Avranas and Stalidis, 1991; Collins et al., 1978; Okada and Akagi, 1987; Bowen, 1981). For a narrow rectangular capillary of the size from 10 to 1000 μm, the stationary levels occur at (Hunter, 1981):

$$z = \pm \frac{W/2}{\sqrt{3}} \tag{5.5}$$

where, z is the distance from the symmetric centre in width direction and W is the width of the rectangular cell. Consequently, the influence of the electroosmotic flux at the stationary levels can be avoided. In this study, a wide rectangular glass cell was made intentionally not only for optical consideration but also for considerable reduction of the possible electroosmotic effect. The results of this work did not show any significant variation as long as the observation of the oil droplet was made in the range from z=-W/4 to z=+W/4. The rectangular cell used in this work is so wide (W=30 *mm*) that only in the thin boundary layers near the cell walls might the electroosmotic effect become relatively appreciable (Doren et al., 1989). In addition, there are some practical measures to prevent the occurrence of the fully developed strong electroosmosis, for instance, by reasonably reducing the strength and the duration of the applied electric field and/or limiting the ionic concentration and/or narrowing down the separation distance between the two electrodes.

On the other hand, it has been realized that the ions constituting the EDL around a charged oil droplet will move under the influence of an externally applied electric filed, even when the droplet itself is in a stationary state. There is an electroosmotic flow in the vicinity of the oil droplet. Such flow will exert a viscous drag force on the stationary droplet and thus affect its force balance condition represented by Equation (5.1). Its effect can be estimated by comparing the viscous drag force, $F_d=6\pi a\mu_w v_{eo}$, with the total body force expressed in Equation (5.1), F_g-F_b:

$$\frac{F_d}{F_g - F_b} = \frac{6\pi a \mu_w v_{eo}}{\frac{4}{3}\pi a^3 \Delta\rho g} \tag{5.6}$$

where, μ_w is the viscosity of the aqueous solution and v_{eo} is the electroosmotic velocity around the oil droplet. v_{eo} can be calculated from the well-known Smoluchowski equation for the electrophoretic mobility (Hunter, 1981),

$$\frac{v_{eo}}{E_w} = \frac{\varepsilon_r \varepsilon_o \zeta}{\mu_w} \tag{5.7}$$

Here, $E_w = \dfrac{\Delta V_0}{l\varepsilon_r}$. Substituting Equation (5.7) into Equation (5.6) and rewriting it yields:

$$\frac{F_d}{F_g - F_b} = \frac{9\varepsilon_0 \zeta E}{2a^2 \Delta\rho g} \tag{5.8}$$

In the measurements, the typical values are $E=\Delta V_0/l \leq 1000$ V/m for the applied electric field, and $a \approx 10$ μm for the droplet radius. If the (maximum) ζ-potential of the oil droplets is assumed to be about ±100 mV, Equation (5.8) indicates that the largest influence of the electroosmotic flow on the force balance of the stationary droplet is less than 8%. As will be shown later on, this error is well within the overall measurement error (15%) of the ζ-potential determined from either Equation (5.3) or Equation (5.4).

5.2.3 Thermally Driven Convection Effect

Another potential problem arises from thermally driven convection current inside the test cell (Graciaa et al., 1995; Sirois and Millar, 1973; Collins, et al., 1978; Okada and Akagi, 1987). Because only a weak illuminating beam is required for the present apparatus, the heat transfer from the light source was sufficiently blocked by using an infrared filter before the light enters the cell. On the other hand, more attention was focused on effectively controlling the primary Ohmic heating due to the applied electric field between the two electrodes. The temperature increase caused by the Ohmic heating is evaluated as follows.

Considering the aqueous solution between the two parallel electrodes inside the test cell and neglecting the oil phase since its concentration is only 0.25% (v/v) in the experiments, the resistance of the aqueous phase, R, can be determined from the following equation:

$$R = \frac{1}{\sigma}\frac{l}{A} \tag{5.9}$$

where, A is the cross-sectional area of the two electrodes; l is their separation distance and σ is the conductivity of the aqueous phase, which is measured in siemens (Ω^{-1} m^{-1} or S/m). The conductivity, the reciprocal of resistivity, is a bulk property of the aqueous phase mainly depending on the concentration and the valence of the electrolyte used. For a given electrolyte at a specified concentration, the conductivity can be related to the equivalent or molar conductivity, λ, measured in m^2 S/mole:

$$\sigma = 1000c\lambda \tag{5.10}$$

where, c is the mole concentration of the electrolyte in mole l^{-1} or M and λ can be easily found in some handbooks (Weast et al., 1989). The Ohmic heating per unit time, Q (J/s), generated by the applied potential voltage, ΔV_0, across the two electrodes, is equal to:

$$Q = \frac{(\Delta V_0)^2}{R} \tag{5.11}$$

When Equations (5.9) and (5.10) are substituted into Equation (5.11), it becomes

$$Q = 1000\,E^2\,c\,\lambda A l \tag{5.12}$$

where, $E=\Delta V_0/l$ is the electric field. If the electric field is imposed for Δt seconds and the heat dissipation through the walls of the test cell is neglected, then the energy balance equation for the aqueous phase between the two electrodes can be written as

$$Q\Delta t = 4186.8\Delta T\, C_v\, \rho_w\, A l \tag{5.13}$$

where, ΔT (^{o}C) is the temperature increase of the aqueous solution; C_v (kcal/kg/^{o}C) is its specific heat capacity and 4186.8 is the conversion factor between kcal and Joule. Bringing Equation (5.12) into Equation (5.13) and rewriting it yields

$$\Delta T = \frac{E^2\sigma\Delta t}{4186.8\,C_v\rho_w} = \frac{E^2 c\lambda\Delta t}{4.1868\,C_v\rho_w} \tag{5.14}$$

Equation (5.14) shows that the temperature increase is proportional to the concentration of the electrolyte in the aqueous solution if the other parameters are held constant.

By choosing the following approximate values for the other parameters in Equation (5.14), E=1000 V/m, Δt=10 s, and C_v=1.0 kcal/kg/^{o}C and ρ_w=998 kg/m^3 for the DIUF water, the variations of the temperature increase are then estimated with the concentration of electrolyte NaCl from 10^{-6} to 10^{-1} M and listed in Table 5.2. It can be concluded from the preliminary calculations that the Ohmic heating and consequently produced thermal convection are negligible in this study, provided that the concentration of the electrolyte added to the aqueous emulsion is kept below some critical upper level, for example, 10^{-3} M for NaCl. Hence, no higher ionic concentrations of any electrolyte than 10^{-3} M were tested in this study.

5.2.4 Electrode Polarization Effect

The effect of electrode polarization was also considered. It can alter the applied electric field to some extent after many ions accumulate on the corresponding electrode of opposite polarity. In order to minimize the electrode polarization influence, it has been recommended to reverse the current flow by switching the polarity of the electric field after each measurement (Hunter, 1981; Stalidis et al., 1990; Avranas and Stalidis, 1991). This procedure was followed in the present work.

5.2.5 Overall Measurement Error Analysis

An error analysis of the ζ-potential measured by the electrical suspension method is given as bellow. Equation (5.3) or Equation (5.4) for determining the ζ-potential can be simply written as

$$\zeta = C\frac{a^2 l}{\Delta V_0} \tag{5.15}$$

where, $C = \frac{\Delta\rho g}{3\varepsilon_r\varepsilon_0 f_1(\kappa a)}$ for Equation (5.3) and $C = \frac{2\Delta\rho g}{9\varepsilon_r\varepsilon_0}$ for Equation (5.4), which can be assumed to be constant in experiment. Taking the logarithmic operation on Equation (5.15) and then differentiating the resultant equation yields

$$\frac{d\zeta}{\zeta} = 2\frac{da}{a} + \frac{dl}{l} - \frac{d(\Delta V_0)}{\Delta V_0} \tag{5.16}$$

From the above relation, the overall error of the present measurements can be expressed as

$$\frac{d\zeta}{\zeta} = \sqrt{[2\frac{da}{a}]^2 + [\frac{dl}{l}]^2 + [\frac{d(\Delta V_0)}{\Delta V_0}]^2} \tag{5.17}$$

As will be discussed in the experimental part, the overall accuracy of determining the oil droplet size (a=10~20 μm) with the present optical system is around da=0.5 μm and the separation distance between the two parallel electrode plates was always set at l=10.0 *mm* with a resolution of dl=0.1 *mm*. In addition, the practical error of the applied voltage across the two electrodes, ΔV_0, was estimated to be $d(\Delta V_0)$=0.1 V, though it could be read to 0.01 V. Choosing typical values as a=10.0 μm and ΔV_0=5.0 V and bringing all the above values into Equation (5.17), the relative error of the measured ζ-potential can be approximated as

$$\frac{d\zeta}{\zeta} \approx 10\% \qquad (5.18)$$

Therefore, using the present experimental technique and apparatus, the overall error of the ζ-potential determined from either Equation (5.3) or Equation (5.4) with the measured a, l and ΔV_0, is less than 15%, an acceptable error for the ζ-potential measurements.

In summary, all the above mentioned effects can be minimized by properly reducing the strength and the duration of the applied electric field and/or limiting the ionic concentration of the aqueous solutions. It should be pointed out that there are some practical limitations in applying the electrical suspension method to measure the ζ-potential of oil droplets. First, in order to reduce the three effects, especially the thermally driven convection inside the test cell, only those more strongly charged smaller oil droplets with less density difference from the aqueous phase can be studied by this method. They can be more readily stopped and suspended in the aqueous solution by applying a lower electric field in a shorter period. On the other hand, the oil droplets should be relatively large in order to measure their sizes accurately using the present optical system. Consequently, the oil droplet sizes should be within an appropriate range. In this study, the oil droplets whose sizes range approximately from 10 to 20 μm in radius are examined. This is not a concern in this work because the measured ζ-potentials of the oil droplets did not show observable size dependence. Secondly, the ionic concentration of the aqueous solutions should be limited to below certain upper level for the same reason. Hence, in these tests, no electrolyte concentration higher than 10^{-3} M or surfactant concentration higher than its critical micelle concentration (CMC) was tested.

5.3 Experimental Aspects of the ζ-Potential Measurements of Silicone Oil Droplets Dispersed in Aqueous Solutions

5.3.1 Apparatus

A schematic diagram of the experimental apparatus is shown in Figure 5.1. In the set-up, a rectangular glass test beaker is placed between a light source and a microscope. The light source and the microscope system mounted with the video camera are same as those described in details in Section 4.3. The internal dimensions of the rectangular glass test cell are 50(L)x30(W)x80(H) *mm*, which can hold about 100 *ml* solution. Inside the cell, two copper electrode plates were aligned horizontally and their separation distance was set at 10.00 *mm* for all the experiments. These two electrodes were connected to a DC constant-voltage power supply (Harrison 6209B, Hewlett-Packard) to apply an external electric field on the oil droplets between them. A polarity switch was also added to the circuit for alternating the polarity of the electric field promptly. The applied voltage between the two electrodes was displayed on a digital multimeter.

5.3.2 Preparation of the Silicone Oil-in-Water Emulsions

Silicone oil No. 1 with density of ρ_o=1050 kg/m^3 and viscosity of μ_o=172.7 mPa s (Aldrich Chemical Co.) was chosen as the dispersed oil phase in making all the O/W emulsions. Its small density difference from the aqueous phase makes it particularly suitable for this experimental study. The pure DIUF water (ρ_w=998 kg/m^3) has an initial conductivity of 1.21x10^{-4} S/m and an equilibrium pH of about 6.5.

The four kinds of aqueous phases used in this study are the same as those tested for determining the Hamaker constants (Tables 4.8 and 4.9): the pure DIUF water (Fisher Scientific, Canada); the aqueous phases with different pH values; the electrolyte solutions containing either NaCl or $AlCl_3$ and the ionic surfactant solutions containing either CTAB or SDS. The pH value of the DIUF water phase was adjusted to a desired value by adding either NaOH or HCl into the pure DIUF water. The electrolyte solutions were prepared by adding either NaCl or $AlCl_3$ at a different concentration (from 10^{-6} M to 10^{-3} M) each time into the pure DIUF water. Two typical ionic surfactants were used to make surfactant solutions: the cationic surfactant cetyltrimethylammonium bromide (CTAB) and the anionic surfactant sodium dodecyl sulphate (SDS). Their critical micelle concentrations (CMC) in water determined from their surface tension-concentration curves were reported to be about $9.2\text{x}10^{-4}$ M for CTAB (Czerniawski, 1966) and $8.1\text{x}10^{-3}$ M for SDS at 25°C (Stalidis et al., 1990). The ionic surfactant solutions were prepared by adding one of the two ionic surfactants at a different concentration (from 10^{-6} M to 10^{-3} M for CTAB or from 10^{-6} M to 10^{-2} M for SDS) each time into the pure DIUF water. Usually a period of more than 12 h was given for these chemicals to be completely dissociated and uniformly distributed in the aqueous phase.

After each aqueous solution was prepared, the general procedure for making each silicone O/W emulsion is as follows. All the silicone O/W emulsions were made by suspending 0.25% (v/v) silicone oil in the aqueous solutions. A sample of 0.5 *ml* silicone oil was added into a beaker with 200 *ml* prepared aqueous solution while a stirrer (Caframo RZR1, Canada) was stirring. The silicone oil was dispersed and then gradually the O/W emulsion was formed. Stirring was continued for 20 min after addition of the silicone oil. The O/W emulsion was aged for at least 2 h so that the possible selective adsorption of the dissociated ions in the aqueous solution onto the oil-water interfaces could reach an equilibrium state, as has been indicated by other researchers (Shinoda et al., 1963; Ives, 1984; Saulnier et al., 1996). It is this type of selective ionic adsorption that was believed to cause the gathering of the excessive electric charge on the oil droplets dispersed in the aqueous solutions (Stachurski and Michalek, 1996). The strength of such excessive electric charge can be represented by the ζ-potential. No noticeable changes in the measured ζ-potentials were observed for a longer ageing. Finally, the aged O/W emulsion was gently poured into the test cell for the ζ-potential measurements. Generally, the silicone O/W emulsion in the cell was unstable and the emulsion droplets sank down slowly.

5.3.3 Experimental Procedure

With the experimental apparatus as illustrated in Figure 5.1, the experiment for each kind of the O/W emulsion was carefully conducted according to the following procedure. First, the rectangular test cell was positioned vertically. The lower electrode plate was placed horizontally on an insulated supporting stage. After the cell was filled with approximate 100 *ml* O/W emulsion and placed between the light source and the microscope, the position of the upper electrode was adjusted. The upper electrode plate was mounted on a translation stage, which could be moved vertically with a resolution of 0.1 *mm*. The separation distance between the two parallel electrodes was adjusted to and fixed at 10.0 *mm* at all times. The two electrodes were connected to a circuit that consists of a power supply, a polarity switch and a digital voltage meter. A certain period was allowed for the oil droplets between the two electrodes to move at their terminal velocities before the actual observation began. Using the set-up, motions of oil droplets can be observed *in situ*.

The microscope and camera were focused on a vertical plane near the symmetric centre of the cell and the computer imaging system was prepared to display and capture the digital images of oil droplets. For an arbitrarily chosen oil droplet moving at its terminal velocity, it was gradually slowed down and finally completely stopped by imposing a suitable electric field. Once the oil droplet was maintained in the stationary state and its image was focused, the instantaneous digital image was acquired and stored automatically in the computer memory. Meanwhile, the digital reading of the applied voltage, ΔV_0, across the two parallel electrodes was recorded. The practical error of the applied voltage was approximated 0.10 V, though it could be read to 0.01 V. The process from initially applying the electric field and adjusting the voltage to completely stopping the droplet usually took less than 10 s. The power supply was turned off immediately after each observation. It was then turned on but with the opposite polarity for 5-10 s to minimize the electrode polarization and turned off again. For each experiment, the above procedure was repeated for other nine oil droplets dispersed in the same aqueous solution. The entire experimental set-up was placed on a vibration-free table and all the measurements were carried out at 22°C.

The stored droplet images can be processed and analyzed later on to determine the sizes of the droplets. The basic aspects of the digital image acquisition process and more experimental details about the computer digital image techniques can be found in Section 4.3 and in the papers published by Neumann and co-workers (Rotenberg et al., 1983; Cheng et al., 1990; Li et al., 1992). For each digital droplet image, a standard grid image was used to calibrate the image and correct possible optical distortion. A special computer digital image processing and analysis program was then executed to digitize the droplet image. The output of the program are two sets of discrete coordinates, *x* and *y* in mm, of the perimeter of the oil droplet. The overall accuracy of the digitized perimeter is around 0.5 μm, at 40x magnification with an additional magnifying phototube. The mean value of the droplet radius, *a*, is determined from the digitized peripheral coordinates. Thus, choosing l=10.0 *mm*, a=10.0 μm and ΔV_0=5.0 V and using their corresponding uncertainties, the overall measurement error of the ζ-potential was estimated to be less than 15% using Equation (5.17).

5.4 Experimental Results and Discussion

During emulsification of the oil phase in an aqueous phase, the silicone oil (No. 1) droplets acquired their electrostatic charges through an emulsification process. During the process, the silicone oil was stirred, broken up into droplets and ultimately dispersed in an aqueous solution. The distribution of the electric charge on an oil droplet together with the balancing charge in the adjacent continuous phase forms the electrical double layer (EDL), which can be best characterized by its thickness, κ^{-1}, and its strength, the ζ-potential. The measured ζ-potential strongly depends on the ionic properties of the aqueous solutions.

In general, several charging mechanisms are responsible for the charge of the oil droplets in the O/W emulsions (Gu and Li, 1997b). Thus the ζ-potential of each oil droplet may also depend on the actual process in which the droplet is formed. But the mean value of the measured ζ-potentials over multiple droplets dispersed in the same aqueous solution should be correlated to the oil and the aqueous properties of the O/W emulsion, provided that the proposed electrical suspension method functions properly. Therefore, only the mean value of the ζ-potential calculated by averaging over ten observed oil droplets dispersed in the same aqueous solution will be mentioned hereafter.

In this paper, silicone oil No. 1 was used as the oil phase for making all the O/W emulsions. All the aqueous solutions were prepared from the pure DIUF water. The ionic properties of the aqueous phase were changed by varying its pH value, the valence and the concentration of electrolyte, as well as the ionic feature and the concentration of ionic surfactant, respectively. The sizes of the observed silicone oil droplets were approximately 10-20 μm in radius. Usually, the applied voltages were approximately 5 V, i.e., $E \approx 500$ V/m, depending on the ζ-potential and the size of the oil droplets under observation.

Nevertheless, there was no observable dependence of the measured ζ-potential values on the droplet sizes. The mean ζ-potential of the silicone oil droplets dispersed in the pure DIUF water was also measured and used as a reference value. The detailed effects of the pH values, the two typical electrolytes and the two ionic surfactants on the measured ζ-potential of the O/W emulsion droplets will be discussed in the following sections.

5.4.1 pH Effect

The pH value was altered from 3.0 to 10.0 by adding standard dilute solutions of either HCl or NaOH into the pure DIUF water. The mean values of the measured ζ-potentials of the silicone oil droplets dispersed in the aqueous phases with various pH values are shown in Figure 5.2. Adding HCl into the pure DIUF water to lower the pH values exponentially increases the concentration of H^+ ions in the aqueous phase. The selective adsorption of H^+ ions onto the oil-water interfaces gradually counteracts and then completely neutralizes the negative ζ-potential. At lower pH values, H^+ ions become the potential-determining ions (p.d.i). Further lowering the pH value leads to the diminishing ζ-potential and even the positive ζ-potential. As seen from Figure 5.2, the point of zero zeta (pzz) is near pH=4.5, which is located slightly in the acid side. If the anionic adsorption of Cl^- ions onto the O/W interfaces is neglected, the pzz can also be referred to as the isoelectric point (iep) in the present case (Jachowicz and Berthiaume, 1989; Noh and Schwarz, 1989). The pzz or iep is same as the point of zero charge (pzc) determined for the same O/W emulsion system (Gu and Li, 1997b), and very close to the published pzz≈5.0 for mineral oil-in-water emulsion droplets (Sanders et al., 1995).

At higher pH values, on the other hand, OH^- ions become the p.d.i. Their adsorption onto the oil-water interfaces results in stronger negative ζ-potential of the oil droplets. As shown in Figure 5.2, the ζ-potential monotonously decreases from +27.7 to –58.3 mV as the pH value increases from 2.68 to 10.32. The ζ-potential of the silicone oil droplets dispersed in the pure DIUF water (pH≈6.5) was measured to be –35.5±2.9 mV, between the above two extremes. In comparison with Cl^- ions at lower pHs or Na^+ ions at higher pHs, H^+ or OH^- ions are much more strongly adsorbed in the region near the oil-water interface such that they determine the ζ-potential of the dispersed droplets in each case. Similar variations of the ζ-potential with the pH value were also observed for other O/W emulsion droplets (Sanders et al., 1995; Deshiikan and Papadopoulos, 1995) and even solid-in-water suspension particles (Hamieh and Siffert, 1994; Chorom and Rengasamy, 1995).

5.4.2 Electrolyte Effects

The variations of the measured ζ-potential with the mole concentration of the following two typical electrolytes, NaCl and $AlCl_3$ from 10^{-6} to 10^{-3} M are plotted in Figure 5.3. Some common trends for these two electrolytes can be readily found. First, at 10^{-6} M, the ζ-potential values are close to the value for the pure DIUF water. At this concentration, these two electrolytes have no significant effects on the ζ-potential. Second, the silicone oil droplets acquire their strongest ζ-potentials near the concentration of 10^{-5} M for either electrolyte, though one ζ-potential is negative and the other is positive. At electrolyte concentrations higher than 10^{-5} M, however, the absolute value of the ζ-potential gradually becomes smaller. A similar tendency was observed for other O/W emulsion systems (Dittgen and Zosel, 1991). This phenomenon may be explained as follows. In general, the silicone oil droplets dispersed in very clean pure water such as the pure DIUF water are only charged to a limited extent because of fewer dissociated ions in the dispersing phase. With addition of an electrolyte, the ζ-potential becomes stronger. At even higher concentrations, however, addition of more electrolyte will considerably reduce the ζ-potential because of the more compressed (thinner) EDL. As a result, the strongest ζ-potential is achieved only when an appropriate amount of electrolyte, say 10^{-5} M, is added.

Furthermore, Figure 5.3 indicates that all the ζ-potential values for NaCl are small and negative in the concentration range of 10^{-6}-10^{-3} M. However, the zeta reversal occurs near 10^{-6}-10^{-5} M for $AlCl_3$. The positive ζ-potentials for the multivalent electrolyte result from the well-known strong selective adsorption of trivalent cations Al^{3+} onto the oil-water interfaces. The multivalent cations are more strongly adsorbed onto the oil-water interfaces, and thus their effects on the ζ-potential are more pronounced than the mono-valent cations Na^+. Therefore, it can be concluded that the ζ-potential depends not only on the concentrations but also on the ionic valences of the electrolyte used.

5.4.3 Effects of Ionic Surfactants

In the experiments with the ionic surfactant solutions, it is found that the adsorption of the ionic surfactants CTAB and SDS onto the silicone oil-in-water emulsion droplets strongly affects the ζ-potential. Figure 5.4 gives the measured results at different concentrations of CTAB (10^{-6}-10^{-3} M) and SDS (10^{-6}-10^{-2} M). At 10^{-6} M, the measured ζ-potential values are close to that for the pure DIUF water. It is seen from Figure 5.4 that the point of zeta reversal (pzr) occurs at a CTAB concentration of around about $3\text{x}10^{-6}$ M. This concentration is very close to the concentration found for another cationic surfactant, cetyldimethylbenzylammonium chloride (CDBACl), at $4\text{x}10^{-6}$ M (Avranas and Stalidis, 1991). During the ζ-potential measurements, it was noticed that, near the pzr, the silicone O/W emulsion was extremely unstable and that quick droplet coalescence was observed. Since a high electric filed is required to suspend a very weakly charged oil droplet and, thus, the thermal convection generated by the electric filed may become appreciable, no attempt was made to measure the accurate pzr for CTAB in this study. When the CTAB concentration is increased from the pzr, the measured ζ-potential becomes positive and increases quickly. The variations of the ζ-potential with CTAB concentration are caused by the well-known cationic adsorption. CTA^+ ions are the p.d.i in this case. Further increase of the CTAB concentration causes the ζ-potential to increase slowly and, finally, to reach its maximum value near +83.1±6.9 mV between 10^{-4} to 10^{-3} M. The saturation of cationic adsorption is considered to occur between the two concentrations. Since its CMC is about $9.2\text{x}10^{-4}$ M (Czerniawski, 1966), no CTAB concentrations higher than 10^{-3} M were tested. Avranas and Stalidis (1991) found a similar saturation pattern for the ζ-potential versus concentration of CDBACl using the electrophoresis technique. In their case, the $CDBA^+$ ions are considered to be the p.d.i and the limiting ζ-potential approaches approximately +55 mV at the surfactant concentration of about $6\text{x}10^{-4}$ M, insensitive to the three oil phases they tested.

Variations of the ζ-potential with log concentration of SDS from 10^{-6} to 10^{-2} M are also shown in Figure 5.4. As expected, the ζ-potential becomes more negative if more SDS is added into the aqueous solution. $C_{12}H_{25}SO_3^{-1}$ ions of SDS are the p.d.i, and their adsorption onto the oil-water interfaces results in the change of the ζ-potential with the SDS concentration. In the literature, the ζ-potential of silicone O/W emulsion droplets was reported to be negative when the emulsions were made with a similar anionic surfactant, sodium octadecyl sulphate (SODS), at $2.8\text{x}10^{-3}$ M (Berthiaume and Jachowicz, 1991). The ζ-potential of heavy oil droplets (B-type) dispersed in 10^{-4} M SDS solution was also found to be negative (Okada and Akagi, 1987). On further increase of the SDS concentration, the anionic adsorption process continues until a maximum negative ζ-potential of -58.4 ± 5.6 mV is attained at $10^{-3} \sim 10^{-2}$ M. The saturation state of the anionic adsorption is considered to be achieved between these two concentrations. Therefore, the curve for SDS shown in Figure 5.4 has an extended S-shape. Since the CMC of SDS at 25°C was determined to be around $8.1\text{x}10^{-3}$ M (Stalidis et al., 1990), the ζ-potential measurements were not continued for the aqueous solutions containing SDS concentrations higher than 10^{-2} M. Stalidis et al. (1990) identified a similar trend for the ζ-potential of three oil phases dispersed in the SDS solutions, again by using the electrophoresis technique. They found the limiting ζ-potential of approximately –60 mV at the SDS concentration of about $8\text{x}10^{-4}$ M, also insensitive to the three oil phases they tested.

All the measured results of the ζ-potential of the silicone oil droplets dispersed in the CTAB or SDS solutions show that these two ionic surfactants can change not only the magnitude of the ζ-potential to a great extent, but also its polarity. Furthermore, these two surfactants not only differ from each other with respect to their ionic properties but have rather different abilities to adsorb onto the oil-water interfaces as well. It is their different activities in the aqueous phase that determine their abilities to influence the ζ-potential of the silicone O/W emulsion droplets.

5.4.4 Summary

In the previous sections, an electrical suspension method has been presented and applied to measure the ζ-potential of silicone oil (No. 1) droplets dispersed in various aqueous solutions. The aqueous properties are altered by varying pH values, electrolytes, and ionic surfactants. The point of zero zeta (pzz) for the silicone oil droplets is found to be about pH=4.5. The measured results have shown that the ζ-potential depends on both the concentration and the ionic valence of the electrolyte dissolved in the aqueous phase. The experimental data also indicate that two widely used ionic surfactants, CTAB and SDS, can significantly change the ζ-potential. The point of zeta reversal (pzr) for CTAB is determined to be around 3×10^{-6} M. When the surfactant concentration approaches the critical micelle concentration (CMC) of each surfactant, the saturation state of the selective ionic adsorption is reached for either surfactant, as evidenced by the limiting ζ-potentials. All the measured ζ-potential values for the two ionic surfactant solutions are in an excellent agreement with those for similar O/W emulsion droplets measured by Stalidis and co-workers (Stalidis et al., 1990; Avranas and Stalidis, 1991) using the electrophoresis technique. The measured values of the ζ-potential have been plotted in Figure 5.2 for various pHs, Figure 5.3 for varying electrolytes, and Figure 5.4 for the ionic surfactant solutions, respectively. Table 5.3 or 5.4 also summarizes all the detailed values of the ζ-potential (ζ_p) of the silicone oil droplets dispersed in various aqueous solutions for convenient reference. In Section 5.9, these measured ζ-potentials (ζ_p) will be directly used to determine the dimensionless EDL parameter Dl and the dimensionless EDL asymmetry parameter Da defined in Equations (3.37a) and (3.37b) in Section 3.8.

The electrical suspension method developed in this study is an excellent alternative tool to the existing electrophoresis technique for measuring the ζ-potential. In practice, it is much simpler and easier to implement. It is particularly suitable for measuring the ζ-potential of the O/W and probably the water-in-oil (W/O) emulsion droplets. In principle, the proposed method can be extended to measure the ζ-potential of any liquid droplets dispersed in another immiscible liquid or even to measure the ζ-potential of fine solid particles suspended in a liquid phase, provided that the density difference between the dispersing phase and the dispersed (or suspended) phase is relatively small.

5.5 The ζ-Potential Measurements of Fiber Surfaces in Contact with Aqueous Solutions

In the previous sections, the ζ-potential (ζ_p) of silicone oil droplets dispersed in various aqueous solutions is measured by using a newly devised electrical suspension method. In order to determine the electrical double layer (EDL) interaction between a spherical oil droplet and a cylindrical fiber, the ζ-potential (ζ_c) of fiber surfaces has to be measured when they are in contact with similar aqueous solutions. As shown in Equations (3.37a) and (3.37b), both ζ_p and ζ_c are equally involved in the dimensionless EDL interaction parameter Dl and the dimensionless EDL asymmetric parameter Da. Physically, it has long been observed in many experiments that, when it is in contact with a liquid medium, any solid surface may be charged and surrounded by the ions of opposite sign from the liquid phase. The overall arrangement of the electric charge on the solid surface, together with the balancing charge in the liquid phase, is also called the electrical double layer (EDL) of the solid-liquid interface or simply the EDL of solid surface (Hunter, 1981). Similarly, such EDL is also characterized by its strength and polarity, ζ, the zeta-potential, and its thickness, κ^{-1}, the Debye-Hückel reciprocal length parameter. Like the electric charge residing at the liquid-liquid interfaces, the EDL characteristics of a solid surface in contact with a liquid phase are also of great importance in many colloidal and interfacial phenomena such as in the studies of deposition phenomena (Adamczyk and van de Ven, 1981b; Adamczyk et al., 1983; Alince, 1989; Alince et al., 1991; Alince and van de Ven, 1993; Jachowicz and Berthiaume, 1989; Berthiaume and Jachowicz, 1991). In addition, values of ζ and κ^{-1} are directly related to the interactions between the solid particles themselves when they are suspended in a liquid solution, i.e., particle coagulation, and thus determine the stability of the suspensions. More recently, the electrokinetic effects, which are caused by the EDL at the solid-liquid interfaces, are found to have a significant influence on the flow characteristics of water through microchannels (Mala and Li, 1997).

Unlike the case for the oil-in-water (O/W) emulsions, there have been few efforts made to determine the ζ-potential of solid-liquid interfaces because of obvious technical complexities and difficulties. There are even fewer data of the ζ-potential of some specific solid-liquid interfaces available in the literature (Jachowicz and Berthiaume, 1989; Sanders et al., 1995; Mala and Li, 1997). Generally, there are two widely used methods to determine the ζ-potential of the EDL at the solid-liquid interfaces. The first method is to crush the solid material into fine particles and to disperse them in the aqueous solution to be tested. Then the electrophoresis technique is implemented to measure the electrophoretic mobilities of these particles. Eventually, the ζ-potential of the finely ground particles (or assumedly the solid material) is calculated from the measured electrophoretic mobilities according to the Helmholtz-Smoluchowski equation for spherical particles (Hunter, 1981). Therefore, the electrophoresis technique can be used for both colloidal emulsion (liquid) droplets and colloidal suspension (solid) particles. Following the above procedure, Sanders et al. (1995) measured the ζ-potential of finely ground microscope slide particles as a function of bulk pH value using a particle electrophoresis apparatus (Rank Brothers, MK II, Cambridge, England). However, a question which naturally arises with the electrophoresis technique for the finely ground solid particles is whether such determined ζ-potential of the finely ground solid particles can truly represent the ζ-potential of the solid-liquid interface prior to crushing. In other words, it is not immediately clear whether and/or to what extent the crushing process itself will change the surface and electrical properties of the solid material to be tested.

The streaming potential technique is a much more widely used method to determine the ζ-potential of a solid surface in contact with a liquid. For example, Mala and Li (1997) used the streaming potential technique to investigate the electrokinetic effects of the EDL on flow characteristics of water through a microchannel between two parallel plates. In particular, they measured the ζ-potential of different plate materials, P-type silicone and glass in contact with water containing different potassium chloride concentrations. Also by using the streaming potential method, Jachowicz and Berthiaume (1989) determined the ζ-potential of untreated hair fibers and the hair fibers modified by adsorption of a saturated layer of cationic polyelectrolyte as a function of pH of the streaming solution.

In this study, the streaming potential technique was used because of its greater simplicity and applicability. Specifically, a microchannel is designed for performing the streaming potential measurements, which consists of two parallel plates of the solid material to be tested. The streaming solution is the aqueous phase to be tested. Since the detailed technical information about the streaming potential technique is well documented in the literature (e.g., Hunter, 1981; Lyklema, 1995), its main principle and technical challenges will be briefed in the next section. Particular attention will be focused on understanding the effect of the surface conductance and determining its role in the electrokinetic phenomenon. Later on, the experimental aspects of the streaming potential measurements will be described in details in Section 5.7. Finally, the measured results of the ζ-potential of the bare glass fiber surfaces and the FC725-precoated glass fiber surfaces in contact with various aqueous solutions will be presented and analyzed in Section 5.8.

With the measured data of the ζ-potential of the silicone oil droplets presented previously and those of the ζ-potential of the glass fiber surfaces in the subsequent sections, some important dimensionless EDL parameters, such as Dl, Da and τ defined in Equations (3.37a,b,c), can be easily calculated (Section 5.9). Furthermore, in conjunction with the consideration of the curvature effect presented in Section 3.9, the EDL interaction between a spherical oil droplet and a cylindrical fiber can be quantified.

5.6 Streaming Potential Technique

5.6.1 The Origin of the Streaming Potential in Microchannel Flows

It has long been observed that most solid surfaces may bear the electrostatic charges when they are in contact with a liquid. Thus the EDL will be formed at the solid-liquid interfaces as long as the liquid contains some amount of dissociated ions. This is because the electrostatic charges on the solid-liquid interfaces will attract the counterions in the liquid to establish an electric field. Usually, the EDL can be further divided into the compact layer and the diffuse double layer (Hunter, 1981). Within the compact layer, the ions are so strongly attracted to the solid surfaces that they are actually immobile. In the diffuse double layer, conversely, the ions are affected much less by the electric field and thus are mobile.

More specifically, the thickness of the diffuse EDL, κ^{-1}, generally ranges from a few nanometers up to several hundreds of nanamters, depending upon the bulk ionic concentration and the other physical properties of the liquid phase. The electrical potential at the boundary between the compact layer and the diffuse double layer is usually referred to as the ζ-potential. Therefore, ζ and κ^{-1} can be used to characterize the EDL strength and polarity and its thickness respectively. In general, for a given liquid medium, the EDL thickness κ^{-1} can be directly calculated from Equation (3.32) since it depends only on the ionic concentration and some other physical properties (i.e. ε_r and T) of the liquid. However, determination of the EDL strength and even polarity (i.e. the ζ-potential) presents a rather more difficult task. For the EDL formed at the solid-liquid interfaces, the streaming potential technique is probably the most effective method to determine the ζ-potential by directly measuring the streaming potential of a liquid when it is forced to flow through a microchannel made of the solid material to be tested. The major principle of the technique and its relevant physical background will be addressed briefly as follows.

When a liquid is forced to flow through a small channel under hydrostatic pressure, the ions in the mobile part of the EDL near the wall are carried towards one end. This constitutes an electrical current called a streaming current, I_s, to flow in the direction of the liquid flow. Then the accumulation of ions downstream sets up an electric field. This field causes a current called the conduction current to flow back in the opposite direction through the bulk of the liquid. When the conduction current, I_c, is equal to the streaming current, a steady state is achieved. The resulting electrostatic potential difference between the ends of the channel is often referred to as the streaming potential due to its flow (streaming) feature. Physically, the electrokinetic effect or phenomenon can be understood in a simpler fashion. When the ions are moved in the diffuse double layer, they draw the liquid nearby to move along with them. Obviously, the motion of the ions in the diffuse double layer is subject to the ζ-potential of the EDL. Thus, the liquid flow characteristics of the small channel are affected by the presence of the EDL at the solid-liquid interfaces. Most importantly, the ζ-potential of the EDL can be directly related the streaming potential. As will be discussed in the experimental part, the latter potential can be measured directly and accurately if some technical efforts and necessary precautions are implemented.

5.6.2 Streaming Potential Equations

Although the streaming potential phenomenon was observed in the experiments long time ago, its relation with the ζ-potential of solid-liquid interfaces has been established only relatively recently. The detailed mathematical derivations of relating the measurable streaming potential, E_s, to the ζ-potential of the EDL for a circular channel can be found in textbooks (e.g., Hunter, 1981; Lyklema, 1995). However, for simplicity, the microchannels made of two parallel plates were used in the present streaming potential measurements. Therefore, a similar relation (called streaming potential equation) is required for this geometric configuration. The mathematical derivations of the streaming potential equations will be limited to a minimum level. Instead, more attention will be focused on the physical understanding. However, it is worthwhile noting that the following procedure is general for establishing a relation between the streaming potential, E_s, and the ζ-potential of the EDL at the solid-liquid interfaces, irrespective of the specific shapes of the microchannels. These concise derivations will also be helpful in obtaining deeper insights into the streaming potential phenomenon. A more comprehensive mathematical model was presented recently by Mala and Li (1997), which deals with the fluid flow through a microchannel between two parallel plates with the presence of the electrokinetic effects.

First, the streaming current is, by its definition, referring to Figure 5.5 and noting the symmetry,

$$I_s = 2\int_0^{\delta/2} V_z(y)\rho(y)W\,dy, \tag{5.19}$$

where $V_z(y)$ represents the velocity profile (varies in the transverse y-direction) of fluid flow along the z-direction and $\rho(y)$ is the distribution of volume density of charge across the parallel channel. W is the width and δ is the thickness of the microchannel. Generally, the detailed hydrodynamic behavior of a rectangular channel is quite complicated. But if the ratio of the width to the thickness is large (i.e. $W/\delta > \sim 20$), the velocity profile in such a narrow rectangular channel is parabolic and symmetrical about the center and is given by the Poiseuille's equation. The velocity profile $V_z(y)$, flow volume flux Q_z and the averaged velocity V_{ave} across the channel as well as the maximum velocity at the geometric center (y=0) $V_{max}=V_z(0)$ are equal to (Hunter, 1981; Panton, 1984):

$$V_z(y) = \frac{-\Delta P\delta^2}{8\mu L}\left[1-\left(\frac{y}{\delta/2}\right)^2\right] = V_{max}\left[1-\left(\frac{y}{\delta/2}\right)^2\right] \tag{5.20a}$$

$$Q_z = \frac{-\Delta P W\delta^3}{12\mu L} \tag{5.20b}$$

$$V_{ave} = \frac{Q_z}{W\delta} = \frac{-\Delta P\delta^2}{12\mu L} = \frac{2}{3}V_{max} \tag{5.20c}$$

where, ΔP is the pressure drop, μ is the viscosity of the streaming solution and L is the length of the microchannel along the flow direction. It is noted that ΔP in the above equations is negative in order to generate the fluid flow along the z-direction. The distribution of volume density of charge across the parallel channel, ρ(y) involved in the integral Equation (5.19), can be directly related to the potential distribution across the channel by the famous Poisson's equation (Hunter, 1981), in the present case, which can be written as:

$$\frac{d^2\psi}{dy^2} = -\frac{\rho(y)}{\varepsilon_r\varepsilon_0} \tag{5.21}$$

Since the EDL is confined to a thin region near the wall of the microchannel, only values of ρ(y) close to y=δ/2 are of importance in determining the streaming current (i.e. the bulk of the moving liquid carries no net charge). In order to integrate Equation (5.19) analytically, near the wall y≈δ/2, the velocity profile given in Equation (5.20a) can be approximated as:

$$V_z(y) = \frac{-\Delta P\delta^2}{8\mu L}[1+(\frac{y}{\delta/2})][1-(\frac{y}{\delta/2})] \approx \frac{-\Delta P\delta^2}{4\mu L}[1-(\frac{y}{\delta/2})] \tag{5.22}$$

Substituting Equations (5.21) and (5.22) into Equation (5.19) gives:

$$I_s = \frac{\varepsilon_r\varepsilon_0\Delta PW\delta^2}{2\mu L}\int_0^{\delta/2}\frac{d^2\psi}{dy^2}[1-(\frac{y}{\delta/2})]dy \tag{5.23a}$$

Further integrating the above integral equation by parts produces:

$$\begin{aligned} I_s &= \frac{\varepsilon_r\varepsilon_0\Delta PW\delta^2}{2\mu L}\{[1-(\frac{y}{\delta/2})]\frac{d\psi}{dy}\Big|_{y=0}^{y=\delta/2} + \frac{1}{\delta/2}\int_0^{\delta/2}\frac{d\psi}{dy}dy\} \\ &= \frac{\varepsilon_r\varepsilon_0\Delta PW\delta^2}{2\mu L}[\frac{1}{\delta/2}\int_0^{\zeta}d\psi] = \frac{\varepsilon_r\varepsilon_0\zeta}{\mu}\frac{\Delta PW\delta}{L} \end{aligned} \tag{5.23b}$$

The first term in the inner bracket disappears because dψ/dy is zero when y=0 and indeed long before y=0. Some may object that the approximation in Equation (5.22) leading to Equation (5.23b) should not hold over the whole integration range. It should be noted, however, that the contributions to the integral are confined entirely to the thin layer near the wall where y≈δ/2 (Hunter, 1981).

The streaming potential, E_s, generated by this current causes a conduction current in the reverse direction given by:

$$I_c = \frac{A_c E_s \lambda_b}{L} + \frac{P_w E_s \lambda_s}{L} = \frac{W\delta E_s \lambda_b}{L} + \frac{2(W+\delta)E_s \lambda_s}{L} \tag{5.24}$$

where, more generally, A_c and P_w are the cross-sectional area and the wetted perimeter; λ_b is the bulk electrical conductivity of the streaming solution and λ_s is the specific surface conductivity. For the rectangular channel ($W \times \delta$), $A_c=W\delta$ and $P_w=2(W+\delta)$. Thus, when a steady state has been established, $I_s+I_c=0$ and so

$$\frac{E_s}{-\Delta P} = \frac{\varepsilon_r \varepsilon_0 \zeta}{\mu[\lambda_b + 2(\frac{1}{W} + \frac{1}{\delta})\lambda_s]} \tag{5.25}$$

Noted that ΔP in the above equation is negative. It is convenient to use $\Delta P_z=-\Delta P$ in the above equation; thus more generally:

$$\frac{E_s}{\Delta P_z} = \frac{\varepsilon_r \varepsilon_0 \zeta}{\mu[\lambda_b + f\lambda_s]} \quad (\lambda_s \neq 0) \tag{5.26a}$$

Equation (5.26a) is often called the streaming potential equation. Here the term in the parentheses is written more generally as $(\lambda_b+f\lambda_s)$ where f is a "form factor" for the channel, equal to the ratio of its wetted perimeter to its cross-sectional area, i.e. $f = \frac{P_w}{A_c}$.

It should be noted that Equation (5.26a) is a general form of the streaming potential equation, regardless of the specific velocity profile and the specific shape of the channel. However, f represents the shape factor of the channel (Hunter, 1981).

5.6.3 Effect of Surface Conductance

In Equation (5.26a), λ_b refers to the conductance of a cube block of streaming liquid of unit cross-sectional area and unit length and is measured in $\text{Ohm}^{-1}\ \text{m}^{-1}$ or S/m. In practice, the bulk conductivity λ_b can be measured directly and accurately. Correspondingly, λ_s refers to the conductance of a square sheet of material of unit area and constant, though negligible, thickness, measured along the length of the square and is measured in Ohm^{-1} or S. Physically, it is the surface equivalent of the bulk conductivity λ_b. In contrast to λ_b, nevertheless, λ_s is a surface excess quantity and thus can not be measured directly. This means that a subtraction step is required in order to obtain λ_s. Depending on the specific method used and the system studied, the subtraction procedure may vary from straightforward to cumbersome. In case the effect of the surface conductivity on the relation between the streaming potential and the ζ-potential is neglected, Equation (5.26a) is simplified as:

$$\frac{E_s}{\Delta P_z} = \frac{\varepsilon_r \varepsilon_0 \zeta}{\mu \lambda_b} \quad (\lambda_s = 0) \qquad (5.26b)$$

Equation (5.26b) is sometimes called the classical streaming potential equation, which is valid only if all or almost all of the conduction current is transported by the bulk liquid, i.e. the first term on the RHS of Equation (5.24) is overwhelmingly dominant. It frequently happens, however, that a significant proportion of the conduction current is transported by the layers near the wall (or even through the solid if it is a good conductor). The accumulated charge in the EDL at the solid-liquid interfaces may then lead to an unusually high surface conductivity. Especially for pure water or aqueous solutions containing lower electrolyte concentrations, the effect of surface conductance is significant since the bulk electrical conductivity is lower. Accordingly, the second term on the RHS of Equation (5.24) becomes either important (maybe even dominant) or at least comparable.

Historically, it took a quite long and difficult time to fully understand and to correctly account for the effect of surface conductivity. The very idea that surface conduction exists is relatively old; the phenomenon has, for instance, been recognized by Smoluchowski early this century (Smoluchowski, 1903). One of the convincing steps was the finding that the ζ-potentials, derived from the classical streaming potential Equation (5.26b) (Note: it is a general form regardless of the shapes of capillaries) using the measured streaming potentials, appeared sometimes size (radius for circular capillaries)-dependent and sometimes not. In the 1930s, when this effect was not yet appreciated, this finding even led to a debate in scientific society on the question whether or not the ζ-potential really was a material- and condition- (e.g., pH, electrolyte concentrations) specific characteristic. Now it is known as the effect of surface conductance. Hence, the spurious radius dependence (often called the radius inconsistency) is caused by not taking account of the effect of surface conductance.

The specific form of the streaming potential equation for a rectangular microchannel can be obtained from Equation (5.25) or (5.26a) as follows:

$$\frac{E_s}{\Delta P_z} = \frac{\varepsilon_r \varepsilon_0 \zeta}{\mu[\lambda_b + 2(\frac{1}{W} + \frac{1}{\delta})\lambda_s]} \quad \textbf{(rectangular channel)} \qquad (5.27a)$$

If the ratio of the width to the thickness of the rectangular channel is large (i.e. W/δ>~20), the velocity profile in such rectangular channel can be described by the Poiseuille's equation. This kind of rectangular channels is simply called as the parallel-plate channels since they are very narrow in their thickness directions. Therefore, for the parallel-plate channel, its streaming potential equation can be derived by dropping the term 1/W as it is much smaller than the term 1/δ in the above equation,

$$\frac{E_s}{\Delta P_z} = \frac{\varepsilon_r \varepsilon_0 \zeta}{\mu(\lambda_b + \frac{2}{\delta}\lambda_s)} = \frac{\varepsilon_r \varepsilon_0 \zeta}{\mu\lambda_b(1 + Du)} \quad \textbf{(parallel - plate channel)} \qquad (5.27b)$$

Where, Du is called the Dukhin number in order to acknowledge Dukhin's important contributions to the EDL relaxation and electrokinetic phenomena. For a parallel-plate capillary, Du number can be defined as (not uniquely), e.g.:

$$Du = \frac{2\lambda_s}{\lambda_b \delta} \qquad (5.27c)$$

The streaming potential equation for a circular channel can be readily derived and expressed as (Hunter, 1981; Lyklema, 1995):

$$\frac{E_s}{\Delta P_z} = \frac{\varepsilon_r \varepsilon_0 \zeta}{\mu(\lambda_b + \frac{2}{r}\lambda_s)} = \frac{\varepsilon_r \varepsilon_0 \zeta}{\mu\lambda_b(1 + 2Du)} \quad \textbf{(circular channel)} \qquad (5.28a)$$

where, r is the radius of the circular channel and for a circular capillary, Du number is defined as (Lyklema, 1995; Lyklema and Minor, 1997):

$$Du = \frac{\lambda_s}{r\lambda_b} \qquad (5.28b)$$

5.6.4 Determination of the ζ-Potential and the Surface Conductance λ_s

In this study, the parallel-plate channel is used to conduct the streaming potential measurements. Now from the experimental point of view, it will be shown how to determine the ζ-potential and the surface conductance λ_s from the measured streaming potentials by using the streaming potential Equation (5.27b). This goal can be achieved by rearranging Equation (5.27b) as below (Lyklema and Minor, 1997)

$$\frac{\varepsilon_r \varepsilon_0 \Delta P_z}{\mu E_s \lambda_b} = \frac{1}{\zeta} + \left(\frac{2\lambda_s}{\zeta \lambda_b}\right)\frac{1}{\delta} \tag{5.29}$$

As seen from Equation (5.29) that, unless the effect of surface conductance is neglected, generally, it is not enough to determine the ζ-potential from one streaming potential data. At least, a second measurement is required in order to find λ_s as well. Alternatively, for a given streaming solution and a given channel material, if measurements are conducted for different gaps (δ), both ζ-potential and λ_s should be constant and thus can be derived from Equation (5.29). The additional experiments are rewarded by producing not only the ζ-potential, but also the surface conductivity λ_s. Also as mentioned before, λ_s can be obtained only by using indirect methods such as the subtraction procedure.

Mathematically, as schematically shown in Figure 5.6, Equation (5.29) indicates a linear relationship between the term $\frac{\varepsilon_r \varepsilon_0 \Delta P_z}{\mu E_s \lambda_b}$ and $\frac{1}{\delta}$ for a given solid-liquid interface. Therefore, if the other quantities, such as ΔP_z, E_s, δ, and λ_b, μ, ε_r, are measured properly for several gaps (i.e. different δ), the remaining task is to bring these measured data into Equation (5.29) and plot the data points in terms of $\frac{\varepsilon_r \varepsilon_0 \Delta P_z}{\mu E_s \lambda_b}$ versus $\frac{1}{\delta}$. Then the ζ-potential and the surface conductivity λ_s can be readily calculated since the intercept and the gradient of the linear curve fit to these points are equal to $\frac{1}{\zeta}$ and $\frac{2\lambda_s}{\zeta \lambda_b}$ (see Figure 5.6), respectively.

In order to plot the linear line in terms of $\frac{\varepsilon_r \varepsilon_0 \Delta P_z}{\mu E_s \lambda_b}$ versus $\frac{1}{\delta}$, all the relevant quantities, ΔP_z, E_s, δ, and λ_b, μ, ε_r, should be determined properly. Among the six to-be-determined quantities required in Equation (5.29), ΔP_z and E_s are dependent on the specific experimental conditions (solid material, liquid properties, gap size and flow conditions) and δ is the separation distance between the two parallel plates. The remaining three parameters, λ_b, μ and ε_r are the liquid properties of the streaming solution. A thorough description of their determinations and the relevant experimental details regarding the streaming potential measurements will be presented in the subsequent section.

5.7 Experimental Aspects of the ζ-Potential Measurements of Glass Surfaces in Contact with Aqueous Solutions

As described above, in the streaming potential measurements, the resulting electrostatic potential difference between the two ends of the microchannel is usually very small, ranging from a few millivolts to hundreds of millivolts, at most up to a couple of thousands of millivolts for extremely strongly charged solid-liquid interfaces. Therefore, the streaming potential E_s must be measured accurately, as a function of the applied pressure ΔP_z and gap size δ, with a high impedance electrometer so that the streaming current I_s and the conduction current I_c are not disturbed. Hence, an experimental set-up of microchannel flow has to be designed carefully to ensure the adequate accuracy of the streaming potential measurements.

5.7.1 Experimental Set-up

In the laboratory of Applied Surface Thermodynamics and Interfacial Phenomena in the Mechanical Engineering Department at the University of Alberta, there is an experimental set-up available for streaming potential measurement. This experimental set-up is used in the present experimental study. A schematic diagram of the experimental set-up used for the streaming potential measurements is shown in Figure 5.7. The entire experimental set-up can be decomposed of four major parts: the microchannel cell; liquid handling system such as driving pump, valve controls and piping layout; a series of measurement transducers (pressure transducer, electrometer and conductivity sensor) and the computer-based data acquisition and processing system. Since a complete technical description of the apparatus can be found in Mala's (1999) Ph.D. dissertation, here, it will be described how to prepare the parallel-plate microchannel and determine its gap, δ. It will also be stated how to assembly the microchannel into the set-up. This will be followed by a brief technical description on the streaming potential measurements, such as the pressure drop measurement, the streaming potential measurement and the conductivity measurement. Some cautions are also mentioned in the description of the experimental procedure.

5.7.2 Preparation and Assembly of the Parallel-Plate Microchannels

So far the experimental apparatus was used to investigate fluid flow and heat transfer studies in microchannels. Thus, for the present streaming potential measurements, the remaining tasks were to carefully prepare each parallel-plate microchannel and properly assemble it into the set-up. Here, it needs emphasizing that the parallel-plate microchannel was chosen because of its simpler geometry and well-known Poiseuille's flow characteristics. In the measurements, its hydrodynamic behavior can ~~be~~ well controlled. Most importantly, as derived in the preceding section, a relationship is well established between the to-be-determined parameters, such as the ζ-potential of the solid-liquid interfaces and the surface conductivity λ_s, and experimentally measurable quantities, such as ΔP_z, E_s, δ, and the liquid properties of the streaming solution such as λ_b, μ and ε_r, which is expressed by the streaming potential Equation (5.29).

In this thesis study, two kinds of solid surfaces were of interest: the bare glass fiber surfaces and the FC725-precoated glass fiber surface. These two glass plates were used to make the parallel-plate microchannels in the streaming potential measurements. First, the pre-cleaned glass microscope slides (7.5cm x 2.5cm) were cut into two pieces of glass plates and the two ends of each piece were polished carefully so that it has a precise dimension of 3.00cm x 2.50cm with the accuracy of about ±0.03 cm. The glass plates were submerged in Acetone for 12 h, rigorously washed with Acetone several times and eventually immersed in the pure DIUF water (Fisher Scientific, Canada) for 12 h. For the microchannels made of two bare glass plates, such cleaned glass plates were dried in air before assembling the two plates together. For the microchannels made of the FC725-precoated glass plates, each cleaned glass plates was dried in air and then coated with the FC725 coating material (3M Product) using the dip-coating method described in Section 4.4. Thus a uniform and smooth coating layer of the FC725 was left on the glass plate. The coated glass plate was suspended vertically and dried in air before use for making the parallel-plate microchannels.

Irrespective of the glass material chosen, each parallel-plate microchannel is made according to the following procedure. In order to have a proper gap size δ for each channel, a plastic shim (Small Parts, Inc., Florida) of proper thickness is cut to form the shape of microchannel and used as a spacer. Two narrow plastic spacers (each width is 0.75 cm) are placed and fixed between two glass plates along their lateral sides by applying a small amount of adhesive on each side of the shim and snapping a piece of glass plate on it each time. The transverse distance between these two spacers is always set at 1.00 cm, i.e. the width of all the microchannels is equal to W=1.00 cm. Of course, the length of each microchannel is L=3.00 cm. However, the thickness (or gap) of the parallel channel depends on the thickness of the shim chosen and the amount of the adhesive applied between the shim and the two glass plates. In this study, plastic shims of three different thickness of 0.001", 0.003" and 0.005" were used and correspondingly the thickness of the microchannels separated by each of them plus the adhesive (approximately 25 μm thick) is around δ=50, 100 and 150 μm as desired. Accordingly, the ratio of W/δ is about 200, 100 and 67, which sufficiently satisfies the conventional requirement for the parallel-plate channel $W/\delta>20$. Thus the velocity profile in such parallel-plate channels can be assuredly assumed to be parabolic and symmetrical about the center and is adequately described by the Poiseuille's equation. The streaming potential Equation (5.29) derived in Section 5.6.4 is valid for the microchannels tested in this work.

Since the thickness of the parallel-plate channel is an important parameter involved in the streaming potential Equation (5.29), at this point, how to accurately measure the thickness (δ) of such assembled parallel-plate microchannels is essential. After the adhesive is dried in air for about 12 h, the thickness of the microchannel is fixed and measured by using the computer digital image techniques. In the measurement, the channel is placed under the microscope and the video camera system. Once the image of the partial cross-section of the channel is focused well, the digital image is acquired and stored automatically in the computer memory. The stored slot image can be digitized and the output data are two sets of discrete coordinates, x and y in mm, of the upper and lower boundaries of the slot. The overall accuracy of the digitization is around 0.5 μm at 40x magnification with an additional magnifying phototube. The mean value of the thickness δ of the parallel-plate microchannel is determined from the digitized boundary coordinates.

Following the thickness measurement, the parallel-plate channel will be assembled into the piping system for the streaming potential measurements. In order to force the streaming solution through the microchannels under high pressure, in this study, an adhesive (epoxy) is used to bond and fix the microchannel cell in the flow system. After the completion of a set of streaming potential measurements, the flow cell is removed and replaced by a new one.

5.7.3 Streaming Potential Measurements

Once the flow cell of either glass fiber material is assembled in the flow system and dried in air, and the to-be-tested streaming solution is prepared, the streaming potential measurements can be started. Typically, the following three major measurements are involved and carried out simultaneously: the pressure drop measurement, the electrical measurement and the conductivity measurement. These measurements will be described in the subsequent paragraphs. The detailed technical information and the specifications of the relevant meters used in this study can be found in Appendix I (Mala, 1999).

Measurement of the pressure drop (ΔP_z) across the parallel-plate microchannel is controlled by a computer and the pressure readings are stored in the computer memory. A pressure transducer (Validyne, Model DP15-20, Engineering Corp., California) is used to measure the pressure difference between the entrance and the exit of the microchannel. Inside the pressure sensor, the elastic sensing element is a flat silicone diaphragm. The sensing elements with different pressure ranges are available and the pressure transducer is calibrated with a dead weight tester calibrator (Budenberg, England).

In order to establish a proper pressure drop (or proper flow rate) across the microchannels, a tubing pump (Masterfex, Model 7550-60, Barnant Co., Illinois) with maximum 100-psi pressure increment is used to drive the solution through the flow cell. This pump can be operated at a fixed or variable flow rates and its flow rate can be specified and controlled either automatically by computer or manually by the operator. The pump automatically adjusts its rotating speed in the range from 60 rpm to 600 rpm to meet the specified flow rate. It is noted from Equation (5.29) that the specific value of the flow rate is not directly required in the streaming potential equation. However, since it is directly related to the pressure drop, the flow rate of the streaming solution through the flow cell is also carefully measured using three different methods. First, the tubing pump always displays a pre-specified flow rate. Second, the flow rate is measured on-line by a magnetic flow sensor (Model MAO-125-S-10-AA, CHEM TEC Equipment Co., Florida). This reading and the pump reading are displayed on-line on the computer monitor. These two flow rates will be compared with the average flow rate calculated by measuring the amount of aqueous solution collected for a known period. The difference among the three flow rates is found to be less than 0.5%.

Theoretically, according to Equation (5.29), the measured streaming potential E_s should be exactly proportional to the pressure drop ΔP_z. However, as will be shown later on, in the practical experimental measurements, this can not be assumed always true for some unknown reason. In fact, it is usually suggested that one should always measure E_s as a function of ΔP_z over a reasonable range to obtain an accurate estimate of the point $(\frac{\varepsilon_r \varepsilon_0 \Delta P_z}{\mu E_s \lambda_b}, \frac{1}{\delta})$ for a given gap size (refer to Figure 5.6). In this investigation, depending on the gap size (δ) of the parallel-plate microchannel to be tested, the flow rates are set properly such that reasonable pressure drops can be achieved across the flow cell. More specifically, for the parallel-plate microchannel of δ=50, 100 and 150 μm, correspondingly, three pre-set flow rates for each channel are 10, 20 and 40 ml/min, 20, 40 and 60 ml/min, 40, 60 and 80 ml/min. Thus the pressure drops for the three chosen flow rates are in the range of from 0.5 to 15 psi for each channel, which cover the pressure drops in the measurements of the electrokinetic effects on liquid flows through parallel-plate microchannels done by Mala and Li (1997) using a commercial electrokinetic analyzer (EKA).

Next is to carefully conduct the electrical measurement of the streaming potential E_s across the two ends of the parallel-plate microchannel. As the streaming potential is an induced potential due to the presence of the EDL at the solid-liquid interfaces, its accurate measurement is essential to this research. The magnitude of the potential is in the range from a few millivolts to thousands of millivolts. This inherently makes its measurements extremely difficult. Therefore, the streaming potential E_s must be measured, as a function of the applied pressure ΔP_z and gap size δ, with a high impedance electrometer so that the streaming current I_s and the conduction current I_c are not disturbed. In this experimental study, two AgCl electrodes (Dri-Ref-450, World Precision Instruments, Inc., Florida) are inserted into the ends of the flow cell with each electrode on each end and connected to an electrometer with high resistance (Model 6517, Keithley Instruments, Inc., Ohio) by a tri-axial cable. As the streaming solution is forced to pass through the microchannel, the accumulation of the ions up-stream and down-stream set up an electric filed with an electrical potential. This potential is the streaming potential detected by the electrodes. The streaming potential is measured by the electrometer remotely controlled by computer and all the potential readings are automatically stored in the computer memory for data processing later.

In additional to two kinds of channel materials used (the bare glass fiber and FC725-precoated glass fiber), four kinds of aqueous phases are used as the streaming solutions for measuring the streaming potentials and thus the ζ-potentials of fiber surfaces in contact with these aqueous solutions. These liquids are the same as those used for determining the Hamaker constants (Tables 4.8 and 4.9) and those used for measuring the ζ-potentials (Tables 5.3 and 5.4) of silicone oil droplets. They are the pure DIUF water (Fisher Scientific, Canada); the aqueous phases with different pH values; the electrolyte solutions containing either NaCl or $AlCl_3$ and the ionic surfactant solutions containing either CTAB or SDS. The last three aqueous solutions are prepared from the pure DIUF water and the detailed procedure for their preparations is described previously (see Sections 4.7 and 5.3.2). In the streaming potential measurements, the viscosity μ, relative dielectric constant ε_r and electrical conductivity λ_b are the important liquid properties required by the streaming potential Equation (5.29). Since the concentrations of the electrolytes or surfactants added to the streaming solutions are usually very low, their effects on the liquid viscosity and dielectric constant can be neglected. Also all the experiments are conducted at room temperature, 22±1°C; thus the liquid viscosity and its dielectric constant are assumed to be constant and chosen as μ=1.0 mPa s and ε_r=80.0 for the pure DIUF water respectively. The electrical conductivity λ_b is measured using a conductivity sensor (Model Inpro 7001/120, Mettler-Toledo Process Analytical Inc., Massachusetts) and connecting it to a CR 7300

Mettler-Toledo conductivity/resistivity transmitter. A small conductivity cell is fabricated in which the conductivity sensor is immersed. The conductivity cell is connected to the outlet of the parallel-plate microchannel cell so that the conductivity can be measured and monitored on -line. The output of the transmitter is displayed on the LCD panel of the transmitter and its analog signal is also sent to and stored in the computer. For the streaming solutions used in the measurements, their electrical conductivity varies considerably from the minimum of λ_b=1.21x10^{-4} S/m for the pure DIUF water to the maximum of λ_b≈340.56x10^{-4} S/m for the electrolyte solution containing 10^{-3} M $AlCl_3$.

5.7.4 Experimental Procedure

After a microchannel is assembled into the flow piping system and an aqueous solution is prepared, the streaming potential measurements will be conducted strictly according to the following general procedure. Step 1, an initial flow rate is set and the entire piping system is checked to see if there is any leaking. Depending on the pre-set flow rate, a long period should be allowed for the fluid flow through the microchannel to reach a steady state. The steady state is considered to be achieved if the variations of the measured pressure drop and the flow rate are within their measurement errors. Also an even longer period is allowed for the conductivity to reach a constant value for a given streaming solution. This process may be called the preparation period of the measurement. Step 2, three readings of the pressure drop ΔP_z and the streaming potential E_s are taken in one flow direction and three others are recorded for the other flow direction. In experiment, the flow direction is switched on purpose mainly for reducing the electrode polarization effect. It is important that, after switched, one should wait until the flow reaches the steady state in the new flow direction. This means one has to repeat the contents of Step 1 after each switch. Step 3 is to repeat Step 2 twice and thus total eighteen readings of ΔP_z and E_s are collected for the chosen flow rate. Step 4 is to repeat the above Steps 1-3 for the second flow rate and the third flow rate, respectively. For each streaming solution (total 25 different streaming solutions tested), three parallel-plate channels are used, which have gap sizes of approximately 50, 100 and 150 μm respectively. All the streaming potential measurements are carried out at room temperature 22°C.

Some cautions have to be exercised during the streaming potential measurements. First of all, in order to minimize the well-known electrode polarization effect, three measures are implemented. Usually the measurement of the streaming potential lasts only about 30 s during which three readings are collected. The electrodes are disconnected from the electrometer during non-measurement intervals. The flow direction is changed after the measurements are done in one direction. Once the experiment for one channel or one streaming solution is completed, the two electrodes are cleaned and rinsed with the DIUF water and eventually put back into the beaker containing 3M KCl solution as recommended by the manufacturer. Second, before using a new streaming solution, the microchannel cell and the entire piping system are rinsed with methanol and then with the DIUF water at a relatively high flow rate. The rinsing procedure presents to be an important measure of removing any remaining trace of the old streaming solution. Lastly, the electrodes should be rinsed thoroughly with the DIUF water several times before they are inserted into the two ends of the flow cell. As stated above, during the non-experiment periods, they are always immersed in the 3M KCl solution. Therefore, it would take a quite long time to rinse the electrodes and to reach the conductivity of the to-be-tested streaming solution if the electrodes were not rinsed prior to use. This is an essential precaution especially when the pure DIUF water is used as a streaming medium.

5.8 Experimental Results and Analyses

For a given streaming solution, after the completion of the streaming potential measurements of each channel at a specified flow rate, the averaged values of total 18 readings of ΔP_z and E_s are used in Equation (5.29) with a constant gap size δ and the bulk conductivity λ_b. Thus for each channel (δ), there are three data points which correspond to three different flow rates. Ideally, these three points should be at the same point if they are plotted according to the streaming potential Equation (5.29) (see Figure 5.6), as the equation requires that E_s be proportional to ΔP_z. However, in practical measurements, the measured streaming potential E_s is not exactly proportional to the applied pressure drop ΔP_z for a microchannel at the three specified flow rates. Typical results are plotted in Figure 5.8 for the pure DIUF water and Figure 5.9 for the electrolyte solution containing 10^{-3} M NaCl.

As was described in Section 5.6.4, instead of determining the ζ-potential directly from a measured streaming potential data using Equation (5.26b), in this study, the ζ-potential at the solid-liquid interfaces is determined from the intercept of the linear curve fit of experimental data $\frac{\varepsilon_r \varepsilon_0 \Delta P_z}{\mu E_s \lambda_b}$ versus $\frac{1}{\delta}$ to the streaming potential Equation (5.29). Hence, it is difficult to directly determine the overall accuracy of the ζ-potential determined by using the streaming potential technique. However, an estimate of the accuracy can be pursued based on Equation (5.26b). Taking the logarithmic operation on the classical streaming potential Equation (5.26b) and then differentiating the resultant equation yields:

$$\frac{d\zeta}{\zeta} = \frac{d\lambda_b}{\lambda_b} + \frac{dE_s}{E_s} - \frac{d(\Delta P_z)}{\Delta P_z} \tag{5.30a}$$

From the above equation, the overall error of the present ζ-potential measurements can be related to the total of the following three measurement errors:

$$\frac{d\zeta}{\zeta} = \sqrt{[\frac{d\lambda_b}{\lambda_b}]^2 + [\frac{dE_s}{E_s}]^2 + [\frac{d(\Delta P_z)}{\Delta P_z}]^2} \tag{5.30b}$$

As was described in the experimental aspects (Section 5.7), every effort is made to measure these three parameters accurately. It is examined that, in this experimental investigation, $\frac{d\lambda_b}{\lambda_b} \leq 2\%$ and $\frac{d(\Delta P_z)}{\Delta P_z} \leq 5\%$. In addition, the standard deviation of the measured E_s for the total 18 readings is found to be less than 5%. However, during the streaming potential measurements, the potential difference between the two electrodes in the case of no flows was checked and found to be non-zero, equaling to 5-10 mV, although the potential difference was zeroed prior to the measurements. This is caused by slightly unbalanced potentials between these two electrodes. Since the most measured values of E_s are greater than 300 mV, the relative influence of the above unbalance potential is approximately 3%. Thus the total uncertainty of the streaming potential measurements is within 8%, i.e. $\frac{dE_s}{E_s} \leq 8\%$. Therefore, the overall accuracy of the present ζ-potential determination from the streaming potential measurements can be estimated from Equation (5.30b):

$$\frac{d\zeta}{\zeta} < 10\% \tag{5.30c}$$

5.8.1 Measurements of Surface Conductance Effect

It can be clearly seen from Figures 5.8 and 5.9 that the term $\frac{\varepsilon_r \varepsilon_0 \Delta P_z}{\mu E_s \lambda_b}$ strongly depends on the gap size (δ) of the microchannel tested. This phenomenon is caused by the surface conduction effect as described previously. Furthermore, with all the experimental data for different channels (different δ) but using the same streaming solution, the ζ-potential and the surface conductance λ_s are determined by plotting the data according to Equation (5.29). For the pure DIUF water (λ_b=1.21x10^{-4} S/m), this plot is shown in Figure 5.8. In this figure, three values need to be examined. First, from the intercept ($\frac{1}{\varsigma_c}$) of the least-square linear curve fit, the zeta-potential at the bare glass fiber-water interfaces is equal to ζ_c=-62.2 mV. This ζ-potential is very close to the measured value of finely ground microscope slide particles (Sanders et al., 1995) and in an excellent agreement with the ζ-potential value ($\zeta_c \approx$-56 mV) published by Mala and Li (1997) for glass fiber-water interfaces. Second, from the slope ($\frac{2\lambda_s}{\varsigma_c \lambda_b}$) of the least-square linear curve fit, the surface conductivity is found to be λ_s=6.30x10^{-8} S, which is reasonable in comparison with the surface conductivity values of order 10^{-9}-10^{-8} S for water in glass capillaries (Overbeek, 1952; Hunter, 1981). Finally, the correlation coefficient (r^2) for the linear curve fit to the experimental data is equal to 0.84. Therefore, the linear relationship between $\frac{\varepsilon_r \varepsilon_0 \Delta P_z}{\mu E_s \lambda_b}$ and $\frac{1}{\delta}$ as predicted by Equation (5.29) is statistically supported by the streaming potential data for the bare glass fiber surface-pure DIUF water interfaces.

It has been noted that, in this study, the ζ-potential of glass surfaces (ζ_c) and the surface conductivity λ_s are determined from the least-square linear curve fit to the measured data points in terms of $\frac{\varepsilon_r \varepsilon_0 \Delta P_z}{\mu E_s \lambda_b}$ versus $\frac{1}{\delta}$. As shown in Figure 5.6 and by

Equation (5.29), the intercept and the gradient of the linear curve fit to these data points are equal to $\frac{1}{\zeta_c}$ and $\frac{2\lambda_s}{\zeta_c\lambda_b}$ respectively. Therefore, it is necessary to make uncertainty estimates of the intercept and the gradient determined from the least-square linear curve fit in order to determine the actual accuracy of ζ_c and λ_s. Based on the linear regression analysis method (Mendenhall and Sincich, 1992) and the experimental data for the pure DIUF water plotted in Figure 5.8, a 95% confidence interval for the intercept (i.e. ζ_c) is found to be approximately 14%. In addition, a 95% confidence interval for the gradient is approximately 8%. Bringing the known uncertainties for the gradient (8%), λ_b (2%) and ζ_c (14%) into the gradient expression $\frac{2\lambda_s}{\zeta_c\lambda_b}$, the overall accuracy of λ_s is found to be about 16%. As was discussed in Section 5.6.3, physically, λ_s is the surface equivalent of the bulk conductivity λ_b. In contrast to λ_b, however, it can not be measured directly in practice. Usually, a subtraction step is required in order to obtain λ_s. Hence, 16% is a reasonable accuracy for the determination of a surface excess quantity such as λ_s. Furthermore, as will be shown in Figure 5.9, the dependence of $\frac{\varepsilon_r\varepsilon_0\Delta P_z}{\mu E_s\lambda_b}$ on $\frac{1}{\delta}$ for the electrolyte solution is much weaker than for the pure water case, though the surface conductivity λ_s is expectedly larger for the electrolyte solution. Therefore, the overall accuracy of ζ_c and λ_s determined from the experimental data for an electrolyte solution will be definitely within 14% and 16% respectively.

Similar results for the electrolyte solution (10^{-3} M NaCl) is given in Figure 5.9, where ζ_c= - 22.7 mV, λ_b=105.72x10^{-4} S/m, λ_s=32.20x10^{-8} S and r^2=0.88. As expected, with addition of the electrolyte, the ζ-potential at the glass fiber-water interfaces is decreased due to the compressed EDL near the interfaces at higher ionic concentration. Also as expected, in comparison with those for the pure DIUF water, both the bulk conductivity λ_b and the surface conductivity λ_s increase when 10^{-3} M NaCl is added. However, it is noticed that the former increases by nearly two orders while the latter increases by approximately five times only. In addition, the dependence of $\frac{\varepsilon_r\varepsilon_0\Delta P_z}{\mu E_s\lambda_b}$ on $\frac{1}{\delta}$ for the electrolyte solution is much weaker than for the pure water case, though the surface conductivity λ_s is expectedly larger for the electrolyte solution. This implies that the surface conductance has less relative effect on the measured streaming potentials since it is much smaller than the bulk conductivity λ_b of the electrolyte solution. λ_b is dominant whereas λ_s is negligible for the aqueous solutions containing higher electrolyte concentrations. At this stage, a quantitative evaluation of surface conductance effect is attempted and will be presented as follows.

The Dukhin number is a dimensionless parameter that might best quantify the relative importance of the surface conductance. For a parallel-plate microchannel, Du can be defined as:

$$Du = \frac{2\lambda_s}{\lambda_b \delta} \tag{5.27c}$$

The above equation clearly indicates that the effect of the surface conductance strongly depends on the channel size (δ) and the ratio of the surface conductivity λ_s to the bulk conductivity λ_b. The size influence of the microchannels on the surface conductance effect can be easily estimated for the pure DIUF water. Using the experimental data shown in Figure 5.8, it is calculated that Du=20.82, 10.41 and 6.94 and correspondingly, ζ_c=-2.9, -5.5 and -7.8 mV if the surface conductance effect is completely neglected for the gap size δ=50, 100 and 150 μm, respectively. Therefore, the absolute magnitude of ζ_c is far underestimated (even by an order) if surface conductance is not taken into account. Furthermore, it can be concluded that the surface conductance effect is overwhelmingly dominant in microchannel streaming potential tests for any pure water. Ignorance of the effect inevitably leads to an unacceptably low ζ-potential determined from the streaming potential measurements. Moreover, this effect is still comparable to (104.1%) the bulk conductivity for pure water flowing through even bigger channels (δ=1 mm).

In addition, as shown by Equation (5.27c), the ratio of the surface conductivity λ_s to the bulk conductivity λ_b also plays an important role in the surface conductance effect. For a series of NaCl concentrations, the bulk conductivity λ_b, the surface conductivity λ_s and the Dukhin numbers are plotted in Figure 5.10. For this figure, Du was calculated from Equation (5.27c) in which δ=10 μm and the data for the pure DIUF water were taken as those at 10^{-7} M NaCl solution. Figure 5.10 shows that, with an increase in the electrolyte concentration, the relative surface conductance effect (Du) is quickly reduced because of a large reduction of the ratio of λ_s to λ_b. It is also found from this figure that, for a large channels (δ=1 mm), the surface conductance effect is still substantial as long as the NaCl concentration is below some critical upper limit such as $4.0\text{x}10^{-4}$ M. Above this electrolyte concentration, the influence of λ_s on the inferred ζ-potential is less than 15% and thus negligible because 15% is a usually acceptable measurement error of the ζ-potential. This finding is experimental support for the claim of the significant effect of surface conductance on the ζ-potential that can be expected in 1 mm capillaries at electrolyte concentrations below about $10^{-3.5}$ M given by Hunter (1981).

In the subsequent sections, the detailed effects of the pH values, the two typical electrolytes and the two ionic surfactants on the measured ζ-potential at the glass fiber-water interfaces will be presented briefly. All the experimental results of the measured ζ-potential for various streaming solutions are further listed in Table 5.3 for the bare glass fiber surfaces and in Table 5.4 for the FC725-precoated glass fiber surfaces. As seen from these two tables, when the streaming solution changes, the measured ζ-potentials for the FC725-precoated glass fiber surfaces are smaller than but follow the same pattern as those for the bare glass fiber surfaces. Therefore, only the experimental data for the bare glass fiber surfaces are discussed. In particular, some effort will be made to present a clear contrast between these effects and those on the measured ζ-potential of the O/W emulsion droplets presented in Section 5.4.

5.8.2 pH Effect

The pH value was altered approximately from 3.0 to 10.0 by adding standard dilute solutions of either HCl or NaOH into the pure DIUF water. The measured ζ-potential at the fiber-water interfaces with various pH values is shown in Figure 5.11. Since addition of HCl into the pure DIUF water to lower the pH values exponentially increases the concentration of H^+ ions in the streaming solution, as expected, the selective adsorption of H^+ ions onto the fiber-water interfaces slightly neutralizes the negative ζ-potential. At lower pH values, H^+ ions become the potential-determining ions (p.d.i). At higher pH values, however, OH^- ions become the p.d.i. Their adsorption onto the fiber-water interfaces results in stronger negative ζ-potential at the interfaces. As shown in Figure 5.11, the ζ-potential monotonically decreases from -38.7 to –84.2 mV as the pH value increases from 2.68 to 10.32. The ζ-potential of the bare glass fiber surface in contact with the pure DIUF water (pH≈6.5) was measured to be –62.2 mV, between the above two extremes. In comparison with Cl^- ions at lower pHs or Na^+ ions at higher pHs, H^+ or OH^- ions are much more strongly adsorbed in the region near the fiber-water interfaces such that they determine the ζ-potential at the fiber-water interfaces, respectively. Similar variations of the ζ-potential with the pH value were also observed for the keratin fibers (Jachowicz and Berthiaume, 1989) and for finely ground microscope slide particles (Sanders et al., 1995).

As shown in Figure 5.11, it is unexpected that, even at pH=2.68, the ζ-potential is still negative. The point of zero zeta (pzz) is not yet achieved for the fiber-water interfaces. In the literature, Jachowicz and Berthiaume (1989) reported that the isoelectric point (iep) is at pH=3.7 for untreated keratin fibers. At a pH lower than 3.7, the fiber surface possesses a cationic character, while at a pH higher than 3.7 the keratin surface assumes a negative potential. In addition, the pzz is found to be at pH≈5.0 at the silicone oil-water (O/W) interfaces (Gu and Li, 1998c), which is very close to the published pzz of mineral oil-in-water emulsion droplets (Sanders et al., 1995). However, it is noted that the ζ-potential of the keratin fibers tested by Jachowicz and Berthiaume (1989) is only slightly negatively valued (ζ_c≈-13 mV at pH≈5.5-9.0) and thus can be easily neutralized (pH=3.7) and even slightly positively valued at pH<3.7. In the present case, the ζ-potential at the glass fiber-water interfaces is strongly negatively valued (ζ_c≈-62.2 mV at pH≈6.5). The selective adsorption of H^+ ions adsorption onto the glass fiber-water interfaces is not strong enough to counteract the strongly negative ζ-potential, though it is comparable to that onto the oil-water interfaces. Recently, Sanders et al. (1995) used a particle electrophoresis apparatus to measure ζ-potentials for finely ground microscope slide particles as a function of bulk pH. Their reported ζ-potential values are all negative at all the pH values (pH≈2-11). Hence, it is difficult to reverse the polarity of the strongly negative ζ-potential at the glass fiber-water interfaces purely by lowering the pH values. In the present tests, the piping system is made of stainless-steel tubes and plexiglass connections. In order to avoid excessive acid corrosion of the piping system and possible chemical contamination, measurements of the streaming potential at any lower pH values than pH=2.68 has not been attempted.

5.8.3 Electrolyte Effects

The variations of the measured ζ-potential at the glass fiber-water interfaces with the mole concentration of the following two typical electrolytes, NaCl and $AlCl_3$ from 10^{-6} to 10^{-3} M are plotted in Figure 5.12. At 10^{-6} M, the measured values of the ζ-potential are very close to the value for the pure DIUF water ($\zeta_c \approx -62.2$ mV). At this concentration, both electrolytes do not have appreciable effect on the ζ-potential. As expected, with increase of electrolyte concentrations higher than 10^{-6} M, the absolute value of the ζ-potential gradually becomes smaller. This pattern has been also reported by Mala and Li (1997) and Sanders et al. (1995). Physically, addition of electrolyte will considerably reduce the ζ-potential because of the thin compressed EDL. It is found that the present values of the ζ-potential for the NaCl electrolyte solution are almost same as those reported by Mala and Li (1997) for the KCl electrolyte solution since the chemical properties of these two electrolytes are quite similar.

Furthermore, Figure 5.12 indicates that variations of the ζ-potential with electrolyte concentration for $AlCl_3$ are greater than those for NaCl. This is because of the well-known strong selective adsorption of trivalent cations Al^{3+} onto the fiber-water interfaces. The multivalent cations are more strongly adsorbed onto the solid-water interfaces, and thus their effects on the ζ-potential are more pronounced than the mono-valent cations Na^+. Therefore, the ζ-potential depends not only on the concentrations but also on the ionic valences of the electrolyte used. It is also noticed that, unlike the case for the ζ-potential at the silicone oil-water interfaces, the ζ-potential at the fiber-water interfaces remains negative even until 10^{-3} M $AlCl_3$. Hence, in comparison with the selective adsorption of trivalent cations Al^{3+} onto the oil-water interfaces, such cationic adsorption onto the glass fiber-water interfaces is much less pronounced and thus has less effect on counteracting their original negative ζ-potential.

5.8.4 Effects of Ionic Surfactants

In the experiments with the ionic surfactant solutions, it was found that the adsorption of the ionic surfactants CTAB and SDS onto the glass fiber-water interfaces strongly affected the ζ-potential. Figure 5.13 gives the measured results at different concentrations of CTAB (10^{-6}-10^{-3} M) and SDS (10^{-6}-10^{-2} M). At 10^{-6} M, the measured values of the ζ-potential are close to that of the pure DIUF water. It is seen from Figure 5.13 that the point of zeta reversal (pzr) occurs at a CTAB concentration between 10^{-4} M and 10^{-3} M. This pzr is in a good agreement with the point of zero charge (pzc) of the mica surface somewhere near 10^{-4} M CTAB reported by Israelachvili and Pashley (1984). When the CTAB concentration is increased from the pzr, the measured ζ-potential becomes positive and increases slowly. Physically, the variations of the ζ-potential with CTAB concentration are caused by the well-known cationic adsorption. CTA^+ ions are the potential-determining ions (p.d.i) in this case. The saturation state of cationic adsorption can be considered to occur between 10^{-4} to 10^{-3} M. Since its CMC is about $9.2\text{x}10^{-4}$ M at 25°C (Czerniawski, 1966), no CTAB concentrations higher than 10^{-3} M were tested. Variations of the ζ-potential at the solid-water interfaces with log concentration of SDS from 10^{-6} to 10^{-2} M are also shown in Figure 5.13. As expected, the ζ-potential becomes more negative if more SDS is added into the aqueous solution. For the anionic surfactant solution, $C_{12}H_{25}SO_3^{-1}$ ions of SDS are the p.d.i, and their adsorption onto the glass-water interfaces leads to the change of the ζ-potential with the SDS concentration. On further increase of the SDS concentration, the anionic adsorption process continues until the strongest negative ζ-potential about -90 mV is attained at 10^{-3}-10^{-2} M. The saturation state of the anionic adsorption is considered to be reached between these two concentrations. Since the CMC of SDS at 25°C was determined to be around $8.1\text{x}10^{-3}$ M (Stalidis et al., 1990), the ζ-potential measurements were not attempted with SDS concentrations higher than 10^{-2} M.

All the measured results of the ζ-potential at the glass fiber surfaces in contact with either CTAB or SDS surfactant solutions show that these two ionic surfactants can change the magnitude of the ζ-potential to a great extent and even its polarity. Furthermore, these two surfactants not only differ from each other with respect to their ionic properties but also have different abilities to adsorb onto the fiber-water interfaces. Therefore, they affect the

ζ-potential to quite different extents. Their abilities to influence the ζ-potential at the glass fiber-water interfaces are determined by their rather different activities in the aqueous phase.

5.9 Determination of the EDL Interaction Parameters *Dl*, *Da* and κ^{-1}

Up to now both the zeta-potential (ζ_p) of the silicone oil droplets dispersed in various aqueous solutions and the zeta-potential (ζ_c) of the glass fiber surfaces in contact with these aqueous phases are determined experimentally. Some important EDL interaction parameters can be easily calculated. The dimensionless EDL parameter Dl, the dimensionless EDL asymmetry parameter Da and the Debye-Hückel reciprocal length parameter κ^{-1} for various aqueous solutions are listed in Table 5.3 for the bare glass fiber surfaces and in Table 5.4 for the FC725-precoated glass fiber surfaces. The value following each "±" sign after the measured ζ_p represents its standard deviation, which is within 13% as predicted by Equation (5.18). In the calculation of Dl from Equation (3.37a), the reference radius of oil droplet is chosen as a=10 μm. Da is calculated directly from Equation (3.37b). κ^{-1}, as defined in Equation (3.32), directly reflects the ionic properties such as the ionic concentration and the ionic valence of the aqueous phase. Typical values of κ^{-1} vary by approximately three orders from near 1 μm at its maximum for the pure DIUF water to about 3 nm for the aqueous solutions containing the highest electrolyte concentration (10^{-3} M $AlCl_3$) or the highest surfactant concentration (10^{-2} M SDS).

It is seen from these two tables that when the aqueous phase is changed, Dl and Da for the FC725-precoated glass fiber surfaces follows the same pattern as those for the bare glass fiber surfaces. At pH values below 6.5, the EDL interaction between the oil droplet and the fiber surface is attractive since they are oppositely charged ($\zeta_p > 0$ while $\zeta_c < 0$). However, such EDL interaction becomes repulsive for the pure DIUF water at pH=6.5. As the pH value further increases, the repulsive EDL interaction is even stronger, achieving its maximum greater than 10^5 for the pure DIUF water. It is also noticed that, as expected, addition of electrolyte into the aqueous phase reduces the EDL interaction by almost five times for NaCl and $AlCl_3$. At 10^{-3} M $AlCl_3$, the dimensionless EDL interaction parameter Dl is of order 10^3. Introduction of CTAB leads both ζ_p and ζ_c

to be positive and thus their repulsive EDL interaction is eventually of order 10^4. Since both ζ_p and ζ_c are negative for the pure DIUF water, the more SDS is added into the aqueous phase, the more negative these two potentials become. This results in the stronger repulsive EDL interaction with the maximum Dl greater than 10^5.

In summary, for the bare glass fiber surfaces, Dl switches its sign and changes about two orders from 10^3 to 10^5 as the aqueous phase changes. Accordingly, Da has the same sign as Dl and ranges from 0.00 to 6.69. For the FC725-precoated fiber surfaces, Dl varies in a smaller range from 10^3 to 10^4, though their Da values changes more greatly. It is anticipated that such great changes in Dl and Da will considerably affect the total colloidal interaction between the silicone oil droplets and the glass fiber surfaces, both of which are immersed in an aqueous solution. Combining the vdW interaction and the EDL interaction together, it is feasible to conduct a thorough numerical study of the general effects of A_d for the vdW interaction and Dl, Da and $\tau=\kappa a$ (or κ^{-1}) for the EDL interaction on the oil droplet deposition processes onto the different fiber surfaces across varying aqueous solutions (Chapter 6). Furthermore, in Chapter 7, their specific influence on the deposition processes will be shown and the numerical predictions based on the experimentally determined A_d (Tables 4.8 and 4.9), Dl, Da and $\tau=\kappa a$ (or κ^{-1}) (Tables 5.3 and 5.4) will be compared with the deposition test data.

Table 5.1 Values of the Henry correction factor $f_1(\kappa a)$ used in Equations (5.2) and (5.3) as a function of κa (Henry, 1931; Abramson et al., 1942; Hunter, 1981)

κa	$f_1(\kappa a)$	κa	$f_1(\kappa a)$
0	1.000	5	1.160
1	1.027	10	1.239
2	1.066	25	1.370
3	1.101	100	1.460
4	1.133	∞	1.500

Table 5.2 Temperature increase of the aqueous solution due to the Ohmic heating, as calculated from Equation (5.14) with the concentration of NaCl from 10^{-6} to 10^{-1} M and E=1000 V/m, Δt=10 s, and C_v=1.0 kcal/kg/°C and ρ_w=998 kg/m^3

NaCl (M)	10^{-6}	10^{-5}	10^{-4}	10^{-3}	10^{-2}	10^{-1}
ΔT (°C)	3.02×10^{-5}	3.02×10^{-4}	2.98×10^{-3}	0.03	0.28	2.55

Table 5.3 Zeta-potential (ζ_p) of silicone oil droplets dispersed in aqueous solutions, zeta-potential (ζ_c) of the bare glass fiber surfaces in contact with aqueous solutions and their EDL interaction parameters (Dl, Da and κ^{-1}) across various aqueous solutions

Aqueous Medium	ζ_p (mV)	ζ_c (mV) [a]	Dl [b]	Da [c]	κ^{-1} (10^{-9} m) [d]
DIUF Water	-35.5±2.9	-62.2	+48200	+0.16	966.46
pH=2.68	+27.7±2.1	-38.7	-23400	-2.06	9.46
pH=3.52	+16.1±1.6	-45.6	-16000	-2.59	24.87
pH=4.20	+7.9±0.5	-50.6	-8700	-4.28	54.41
pH=6.50	-35.5±2.9	-62.2	+48200	+0.16	966.46
pH=7.20	-43.7±3.5	-63.8	+60900	+0.07	918.18
pH=8.93	-49.9±4.9	-70.0	+76300	+0.06	148.14
pH=10.32	-58.3±5.5	-84.2	+107200	+0.07	29.90
10^{-6} M NaCl	-40.1±4.2	-58.6	+51300	+0.07	305.62
10^{-5} M NaCl	-45.9±4.3	-39.9	+40000	+0.01	96.65
10^{-4} M NaCl	-28.2±2.9	-27.4	+16900	0.00	30.56
10^{-3} M NaCl	-23.5±2.1	-22.7	+11600	0.00	9.66
10^{-6} M $AlCl_3$	-35.5±3.1	-56.2	+43600	+0.11	124.77
10^{-5} M $AlCl_3$	+46.2±4.2	-30.4	-30700	-2.09	39.46
10^{-4} M $AlCl_3$	+43.4±4.1	-21.3	-20200	-2.26	12.48
10^{-3} M $AlCl_3$	+26.9±2.8	-14.9	-8600	-2.18	3.95
10^{-6} M CTAB	-28.6±2.6	-54.2	+33900	+0.21	305.62
10^{-5} M CTAB	+40.0±3.5	-25.4	-22200	-2.10	96.65
10^{-4} M CTAB	+82.4±6.4	-7.3	-13100	-6.69	30.56
10^{-3} M CTAB	+83.1±6.9	+5.7	+10300	+6.32	9.66
10^{-6} M SDS	-35.9±2.8	-62.6	+49100	+0.16	305.62
10^{-5} M SDS	-40.0±3.7	-75.4	+65900	+0.21	96.65
10^{-4} M SDS	-46.3±4.1	-85.1	+86000	+0.19	30.56
10^{-3} M SDS	-56.8±5.2	-90.5	+112200	+0.11	9.66
10^{-2} M SDS	-58.4±5.6	-92.0	+117300	+0.11	3.06

[a] As estimated from Equation (5.30c), the overall accuracy for the ζ_c measured by the streaming potential technique is within 15%.

[b] Calculated from Equation (3.37a) in which the radius of oil droplet is chosen as a=10 μm.

[c] Calculated from Equation (3.37b).

[d] Calculated from Equation (3.32). For the pure DIUF water, its ionic concentration is assumed to be 10^{-7} M.

Table 5.4 Zeta-potential (ζ_p) of silicone oil droplets dispersed in aqueous solutions, zeta-potential (ζ_c) of the FC725-precoated glass fiber surfaces in contact with aqueous solutions) and their EDL interaction parameters (Dl, Da and κ^{-1}) across various aqueous solutions

Aqueous Medium	ζ_p (mV)	ζ_c (mV) [a]	Dl [b]	Da [c]	κ^{-1} (10^{-9} m) [d]
DIUF Water	-35.5±2.9	-24.5	+19000	+0.07	966.46
pH=2.68	+27.7±2.1	-15.3	-9200	-2.18	9.46
pH=3.52	+16.1±1.6	-18.0	-6300	-2.01	24.87
pH=4.20	+7.9±0.5	-20.0	-3500	-2.46	54.41
pH=6.50	-35.5±2.9	-24.5	+19000	+0.07	966.46
pH=7.20	-43.7±3.5	-25.2	+24000	+0.16	918.18
pH=8.93	-49.9±4.9	-27.6	+30100	+0.18	148.14
pH=10.32	-58.3±5.5	-33.2	+42300	+0.16	29.90
10^{-6} M NaCl	-40.1±4.2	-23.1	+20200	+0.16	305.62
10^{-5} M NaCl	-45.9±4.3	-15.7	+15700	+0.63	96.65
10^{-4} M NaCl	-28.2±2.9	-10.8	+6700	+0.50	30.56
10^{-3} M NaCl	-23.5±2.1	-9.0	+4600	+0.50	9.66
10^{-6} M $AlCl_3$	-35.5±3.1	-22.2	+17200	+0.11	124.77
10^{-5} M $AlCl_3$	+46.2±4.2	-12.0	-12100	-3.05	39.46
10^{-4} M $AlCl_3$	+43.4±4.1	-8.4	-8000	-3.68	12.48
10^{-3} M $AlCl_3$	+26.9±2.8	-5.9	-3500	-3.39	3.95
10^{-6} M CTAB	-28.6±2.6	-21.4	+13400	+0.04	305.62
10^{-5} M CTAB	+40.0±3.5	-10.0	-8700	-3.13	96.65
10^{-4} M CTAB	+82.4±6.4	-2.9	-5200	-15.22	30.56
10^{-3} M CTAB	+83.1±6.9	+2.2	+4000	+17.90	9.66
10^{-6} M SDS	-35.9±2.8	-24.7	+19400	+0.07	305.62
10^{-5} M SDS	-40.0±3.7	-29.7	+25900	+0.04	96.65
10^{-4} M SDS	-46.3±4.1	-33.6	+34000	+0.05	30.56
10^{-3} M SDS	-56.8±5.2	-35.7	+44300	+0.11	9.66
10^{-2} M SDS	-58.4±5.6	-36.3	+46300	+0.12	3.06

[a] As estimated from Equation (5.30c), the overall accuracy for the ζ_c measured by the streaming potential technique is within 15%.

[b] Calculated from Equation (3.37a) in which the radius of oil droplet is chosen as a=10 μm.

[c] Calculated from Equation (3.37b).

[d] Calculated from Equation (3.32). For the pure DIUF water, its ionic concentration is assumed to be 10^{-7} M.

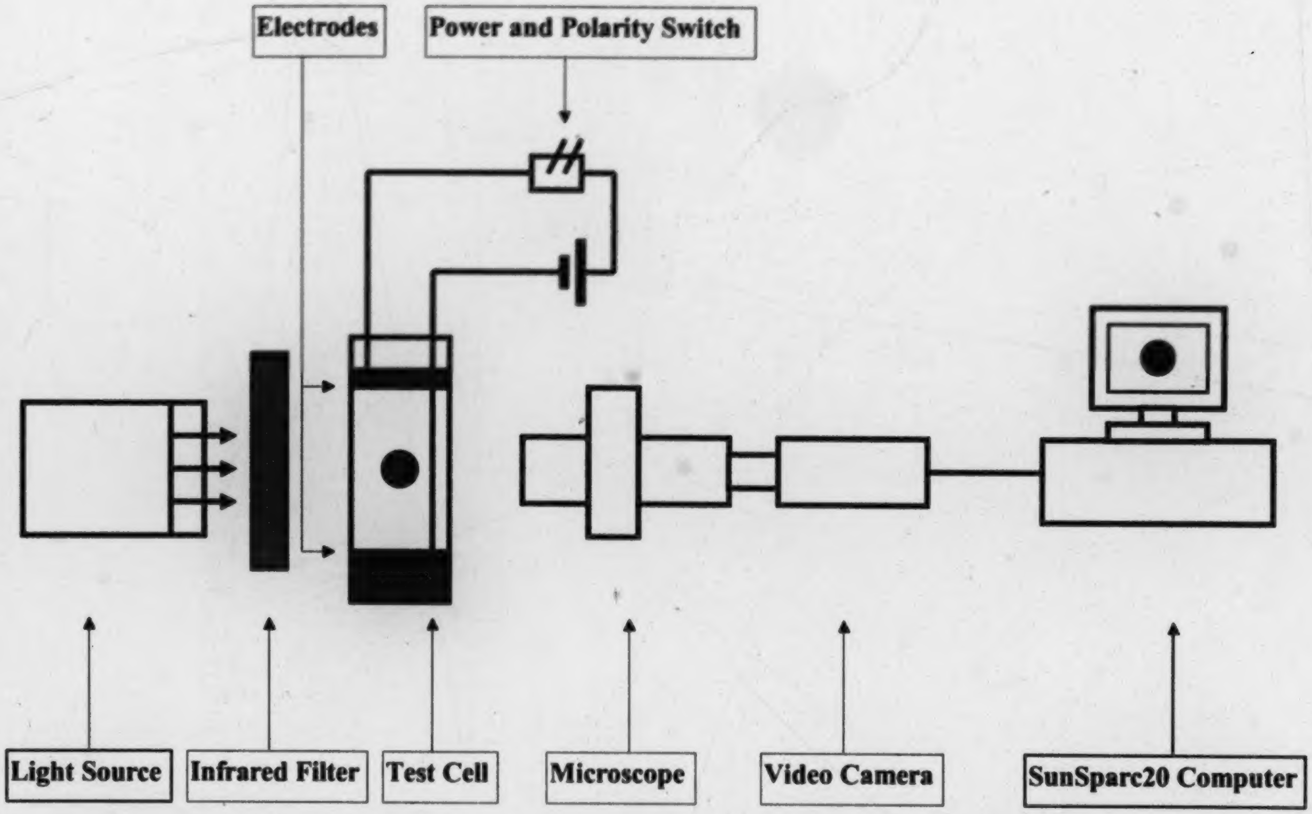
Electrodes
Power and Polarity Switch
Light Source
Infrared Filter
Test Cell
Microscope
Video Camera
SunSparc20 Computer

Figure 5.1 Experimental set-up for measuring the ζ-potential of the silicone oil droplets dispersed in aqueous solutions by using an electrical suspension method

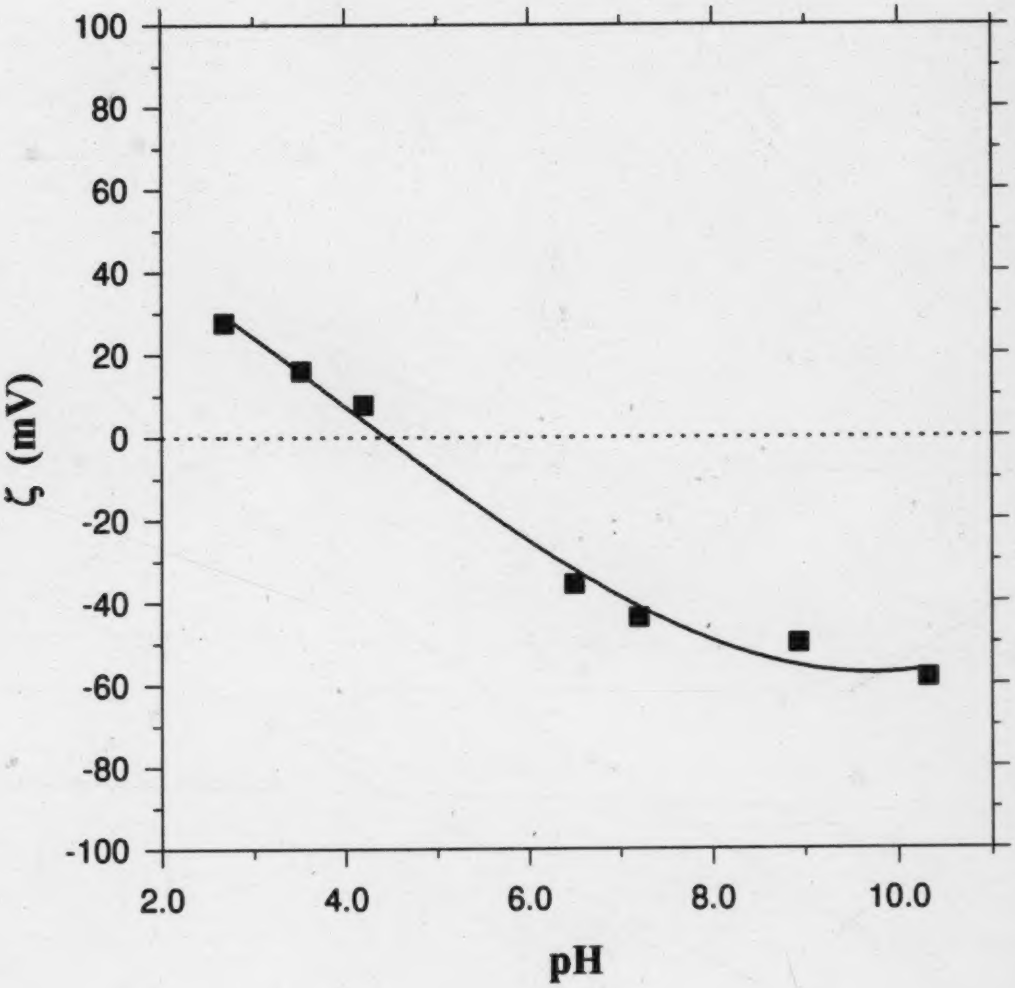

Figure 5.2 The ζ-potential of the silicone oil (no. 1) droplets as a function of pH of the aqueous phase

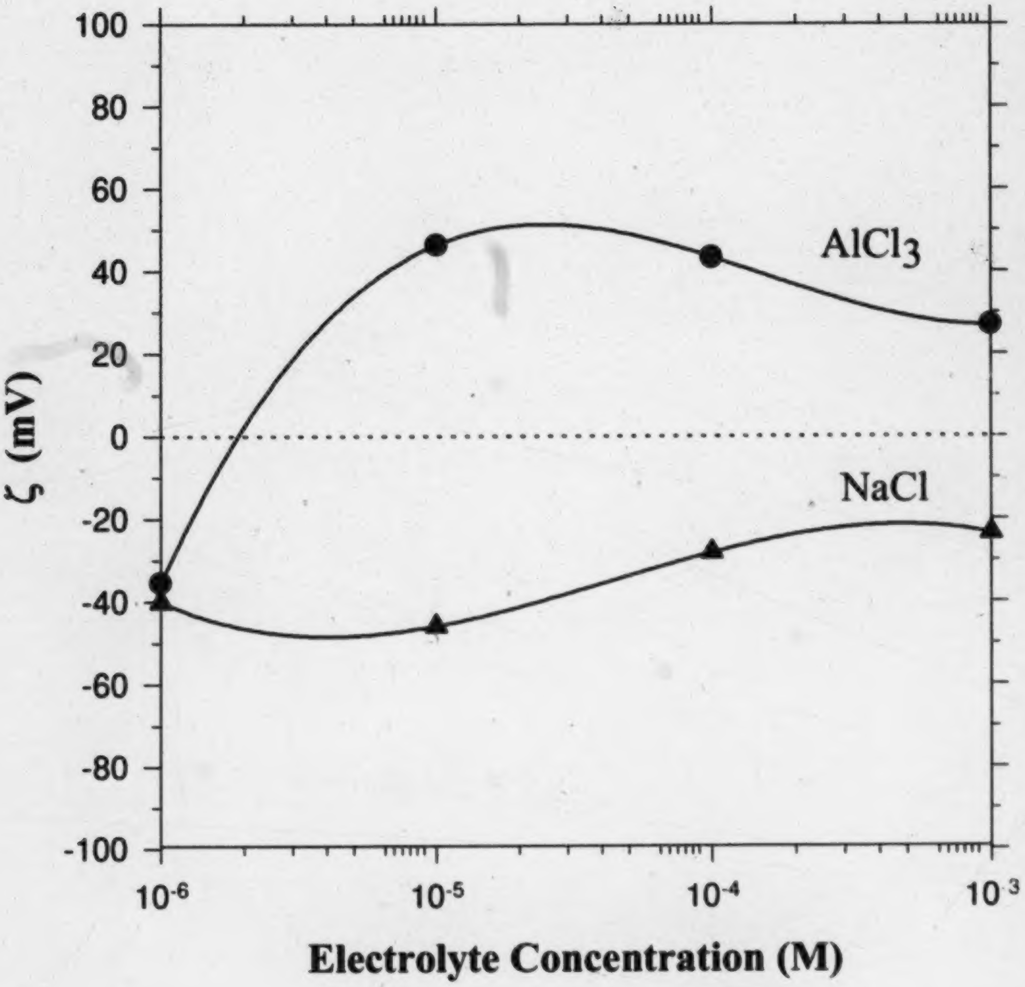

Figure 5.3 The ζ-potential of the silicone oil (no. 1) droplets versus log concentration of two electrolytes with different valences

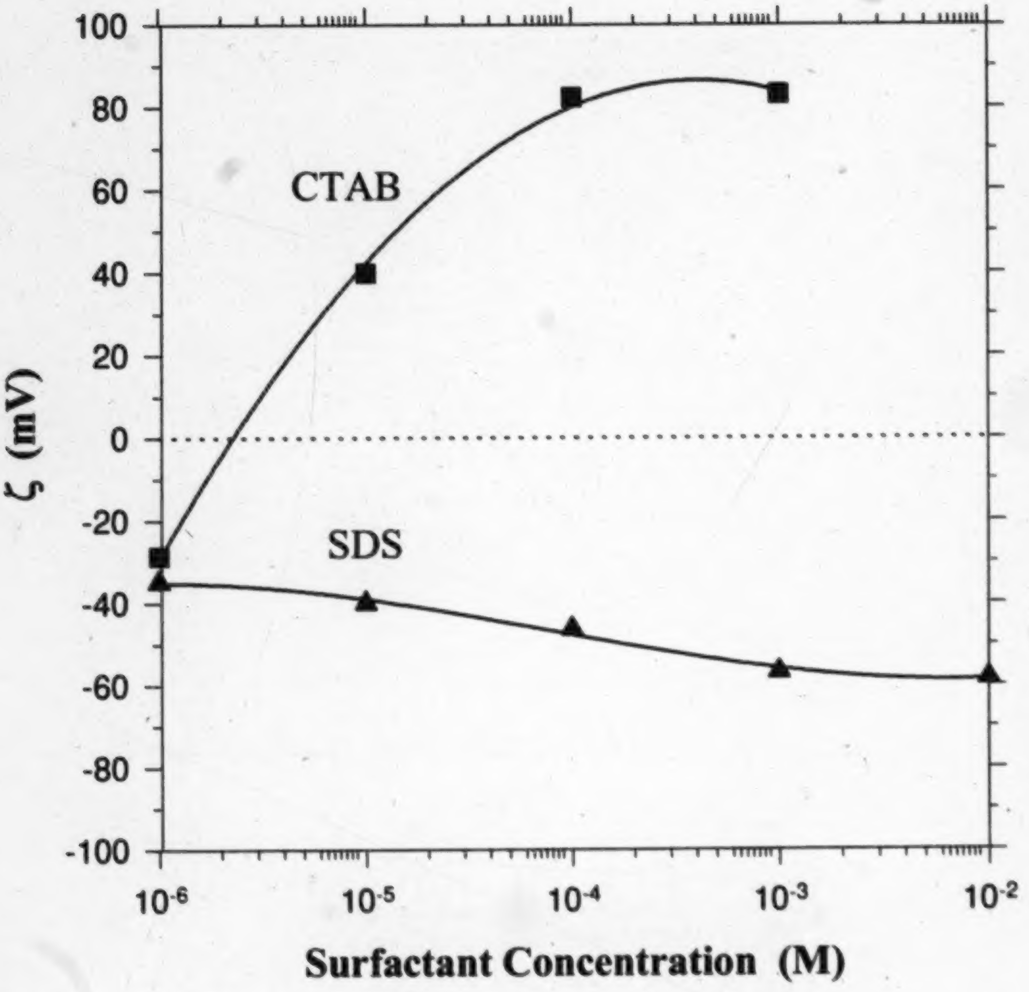

Figure 5.4 The ζ-potential of the silicone oil (no. 1) droplets versus log surfactant concentration of CTAB or SDS

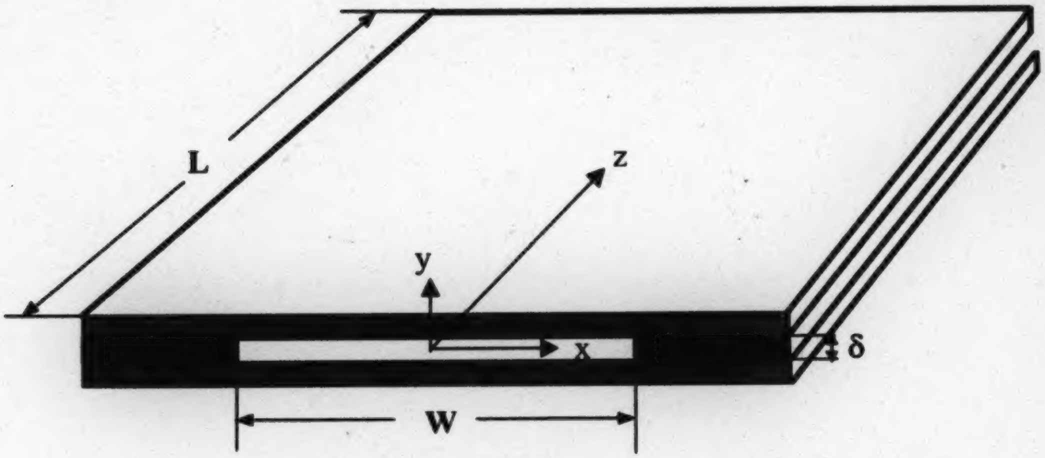

Figure 5.5 Parallel-plate microchannel used in the streaming potential measurements

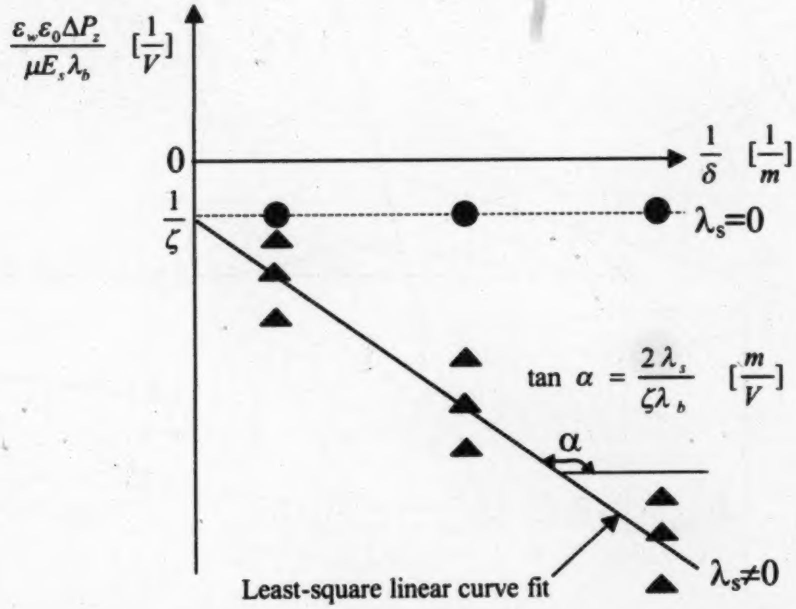

Figure 5.6 The linear relations of $\frac{\varepsilon_w \varepsilon_0 \Delta P_z}{\mu E_s \lambda_b}$ versus $\frac{1}{\delta}$ for the cases of λ_s=0 and λ_s≠0 for determining the ζ-potential at the solid-liquid interfaces and the surface conductivity λ_s from Equation (5.29), using the streaming potential technique

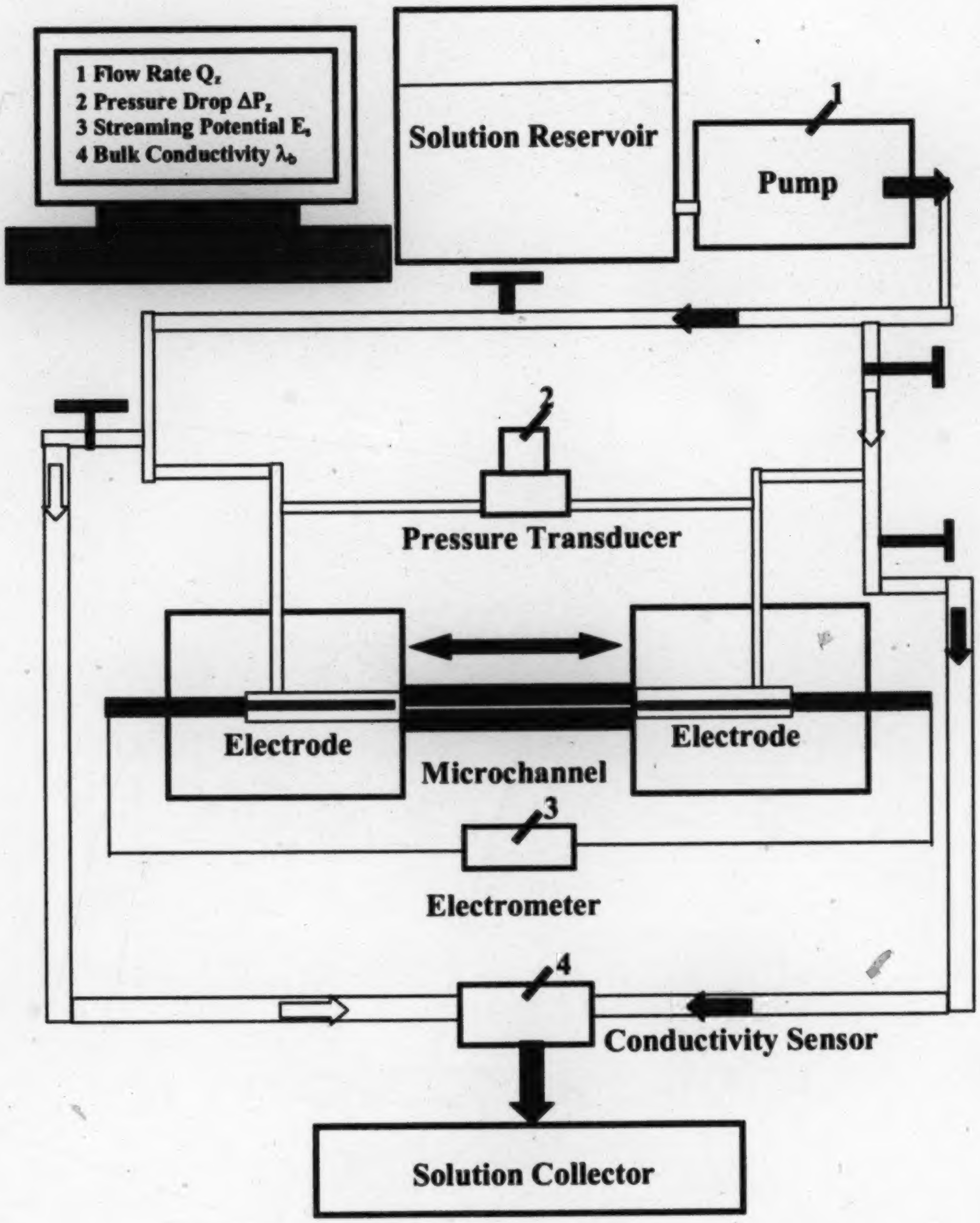
1 Flow Rate Q_z
2 Pressure Drop ΔP_z
3 Streaming Potential E_s
4 Bulk Conductivity λ_b
Solution Reservoir
1
Pump
2
Pressure Transducer
Electrode
Electrode
Microchannel
3
Electrometer
4
Conductivity Sensor
Solution Collector

Figure 5.7 Schematic of experimental set-up for the streaming potential measurements of the parallel-plate microchannel

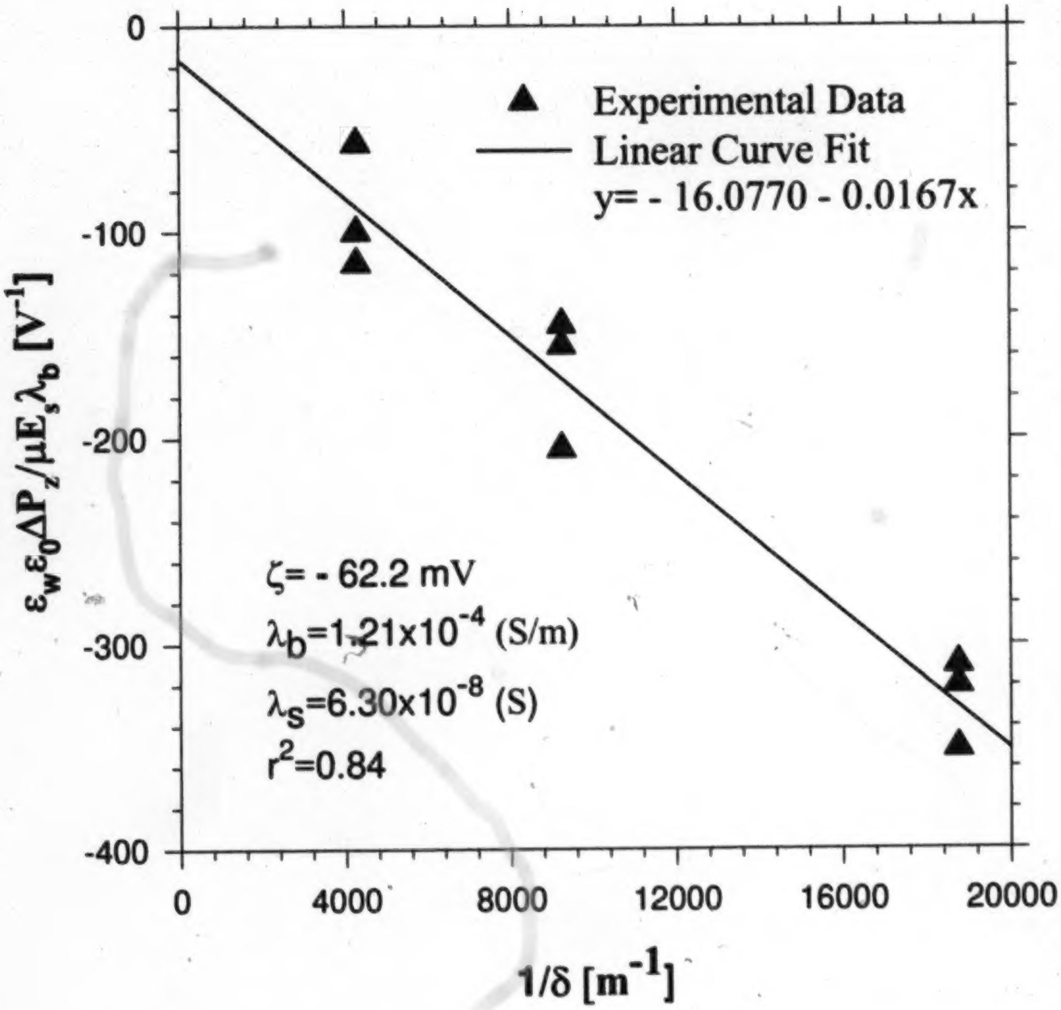

Figure 5.8 Experimental data of the streaming potential measurements and their linear curve fit using Equation (5.29) for the pure DIUF water

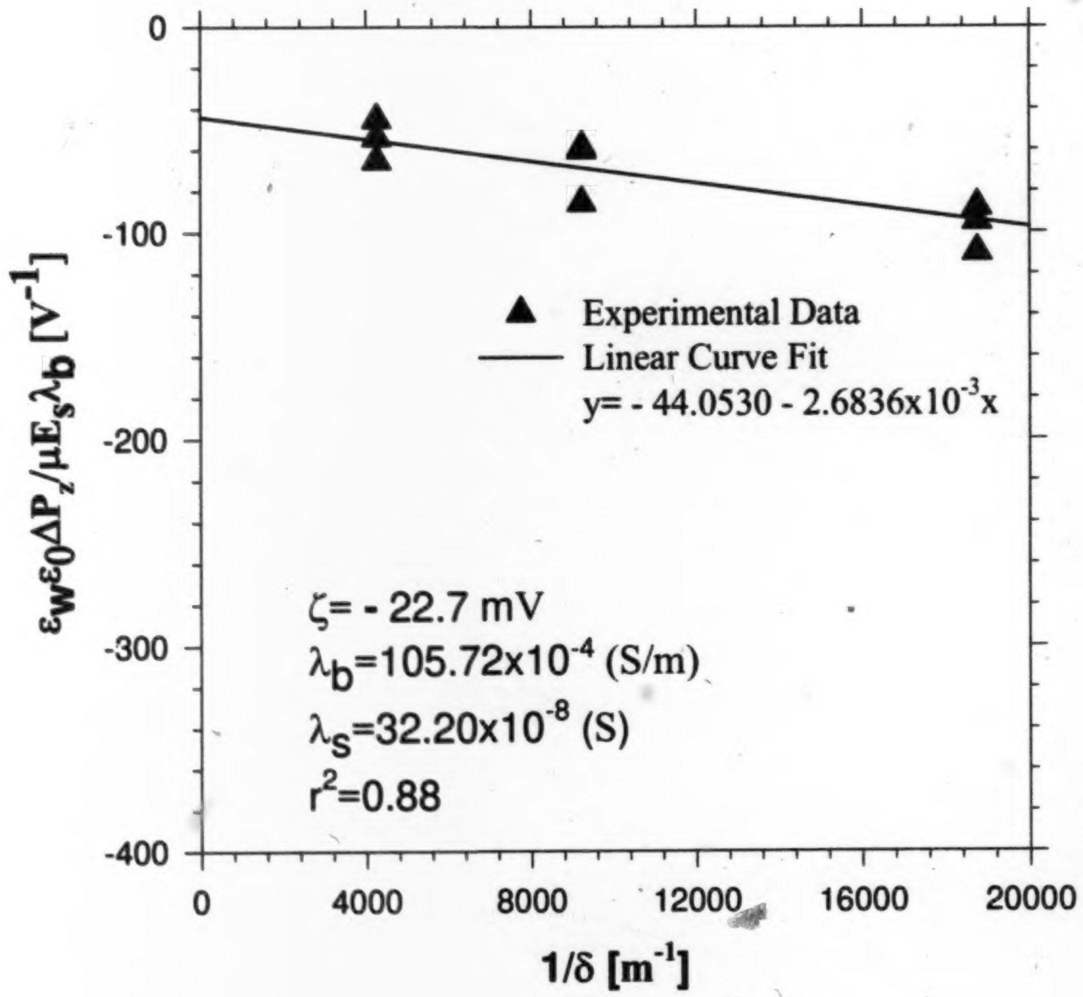

Figure 5.9 Experimental data of the streaming potential measurements and their linear curve fit using Equation (5.29) for the electrolyte solution of 10^{-3} M NaCl

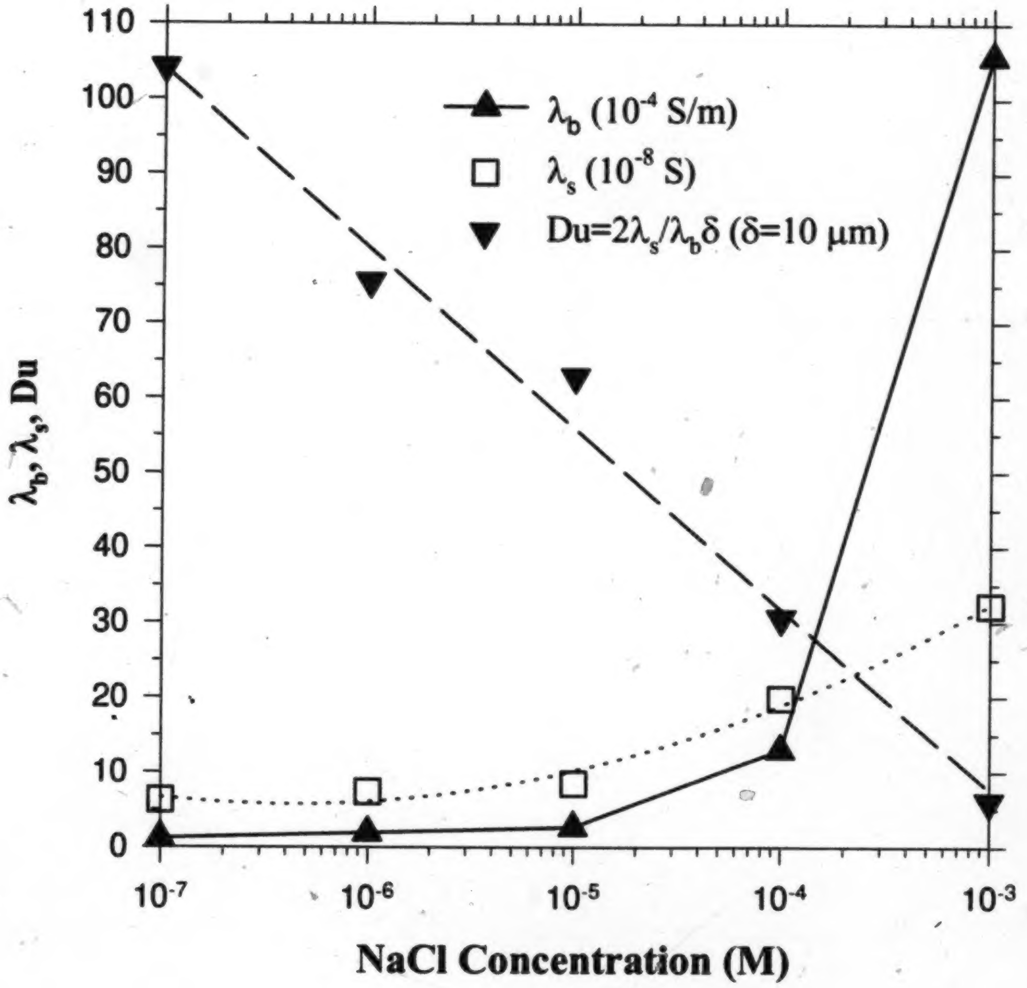

Figure 5.10 Variations of the bulk conductivity (λ_b), the surface conductivity (λ_s) and the Dukhin numer (Du) with log concentration of electrolyte NaCl

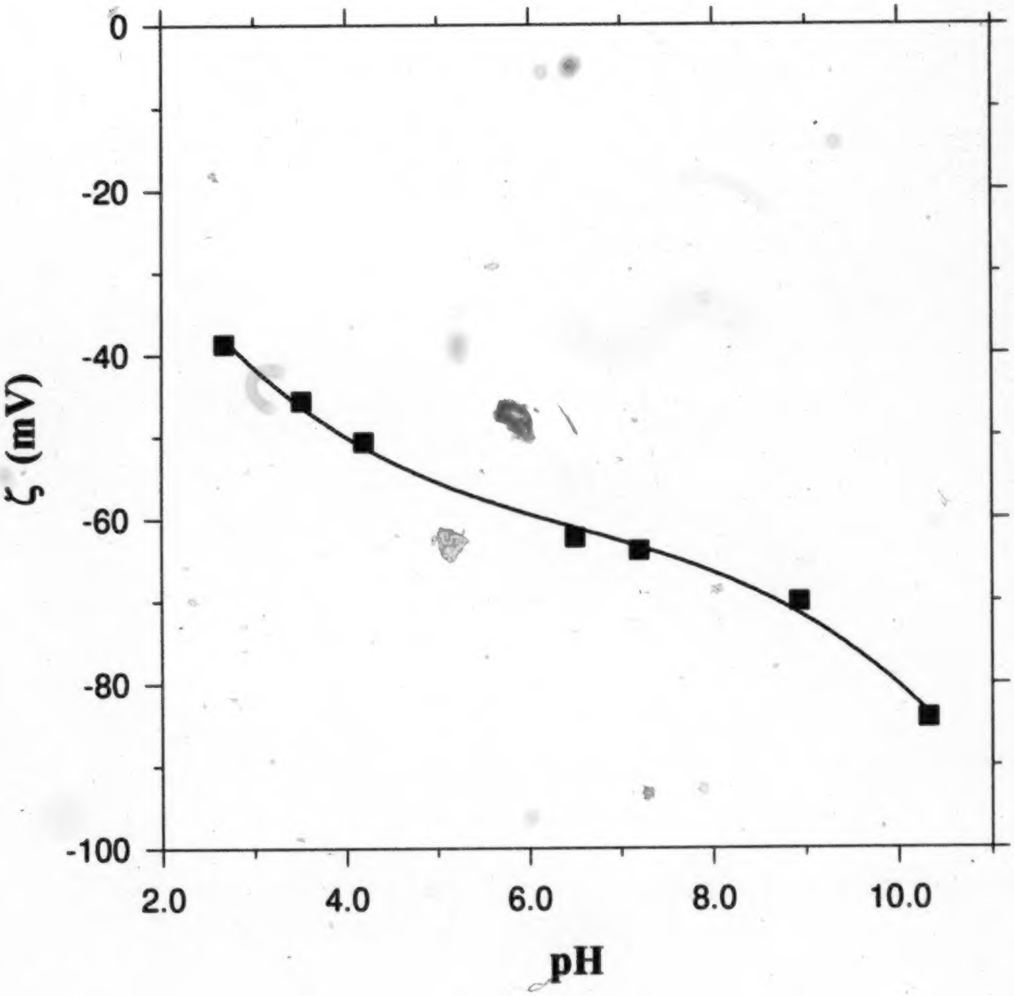

Figure 5.11 Variations of the ζ-potential of glass surfaces with pH of the aqueous phase

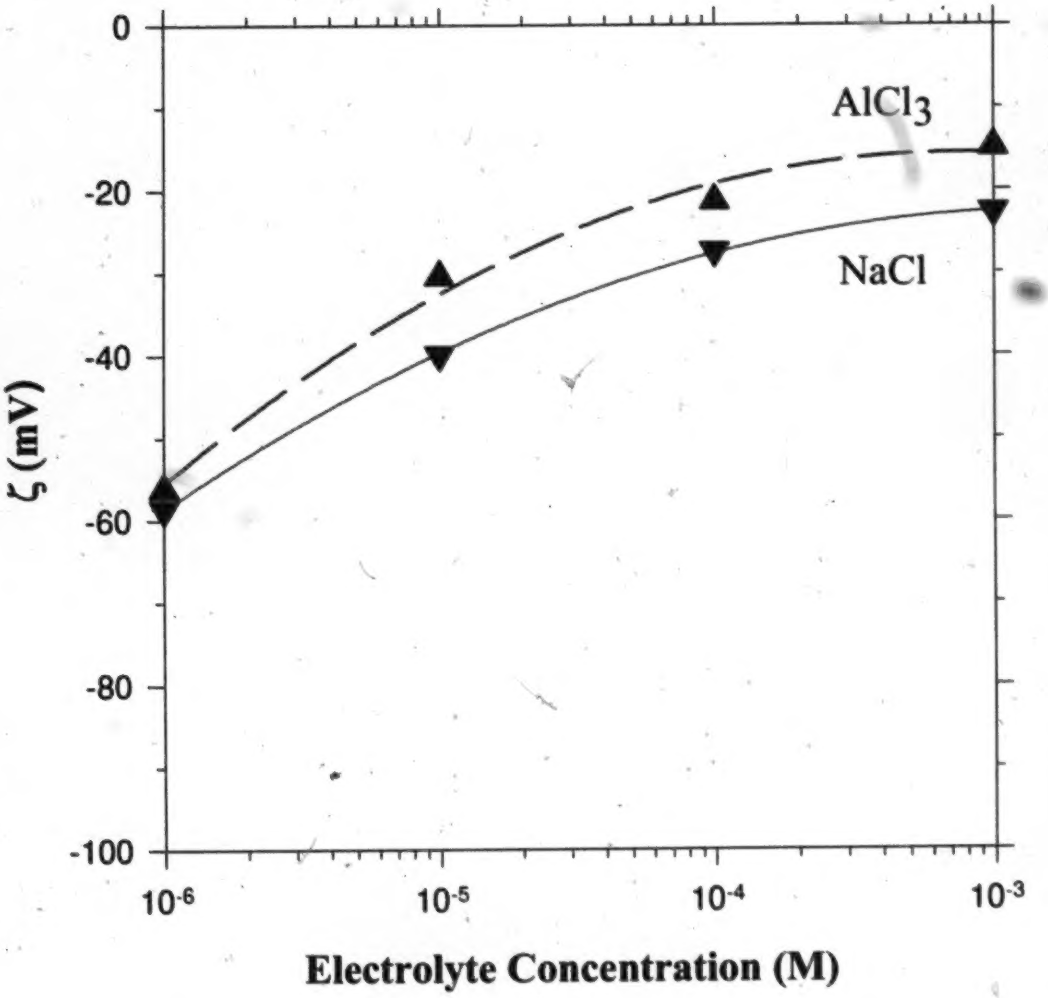

Figure 5.12 Variations of the ζ-potential of glass surfaces with log concentration of two electrolytes having difference valences

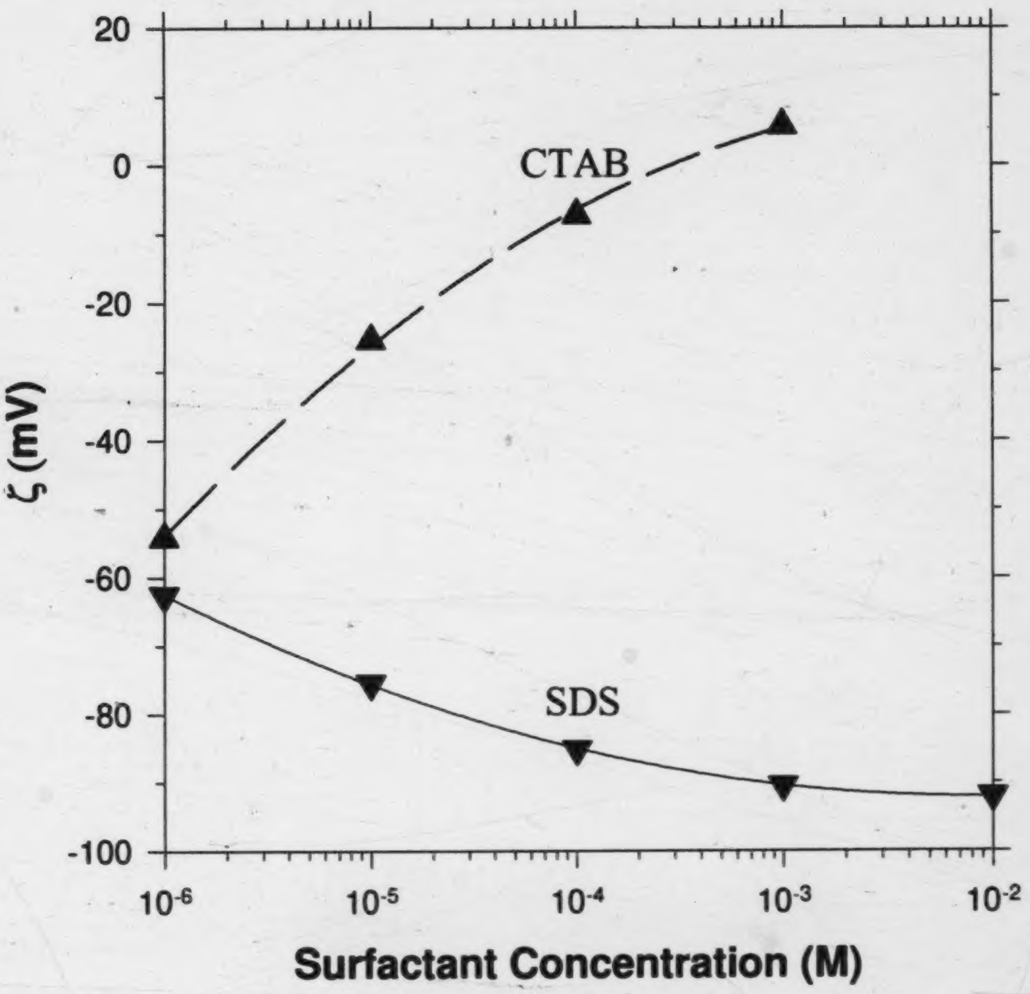

Figure 5.13 Variations of the ζ-potential of glass surfaces with log concentration of two surfactants CTAB and SDS

Chapter 6

Numerical Solutions of Mass Transport Equations

6.1 1-D Mass Transport Equation

6.1.1 Analytical Solution

In Section 2.3, it was shown that, in the absence of external forces, the oil droplet transfer flux onto the solid collector is governed by:

$$\frac{1}{r}\frac{d}{dr}\left[-r\frac{dn(r)}{dr}+\frac{rn(r)F_{col}(r)}{\mathrm{k}T}\right]=0 \tag{6.1}$$

where $\underline{F_{col}(r)} = F_{col}(r)\underline{i_r}$ and thus n=n(r), i.e. both the colloidal force and the droplet number concentration change only along the radial direction in the chosen cylindrical coordinate system (r, ϕ, z) shown in Figure 2.2. Integrating the above equation one time gives:

$$r\frac{dn(r)}{dr}-\frac{rn(r)F_{col}(r)}{\mathrm{k}T}=C_1 \tag{6.2}$$

where C_1 is a constant to be determined. Equation (6.1) as it stands is a second-order ordinary differential equation (ODE). In order to find a unique solution for this equation, two boundary conditions should be specified. The following two boundary conditions are used:

$$n(r)\Big|_{r=r_\infty}=n_\infty \tag{6.3a}$$

$$n(r)\Big|_{r=r_0}=n_0=0 \tag{6.3b}$$

where n_∞ is the oil droplet number concentration in the bulk emulsion at $r=r_\infty$ (an "infinite" distance from the fiber surface. Equation (6.3a) expresses a natural boundary condition, i.e. as r approaches infinity, the droplet number concentration should approach n_∞ in the bulk phase of the emulsion. The second condition given in Equation (6.3b) is often referred to as a "perfect sink" approximation, which is widely used in a number of publications (Adamczyk and van de Ven, 1981b; Adamczyk et al., 1983; Elimelech, 1991; Sanders, et al., 1995). It states that all droplets will be irreversibly attached to the fiber surface once they have reached the so-called primary energy minimum (PEM) region. The PEM is usually deeper than 25 kT and generally located near δ_{PEM}, i.e., $r_0=R+a+\delta_{PEM}$, where R is the radius of the cylindrical fiber and a is the radius of oil droplet. Physically, this condition is valid because once the oil droplets are close to the PEM region, the colloidal interaction force, particularly the attractive vdW force, is so strong that they will be irreversibly trapped in the PEM region and thus deposition occurs.

Using the boundary condition Equation (6.3b), C_1 in Equation (6.2) is equal to:

$$C_1 = r_0 \frac{dn(r)}{dr}\Big|_{r=r_0} = -\frac{r_0 J_0}{D_\infty} \tag{6.4a}$$

Here,

$$J_0 = -D_\infty \frac{dn(r)}{dr}\Big|_{r=r_0} \tag{6.4b}$$

where J_0 is the mass transfer flux of oil droplets toward the fiber surface ($J_0<0$ for deposition case). J_0 is an important quantity to describe how quickly the deposition process happens and will be determined later on. Eventually, droplet concentration distribution is obtained by further integrating Equation (6.2), using Equation (6.4a)

$$n(r) = e^{\int \frac{F_{col}(r)}{kT} dr} [-\frac{r_0 J_0}{D_\infty} \int \frac{1}{r} e^{-\int \frac{F_{col}(r)}{kT} dr} dr + C_2] \tag{6.5}$$

Both J_0 and C_2 given in Equation (6.5) are dependent on the above two boundary conditions given in Equations (6.3a,b).

Equation (6.5) as well as the two boundary conditions, Equations (6.3a.b), can be simplified by introducing the following dimensionless variables and parameters:

$$\bar{n} = \frac{n}{n_\infty},\ H = \frac{r-R-a}{a},\ \bar{F}_{col}(H) = \frac{F_{col}(r)}{\frac{kT}{a}},\ A = \frac{R}{a}, \tag{6.6}$$

where H is the dimensionless separation distance or gap between droplets and fiber surface. Thus Equations (6.3a,b), (6.4b) and (6.5) become,

$$\bar{n}(H)\big|_{H=H_\infty} = 1 \tag{6.7a}$$

$$\bar{n}(H)\big|_{H=H_0} = 0 \tag{6.7b}$$

and

$$Sh = -\frac{J_0}{\frac{D_\infty n_\infty}{a}} = \frac{d\bar{n}(H)}{dH}\Big|_{H=H_0} \tag{6.8}$$

$$\bar{n}(H) = e^{\int \bar{F}_{col}(H)dH}[Sh\int \frac{g(H_0)}{g(H)} e^{-\int \bar{F}_{col}(H)dH} dH + \overline{C_2}] \tag{6.9}$$

where $H_\infty = \frac{r_\infty - R - a}{a}$, $H_0 = \frac{\delta_{PEM}}{a} = \bar{\delta}_{PEM}$, g(H)=H+1+A, $\overline{C_2} = \frac{C_2}{n_\infty}$. As defined in Equation (6.8), Sh is the Sherwood number (Sh>0 for deposition case), which represents the dimensionless mass transport flux and can be calculated from the gradient of the dimensionless droplet concentration profile at the PEM region where $H_0 = \bar{\delta}_{PEM}$. Noting the axisymmetry involved in the deposition system, the mass transfer flux J_0 or the Sherwood number (Sh) is constant over the entire collector if only the vdW and EDL interaction forces are taken into account. Equation (6.9) is the analytical solution of the one-dimensional (1-D) mass transport Equation (6.1). In principle, once the other dimensionless parameters, $\bar{F}_{col}(H)$, H_∞, H_0 and A are given, the two dimensionless constants, Sh and $\overline{C_2}$ involved in Equation (6.9), can be determined from the boundary conditions in Equations (6.7a.b).

However, it is usually difficult to obtain an explicit expression of the analytical solution Equation (6.9) for 1-D mass transport Equation (6.1) unless $\bar{F}_{col}(H)$ can be expressed explicitly as an extremely simple function. Moreover, it is also difficult to determine Sh and $\overline{C_2}$ directly from the boundary conditions Equations (6.7a,b). The colloidal force $\bar{F}_{col}(H)$ consists of the vdW interaction force $\bar{F}_{vdW}(H)$ and the EDL interaction force $\bar{F}_{EDL}(H)$. As were derived in Chapter 3, the vdW and EDL interaction forces between a spherical oil droplet and a cylindrical fiber are complicated functions which themselves are also expressed in the form of integral equations. This fact makes it almost impossible to obtain any meaningful explicit expression by integrating Equation (6.9) directly. Alternatively, the droplet number concentration distribution function, n(r), can be readily determined by integrating Equation (6.1) numerically, in conjunction with the boundary conditions given by Equations (6.3a,b).

6.1.2 Numerical Solution

By using the dimensionless variables and parameters defined in Equation (6.6), Equation (6.2) can be changed into:

$$\frac{d\bar{n}(H)}{dH} - \bar{F}_{col}(H)\bar{n}(H) = Sh\frac{g(H_0)}{g(H)} \tag{6.10}$$

Equation (6.10) can be integrated numerically by using, e.g., the 4th-order Runge-Kutta technique. The boundary conditions remain the same as those given in Equations (6.7a,b).

Recognizing that Equation (6.10) is a linear ordinary differential equation, one can relate a guess value for Sh to the corresponding value of the bulk droplet concentration by

$$\frac{(Sh)_{actual}}{(Sh)_{guess}} = \frac{(\bar{n}_\infty)_{actual}}{(\bar{n}_\infty)_{cal}} = \frac{1}{(\bar{n}_\infty)_{cal}} \tag{6.11}$$

In this way, the second boundary condition, where $\bar{n}(H_0) = 0$ and $Sh = \frac{d\bar{n}(H_0)}{dH}$, is satisfied by assigning a value to Sh, since its actual value is unknown. This value is represented by $(\mathrm{Sh})_{\mathrm{guess}}$ in the above equation. The numerical solution of $\bar{n}(H)$ can be obtained by directly integrating Equation (6.10) from the second boundary condition where $\bar{n}(H_0) = 0$ to some "infinite" distance $H = H_\infty$. This calculation subsequently provides a value of the bulk droplet concentration at $H = H_\infty$, which is expressed as $(\bar{n}_\infty)_{cal}$ in the above relation. This value may not be equal to unity as required by the first boundary condition, i.e. $(\bar{n}_\infty)_{actual} = 1$ at $H = H_\infty$. Hence, the only remaining unknown quantity in Equation (6.11) is $(\mathrm{Sh})_{\mathrm{actual}}$, the actual value of the dimensionless mass transfer rate at the collector surface. Once $(\mathrm{Sh})_{\mathrm{actual}}$ is found, the actual distribution of oil droplet number concentration $\bar{n}(H)$ can be uniquely determined by again numerically integrating Equation (6.10) from $H=H_0$, where $\bar{n}(H_0) = 0$, to $H=H_\infty$, where $\bar{n}(H_\infty) = 1$.

Computational tests are performed to estimate the influence of the lower (H_0) and the upper (H_∞) integration limits on the droplet concentration distribution. It is found that the calculated results become insensitive to the chosen values of the lower and the upper integration limits as long as $H_0 \leq 5\text{x}10^{-3}$ and $H_\infty \geq 20$. A sensitivity analysis for the upper integration limit H_∞ was implemented with respect to the final numerical results (i.e. Sh number) of the 1-D model predictions and will be presented in Section 6.1.5. Therefore, in the numerical simulations, the lower and the upper integration limits are taken as $H_0=10^{-3}$ and $H_\infty=40$, respectively.

6.1.3 The Colloidal Force and the Transforming Function

In Equation (6.10), $\overline{F}_{col}(H)=\overline{F}_{vdW}(H)+\overline{F}_{EDL}(H)$ represents the total force of the retarded dimensionless vdW interaction force and the dimensionless EDL interaction force between an oil droplet and a cylindrical fiber surface. If the cylindrical fiber is assumed to be infinitely long so that its end effects on the deposition process can be ignored, these two forces can be expressed as follows, using Equation (3.17b) in Section 3.2 and Equation (3.22) in Section 3.3 for $\overline{F}_{vdW}(H)$ and Equation (3.51) in Section 3.9.3 for $\overline{F}_{EDL}(H)$:

$$\overline{F}_{vdW}(H)=\frac{F_{vdW}(H)}{\frac{\mathbf{k}T}{a}}=A_d[(\frac{6\overline{\lambda}}{\overline{\lambda}+\overline{s}H})\overline{F}_2(H,A)+\frac{6\overline{\lambda}\,\overline{s}}{(\overline{\lambda}+\overline{s}H)^2}\overline{V}_2(H,A)] \qquad (6.12a)$$

and

$$\overline{F}_{EDL}(H)=\frac{F_{EDL}(H)}{\frac{\mathbf{k}T}{a}}=\overline{F}_2(H) \qquad (6.12b)$$

where, $A_d=\frac{A_{132}}{6\mathbf{k}T}$ is the dimensionless adhesion number. Functions $\overline{F}_2(H,A)$ and $\overline{V}_2(H,A)$ in Equation (6.12a) are given by Equations (3.18) and (3.11) respectively. As was discussed in details in Section 3.4, $\overline{s}$ is a constant equal to 11.116 and $\overline{\lambda}$ is chosen as 0.01 (corresponding to a=10 μm) in the numerical simulations. It is also noted that, in Chapter 3, the vdW interaction force is alternatively nondimensionalized by $\frac{A_{132}}{a}$ as defined in Equation (3.17a) for convenience over there. Equations (6.12a.b) show that $\overline{F}_{vdW}(H)$ and $\overline{F}_{EDL}(H)$ are functions of the dimensionless separation distance H. Furthermore, Equation (6.12a) indicates that the dimensionless vdW interaction force $\overline{F}_{vdW}(H)$ also depends on two dimensionless parameters: A and A_d. In Equation (6.12b), function $\overline{F}_2(H)$ for the EDL interaction force is expressed by Equation (3.51). Referring to Equation (3.51), the EDL interaction force $\overline{F}_{EDL}(H)$ also depends A and the other three dimensionless EDL interaction parameters: Dl, Da and τ. In this chapter, Equations (6.12a,b) will be used to calculate the overall dimensionless colloidal force $\overline{F}_{col}(H)=\overline{F}_{vdW}(H)+\overline{F}_{EDL}(H)$ required in the mass transport equations.

It has been pointed out in Chapter 3 that both the vdW and EDL interaction forces are extremely stiff functions of the dimensionless separation distance H. Therefore, the adaptive integration technique was utilized in order to predict these two forces accurately over the large range of H ($10^{-3}\leq H\leq 100$). For the same reason, Equation (6.10) is characterized by an extremely rapid change near the location of the PEM $H=H_0$, where these two colloidal forces decay very rapidly with H. It is also seen that here the dimensionless distance variable H changes more than four orders from approximately $H_0=10^{-3}$ to $H_\infty=40$. Hence, some effort should be made in order to improve the accuracy of numerical predictions of the droplet concentration distribution and the Sh number from Equation (6.10). Here, a special transforming function is introduced in the numerical scheme to transform the dimensionless separation distance H into a new variable α by:

$$\alpha=\frac{\ln(\frac{H}{H_0})}{\ln(\frac{H_\infty}{H_0})} \tag{6.13}$$

This transforming function ensures a continuous change of the mesh size in the new radial coordinate α from 0 to 1, corresponding to the change of H from $H_0=10^{-3}$ to $H_\infty=40$. In addition, a uniform mesh size for α ($0\leq\alpha\leq 1$) can be used and calculation accuracy can be improved by simply reducing the mesh size. Accordingly, Equation (6.10) and its boundary conditions Equations (6.7a,b) can be transformed as follows:

$$\frac{d\overline{n}(\alpha)}{d\alpha}-\overline{F}_{col}(\alpha)B(\alpha)\overline{n}(\alpha)=Sh\frac{G(0)}{G(\alpha)}B(\alpha) \tag{6.14}$$

$$\overline{n}(\alpha)\Big|_{\alpha=1}=1 \tag{6.15a}$$

$$\bar{n}(\alpha)|_{\alpha=0} = 0 \tag{6.15b}$$

where, $B(\alpha) = H_0(\frac{H_\infty}{H_0})^\alpha \ln(\frac{H_\infty}{H_0}), H(\alpha) = H_0(\frac{H_\infty}{H_0})^\alpha$ and

$G(\alpha) = g[H(\alpha)] = H_0(\frac{H_\infty}{H_0})^\alpha + 1 + A$

This kind of transformation will make the numerical integration not only much easier (constant mesh size) but also much more accurate and efficient (quick convergence).

6.1.4 1-D Numerical Results and Discussion

Based on the DLVO theory, the total colloidal force is composed of the vdW interaction force and the EDL interaction force. As stated above, the overall colloidal force $\bar{F}_{col}(H)$ between the oil droplets and the cylindrical fiber surfaces in the aqueous phases can be fully described by the following dimensionless parameters: A and A_d for the vdW force, and A, Dl, Da and τ for the EDL force. With the transformed governing Equation (6.14) and the boundary condition Equations (6.15a,b), a parametric study can be conducted for these dimensionless parameters. Because the total colloidal interactions are characterized by five dimensionless parameters, i.e. A, A_d, Dl, Da and τ, a systematic study of their effects on the deposition process is prohibitive. Since the curvature effects of the cylindrical fiber represented by $A = \frac{R}{a}$ on the vdW and EDL interaction forces have been thoroughly investigated in Chapter 3, it will be chosen as A=10 as a typical input value. In addition, the dimensionless asymmetric EDL parameter Da is chosen as Da=0 for simplicity. Therefore, some typical values for the remaining three dimensionless parameters were chosen as follows. (i) A_d=0.06, 0.60 and 6.00, represent weak, middle and strong vdW interactions respectively; (ii) Dl=-10^5, -10^4, -10^3, which represent the strong attractive EDL interactions, +10, +20 and +30, which represent the repulsive EDL interactions; and (iii) τ=κa=5 (lower electrolyte concentrations or smaller oil droplets), 10 and 100 (higher electrolyte concentrations or larger oil droplets). These values cover almost all practical cases of interest. Their selections are also based on those values that have been determined in the previous chapters, e.g., A_d=0.16-5.35 (see Tables 4.8 and 4.9), Dl≈±(10^3-10^5) and τ≈4-1000 (Tables 5.3 and 5.4). The detailed numerical results of the influence of these three dimensionless parameters on the local dimensionless droplet number concentration distributions $\bar{n}(H)$ and particularly the dimensionless mass transfer rate Sh numbers will be presented and analyzed in the following paragraphs.

The typical profile of the oil droplet number concentration $\bar{n}(H)$ is shown in Figure 6.1a in which H is plotted on a linear scale and in Figure 6.1b in which H is plotted in common log scale with A_d=6.0, Dl=-10^3 and τ=5. The Sherwood number is found to be Sh=0.0645 in this case. These two figures show that the droplet number concentration changes continuously from zero close to the solid surface where $H=H_0$ to unity at the "infinity" $H=H_\infty$ such that the two boundary conditions expressed by Equations (6.7a,b) are satisfied. In particular, as clearly seen from Figure 6.1b, the droplet number concentration remains zero at smaller $H \leq 1.0$. This depletion zone, where $\bar{n}(H)$=0, is caused by the "perfect sink" approximation, $\bar{n}(H_0) = 0$. In the present case, both strong attractive vdW and EDL interaction forces are assumed. Hence, once the droplets are in the vicinity of the solid surface ($H \leq 1.0$), they are strongly attracted by the surface and thus irreversibly trapped into the PEM region. Moreover, it is also noted that Figure 6.1b gives a more clear and representative picture of the actual droplet number concentration distribution, especially at smaller H values. The region at smaller H values is much more interesting than the region farther away from the solid surface because the Sherwood number is defined at $H=H_0$ and equal to the local slope of the concentration profile. The droplet number concentration distribution near $H=H_0$ will directly affect the deposition rate of the oil droplet onto the solid surface. In addition, Figure 6.1b justifies necessity of the transforming function introduced in Equation (6.13). Hereafter, only the droplet number concentration profiles with H in the log scale will be plotted.

Figure 6.2a shows $\bar{n}(H)$ for A_d=0.06, 0.60 and 6.00 at Dl=+10 and -10^3 respectively (τ=5). The Sh number versus A_d is plotted in Figure 6.2b for the same values of A_d, Dl and τ. It is seen from Figure 6.2b that, when either Dl≥+20 or Dl≤-10^3, Sh is strongly dependent on Dl only, regardless of A_d from 0.06 to 6.00. This means that such deposition processes are dominated by the EDL interaction force, irrespective of its repulsive or attractive features. Only when Dl=+10 (τ=5), for weak repulsive EDL interaction, the vdW force (A_d) becomes comparable to the EDL force and thus important in determining the mass transfer rate. Correspondingly, Sh increases from below 0.035 to above 0.045 as A_d increases from 0.06 to 6.00. In this case, as shown in Figure 6.2a, $\bar{n}(H)$ profile slightly changes as A_d is altered. In comparison with the those for the strong attractive EDL force ($Dl=-10^3$), the droplet number concentration distributions also clearly indicate that the repulsive EDL force enables the depletion zone rather closer to the solid surface (within $H \le 0.1$) and causes $\bar{n}(H)$ to increase more quickly in the intermediate range of $0.1 \le H \le 1.0$. Farther away from the solid surface, the vdW becomes predominant and thus $\bar{n}(H)$ reaches unity at $H=H_\infty$. Hence, based on the numerical calculations presented here, it can be concluded that the attractive vdW interaction is a necessary condition to ensure deposition occurring. Nevertheless, it only affects the droplet number concentration distribution $\bar{n}(H)$ and the mass transfer rate Sh to a limited extent.

The specific effect of the dimensionless EDL interaction parameter Dl on the deposition process is shown in Figure 6.3a for the droplet number concentration distribution $\bar{n}(H)$ at $A_d=6.00$ and $\tau=5$. This figure clearly shows the variation of $\bar{n}(H)$ with Dl. As the attractive EDL interaction is reduced, the depletion zone is reduced from $H \approx 2.0$ for $Dl=-10^5$ to $H \approx 1.0$ for $Dl=-10^3$. Once the EDL interaction becomes repulsive ($Dl>0$), the depletion zone rapidly shrinks within $H \le 0.3$. On the other hand, when $Dl=+20$ or $+30$, $\bar{n}(H)$ increases quickly beyond the depletion zone. As indicated before, since the attractive vdW force at $A_d=6.00$ is comparable in magnitude to the repulsive EDL force at $Dl=+10$, in this case $\bar{n}(H)$ (the dotted line in Figure 6.3a) increases slowly at the smaller H ($0.1 \le H \le 1.0$), followed by a rapid increase to $\bar{n}(H_\infty)=1$. This phenomenon is caused by the following competing facts between the vdW and EDL interactions at different ranges of the dimensionless separation distance H: (i) at $H \ll 1$ ($10^{-3} \le H \le 0.1$), the attractive $\bar{F}_{vdW}(H)$ is dominant and thus the depletion zone forms; (ii) at $H \approx 1$ ($0.1 \le H \le 1$), the repulsive $\bar{F}_{EDL}(H)$ counteracts the attractive $\bar{F}_{vdW}(H)$ and thus

$\bar{n}(H)$ increases gradually; (iii) at H»1 (1≤H≤40), again the attractive $\bar{F}_{vdW}(H)$ plays a major role in determining the droplet number concentration distribution.

The above analyses are also supported by variation of the dimensionless mass transfer rate Sh with the dimensionless EDL interaction parameter Dl shown in Figure 6.3b. As expected, with the increase in the attractive EDL interaction, Sh increases. However, once $\bar{F}_{EDL}(H)$ becomes repulsive (Dl>0), Sh is reduced much more quickly. It is noticed that the reduced radius τ=κa of the oil droplet also plays an important role in determining the effect of $\bar{F}_{EDL}(H)$ on Sh. The smaller τ is, the larger its influence is on Sh. Especially when τ=100, the effect of $\bar{F}_{EDL}(H)$ on Sh becomes negligible and thus the deposition process is solely controlled by the attractive $\bar{F}_{vdW}(H)$. As was discussed in detail in Section 3.10 and expressed by Equation (3.52), the appreciable EDL interaction occurs only within a region (H≤H$_{max}$), where $H_{max} = \frac{3}{\tau}$. Therefore, if τ=100, $\bar{F}_{EDL}(H)$ is only noticeable within a rather small region (H≤0.03). When the oil droplets are farther away from the solid surface, $\bar{F}_{EDL}(H)$ can be completely ignored in comparison with $\bar{F}_{vdW}(H)$.

The detailed effects of the reduced radius τ of the droplet on the deposition process are shown in Figure 6.4a for $\bar{n}(H)$ and in Figure 6.4b for Sh, respectively. As shown in Figure 6.4a, as long as the EDL interaction is repulsive (Dl>0), the depletion zone is generally compressed within H≤0.1. But the droplet number concentration profile has a quite different shape for a different value of τ. Accordingly, Figure 6.4b indicates that in this case Sh is strongly dependent on the specific value of τ. However, for the attractive EDL interaction (Dl<0), these two figures show that both $\bar{n}(H)$ and Sh slightly changes as τ changes. As τ approaches 100, the effect of $\bar{F}_{EDL}(H)$ on the deposition process becomes vanishing and thus Sh approaches 0.0597. This limiting Sh value corresponds to the deposition case in which only the attractive $\bar{F}_{vdW}(H)$ (A_d=6.00) exists between the oil droplet and the solid surface.

6.1.5 Limitations of the 1-D Numerical Model

The 1-D numerical describes the static steady state deposition of dilute emulsion droplets onto a cylindrical surface. Strictly speaking, however, the static deposition is essentially a transient process. After the deposition starts, more and more oil droplets will attach to the fiber surface. Accordingly, the surface properties of the fiber will change gradually. In particular, the vdW and EDL interactions between the incoming oil droplets and the partially coated fiber surface will be modified. This will affect the validity of the "perfect sink" approximation, $\bar{n}(H)\big|_{H=H_0}=0$, a widely used boundary condition in the PEM region. In comparison with the mass diffusion produced by the colloidal interactions, the transient term in the mass transfer equation may play certain role in the static deposition. On the other hand, as the deposition proceeds, the mass diffusion boundary layer becomes thicker and thicker. Thus it becomes increasingly difficult to seek a numerical solution that satisfies simultaneously the two far field boundary conditions, $\bar{n}(H)\big|_{H=\infty}=1$ and $\frac{d\bar{n}(H)}{dH}\big|_{H=\infty}=0$. It may take a long time for these two far field boundary conditions to asymptote to a steady state. Hence, some further analyses are needed to justify the approach of using a steady state formulation to model the deposition process. More specifically, it needs to be proven that the "perfect sink" approximation is still valid for a limited deposition duration. An order-of-magnitude analysis will be performed to investigate the importance of the transient term. Furthermore, a parametric study will show that the far field boundary conditions do not affect appreciably the predicted deposition rate at the fiber surface.

As will be noted in Chapter 7, in this study, the deposition period of the first 15 min is not accounted for in the deposition measurements because the deposition during this period is caused largely by the insertion of the fiber rather than solely by the colloidal interactions. Choosing $a_{ave}\approx 10$ μm in Equation (7.4), the dimensionless thickness of the mass diffusion boundary layer, $\frac{\sqrt{D_\infty t}}{a_{ave}}$, is nearly equal to unity at t=15 min. As shown in Figures 6.2a, 6.3a and 6.4a for the dimensionless droplet number concentration distributions, the droplet depletion zones where $\bar{n}(H)=0$ extend from H_0=0.001 to H≈1.

Therefore, the actual deposition process is close to a steady state when t>15 min. Also as will be shown in Chapter 7, only a small fraction of the fiber surface is covered by the attached oil droplets until t=90 min. Hence, the "perfect sink" approximation remains a good assumption in the present case.

An order-of-magnitude analysis is implemented to support the claim that the transient term is not important in the deposition process, particularly at small separation distances. For the cylindrical coordinate system (r, ϕ, z) shown in Figure 2.2 and the 1-D unsteady deposition case, substituting Equations (2.10) and (2.11) into Equation (2.1) yields:

$$\frac{\partial n(r,t)}{\partial t}+\frac{D_\infty}{r}\frac{\partial}{\partial r}[-r\frac{\partial n(r,t)}{\partial r}+\frac{rn(r,t)F_{col}(r)}{\mathbf{k}T}]=0$$

Setting $\Delta n = n_\infty$, $\Delta t \approx \frac{(aH)^2}{D_\infty}$, $\Delta r = aH$ and $r = R+a+aH$ in the above equation, the ratio of the droplet migration caused by the total colloidal force to the contribution of the transient term can be estimated as follows:

$$\frac{\frac{D_\infty}{r}\frac{\partial}{\partial r}[\frac{rn(r,t)F_{col}(r)}{\mathbf{k}T}]}{\frac{\partial n(r,t)}{\partial t}} \sim \frac{\frac{D_\infty}{R+a+aH}\cdot\frac{1}{aH}\cdot\frac{(R+a+aH)n_\infty F_{col}(r)}{\mathbf{k}T}}{\frac{n_\infty}{\frac{(aH)^2}{D_\infty}}} = H\cdot\overline{F}_{col}(H)$$

where H is the dimensionless separation distance and $\overline{F}_{col}(H)$ is the dimensionless colloidal force as defined in Equation (6.6). The above expression indicates that the deposition process is controlled by the colloidal force as long as the term $H\cdot\overline{F}_{col}(H)$ is greater than unity. As shown in Figures (3.4) and (3.7), the ratio $H\cdot\overline{F}_{col}(H)$ remains larger than unity in the range of $H=H_0$ to $H\approx 1$. This conclusion is consistent with the predicted droplet depletion zones ($H_0 \le H < 1$) for most cases. The droplet number concentration distributions at $H \le 1$ depend strongly on the vdW and EDL interactions, which are known to be effective at small separation distances. Thus the Sh number, $Sh=\frac{d\overline{n}(H)}{dH}\Big|_{H=H_0}$, as defined in Equation (6.8), should also depend heavily on the colloidal interactions. When H>1, the transient term plays an appreciable role in determining the droplet number concentration distributions. The magnitude of the transient term increases since the vdW force decreases with $\frac{1}{H^4}$ as shown in Equation (3.18) and the EDL force decreases exponentially as shown in Equation (3.38) for the sphere-flat plate system.

It has been realized that, at large separation distances, the diffusion caused by the gradient of the droplet number concentration and the effect of the transient term on the overall droplet number concentration distributions may become increasingly important. Nevertheless, the computed Sh number should be insensitive to the specific value of the "infinite" separation distance H_∞ used in the numerical simulations since Sh number is defined in the PEM region. In this study, a sensitivity analysis for H_∞ was conducted with respect to the Sh number of the 1-D model predictions. Figure 6.4c shows the results of the parametric study. In this figure, the two dotted lines represent the limits of 10% deviation from the $Sh_{cal}=0.0295$ for $H_\infty=40$. It is found from Figure 6.4c that all the computed Sh numbers for $H_\infty \geq 20$ are within the limits. Since the measurement error of the deposition tests is approximately 10% (see Chapter 7), the specific value of H_∞ used in the numerical predictions should not affect the Sh_{cal} appreciably as long as $H_\infty \geq 20$. Furthermore, it can be concluded that the droplet number concentration distributions at large separation distances or the far field boundary condition(s) have no significant effect on the steady state deposition.

Finally, if the actual deposition process is always in a strong transient state, the measured Sh numbers should always decrease as the deposition proceeds. As will be shown in Chapter 7, however, the measured Sh_{exp} was found to be constant and that no saturation states of deposition were observed in all the deposition measurements. The number of the attached oil droplets on the fiber surfaces always increases linearly (i.e. constant Sh) with the deposition time until t=90 min.

In summary, though the actual static deposition is a typical transient process, under certain conditions, the present steady state 1-D numerical model can be used to simulate the practical deposition case. It must be remembered that the steady state model is applicable only to the region close to the solid surface, where the vdW and EDL forces are dominant. In addition, the present 1-D numerical model is valid only for the static deposition of dilute emulsion droplets onto a cylindrical surface. It can only be used to predict the deposition case in which the overall surface coverage is low, i.e. small Sh number and short deposition duration. It is worthwhile to reiterate that the 1-D model does not take into account any external force fields. When external force fields are present, the deposition process becomes a multi-dimensional problem. In the following section, the deposition case in the presence of the gravitational field and the electric field will be studied. A two-dimensional (2-D) deposition model and its numerical solution will be presented.

6.2 2-D Mass Transport Equation

The one-dimensional mass transport equation is obtained in the absence of any external force fields other than the vdW and EDL interaction forces. In this case, since the colloidal forces (the vdW and EDL interactions) are oriented only in the radial direction and their magnitudes depend only on the gap width between the oil droplet and the fiber surface, the general mass transport equation reduces to the 1-D second-order ODE, i.e. Equation (6.1). In the preceding section, the detailed effects of the two universally existing colloidal interactions on the droplet number concentration distribution and the mass transfer rate onto the solid surfaces were studied. Nevertheless, if the external force fields are present, the local mass transfer rate will depend not only on the magnitudes of these fields but also on their orientation relative to the fiber surface. This presents the two dimensional problem. The purpose of this section is to obtain the numerical solution of 2-D mass transfer equation and thus to examine the deposition process in the presence of the two frequently encountered external force fields: the gravitational field and the electric field. The general 2-D mass transfer equation has been derived in Chapter 2 and expressed by Equation (2.22):

$$\frac{\partial^2 \bar{n}}{\partial H^2} + g_1(H,\phi)\frac{\partial \bar{n}}{\partial H} - g_2(H,\phi)\frac{\partial \bar{n}}{\partial \phi} - g_3(H,\phi)\bar{n}(H,\phi) + g_4(H)\frac{\partial^2 \bar{n}}{\partial \phi^2} = 0 \qquad (6.16)$$

where:

$$g_1(H,\phi) = \frac{d}{dH}\{\ln[f_1(H)g(H)]\} - \bar{F}_H(H,\phi),$$

$$g_2(H,\phi) = \frac{f_4(H)\overline{F}_\phi(\phi)}{f_1(H)g(H)},$$

$$g_3(H,\phi) = \overline{F}_H(H,\phi)\frac{d}{dH}\{\ln[f_1(H)g(H)]\} + \frac{d\overline{F}_{col}(H)}{dH} + \frac{f_4(H)}{f_1(H)}\frac{(Gr \pm Ef)\cos\phi}{g(H)},$$

$$g_4(H) = \frac{f_4(H)}{f_1(H)g^2(H)},$$

$f_1(H)$ and $f_4(H)$ are the universal hydrodynamic correction coefficients (UHCC) and their analytical expressions are listed in Equations (2.17a,b) (Masliyah, 1994),

$g(H) = H + 1 + A,$

$\overline{F}_H(H,\phi) = \dfrac{F_r(r,\phi)}{\frac{kT}{a}} = \overline{F}_{col}(H) - (Gr \pm Ef)\cos\phi$ is the component of the total dimensionless force in $\underline{i_H}$ direction,

$\overline{F}_\phi(\phi) = \dfrac{F_\phi(\phi)}{\frac{kT}{a}} = (Gr \pm Ef)\sin\phi$ is the component of the total dimensionless force in $\underline{i_\phi}$ direction,

$\overline{F}_{col}(H) = \dfrac{F_{col}(H)}{\frac{kT}{a}} = \overline{F}_{vdW}(H) + \overline{F}_{EDL}(H)$ is the total dimensionless colloidal force that has the component in $\underline{i_H}$ direction only, $\overline{F}_{vdW}(H)$ and $\overline{F}_{EDL}(H)$ are given in Equations (6.12a,b),

$Gr = \dfrac{\frac{4}{3}\pi a^3(\rho_o - \rho_w)g}{\frac{kT}{a}}$ is the dimensionless gravity number,

and $Ef = \dfrac{q|\underline{E}|}{\frac{kT}{a}}$ is the dimensionless electric field number.

It is noted that the angular diffusion term $\dfrac{\partial^2 \overline{n}}{\partial\phi^2}$ in Equation (6.16) is usually negligible since its coefficient $g_4(H)$ is sufficiently small for most practical cases where

A»1. Thus the above elliptical second-order PDE can be simplified as the following parabolic second-order PDE:

$$\frac{\partial^2 \bar{n}}{\partial H^2} + g_1(H,\phi)\frac{\partial \bar{n}}{\partial H} - g_2(H,\phi)\frac{\partial \bar{n}}{\partial \phi} - g_3(H,\phi)\bar{n}(H,\phi) = 0 \qquad (6.17)$$

The same strategy was utilized by Adamczyk and van de Ven (1981b) to simplify their elliptical PDE of mass transfer. However, it should be emphasized that the whole term, $g_4(H)\frac{\partial^2 \bar{n}}{\partial \phi^2}$, is omitted solely because A^{-2} in its multiplier $g_4(H)$ is sufficiently small and thus the whole term is negligible. Physically, such omission does not imply $\frac{\partial^2 \bar{n}}{\partial \phi^2} \approx 0$. In other word, $\bar{n}(H,\phi)$ should not be considered to be a linear function of ϕ.

6.2.1 Boundary Conditions

Equation (6.17) as it appears is a linear homogeneous parabolic second-order 2-D PDE whose solution can be achieved only by using numerical methods. In order to find a unique solution of Equation (6.17), similar to the 1-D case, the boundary conditions with respect to H can be specified as:

$$\bar{n}(H,\phi)\big|_{H=H_*} = 1 \qquad 0 \le \phi \le \pi \qquad (6.18a)$$

$$\bar{n}(H,\phi)\big|_{H=H_0} = 0 \qquad 0 \le \phi \le \pi \qquad (6.18b)$$

Equations (6.18a,b) represent the first kind of boundary conditions, which are also referred to as the Dirichlet boundary conditions (DBCs). In addition, appropriate boundary conditions with respect to ϕ are needed in order to find the unique numerical solution of Equation (6.17) for a 2-D deposition case. However, the general deposition of droplets onto a solid surface in the presence of arbitrarily oriented external force fields can not be readily analyzed numerically, even by use of sophisticated numerical methods. Hence, focus will be placed on the external forces that are composed of the gravitational field and the electric filed only. The latter is applied vertically either downward or upward and normal to the solid surface, assuming that the cylindrical fiber is placed horizontally inside the deposition cell. Thus the "symmetry" boundary conditions can be applied:

$$\frac{\partial \bar{n}(H,\phi)}{\partial \phi}\Big|_{\phi=0} = 0 \quad (H_0 \le H \le H_\infty) \qquad (6.19a)$$

$$\frac{\partial \bar{n}(H,\phi)}{\partial \phi}\Big|_{\phi=\pi} = 0 \quad (H_0 \le H \le H_\infty) \qquad (6.19b)$$

Unlike the DBCs for $\bar{n}(H,\phi)$ with respect to H, the boundary conditions for $\bar{n}(H,\phi)$ with respect to ϕ are classified as the second kind of boundary conditions, which are also called the Neumann boundary conditions (NBCs). It is also seen from the function $\overline{F}_H(H,\phi)$ defined in Equation (6.16) that the component of the total dimensionless external forces $(Gr \pm Ef)$ in $\underline{i_H}$ direction always reaches its extremes at the upper and lower apex points where ϕ=0 and π, respectively. At these two points, $\overline{F}_\phi(\phi)$ becomes zero. Consequently, it is anticipated that the minimum and the maximum deposition rates always occur at ϕ=0 and π, correspondingly.

6.2.2 Calculation of Sh (ϕ) and $\overline{Sh}$

Similar to the 1-D situation, the dimensionless mass transfer rate, the Sherwood number in 2-D problem, can be defined as:

$$Sh = -\frac{J_0}{\frac{D_\infty n_\infty}{a}} = f_1(H_0)\frac{\partial \bar{n}(H,\phi)}{\partial H}\Big|_{H=H_0} = Sh(\phi) \qquad (6.20a)$$

In the present case, Sh becomes a local quantity, i.e. a function of the angular coordinate ϕ because the concentration gradient changes with ϕ. As discussed above, since the component of the total dimensionless external forces $(Gr \pm Ef)$ in $\underline{i_H}$ direction always achieves its extremes at ϕ=0 and π respectively, Sh(ϕ) should approach its maximum or minimum value at the same azimuthal direction, i.e. $\frac{dSh(\phi)}{d\phi}\Big|_{\phi=0,\pi} = 0$. The average (overall) dimensionless mass transfer rate around the cylinder $\overline{Sh}$ is defined as:

$$\overline{Sh} = \frac{1}{\pi}\int_0^\pi Sh(\phi)d\phi \qquad (6.20b)$$

Therefore, once the droplet number concentration distribution $\bar{n}(H,\phi)$ is determined from Equation (6.17), the local mass transfer rate Sh(ϕ) and the overall mass transfer rate around the cylinder $\overline{Sh}$ can be found from Equations (6.20a, b).

6.2.3 Transforming Functions

Equation (6.17), together with the boundary conditions given in Equations. (6.18a,b) and the "symmetry" boundary conditions given in Equations (6.19a,b), can be solved numerically by using some numerical methods, e.g., the implicit Crank-Nicolson method. Similar to 1-D case, Equation (6.17) is characterized by a rapid change of its multipliers near the location of the PEM where the vdW and EDL interaction forces decay quickly with H. It is also noticed that the dimensionless variable H changes from $H_0=10^{-3}$ to $H_\infty=40$ and that ϕ ranges from 0 to π. Hence, care should be taken in order to solve the equation accurately and efficiently. In this study, two special transforming functions were used in the numerical scheme and enable a continuous changing of the mesh size in the new radial coordinate α and the new azimuthal coordinate β, respectively,

$$\alpha = \frac{\ln(\frac{H}{H_0})}{\ln(\frac{H_\infty}{H_0})} \qquad (6.21a)$$

$$\beta = 1 - \frac{\phi}{\pi} \qquad (6.21b)$$

Thus, as shown in Figures 6.5a and 6.5b, the physical domain ($H_0 \le H \le H_\infty$, $0 \le \phi \le \pi$) is transformed into the domain for the two new variables, α and β ($0 \le \alpha \le 1$, $0 \le \beta \le 1$).

Substituting Equations (6.21a,b) into Equation (6.17), as well as its boundary conditions Equations (6.18a.b) and the so-called "symmetry" boundary conditions Equations (6.19a,b), yields

$$\frac{\partial^2 \bar{n}}{\partial \alpha^2} + G_1(\alpha,\beta)\frac{\partial \bar{n}}{\partial \alpha} + G_2(\alpha,\beta)\frac{\partial \bar{n}}{\partial \beta} + G_3(\alpha,\beta)\bar{n}(\alpha,\beta) = 0 \qquad (6.22)$$

$$\bar{n}(\alpha,\beta)\big|_{\alpha=1} = 1 \qquad 0 \le \beta \le 1 \qquad (6.23a)$$

$$\bar{n}(\alpha,\beta)\big|_{\alpha=0}=0 \qquad 0\le\beta\le 1 \tag{6.23b}$$

$$\frac{\partial\bar{n}(\alpha,\beta)}{\partial\beta}\bigg|_{\beta=1}=0 \qquad 0\le\alpha\le 1 \tag{6.24a}$$

$$\frac{\partial\bar{n}(\alpha,\beta)}{\partial\beta}\bigg|_{\beta=0}=0 \qquad 0\le\alpha\le 1 \tag{6.24b}$$

where

$$G_1(\alpha,\beta)=\frac{d}{d\alpha}\{\ln[F_1(\alpha)G(\alpha)]\}-\bar{F}_\alpha(\alpha,\beta)B(\alpha)-\ln(\frac{H_\infty}{H_0}),$$

$$G_2(\alpha,\beta)=\frac{F_4(\alpha)\bar{F}_\beta(\beta)}{F_1(\alpha)G(\alpha)}\frac{B^2(\alpha)}{\pi},$$

$$G_3(\alpha,\beta)=-B(\alpha)\bar{F}_\alpha(\alpha,\beta)\frac{d}{d\alpha}\{\ln[F_1(\alpha)G(\alpha)]\}-B(\alpha)\frac{d\bar{F}_{col}[H(\alpha)]}{d\alpha}$$
$$+B^2(\alpha)\frac{F_4(\alpha)(Gr\pm Ef)\cos(\pi\beta)}{F_1(\alpha)G(\alpha)}$$

$H(\alpha)=H_0(\frac{H_\infty}{H_0})^\alpha$, $G(\alpha)=g[H(\alpha)]=H(\alpha)+1+A$, $F_i(\alpha)=f_i[H(\alpha)]$, $i=1, 4$, and,

$$B(\alpha)=\frac{dH(\alpha)}{d\alpha}=H_0(\frac{H_\infty}{H_0})^\alpha\ln(\frac{H_\infty}{H_0})=H(\alpha)\ln(\frac{H_\infty}{H_0}),$$

$$\bar{F}_\alpha(\alpha,\beta)=\bar{F}_{col}[H(\alpha)]+(Gr\pm Ef)\cos(\pi\beta),$$

$$\bar{F}_\beta(\beta)=(Gr\pm Ef)\sin(\pi\beta),$$

$$Gr=\frac{\frac{4}{3}\pi a^3(\rho_o-\rho_w)g}{\frac{\mathbf{k}T}{a}},$$

$$Ef=\frac{q|E|}{\frac{\mathbf{k}T}{a}}.$$

It is noted that the total dimensionless external force $\bar{F}_{ext}=Gr\pm Ef$ is constant independent of the separation distance H, where Gr represents the dimensionless gravity number for the gravitational field and Ef is the dimensionless electric field number. Later on, these two dimensionless parameters will be examined to determine their effect on the dimensionless mass transfer rate Sh(ϕ) and $\overline{Sh}$.

As will be discussed in detail in the next section, the implicit Crank-Nicolson approximation of Equation (6.22) is unconditionally stable and convergent, the mesh size does not affect the stability of numerical solution and thus is chosen solely based on accuracy requirement. The accuracy of the numerical solutions is checked by varying the mesh sizes and only results that are insensitive to these changes, i.e. the relative differences are within 0.01%, are considered accurate.

6.2.4 The Crank-Nicolson Method

Equation (6.22) is a typical parabolic second-order linear homogeneous PDE of diffusion problem, which can be numerically solved by using the well-known Crank-Nicolson method (Hoffman, 1992). In the literature, the Crank-Nicolson method was successfully applied to solve the mass transport equations in the case of parallel-plate and cylindrical channels (Adamczyk and van de Ven, 1981a) and for deposition of Brownian particles onto cylindrical collectors (Adamczyk and van de Ven, 1981b). For the physical domain shown in Figure 6.5a and the transformed domain shown in Figure 6.5b, the finite difference stencil for the Crank-Nicolson scheme is illustrated in Figure 6.5c. It can be seen from Figure 6.5c that the values at six points are required in every calculation step. Based on the Crank-Nicolson scheme, the derivative n_α (from now on, $\bar{n}$ is substituted by n for simplicity) at the mid-grid point (i, j+0.5) can be approximated by the second-order centered-difference (SOCD) expression. Similarly, the partial derivative $n_{\alpha\alpha}$ can be approximated by the average value of the second-order centered-space (SOCS) expression. Each derivative term in Equation (6.22) can be approximated by its algebraic finite difference approximation (FDA),

$$n_{\alpha\alpha}\Big|_{i,j+0.5}=\frac{1}{2}(n_{\alpha\alpha}\Big|_{i,j+1}+n_{\alpha\alpha}\Big|_{i,j})=\frac{1}{2}[\frac{n_{i+1,j+1}-2n_{i,j+1}+n_{i-1,j+1}}{\Delta^2\alpha}+\frac{n_{i+1,j}-2n_{i,j}+n_{i-1,j}}{\Delta^2\alpha}]$$

$$n_{\alpha}\Big|_{i,j+0.5}=\frac{1}{2}(n_{\alpha}\Big|_{i,j+1}+n_{\alpha}\Big|_{i,j})=\frac{1}{2}[\frac{n_{i+1,j+1}-n_{i-1,j+1}}{2\Delta\alpha}+\frac{n_{i+1,j}-n_{i-1,j}}{2\Delta\alpha}]$$

$$n_{\beta}\Big|_{i,j+0.5}=\frac{n_{i,j+1}-n_{i,j}}{\Delta\beta}, \text{ and}$$

$$n\Big|_{i,j+0.5} = \frac{n_{i,j+1} + n_{i,j}}{2}$$

where, Δα and Δβ are the mesh sizes and the subscripts i and j represent the grid numbers of the new variables α and β respectively. Substituting the above FDAs and the expression of $n_{i,j+0.5}$ into Equation (6.22) produces the algebraic finite difference equation (FDE),

$$\frac{1}{2}[\frac{n_{i+1,j+1} - 2n_{i,j+1} + n_{i-1,j+1}}{\Delta^2\alpha} + \frac{n_{i+1,j} - 2n_{i,j} + n_{i-1,j}}{\Delta^2\alpha}] +$$
$$\frac{G_1(i,j+0.5)}{2}[\frac{n_{i+1,j+1} - n_{i-1,j+1}}{2\Delta\alpha} + \frac{n_{i+1,j} - n_{i-1,j}}{2\Delta\alpha}] +$$
$$G_2(i,j+0.5)[\frac{n_{i,j+1} - n_{i,j}}{\Delta\beta}] + \frac{G_3(i,j+0.5)}{2}[n_{i,j+1} + n_{i,j}] = 0$$

Multiplying the above equation by Δβ and rearranging the resultant equation gives:

$$[\frac{\Delta\beta}{2\Delta^2\alpha} - \frac{\Delta\beta}{4\Delta\alpha}G_1(i,j+0.5)]n_{i-1,j+1} + [-\frac{\Delta\beta}{\Delta^2\alpha} + G_2(i,j+0.5) + \frac{\Delta\beta}{2}G_3(i,j+0.5)]n_{i,j+1} +$$
$$[\frac{\Delta\beta}{2\Delta^2\alpha} + \frac{\Delta\beta}{4\Delta\alpha}G_1(i,j+0.5)]n_{i+1,j+1} + [\frac{\Delta\beta}{2\Delta^2\alpha} - \frac{\Delta\beta}{4\Delta\alpha}G_1(i,j+0.5)]n_{i-1,j} +$$
$$[-\frac{\Delta\beta}{\Delta^2\alpha} - G_2(i,j+0.5) + \frac{\Delta\beta}{2}G_3(i,j+0.5)]n_{i,j} + [\frac{\Delta\beta}{2\Delta^2\alpha} + \frac{\Delta\beta}{4\Delta\alpha}G_1(i,j+0.5)]n_{i+1,j} = 0$$

This equation can be further simplified as:

$$a_{i,j}n_{i-1,j+1} + b_{i,j}n_{i,j+1} + c_{i,j}n_{i+1,j+1} + a_{i,j}n_{i-1,j} + d_{i,j}n_{i,j} + c_{i,j}n_{i+1,j} = 0 \qquad (6.25a)$$

or

$$a_{i,j}(n_{i-1,j} + n_{i-1,j+1}) + b_{i,j}n_{i,j+1} + c_{i,j}(n_{i+1,j} + n_{i+1,j+1}) + d_{i,j}n_{i,j} = 0 \qquad (6.25b)$$

where:

$a_{i,j} = C - D \cdot G_1(i, j+0.5)$

$b_{i,j} = -2C + G_2(i, j+0.5) + 0.5\Delta\beta \cdot G_3(i, j+0.5)$

$c_{i,j} = C + D \cdot G_1(i, j+0.5)$

$d_{i,j} = -2C - G_2(i, j+0.5) + 0.5\Delta\beta \cdot G_3(i, j+0.5)$

$$C = \frac{\Delta\beta}{2\Delta^2\alpha}, \quad D = \frac{\Delta\beta}{4\Delta\alpha}$$

It is noted that the four multipliers, $a_{i,j}$, $b_{i,j}$, $c_{i,j}$ and $d_{i,j}$, are not only dependent on the mesh sizes $\Delta\alpha$ and $\Delta\beta$ through the coefficients C and D, but also dependent on the values of the three functions, $G_1(\alpha,\beta)$, $G_2(\alpha,\beta)$ and $G_3(\alpha,\beta)$ at the mid-grid point (i, j+0.5). In terms of Equations (6.25a,b), the four multipliers, $a_{i,j}$, $b_{i,j}$, $c_{i,j}$ and $d_{i,j}$, are marked beside their corresponding grid point(s) in Figure 6.5c. Obviously, multipliers $a_{i,j}$ and $c_{i,j}$ are symmetric in the two levels for the grid points at (i-1, j or j+1) and at (i+1, j or j+1), respectively. Prior to solving the resultant algebraic FDE, Equation (6.25a) or Equation (6.25b), it is useful to carefully examine some major numerical properties of the Crank-Nicolson method. First, it can be easily proved that the Crank-Nicolson approximation of the PDE is consistent and unconditionally stable and that, by the Lax equivalent theorem, such approximation of Equation (6.22) is also convergent (Hoffman, 1992). Secondly, Hoffman (1992) also showed that the truncation error of the FDE produced from the Crank-Nicolson approximation is in the order of $O(\Delta^2\beta)+O(\Delta^2\alpha)$ for the present case. This can be proved from the first form and the second form of the modified difference equation (MDE) of Equation (6.25a) or Equation (6.25b). The MDE is obtained by writing each term in either equation as a Taylor series for $n(\alpha,\beta)$ about the mid-grid point (i, j+0.5). Finally, for a given value of $c = \dfrac{\Delta\beta}{G_2\Delta^2\alpha}$, $\Delta\beta = c\cdot G_2\Delta^2\alpha$. Thus, as $\Delta\alpha$ is successively halved, $\Delta\beta$ is quartered. Consequently, the $O(\Delta^2\beta)$ term should decrease by a factor of approximately 16 and the $O(\Delta^2\alpha)$ term should decrease by a factor of approximately four as $\Delta\alpha$ is halved for a constant c. The total error decreases by a factor of approximately four, indicating that the $O(\Delta^2\alpha)$ term is the dominant error term. Hence, the calculation step for β and especially the mesh size for α are chosen purely based on the accuracy requirements. In summary, the implicit Crank-Nicolson method is a two-level, six-point, single-step and second-order unconditionally stable and convergent approximation. In order to obtain the numerical solution of the PDE, Equation (6.22), a set of linear finite difference equations (FDEs), Equation (6.25a or b) at all the discrete grid points, have to be solved simultaneously in conjunction with the relevant boundary conditions.

6.2.5 Solution of the Finite Difference Equations (FDEs)

The FDEs given in Equation (6.25a or b) are applicable only at the interior points. If the range of $0 \le \alpha \le 1$ is divided into imax grids and the range of $0 \le \beta \le 1$ is divided into jmax grids, the interior points are (i, j) and the droplet number concentrations at these points are $n_{i,j}$, where i(α)=1~imax-1, j(β)=1~jmax-1. For instance, at the first level of i=1~imax-1, j=0, a set of linear equations can be obtained from Equation (6.25a) and written as follows:

$$\begin{cases} i=1, j=0 \qquad a_{1,0}n_{0,1}+b_{1,0}n_{1,1}+c_{1,0}n_{2,1}+a_{1,0}n_{0,0}+d_{1,0}n_{1,0}+c_{1,0}n_{2,0}=0 \\ i=2, j=0 \qquad a_{2,0}n_{1,1}+b_{2,0}n_{2,1}+c_{2,0}n_{3,1}+a_{2,0}n_{1,0}+d_{2,0}n_{2,0}+c_{2,0}n_{3,0}=0 \\ \qquad\qquad\qquad \cdots\cdots \\ i=i\max-1, j=0 \qquad a_{i\max-1,0}n_{i\max-2,1}+b_{i\max-1,0}n_{i\max-1,1}+c_{i\max-1,0}n_{i\max,1} \\ \qquad +a_{i\max-1,0}n_{i\max-2,0}+d_{i\max-1,0}n_{i\max-1,0}+c_{i\max-1,0}n_{i\max,0}=0 \end{cases} \tag{6.26}$$

It is obvious that one can not solve the above equations alone since there are only total (imax-1) linear equations for 2(imax+1) unknown variables, $n_{i,j}$, i=0~imax, j=0~1 in Equation (6.26). Additional (imax+3) relations are required, which, as will be discussed later, can be found from the boundary conditions at i=0, imax and j=0, 1, as well as at i=1~imax-1, j=0. Next, by applying Equation (6.25a) directly at the second level of i=1~imax-1, j=1, similar (imax-1) equations can be written down. If at this stage all the values at the last level, $n_{i,1}$, i=0~imax, are known from the above calculation, then there are only (imax-1) equations at the new level for (imax+1) unknown variables, $n_{i,2}$, i=0~imax. Two extra relations are needed and can also be given from the boundary conditions at (0, 2) and (imax, 2) for $n_{0,2}$ and $n_{imax,2}$, respectively. Therefore, the numerical calculation at the interior points can proceed from one level to another and eventually stop at j=jmax-2.

The boundary points are the points either at i=0, imax or at j=0, jmax, respectively. There are two kinds of boundary conditions involved in this study. They can be used either to determine the values at the boundary points directly (the first kind) or to relate the values at the boundary points to those at the interior points (the second kind). As shown in Equations (6.23a,b), the values of $n_{i,j}$ are specified at the boundaries, i=0 (α=0) and i=imax (α=1), irrespective of β values. These boundary conditions can be simply expressed as:

$$n_{0,j} = 0, \qquad n_{i\max,j} = 1 \qquad (0 \le j \le j\max) \tag{6.27}$$

These two boundary conditions are classified as the first kind or the Dirichlet boundary conditions (DBCs). Obviously, Equation (6.27) provides the two additional relations previously required at any levels j≥1, e.g., $n_{0,2}$ and $n_{imax,2}$ at the second level j=1. Furthermore, the following relations can be readily attained by choosing j=0, 1 in the above equation, respectively,

$$\begin{cases} n_{0,0} = 0, & n_{i\max,0} = 1 \\ n_{0,1} = 0, & n_{i\max,1} = 1 \end{cases} \tag{6.28}$$

Equations (6.24a,b) express the second kind or the Neumann boundary conditions (NBCs) at j=0 (β=0) and j=jmax (β=1), respectively. At j=0, the boundary condition can be approximated by the explicit Euler method,

$$n_{i,1} - n_{i,0} = 0 \qquad O(\Delta^2\beta) \quad (1 \le i \le i\max - 1) \tag{6.29a}$$

Equation (6.29a) and Equation (6.28) together provide the exact (imax+3) relations needed for solving Equation (6.26). Similarly, at j=jmax,

$$n_{i,j\max} - n_{i,j\max-1} = 0 \quad O(\Delta^2\beta) \quad (1 \le i \le i\max - 1) \tag{6.29b}$$

Equation (6.29b) can be used to relate the unknown values of $n_{i,jmax}$ at the level j=jmax to the values of $n_{i,jmax-1}$ at the sub-level j=jmax-1, which should be known from the above numerical calculations for the interior points starting from j=0 to j=jmax-2. With the values given in Equation (6.27) at j=jmax, all the values of $n_{i,jmax}$ (i=0~imax) at the level j=jmax are thus determined. Combining all the values of $n_{i,j}$, (i=0~imax, j=0~jmax) at the interior points and the boundary points together, the algebraic solution of the FDEs, Equation (6.25a), is achieved in the whole transformed domain, i.e. α=0~1 and β=0~1.

Based on the above numerical manipulations, in principle, some proper algorithm can be utilized to solve all the relevant linear equations, Equation (6.26) for the interior points and Equations (6.27) through (6.29a,b) for the boundary points, and find all the values of $n_{i,j}$ (i=0~imax, j=0~jmax). However, it is not a trivial task to solve the total (imax+1)x(jmax+1) linear equations directly, particularly in consideration of the fact that there are six non-zero coefficients in Equation (6.25a) for all the interior points (i=1~imax-1, j=1~jmax-1). For example, in order to achieve more accurate numerical results, if both imax and jmax are chosen as 1000 and thus Δα=Δβ=0.001, one has to solve over one million linear equations simultaneously. Instead of pursuing the direct solution of the finite difference equations at the interior points and the equations representing the relevant boundary conditions, in this study, a simple iteration method is devised to find the solution of the linear equations. This iteration procedure will be described as follows.

Basically, the iteration calculation starts from the point at i=1, j=0. Six variables are involved in Equation (6.25a) at this point. They are $n_{0,0}$, $n_{1,0}$ and $n_{2,0}$ at the level j=0, as well as $n_{0,1}$, $n_{1,1}$ and $n_{2,1}$ at the level j=1 as shown in the first expression in Equation (6.26). It is known that $n_{0,1}=n_{0,0}=0$ from Equation (6.28) and that $n_{1,1}=n_{1,0}$ and $n_{2,1}=n_{2,0}$ from Equation (6.29a). Thus, there are only two independent unknown variables in Equation (6.25a) at i=1, j=0:

$$n_{2,0} = -\frac{(b_{1,0} + d_{1,0})}{2c_{1,0}} n_{1,0} \qquad (6.30a)$$

If a guess value for $(n_{1,0})_{guess}$ is given, $n_{2,0}$ can be determined from the above equation. The general form of Equation (6.30a) at j=0 will be, using Equation (6.25b):

$$n_{i+1,0} = -\frac{2a_{i,0}n_{i-1,0} + (b_{i,0} + d_{i,0})n_{i,0}}{2c_{i,0}} \quad (1 \le i \le i\max - 1) \qquad (6.30b)$$

Note that when i=1 and $n_{0,0}=0$, Equation (6.30b) reduces to Equation (6.30a). Such numerical procedure can proceed until i=imax-1 and $(n_{imax,0})_{cal}$ is determined. Since the $(n_{imax,0})_{actual}$ should be equal to unity as required by Equation (6.27) at i=imax, j=0, $(n_{1,0})_{guess}$ can be adjusted accordingly and the iteration calculation continues until $(n_{imax,0})_{cal}$ is sufficiently close to unity within a specified precision. Once all the values of $n_{i,0}$ (i=0~imax) at the level j=0 are obtained, according to the two boundary conditions given in Equation (6.27) and Equation (6.29a), all the values of $n_{i,1}$ at the level j=1 will be same as their corresponding values of $n_{i,0}$ at the level j=0, i.e. $n_{i,1}=n_{i,0}$ (i=0~imax).

The above iteration procedure can be also used to find the values of $n_{i,j+1}$ at all the remaining levels j=1~jmax-2. For instance, at i=1, $n_{0,j+1}=n_{0,j}=0$ from Equation (6.27) and $n_{1,j}$ and $n_{2,j}$ at the previous level are known. Using Equation (6.25a) gives:

$$n_{2,j+1} = -\frac{b_{1,j}n_{1,j+1} + d_{1,j}n_{1,j} + c_{1,j}n_{2,j}}{c_{1,j}} \quad i = 1, j \ge 1 \qquad (6.31a)$$

Similarly, if a guess value for $(n_{1,j+1})_{guess}$ is chosen, $n_{2,j+1}$ can be found from the above equation. More generally, one has

$$n_{i+1,j+1} = -\frac{a_{i,j}(n_{i-1,j+1} + n_{i-1,j}) + b_{i,j}n_{i,j+1} + d_{i,j}n_{i,j} + c_{i,j}n_{i+1,j}}{c_{i,j}} \qquad i \geq 1, j \geq 1 \qquad (6.31b)$$

Thus $(n_{1,j+1})_{guess}$ can be adjusted accordingly to make $(n_{imax,j+1})_{cal}$ adequately close to unity as required by Equation (6.27), j=1~jmax-2. In addition, all the values of $n_{i,jmax}$ at the level j=jmax should be same as the values of $n_{i,jmax-1}$ at the level j=jmax-1 according to the so-called "symmetry" boundary condition at j=jmax given in Equation (6.29b), i.e. $n_{i,jmax}= n_{i,jamx-1}$ (i=1~imax-1). In particular, $n_{0,jmax}=0$, $n_{imax,jmax}=1$ from Equation (6.27). Ultimately, all the values of $n_{i,j}$ (i=0~imax, j=0~jmax) have been found. Therefore, by using the simple iteration method presented here, there is no need to directly solve the total (imax+1)x(jmax+1) linear equations. Furthermore, it is much more easier to check the numerical results and find the accurate numerical solution of the FDEs over the entire transformed domain ($0\leq\alpha\leq1$, $0\leq\beta\leq1$). Eventually, the droplet number concentration distribution $n(\alpha,\beta)$ or $\bar{n}(\alpha,\beta)$ over the transformed domain ($0\leq\alpha\leq1$, $0\leq\beta\leq1$) can be transformed back into $\bar{n}(H,\phi)$ over the physical domain ($H_0\leq H\leq H_\infty$, $0\leq\phi\leq\pi$) because the old variables H and ϕ can be related to the new variable α and β by using the following two inverse transforming functions, see Equations (6.21a,b):

$$H(\alpha) = H_0\left(\frac{H_\infty}{H_0}\right)^\alpha \qquad 0 \leq \alpha \leq 1 \qquad (6.32a)$$

$$\phi(\beta) = (1-\beta)\pi \qquad 0 \leq \beta \leq 1 \qquad (6.32b)$$

6.2.6 2-D Numerical Results and Discussion

If there are external force fields involved in the deposition system, the corresponding mass transfer process becomes a two-dimensional (2-D) problem. In particular, the case in which only the gravitational field and the electric field are present is of great interest. If the electric field is applied vertically either downward or upward, these two external fields will be always normal to the axis of the cylindrical fiber, assuming it is placed horizontally. Thus the total dimensionless external force is equal to, referring Equation (6.22):

$$\overline{F}_{ext} = Gr \pm Ef \tag{6.33a}$$

$$Gr = \frac{\frac{4}{3}\pi a^3(\rho_o - \rho_w)g}{\frac{\mathbf{k}T}{a}} \tag{6.33b}$$

$$Ef = \frac{q|\underline{E}|}{\frac{\mathbf{k}T}{a}} = \frac{4\pi a^2 q_e|\underline{E}|}{\frac{\mathbf{k}T}{a}} \tag{6.33c}$$

where q is the total electrostatic charge on the oil droplet and q_e is the electrostatic charge per unit surface area of the oil droplet. q_e is sometimes also called the specific surface charge or the surface charge density. It is noted that, unlike the vdW and EDL forces, $\overline{F}_{ext}$ given in Equation (6.33a) is constant, irrespective of the separation distance. Prior to examining their effects on the dimensionless droplet number concentration distribution and the dimensionless mass transfer rate Sh(ϕ) and $\overline{Sh}$, the magnitudes of the dimensionless gravity number Gr and the dimensionless electric field number Ef have to be estimated. Since these two forces strongly depend on the size of the droplet and, for relatively large droplets, they are several orders larger than the total colloidal forces, only small droplets of radii around a=1 μm are considered in the following estimation. Substituting the density difference between the silicone oil No. 1 and the DIUF water $\Delta\rho=\rho_o-\rho_w=52$ kg/m^3 into Equation (6.33b) yields Gr=0.52. Ef is estimated to be -0.62 from Equation (6.33c) if the typical values for q_e and $|\underline{E}|$ are chosen as -200 μC/m^2 (Gu and Li, 1997b) and 1.0 V/m (in a very weak electric field) respectively. The specific effects of the vdW and EDL forces on the deposition phenomena were studied in the last section. In this section, the following values of A_d=6.00, A=10, $\bar{s}$=11.116 and $\bar{\lambda}$=0.1 (corresponding to a=1 μm) will be chosen for the attractive vdW force and the EDL force is completely ignored (i.e. Dl=0) in the numerical modeling. It is further assumed that the electric field be applied upward and thus $\overline{F}_{ext} = Gr - Ef$, in order to avoid the case in which these two external force fields counteract each other. Specifically, the following five typical cases were selected for the numerical simulations: (1) Gr=0.50, Ef=-0.50 and thus $\overline{F}_{ext}$=1.00; (2) Gr=0.05, Ef=-0.05 and thus $\overline{F}_{ext}$=0.1; (3) Gr=0.02, Ef=-0.02 and thus

$\overline{F}_{ext}$=0.04; (4) Gr=0.01, Ef=-0.01 and thus $\overline{F}_{ext}$=0.02; and (5) Gr=0, Ef=0 and thus $\overline{F}_{ext}$=0, i.e. in the absence of any external force fields. The numerical results of the 2-D deposition modeling for these five situations will be presented in the subsequent paragraphs. In particular, the influence of the total external force field $\overline{F}_{ext}$ on Sh(ϕ), $\overline{Sh}$ and $\overline{n}(H,\phi)$ will be discussed.

Figure 6.6 shows Sh(ϕ) versus ϕ for the 2-D deposition case in which Gr=0.50, Ef=-0.50 and thus $\overline{F}_{ext}$=1.00. In this case the average Sherwood number is equal to $\overline{Sh}$=1.4304. As clearly indicated in the figure, Sh(ϕ) changes greatly around the solid surface in the azimuthal direction $\underline{i}_\phi$. More specifically, the maximum Sherwood number is achieved at ϕ=0, where Sh(0)=4.5432. This Sh number is nearly two orders greater than that for the case $\overline{F}_{ext}$=0. Therefore, in comparison with the colloidal forces, the external force fields overwhelmingly dominate the deposition when Gr=0.50, Ef=-0.50 and thus $\overline{F}_{ext}$=1.00. It is seen from the plot that Sh(ϕ) decreases dramatically with ϕ and becomes negligible when ϕ≥100°. Physically, this means that the upper part (0≤ ϕ<100°) of the cylindrical surface is heavily covered by the oil droplets while there are almost no deposited oil droplets onto its lower part (100°≤ϕ≤180°). This is because in the present case both the gravitational filed and the electric field exert downward forces on the oil droplets. Hence, the total external force functions as an attractive force at the upper part to assist the deposition occurring whereas it acts as a repulsive force at the lower part to counteract the deposition rate produced by the attractive vdW force.

Similar variations of Sh(ϕ) with ϕ for the other four cases are plotted in Figure 6.7. It is seen that these two external force fields control the deposition rate until Gr=0.01and Ef=-0.01, i.e. until $\overline{F}_{ext}$=0.02. The deposition rates at ϕ<90° are usually much larger than those at ϕ>90°. At ϕ=90°, the influence of the external force fields on the deposition is absent and thus Sh(90°) is equal to 0.0606. When Gr=0, Ef=0, i.e. $\overline{F}_{ext}$=0, a uniform deposition rate Sh=0.0606 is obtained over the entire cylindrical surface.

The above analyses are well verified by the dimensionless droplet number concentration distributions $\overline{n}(H,\phi)$ versus H and ϕ, which are plotted in Figure 6.8a (H in linear scale) and Figure 6.8b (H in log scale) when Gr=0.05 and Ef=-0.05, i.e. $\overline{F}_{ext}$=0.1. As shown in Figure 6.8a, the 3-D plot clearly indicates that the droplet number concentration profiles quickly change from concave shape at smaller ϕ to convex shape at larger ϕ. Correspondingly, Figure 6.8b shows that, as ϕ increases from 0° to 180°, the depletion zone (i.e. $\overline{n}(H,\phi)$=0) is compressed from H≈4.0 at ϕ=0° to only H≈1.0 at ϕ=180°. As discussed above, this phenomenon is simply caused by the fact that the total external force functions as an attractive force at the upper part to assist the deposition occurring while it acts as a repulsive force at the lower part to counteract the deposition rate produced by the attractive vdW force. In summary, the 2-D numerical model developed in this section can be used to study the 2-D deposition processes in which both the external force fields and the colloidal forces are present.

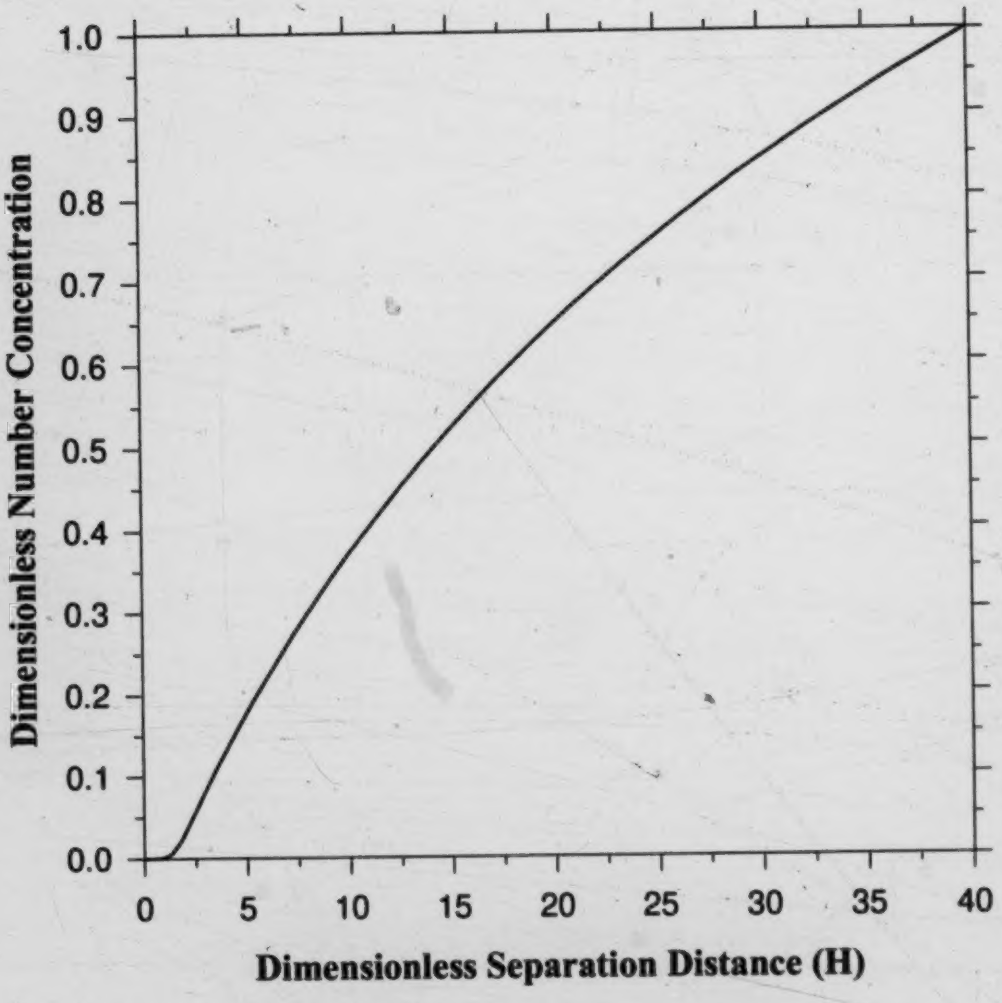

Figure 6.1a Dimensionless droplet number concentration distribution (H in linear scale)

A_d=6.00, Dl=-1000, τ=5, Sh=0.0645

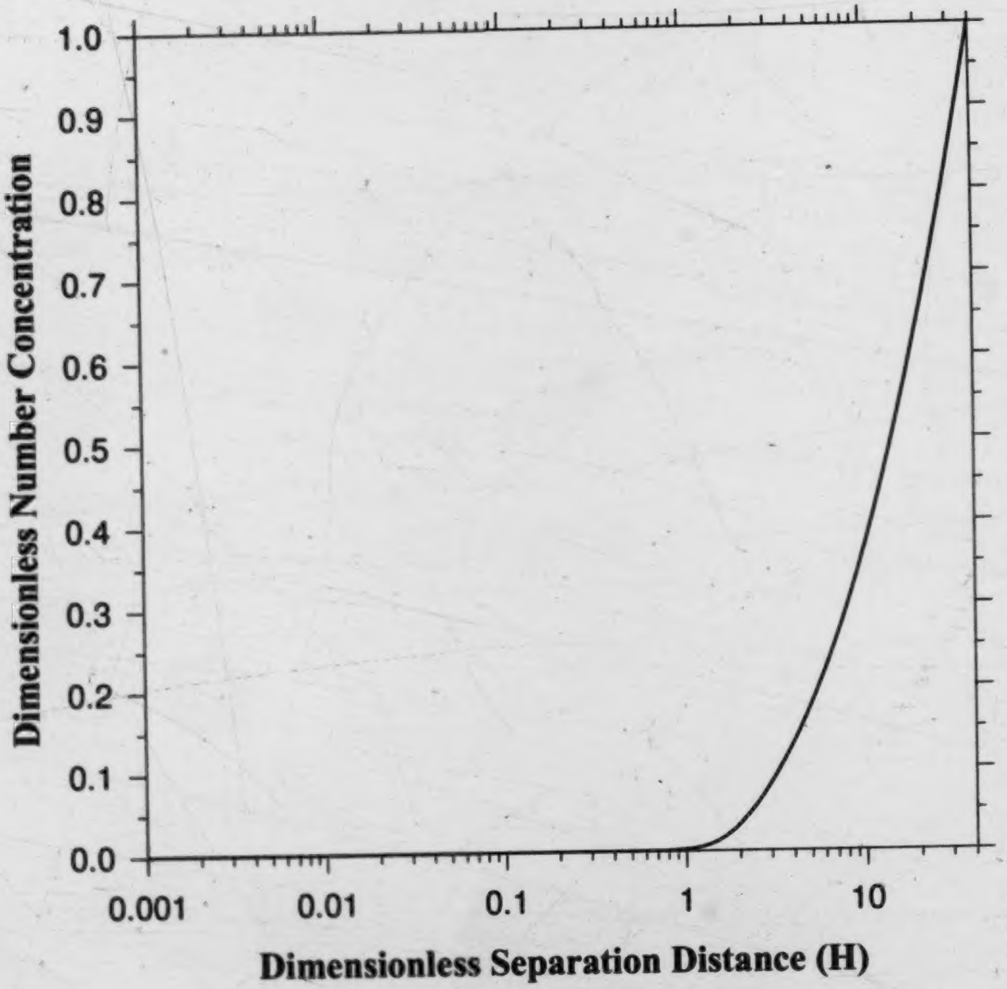

Figure 6.1b Dimensionless droplet number concentration distribution (H in log scale)
A_d=6.00, Dl=-1000, τ=5, Sh=0.0645

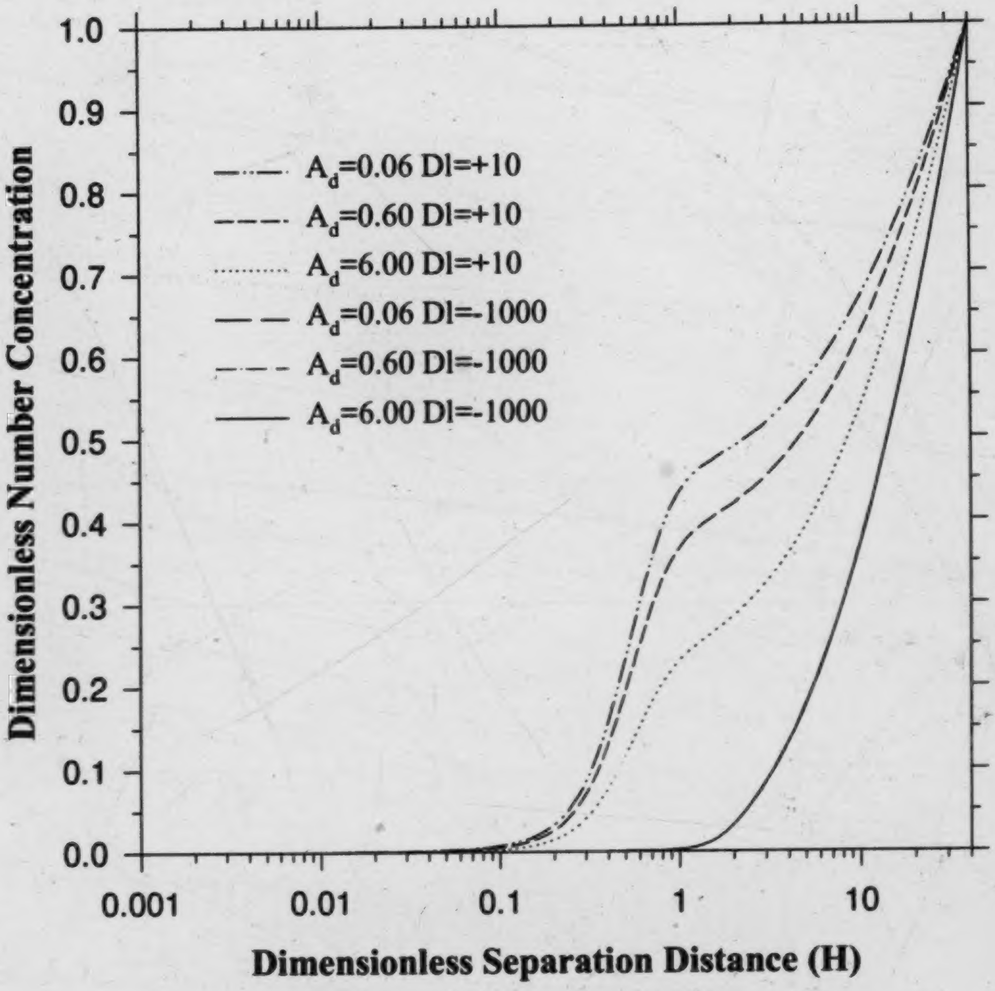

Figure 6.2a Dimensionless droplet number concentration distributions (τ=5)

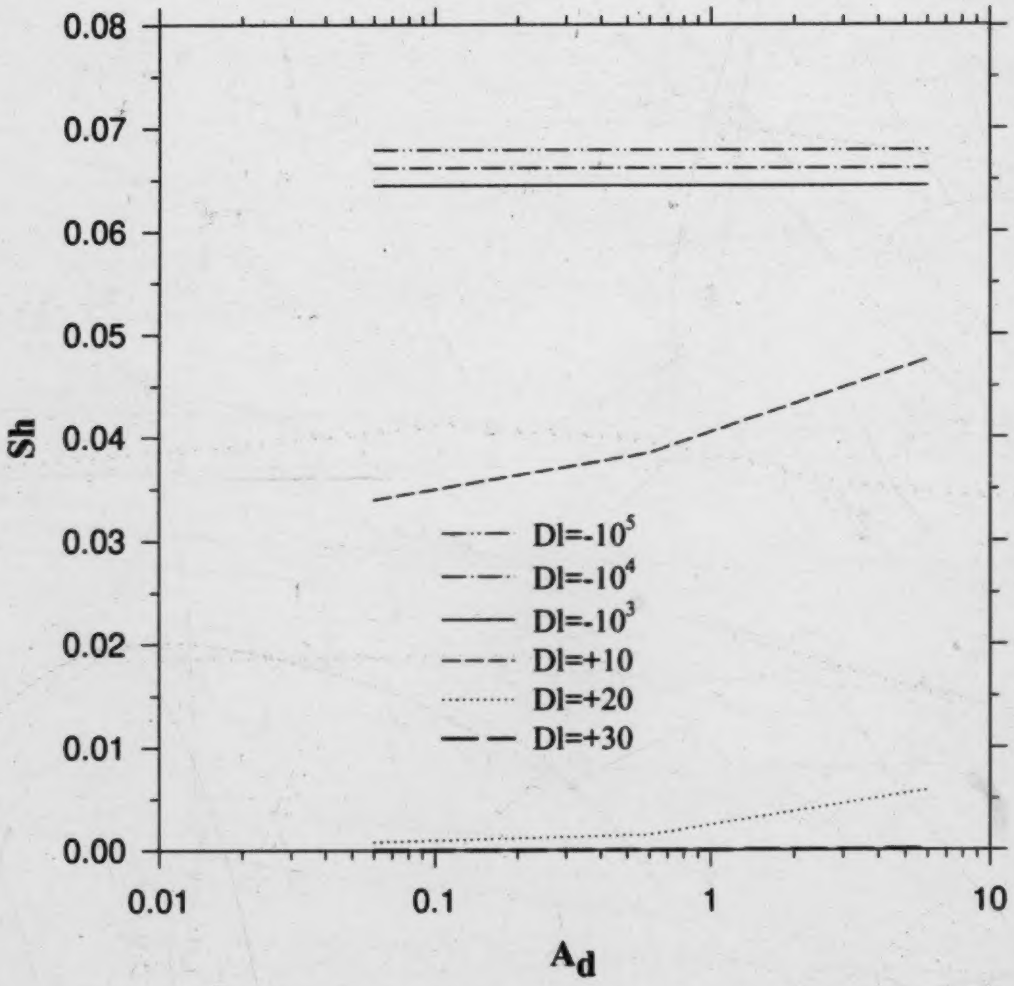

Figure 6.2b Variation of dimensionless mass transfer rate Sh with dimensionless deposition number A_d (τ=5)

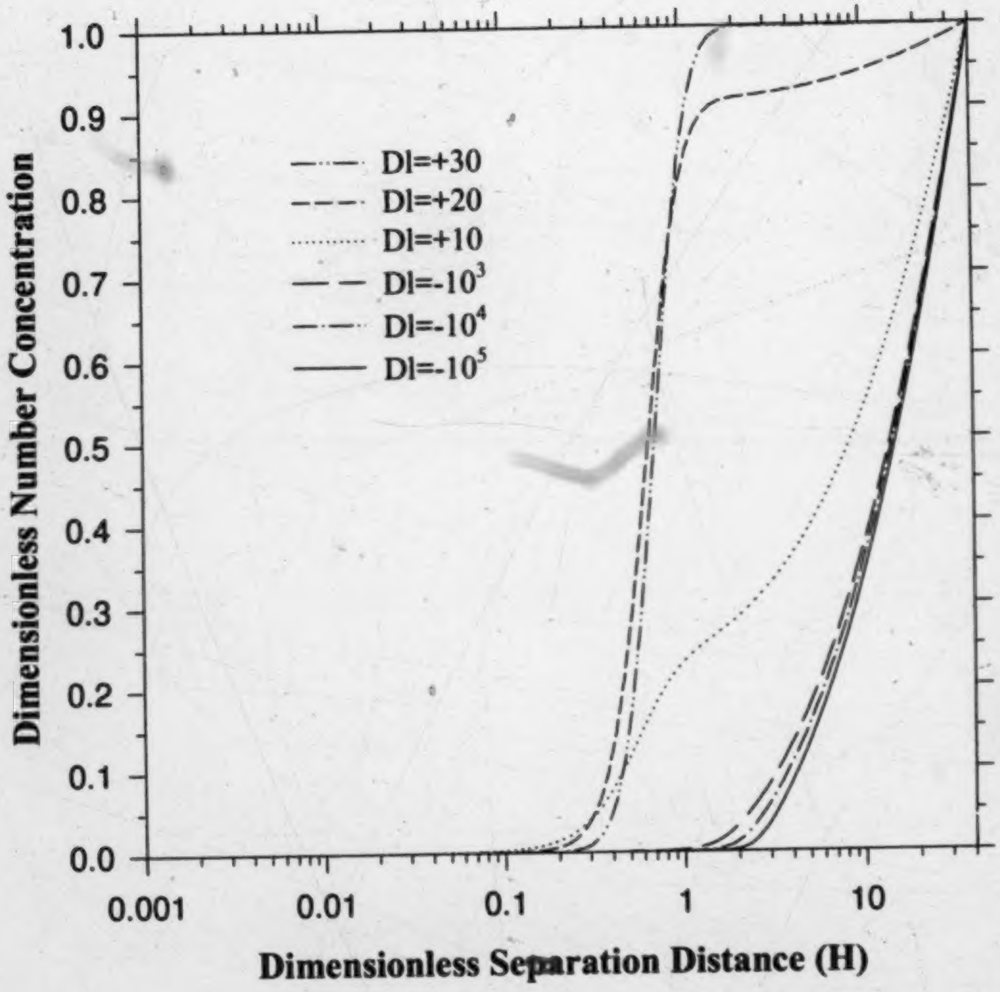

Figure 6.3a Dimensionless droplet number concentration distributions (A_d=6.00 τ=5)

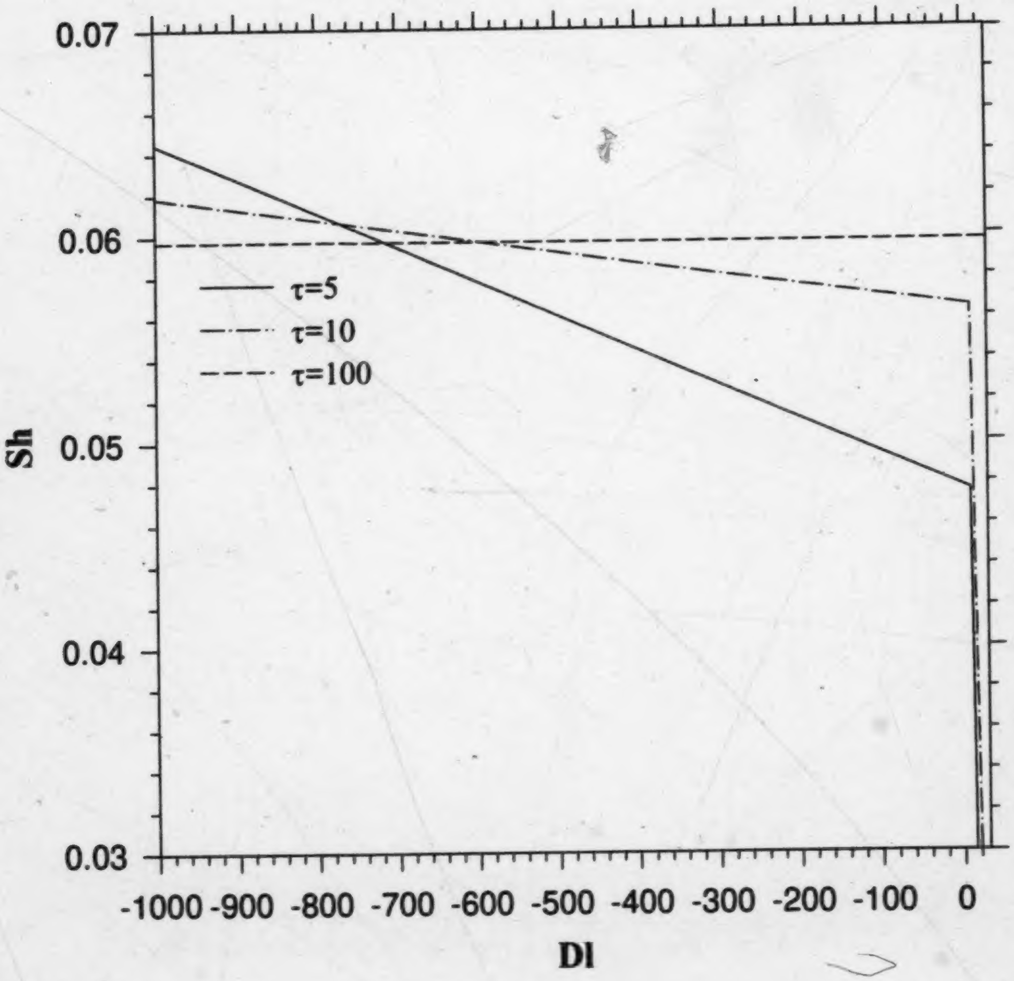

Figure 6.3b Variation of dimensionless mass transfer rate Sh with dimensionless EDL parameter Dl (A_d=6.00)

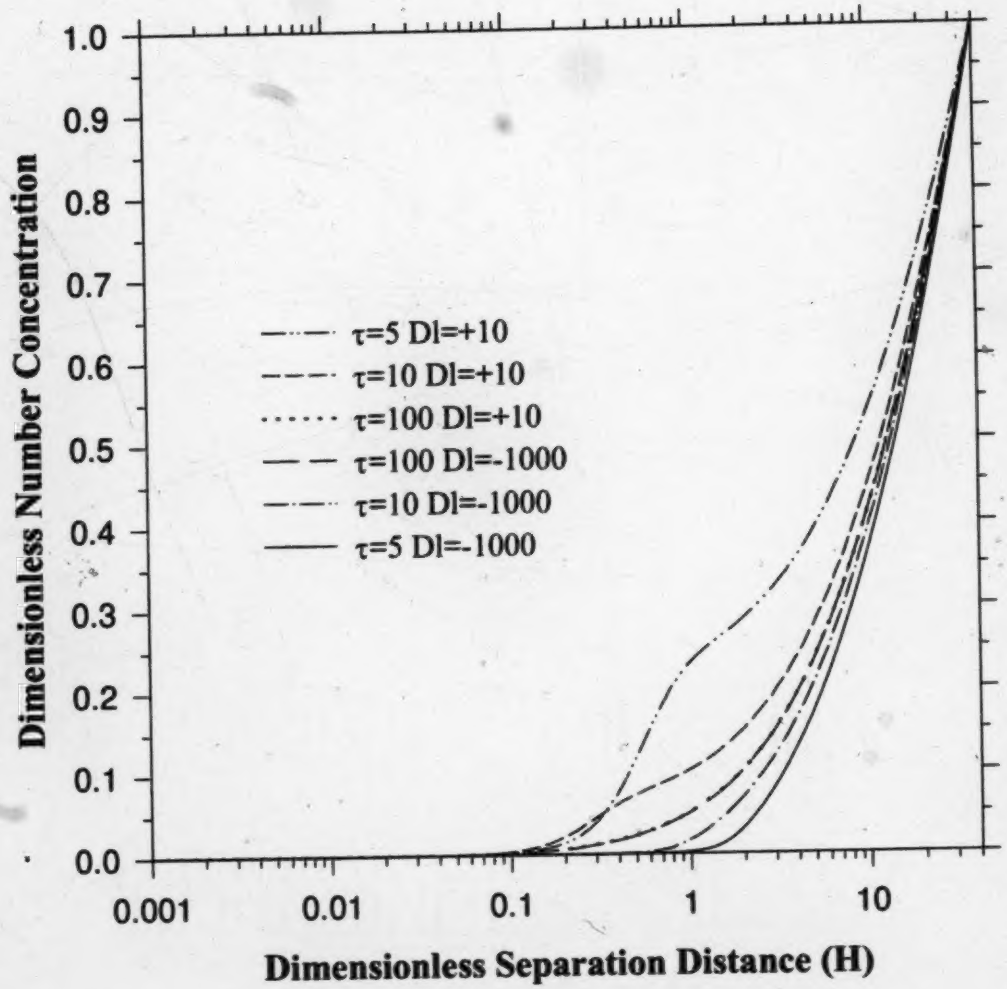

Figure 6.4a Dimensionless droplet number concentration distributions (A_d=6.00)

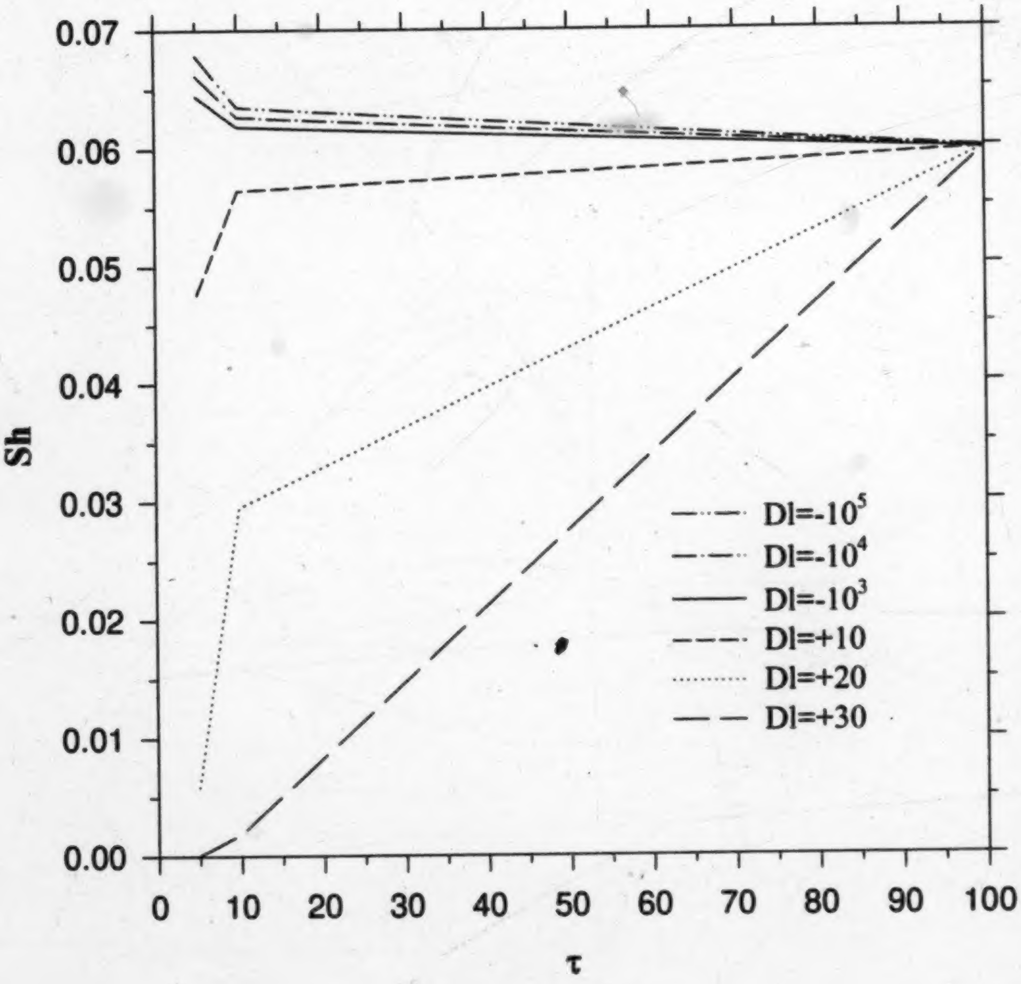

Figure 6.4b Variation of dimensionless mass transfer rate Sh with reduced radius of the oil droplet τ (A_d=6.00)

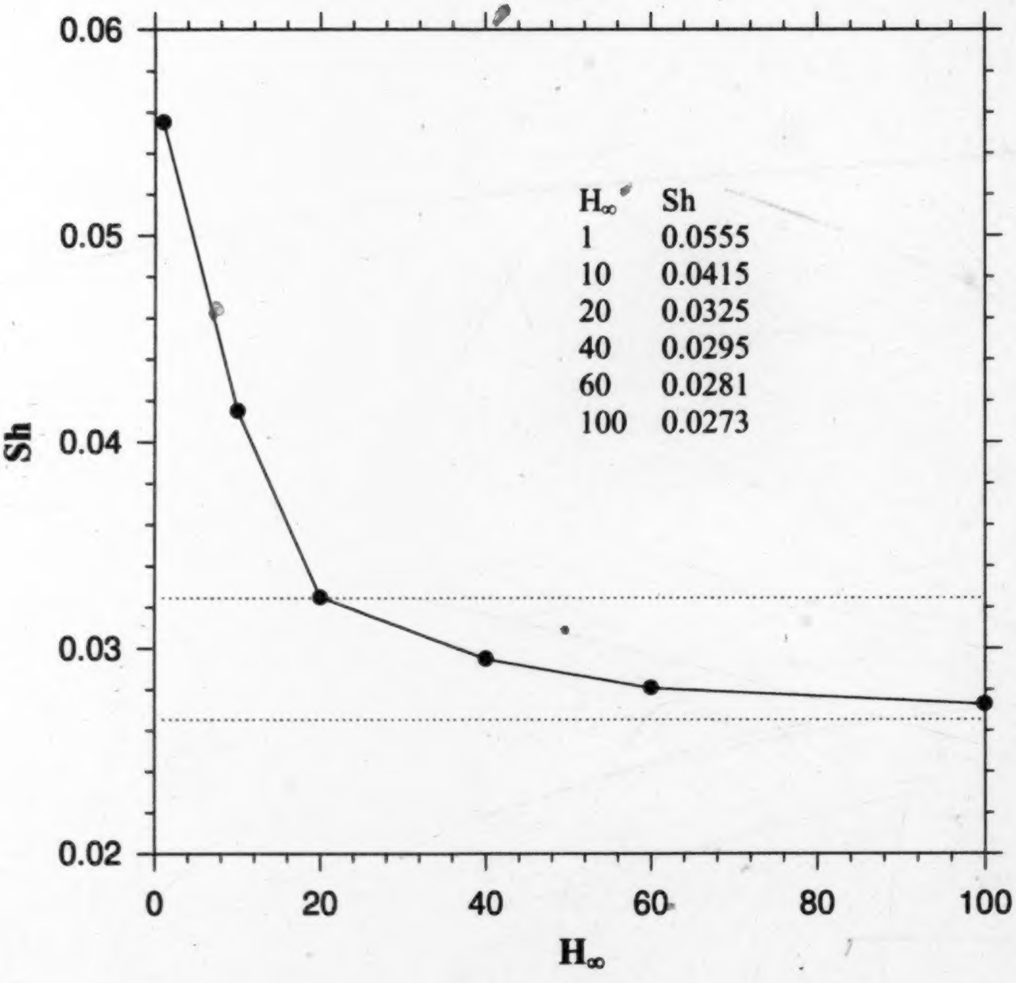

H_∞	Sh
1	0.0555
10	0.0415
20	0.0325
40	0.0295
60	0.0281
100	0.0273

Figure 6.4c Variation of dimensionless mass transfer rate Sh with H_∞ used in the numerical simulations (A_d=6.00, Dl=+20, τ=10). The two dotted lines represent the limits of 10% deviation from the Sh_{cal}=0.0295 for H_∞=40.

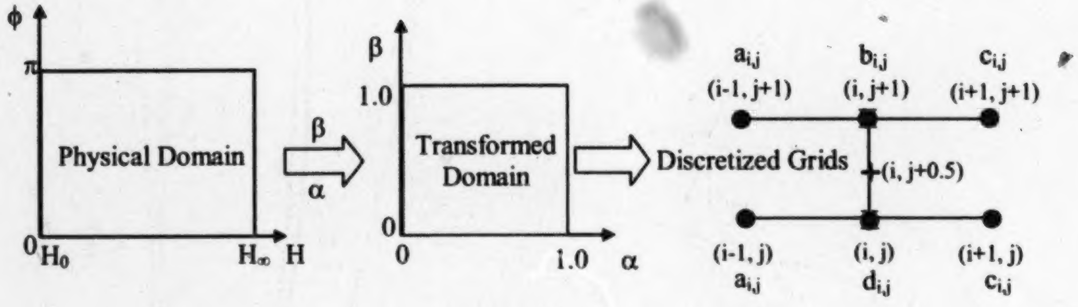
ϕ
π
0
H_0
H_∞
H
Physical Domain
β
α
β
1.0
0
0
1.0
α
Transformed Domain
Discretized Grids
$a_{i,j}$
(i-1, j+1)
$b_{i,j}$
(i, j+1)
$c_{i,j}$
(i+1, j+1)
(i, j+0.5)
(i-1, j)
$a_{i,j}$
(i, j)
$d_{i,j}$
(i+1, j)
$c_{i,j}$

Figure 6.5a

Figure 6.5b

Figure 6.5c

Figure 6.5a (left) The physical domain for the 2-D deposition problem; Figure 6.5b (middle) The transformed domain for the numerical simulation; Figure 6.5c (right) The finite difference stencil for the Crank-Nicolson scheme, where each multiplier, $a_{i,j}$, $b_{i,j}$, $c_{i,j}$, $d_{i,j}$, in Equation (6.25a) is placed beside its corresponding grid point(s)

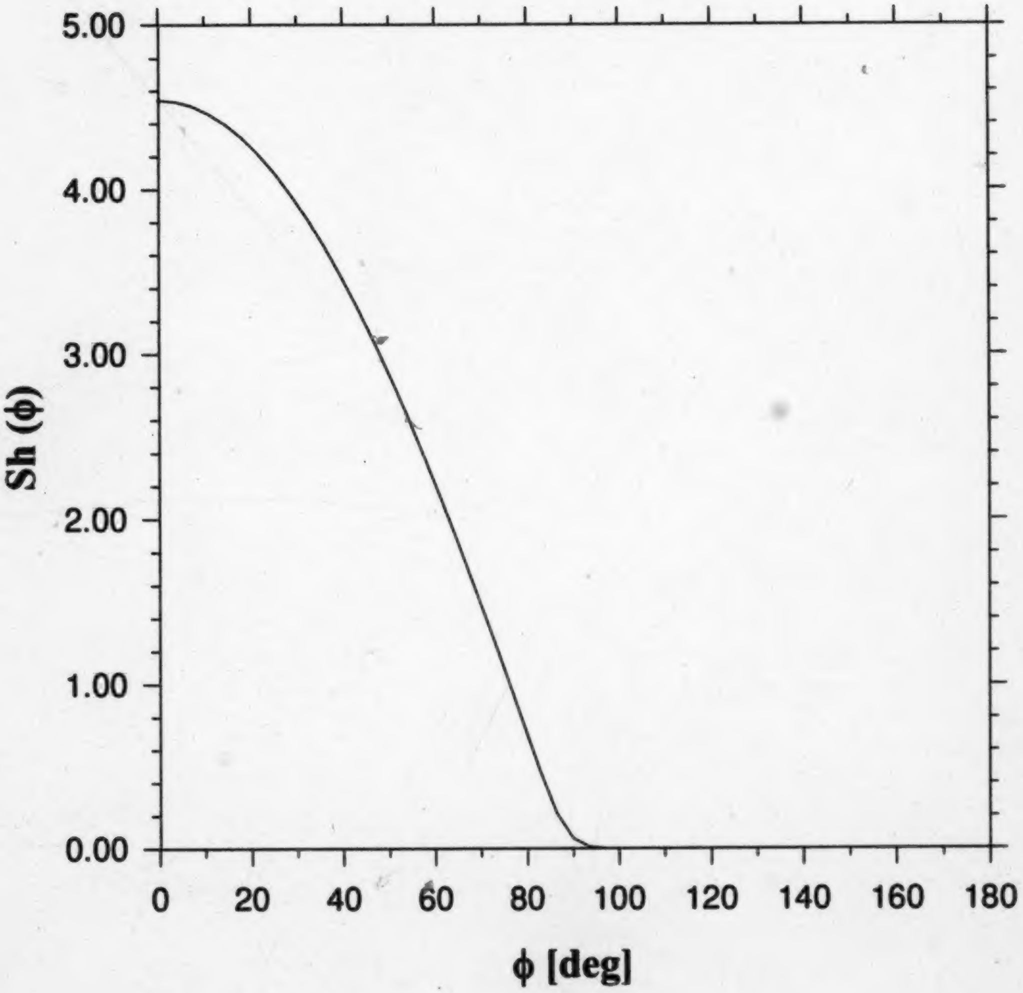

Figure 6.6 Sh(ϕ) number versus ϕ in 2-D deposition case
(A_d=6.00, Dl=0, Gr=0.50, Ef=-0.50, Sh_{ave}=1.4304)

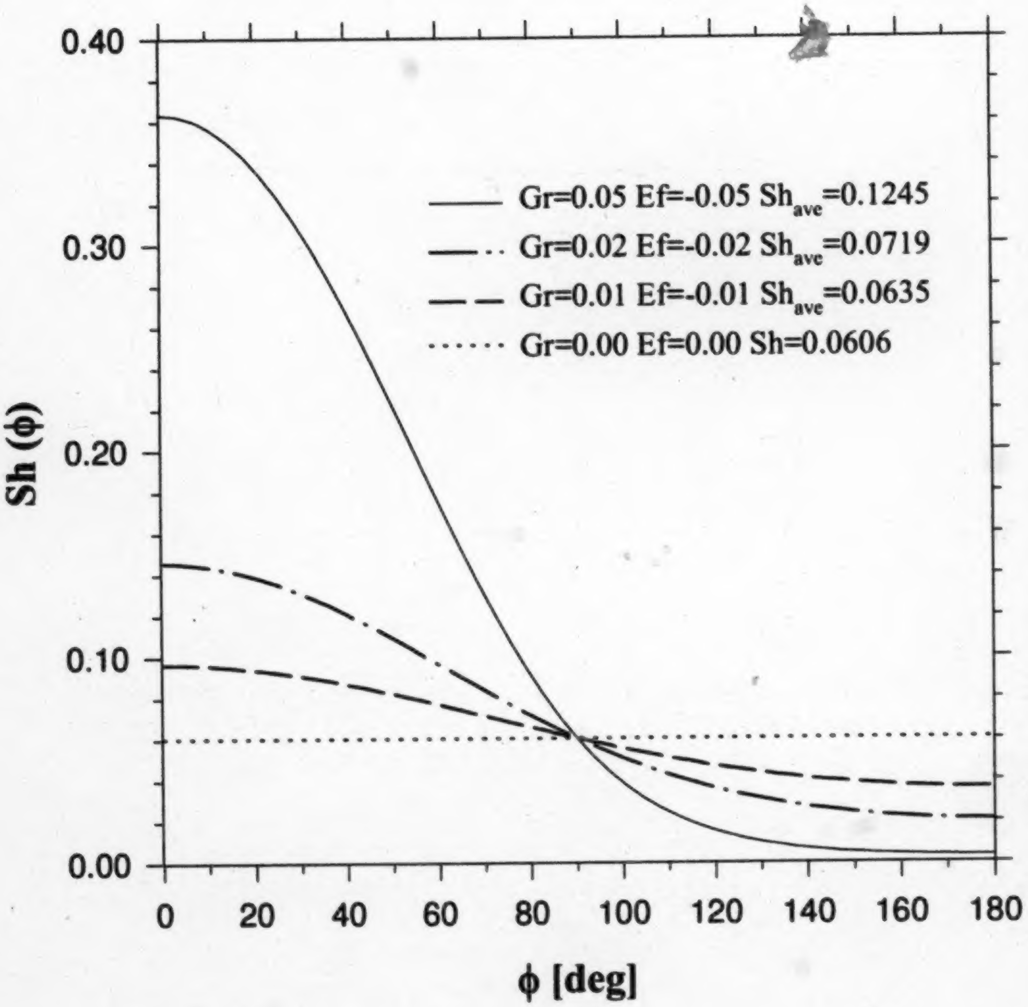

Figure 6.7 Sh(ϕ) number versus ϕ in 2-D deposition case
(A_d=6.00, Dl=0)

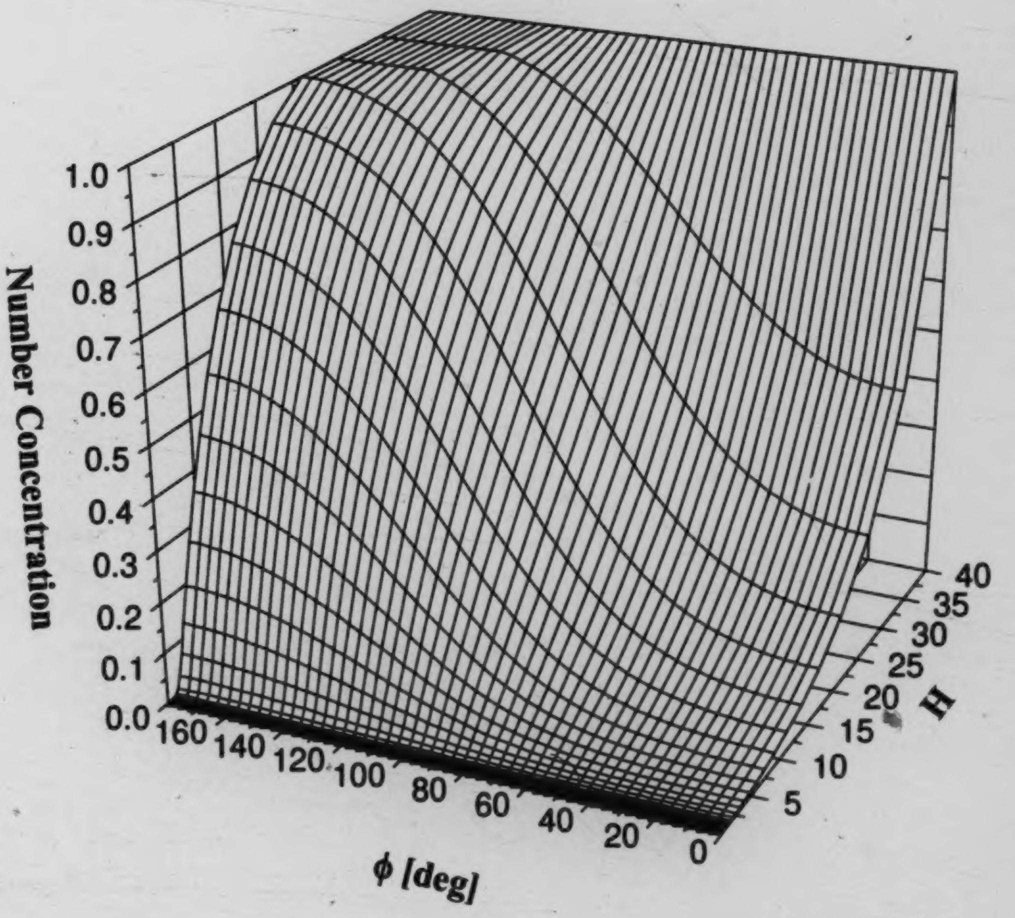

Figure 6.8a Dimensionless droplet number concentration distribution versus H and ϕ in 2-D deposition case (H in linear scale) (A_d=6.00, Dl=0, Gr=0.05, Ef=-0.05, Sh_{ave}=0.1245)

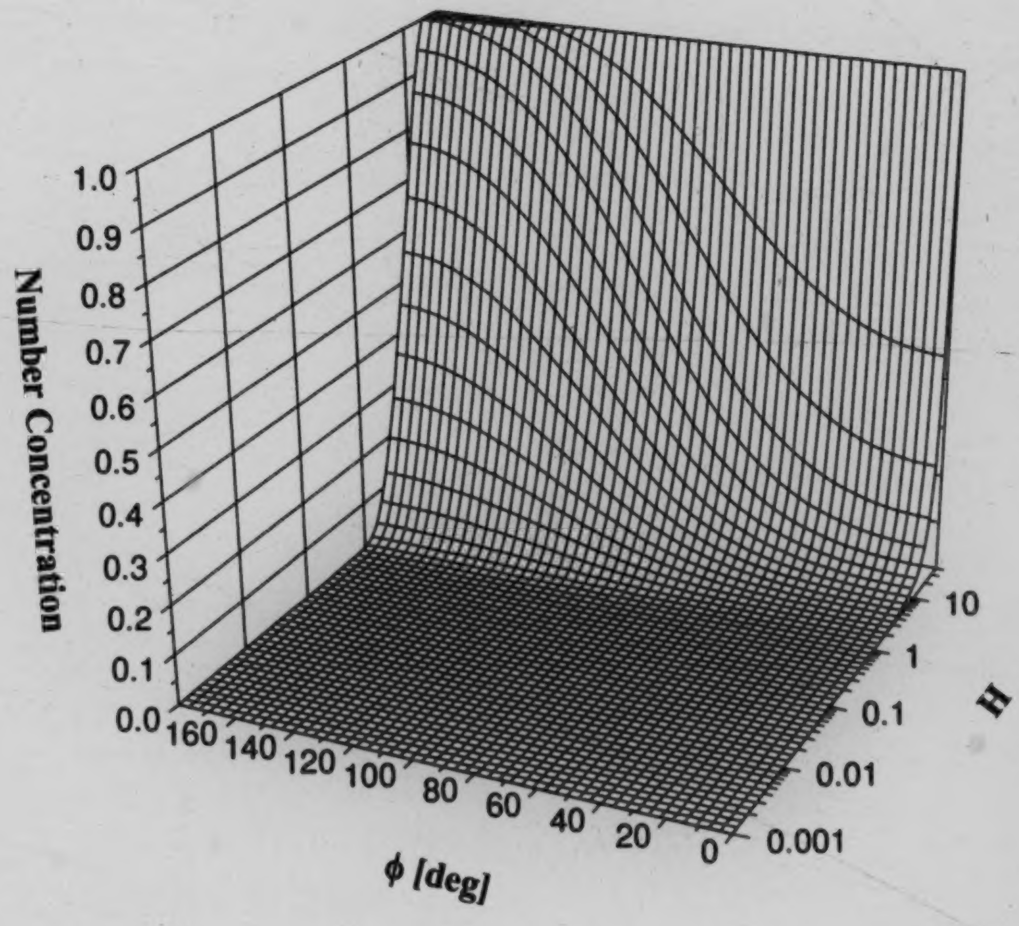

Figure 6.8b Dimensionless droplet number concentration distribution versus H and ϕ in 2-D deposition case (H in log scale)
(A_d=6.00, Dl=0, Gr=0.05, Ef=-0.05, Sh_{ave}=0.1245)

Chapter 7

Experimental Results for Deposition Tests and Their Comparison with the Numerical Predictions

7.1 Introduction

In Chapter 2, it was shown that the deposition mass transfer processes are governed by the colloidal forces and the external force fields. If only the colloidal forces are involved in the deposition system, the mass transfer equation is a second-order ODE and thus deposition becomes a 1-D problem. Based on the framework of the existing DLVO theory, the overall colloidal force is composed of the vdW interaction force and the EDL interaction force, i.e. $\overline{F}_{col}(H) = \overline{F}_{vdW}(H) + \overline{F}_{EDL}(H)$. For the deposition of any spherical particles onto cylindrical fiber surfaces, in Chapter 3, general numerical methods are presented to evaluate the curvature and relative size effects of the cylinder to the spherical droplet on both the vdW interaction and EDL interaction. Also it has been shown that the total dimensionless colloidal force $\overline{F}_{col}(H)$ between the oil droplets and the cylindrical fiber surfaces in the aqueous phases can be fully described by the following dimensionless parameters: A and A_d (or A_{132}) for the vdW force, and A, Dl, Da and τ (or κ^{-1}) for the EDL force. Here, A is the ratio of the radius of cylinder to the radius of the oil droplets. Previously, several important parameters were determined properly, such as the dimensionless adhesion numbers A_d (Tables 4.8 and 4.9 in Chapter 4) and the dimensionless EDL interaction parameters Dl, Da and κ^{-1} for the silicone oil droplet interacting with the bare glass surfaces and the FC725-precoated glass surfaces across various aqueous solutions (Tables 5.3 and 5.4 in Chapter 5).

In Section 6.1, a numerical procedure has been devised and a parameter study of these dimensionless parameters has been carried out. For arbitrarily chosen values of these dimensionless parameters, their detailed effects on the deposition phenomena were examined by numerically solving the mass transport equation, in which only the colloidal forces are involved (1-D model). At this stage, however, there are two tasks that naturally come up and are to be completed. First, the effects of colloidal forces on the deposition processes were not yet studied experimentally for any practical cases. Secondly, it is still to be determined whether the theoretical predictions of the proposed 1-D numerical model are in an acceptable agreement with the experimental results for these practical deposition cases.

In the present chapter, a systematic deposition experiment has been designed to carefully examine the detailed influence of the colloidal forces on the practical deposition processes of the silicone oil droplets onto two kinds of glass fiber surface in a variety of aqueous solutions. The fiber-water-oil deposition systems are exactly the same as those dealt with in Chapters 4 and 5. These deposition data for each specific case will be compared with the numerical predictions of the 1-D model. Instead, the experimentally determined dimensionless parameters are used in the present numerical simulations. Specifically, the dimensionless adhesion numbers A_d for the vdW interaction are taken from Tables 4.8 and 4.9 and the dimensionless EDL interaction parameters Dl, Da and κ^{-1} for the EDL interaction are chosen from Tables 5.3 and 5.4.

7.2 Experimental

7.2.1 Materials

For all the deposition tests, two kinds of glass fiber bars were used: the bare glass bar and the FC725-precoated one. The former is a typical hydrophilic surface, while the latter represents a typical hydrophobic surface. As was described in Chapter 4, their solid surface tensions γ_{fv} can be determined from the equation of state for interfacial tensions, Equation (4.26a). The contact angle θ of the pure DIUF water-vapor interface is about $10.1^{\circ}\pm1.7^{\circ}$ on the bare glass surface and $115.6^{\circ}\pm0.9^{\circ}$ on the FC725-precoated glass surface respectively. Therefore, γ_{fv} is found to be 71.56 ± 0.39 mJ/m^2 for the bare glass fiber surface and 13.87 ± 0.51 mJ/m^2 for the FC725-precoated glass surface.

These two types of glass bars were used as cylindrical fiber surfaces in the deposition test. They are prepared according to the following procedure. First, the precleaned standard glass bar of radius R_c=1.5 mm was heated and stretched to make longer and thinner glass bar with radius about R=200-300 μm. Then the resultant glass bar was cut into pieces, each of 3.0 cm long. As will be described later on, the actual radius R of each glass bar was measured individually with resolution of 1.0 μm. The glass bars were submerged in Acetone for 12 h, rigorously washed with Acetone several times and eventually immersed in the pure DIUF water (Fisher Scientific, Canada) for 12 h. For the deposition tests with the bare glass bars, such cleaned glass plates were dried in air before they were assembled on an deposition shelf. For the deposition tests with the FC725-precoated glass bars, each of such cleaned glass bars was dried in air and then coated with the FC725 coating material (3M Product) by using the dip-coating method as was described in Section 4.4. Thus a uniform and smooth coating layer of the FC725 (hydrophobic material) was left on the glass bar. The coated glass bar was suspended vertically and dried in air prior to being assembled on the deposition shelf.

Silicone oil No. 1 with density of ρ_o=1050 kg/m^3 and viscosity of μ_o=172.7 mPa s (Aldrich Chemical Co.) was chosen as the dispersed oil phase in the deposition tests. Its small density difference from the aqueous phase greatly facilitates making stable oil-in-water (O/W) emulsions for this experimental study. The silicone oil-air surface tension is equal to γ_{ov}=26.10±0.14 mJ/m^2 at 22°C.

Four kinds of aqueous phases were used as the continuous phase each time in making the O/W emulsions and deposition experiments. These aqueous solutions were exactly the same as those tested for determining the Hamaker constants (Tables 4.8 and 4.9) and those used in measuring the ζ-potential measurements of silicone oil droplets and the glass surfaces (Tables 5.3 and 5.4). They were the pure DIUF water (Fisher Scientific, Canada); the aqueous phases with different pH values; the electrolyte solutions containing either NaCl or $AlCl_3$ and the ionic surfactant solutions containing either CTAB or SDS. The pure DIUF water with a density of ρ_w=998 kg/m^3 has a liquid-air surface tension of γ_{wv}=72.66±0.31 mJ/m^2 at 22°C, an initial conductivity of 1.21×10^{-4} S/m and an equilibrium pH of about 6.5. The interfacial tension for pure water-oil interface is equal to γ_{ow}=35.31±0.44 mJ/m^2. In the preparation of the aqueous phases with different pH values, the pH value of the DIUF water was adjusted to a desired value by adding either NaOH or HCl into the pure DIUF water. The electrolyte solutions were prepared by adding either NaCl or $AlCl_3$ at a different concentration (from 10^{-6} M to 10^{-3} M) each time into the pure DIUF water. Two typical ionic surfactants were used to make surfactant solutions: the cationic surfactant cetyltrimethylammonium bromide (CTAB) and the anionic surfactant sodium dodecyl sulphate (SDS). Their critical micelle concentrations (CMC) in water determined from their surface tension-concentration curves were reported to be about 9.2×10^{-4} M for CTAB (Czerniawski, 1966) and 8.1×10^{-3} M for SDS at 25°C (Stalidis et al., 1990). The ionic surfactant solutions were prepared by adding one of the two ionic surfactants at a different concentration (from 10^{-6} M to 10^{-3} M for CTAB or from 10^{-6} M to 10^{-2} M for SDS) each time into the pure DIUF water. Usually a period of more than 12 h was given for these chemicals to be completely dissociated and uniformly distributed in the aqueous phase.

7.2.2 Preparation of the Silicone Oil-in-Water (O/W) Emulsions

After each aqueous solution was prepared, the general procedure for making each silicone O/W emulsion for the deposition tests was as follows. All the silicone O/W emulsions were made by suspending 0.25% (v/v) silicone oil in the aqueous solutions. A sample of 1.0 ml silicone oil was added into a beaker with 400 ml prepared aqueous solution. Inside the beaker, a homogenizer (Gifford-Wood Homogenizer, Greerco Corp., Hudson, New Hampshire) was stirring at a pre-set speed of 2000 rpm. The silicone oil was dispersed and then gradually the O/W emulsion was formed. Stirring was continued for 20 min after addition of the silicone oil. It was found through trial and error that, by stirring the oil-water mixture at the speed of 2000 rpm for 20 min, the sizes of most silicone droplets are in a desired range of a=5-15 μm. More importantly, such prepared O/W emulsions are stable, i.e. no appreciable size changes were observed for more than 12 h, though usually the entire deposition test for each fiber-water-oil deposition system can be completed within only a few hours. The fresh O/W emulsion was aged for at least 2 h so that a stable droplet size distribution of the O/W emulsion droplets could be reached. Finally, the aged O/W emulsion was gently poured into a glass beaker for deposition test. Usually, about 5 min was allowed for the agitated emulsion to "calm down" inside the test cell, which was followed by the measurements of droplet sizes (Section7.2.4) and introduction of the deposition shelf.

7.2.3 Deposition Cell

Two glass bars of the same kind (about 3 cm long each) were used each time and assembled on an deposition shelf in parallel. Then the deposition shelf was inserted into the glass beaker full of the O/W emulsion and positioned vertically. A block diagram of the experimental apparatus for deposition test is shown in Figure 7.1. In the set-up, the deposition cell is placed on a three-dimensional translation stage with a vertical resolution of 0.1 mm, which is positioned between a light source and a microscope. By using this 3-D translation stage, during the deposition test, the deposition cell can be readily moved in the three directions at will. The light source and the microscope system mounted with the video camera are same as those described in details in Section 4.3. The internal dimensions of the rectangular deposition cell are 50(L)x30(W)x80(H) *mm*, which can hold approximately 100 *ml* solution. Inside the deposition cell, two glass bars have about a 2.5 cm length fully exposed to the bulk emulsion phase. They are separated from each other by approximately 1 cm so that their deposition processes will proceed independently.

7.2.4 Deposition Measurements

Immediately after insertion, deposition of the silicone oil droplets onto the glass bars begins. It is an obvious fact that the initial deposition rate will not only depend on the fiber-water-oil deposition system under investigation, but also largely depend on the specific insertion process. Therefore, such initial random deposition period should be discarded in the formal deposition measurements. In the deposition test, the number of the attached oil droplets was counted at t=15 min after the deposition shelf was introduced. Such counting is then conducted at t=30, 60 and 90 min after the initial deposition, respectively. Hence, a total effective deposition period of 75 min is observed. The detailed counting procedure is described as below.

At t=15 min after the insertion of the deposition shelf, the deposition cell, including the deposition shelf and glass bars, are moved by using the 3-D translation stage either to the right or left (x-axis) so that either one of the two glass bars is within the scope of the microscope and camera system set at x40 magnification. Then the image of attached droplets on the glass bar can be observed clearly by adjusting the focal distance, i.e. by using the 3-D translation stage to move the deposition cell forward or backward (y-axis). Such observation and counting procedure of the attached oil droplets is continued 10-mm (l=10 mm) long either upward or downward along the axial direction of the glass bar. This is done by using the 3-D translation stage to move the deposition cell upward or downward (z-axis). Since the diameter of the glass bar is usually larger than the width (w) of the digital image covered by the microscope and camera system at x40 magnification, the actual deposition area under observation is a partial lateral surface area of the glass cylinder. The front view of this deposition area looks like a rectangular (w x l). This counting procedure is repeated for the other glass bar and the deposition observation is carried out at t=15, 30, 60 and 90 min after the initial introduction of the deposition shelf. For each kind of aqueous solution, the above mentioned measurement procedure is repeated once for the same glass fiber surface. Hence, for a given fiber-water-oil deposition system, a total of four numbers of the attached droplets are collected at t=15, 30, 60 and 90 min respectively in each deposition test. The overall experimental procedure remains invariable, regardless of the specific glass surface and O/W emulsion used. The entire experimental set-up was placed on a vibration-free table and all the deposition measurements were conducted at room temperature 22°C.

The complete deposition measurement is composed of the following four major measurements: droplet size measurements; cylinder size measurements; deposition area measurements and number counting of the attached droplets. By going through these measurements, the dimensionless mass transfer or deposition rate Sh can be determined (see Section 7.2.5). Same microscope and camera system was used at x40 magnification to measure the radius *a* of the silicone oil-in-water emulsion droplets. As was mentioned in Section 7.2.2, the proper stirring speed and duration in making the O/W emulsions were found by trial and error so that the radii of most observed oil droplets are in the range of a=5-15 μm, with an average radius of $a_{ave} \approx 10$ μm. This size range can be well observed and measured by using the present optical system. The droplet size measurements were conducted prior to the introduction of the deposition shelf. In the measurements, 100 snapshots of the oil droplets were taken randomly and their instantaneous digital images were acquired and stored in the computer memory. The procedure for determining the radius *a* of each droplet from each snapshot has been described in detail in Section 5.3.3 and the overall accuracy of the droplet size measurement is around 0.5 μm. The average radius a_{ave} is determined from the radii of 100 oil droplets under scrutiny. Once a_{ave} is known, the droplet number concentration n_∞ in the bulk emulsion can be estimated from the total volume conservation of the oil phase. The above microscope and camera system was also used to measure the radius R of each glass bar, except that the optical system was set at x16 magnification in this case. Generally, R is in the range of 200-300 μm and the overall accuracy of its determination is approximately 1.0 μm.

The next task was to determine the deposition area. As is schematically shown in Figure 7.2a, the actual deposition area under observation (represented by dotted line) is a fraction of the lateral surface area of the glass bar. Furthermore, this deposition surface area under examination (again represented by dotted line) is magnified and shown in Figure 7.2b. From this diagram, it is found that the actual deposition area S is equal to:

$$S = 2Rl\sin^{-1}\left(\frac{w/2}{R}\right) \tag{7.1}$$

where w is the width of the snapshot covered by the microscope and camera system at x40 magnification and l is the length observed along the axial direction of the glass cylinder. For the optical system used in the present deposition measurements, w is usually about 350 μm and can be determined with an accuracy of 0.5 μm. The length l is always chosen as 10 mm and can be read up to 0.1 mm, equal to the vertical resolution of the 3-D translation stage. If the width is much smaller than the radius of glass bar, i.e. $\frac{w}{R} \ll 1$, then $\sin^{-1}\left(\frac{w/2}{R}\right) \approx \frac{w/2}{R}$. Substituting the approximate expression for $\sin^{-1}\alpha \approx \alpha$ at $\alpha \approx 0$ into Equation (7.1) yields $S \approx wl$, the surface area of a rectangular. Finally, the number N(t) of attached droplets onto the glass surface is counted at t=15, 30, 60, 90 min, respectively. Usually, deposition rate is extremely high in the first 15 min, which is caused by insertion movement of the glass fibers into the O/W emulsions. This is followed by a constant low deposition rate for the remaining deposition period. This constant low deposition rate is attributed to the presence of the vdW and EDL forces acting between the oil droplets and the glass surface in the aqueous solution. In all the deposition measurements, no saturation state of deposition, i.e. the attached droplet number remains unchanged, was observed until 90 min.

A typical snapshot (produced by a laser printer) of such attached droplets onto cylindrical glass bar is shown in Figure 7.3. In this digital image, the attached oil droplets can be clearly seen and thus counted. Generally, their deposition onto the glass surface is found to be irreversible. Furthermore, such attached droplets may not be uniformly distributed from place to place. However, statistically, their overall distribution or surface coverage is strongly related the properties of the fiber-water-oil system under examination. It is also worthwhile mentioning that, in this experimental deposition study, the surface coverage is extremely low. For example, until 90 min, the maximum total number of the attached oil droplets recorded in all the deposition cases is less than 400 on the deposition area of $S \approx wl$. Given w≈350 μm and l=10 mm, if the average radius of the attached droplets is assumed to be about 15 μm on the glass surface, then the possible peak surface coverage of the attached oil droplets at the end of each deposition test is only about 8.1%. Therefore, as the deposition proceeds, the attached oil droplets do not modify the surface properties of the glass bar to an appreciable extent. The so-called "blocking/masking effect" of the attached oil droplets on the upcoming droplets onto the glass surface is sufficiently negligible. On the other hand, there always remains an adequately large number of the silicone oil droplets freely moving in the bulk emulsion. It is due to these two facts that no saturation states of deposition were observed in all the deposition measurements. The number of the attached droplets always increases linearly with the deposition time until t=90 min.

7.2.5 Determination of Sh

After the completion of the deposition test for a given fiber-water-oil deposition system, the droplet number transfer rate J_{exp}, the dimensionless mass transfer rate Sh can be determined from the measured number N(t) of the attached droplets on the deposition area S in the period of Δt:

$$J_{exp} = -\frac{N(t+\Delta t) - N(t)}{S\Delta t} \qquad t \geq 15\,\text{min} \tag{7.2}$$

$$Sh_{exp} = -\frac{J_{exp}}{\frac{D_\infty n_\infty}{a_{ave}}} \tag{7.3}$$

where:

$$D_\infty = \frac{\mathrm{k}T}{6\pi\mu a_{ave}} \tag{7.4}$$

As was mentioned in Section 7.2.4, for a given fiber-water-oil deposition system, the entire deposition experiment was repeated once. In each deposition test, two glass bars were assembled on the deposition shelf and four numbers of N(t) were taken for each glass bar at t=15, 30, 60 and 90 min respectively. Hence, for each deposition system under investigation, a total of twelve measured values for J_{exp} or Sh are obtained from Equation (7.2) or Equation (7.3). It is noted that the deposition period of the first 15 min was not accounted in the data processing because the deposition during this period is caused largely by the insertion motion rather than solely by the colloidal forces. Only the average Sh numbers over the twelve measured values will be mentioned hereafter and compared with the numerical predictions in the subsequent section. In the present deposition tests, the overall repeatability for the dimensionless mass transfer rate Sh number was found to be within 10%. For a variety of aqueous solutions, the vdW interaction parameter (A_d) and the EDL interaction parameters (Dl, Da and κ^{-1}), as well as the detailed deposition test data and the numerical results are listed in Table 7.1 for the bare glass surface and Table 7.2 for the FC725-precoated glass surface respectively.

7.3 Deposition Experimental Results and Their Comparison with the Numerical Predictions

7.3.1 pH Effect

The pH value was altered approximately from 3.0 to 10.0 by adding standard dilute solutions of either HCl or NaOH into the pure DIUF water. The measured dimensionless mass transfer rates, Sh numbers, of the silicone oil droplets onto two different glass surfaces with various pH values are shown in Figure 7.4a. Their numerical results are also included in the same figure for comparison. This figure clearly shows that, for the bare glass surface and the FC725-precoated glass surface, both measured Sh numbers and the numerical results monotonically decrease as pH values increases. As were shown in Tables 5.3 and 5.4, this is because the ζ-potentials of both the silicone oil droplets and the two glass surfaces are strong and have the same polarity (negative) when they are in contact with the aqueous phases having higher pHs. Thus the reduction of Sh is attributed to the increasingly strong repulsive EDL interaction as pH value increases. It is also noticed from Table 7.2 that, for the FC725-precoated glass surface, such reduction tendency is further strengthened by a rapid reduction in the vdW interaction with increasing pH values.

More specifically, for bare glass surface, the numerical predictions of Sh are in an excellent agreement with the experimental results within the experimental error, though generally the latter are slightly larger than the former. Thus it can be concluded that the deposition process of the silicone oil droplets onto the bare glass surface (hydrophilic) can be satisfyingly described by the mass transfer equation based on the existing DLVO theory, in which both the vdW and EDL interactions are included. It is also seen from Figure 7.4a that the numerical model predicts lower Sh for the FC725-precoated glass surface than that for the bare glass surface when pH is below 4.5, which is located slightly in the acid side. However, this pattern is reversed at pH above 4.5. This change can be explained as follows. As seen from Figure 5.2, this pH value corresponds to the point of zero zeta (pzz) of the silicone oil droplets dispersed in the aqueous phase. At higher pHs, Tables 5.3 and 5.4 indicate that the ζ-potential of the bare glass surface is more than twice stronger than that of the FC725-precoated glass surface. As discussed above, at higher pHs, the reduction of Sh is attributed to the increasingly strong repulsive EDL interaction for the both glass surfaces. Therefore, at higher pHs (pH≥5.0), smaller Sh for the bare glass surface is mainly caused by its much stronger repulsive EDL interaction, though its vdW interaction A_d is stronger than that for the FC725-precoated glass surface.

It is noted from Figure 7.4a that the experimentally measured Sh numbers for the FC725-precoated glass surface are significantly larger than the corresponding numerical predictions over the entire pH range, particularly at even smaller pHs. They are also larger than those measured Sh values for the bare glass surface over the entire pH range. It becomes obvious that, unlike the deposition case of the silicone oil droplets onto the hydrophilic surface such as the bare glass surface, the deposition of the silicone oil droplets onto the hydrophobic surface such as the FC725-precoated glass surface can not be adequately predicted by using the classical DLVO theory alone. In other words, there is some additional attractive non-DLVO force operating in the deposition of the hydrophobic surface (oil droplets) onto the other hydrophobic surface (FC725-precoated surface) in aqueous solutions in the present case. In the literature, the attractive interaction between two hydrophobic surfaces in water has been known to be unusually strong in several cases (Israelachvili and Pashley, 1984). Such "hydrophobic interaction" belongs to a class of important phenomena collectively referred to as the "hydrophobic effect". Hence, in the deposition tests, the unusual large Sh for the FC725-precoated glass surface may be also caused by the hydrophobic interaction between these two hydrophobic surfaces in aqueous phases. Furthermore, the deviation of the measured Sh values from the theoretical predictions represents the portion attributable to the hydrophobic effect. A brief description of the hydrophobic effect and particularly its influence on the present deposition rate Sh will be presented later in Section 7.4.

In order to gain insight into the dominant driving force in the deposition process, it is necessary to study the competition between the vdW interaction and the EDL interaction under certain practical conditions. Figure 7.4b shows the EDL, vdW and the total dimensionless interaction potentials between the silicone oil droplet and the bare glass fiber in the pure DIUF water. The relevant dimensionless parameters used to calculate the dimensionless vdW and EDL interaction potentials are chosen from Table 7.1 and further listed as follows: A_d=5.35, Dl=+48200, Da=+0.16 and τ=10. By using the 1-D numerical model presented in Chapter 6, the dimensionless mass transfer rate Sh number is found to be Sh_{cal}=0.0153, which is in an excellent agreement with the measured value Sh_{exp}=0.0168. Three important features can be identified in Figure 7.4b and are discussed below. First, the calculated primary energy minimum (PEM) is equal to -2244.6 at the PEM region H_0=0.001. The PEM point is not included in the figure for graphic reason. This PEM is far deeper than 25 kT, a usually accepted value for the PEM. Therefore, the "perfect sink" approximation as expressed by Equation (6.3b) or (6.7b) is valid for the present deposition tests. Physically, this approximation implies that all the silicone oil droplets will be irreversibly attached onto the fiber surface once they are in the vicinity of the PEM region. This is because the dimensionless vdW interaction potential decays approximately with $\frac{1}{H}$ at H«1, referring to Equation (3.15), and with $\frac{1}{H^3}$ at H»1, referring to Equation (3.16). The dimensionless retarded vdW interaction force for the present sphere-cylinder system is also shown in Figure 3.4. However, the dimensionless EDL interaction potential decays exponentially with H (see Equation (3.36) for the sphere-flat plate case and Figure 3.7 for the EDL interaction force between a sphere and a cylinder). Therefore, at small separation distances such as $H<0.005$ in the present case, the attractive vdW interaction is dominant and ensures deposition. Secondly, in Figure 7.4b, there is an energy barrier equal to +24.1 at $H\approx0.008$. This large energy barrier is formed due to strong repulsive EDL interaction between the silicone oil droplet and the bare glass fiber in the pure DIUF water. In this particular case, both EDLs at the oil-water interface and at the fiber-water interface are negatively charged (see Table 5.3). Finally, a secondary energy minimum (SEM) is found to be -3.9 at $H\approx0.027$. In the deposition tests, this SEM region may be responsible for attracting and bringing the silicone oil droplets from the far field into the proximity of the energy barrier. Furthermore, some of these oil droplets in the vicinity of the SEM region will overcome the energy barrier and enter the PEM region. As mentioned above, in the present case, the PEM is so strong that, once the oil droplets overcome the energy barrier, they will be irreversibly trapped in the PEM region and thus permanent deposition occurs.

7.3.2 Electrolyte Effects

The variations of the measured and calculated dimensionless mass transfer rate Sh of the silicone oil droplets onto the bare glass surface with the mole concentration of the following two typical electrolytes, NaCl and $AlCl_3$ from 10^{-6} to 10^{-3} M are plotted in Figure 7.5a. Two common points for these two electrolytes can be readily identified. First, at 10^{-6} M, both experimentally measured and numerically predicted Sh values for these two electrolyte solutions are close to the value for the pure DIUF water case. At this concentration, these two electrolytes do not have an appreciable effect on modifying the deposition. Second, the measured Sh increases monotonically as the electrolyte concentration of either NaCl or $AlCl_3$ increases from 10^{-6} to 10^{-3} M. The numerical predictions for these two electrolytes not only follow the same trend but also agree well with the experimental data over these electrolyte concentrations, though the theoretical Sh for $AlCl_3$ remains nearly constant at the electrolyte concentration higher than 10^{-5} M. As seen in Table 7.1, such increase of Sh with the electrolyte concentration is due to slightly increased A_d and the strong neutralization effect of the electrolytes on the ζ-potentials of the silicone oil droplets and the bare glass surfaces. For example, Table 5.3 shows that, as the concentration of NaCl increases from10^{-6} to 10^{-3} M, the negative ζ-potentials of the oil phase and the glass surface are much weaker (about half). As a result, the repulsive EDL interaction (DI) between them is reduced by a factor of four. It is also shown in this table that, as the $AlCl_3$ concentration further increases, the ζ-potential of the silicone oil droplets even becomes positive. The zeta reversal occurs near 10^{-6}-10^{-5} M for $AlCl_3$. As indicated in Section 5.4.2, the positive ζ-potential for the multivalent electrolyte results from the well-known much stronger adsorption of the trivalent cations Al^{3+} onto the oil-water interfaces than that of the monovalent Na^+. This also explains why Sh for $AlCl_3$ is considerably larger than that for NaCl.

Furthermore, it is also noticed from this plot that the experimentally measured Sh numbers for NaCl and $AlCl_3$ do not change significantly when both electrolyte concentrations approach 10^{-3} M. This is an expected result because, at higher electrolyte concentrations, addition of more electrolyte will considerably reduce the ζ-potentials of silicone oil droplets and the glass surface due to the more compressed (thinner) EDLs. Therefore, at even higher electrolyte concentrations, a limiting Sh will be achieved because the vdW interaction does not change appreciably and the EDL interaction plays a much less pronounced role in deposition than at lower electrolyte concentrations.

Figure 7.5b shows the dimensionless mass transfer rate Sh number versus log concentration of the two electrolytes for the FC725-precoated glass surface. In contrast with the above mentioned trends for the bare glass surface, the measured Sh decreases slightly as the electrolyte concentration of either NaCl or $AlCl_3$ increases from 10^{-6} to 10^{-3} M. It is also shown in this plot that Sh values for these two electrolytes are close to each other. Specifically, Sh numbers for NaCl are slightly larger than those for $AlCl_3$, consistent with their corresponding A_d values given in Table 7.2. These two facts suggest that in this case the EDL interaction is not an important driving force in deposition. It can be easily found from Table 5.4 that, unlike the bare glass surface, the FC725-precoated glass surface is only charged to a limited extent when it is contact with aqueous phase. Hence, in comparison with the vdW interaction, the EDL interaction between the silicone oil droplets and the FC725-precoated glass surface is no longer a dominant force in the deposition of the silicone oil droplets onto this solid surface. In contrast to the increase of A_d with the electrolyte concentration of either NaCl or $AlCl_3$ for the bare glass surface given in Table 7.1, the dimensionless adhesion number A_d for the FC725-precoated glass surface listed in Table 7.2 decreases appreciably as the electrolyte concentration increases from 10^{-6} to 10^{-3} M. As a result, the slow reduction of Sh shown in Figure 7.5b is largely attributed to gradual reduction of A_d. Again in contrast to the results for the bare glass surface plotted in Figure 7.5a, Figure 7.5b shows a much greater difference between the measured Sh_{exp} and the predicted Sh_{cal}. As was mentioned in Section 7.3.1, the larger Sh_{exp} is also attributed to the so-called hydrophobic effect, which will be discussed exclusively in Section 7.4.

7.3.3 Effects of Ionic Surfactants

In Sections 5.4.3 and 5.8.4, it has been shown that the adsorption of the ionic surfactants CTAB and SDS onto either the silicone oil-in-water emulsion droplets or the glass fiber-water interfaces strongly affects their ζ-potentials. Therefore, it is expected that such adsorption will also strongly affect the deposition process of the oil droplets onto the glass fiber surfaces in the ionic surfactant solutions. Figure 7.6a gives the dimensionless mass transfer rate Sh numbers for the bare glass surface at different concentrations of CTAB (10^{-6}-10^{-3} M) and SDS (10^{-6}-10^{-2} M). At 10^{-6} M, both the measured and numerical Sh numbers are close to that for the pure DIUF water. It is seen from Figure 7.6a that Sh increases considerably with CTAB concentration from 10^{-6} M and 10^{-4} M, though the dimensionless adhesion number A_d is slightly reduced in the same range of CTAB concentrations (see Table 7.1). This suggests that the EDL interaction is a dominant factor in the deposition in this cationic surfactant solution.

Physically, such variations of Sh number with CTAB concentration are caused by the well-known cationic adsorption onto the silicone oil-water interfaces and the glass fiber-water interfaces. Specifically, it is shown in Figure 5.4 and Table 5.3 that the measured ζ-potential ζ_p of the silicone oil droplets becomes positive and increases quickly when the CTAB concentration is higher than 3×10^{-6} M, the point of zeta reversal (pzr). A further increase of the CTAB concentration results in a slow increase of the ζ-potential and, finally, to reach its maximum value near +83.1±6.9 mV between 10^{-4} to 10^{-3} M. The saturation of cationic adsorption onto the oil-water interfaces is considered to occur between the two concentrations. On the other hand, Figure 5.13 and Table 5.3 also indicate that the measured negative ζ-potential ζ_c of the glass-water interfaces is gradually neutralized by the cationic adsorption onto these two interfaces. Eventually, the saturation state of cationic adsorption onto the glass-water interfaces occurs between 10^{-4} to 10^{-3} M. Close to these two concentrations, $\zeta_c\approx0$, indicating that the glass-water interfaces become almost electrically neutral. As shown in Figure 7.6a and Table 7.1, both measured Sh numbers and the numerical predictions are in accordance with the above trends. Further increase of the CTAB concentration leads to the maximum Sh value occurring at 10^{-4}-10^{-3} M.

Variations of Sh with log concentration of SDS from 10^{-6} to 10^{-2} M are also shown in Figure 7.6a. As expected, Sh decreases monotonically when more SDS is added into the aqueous solution. This is because, as discussed in Sections 5.4.3 and 5.8.4 and further summarized in Table 5.3, the ζ-potentials of the silicone oil droplets and the glass surfaces in the anionic solution become more negative due to the intensified anionic adsorption as more SDS is introduced into the aqueous phase. On further increase of the SDS concentration, Figures 5.4 and 5.13 show that such anionic adsorption continues until the strongest negative ζ-potentials, ζ_p=-58.4 mV for the oil-water interfaces and ζ_c= -90 mV for the glass-water interfaces, are attained at 10^{-3}-10^{-2} M. The saturation state of the anionic adsorption is considered to be reached between these two concentrations for the both interfaces. Accordingly, Sh approaches its minimum at the SDS concentration of 10^{-3}-10^{-2} M. It is noticed that decreasing tendency of Sh with the SDS concentration is also strengthened by gradually reduced vdW attractive interaction (see A_d in Table 7.1).

Finally, it is worthwhile pointing out that the numerical predictions of Sh with the SDS concentration are in an excellent agreement with the measured values for the anionic surfactant. For the cationic surfactant CTAB, a fairly good agreement between the experimentally measured and numerically calculated Sh numbers is also achieved, though the numerical curve is somewhat bumpy because the numerical calculations are carried out at discrete surfactant concentrations only. In addition, both the experimental and numerical results suggest that the limiting Sh is obtained at higher CTAB concentrations. This fact suggests that further increase of CTAB concentration beyond the tested concentration range might not lead to even higher deposition rates in the deposition experiments. This becomes an obvious conclusion since, at the CTAB concentration greater than 10^{-3} M, both limiting ζ_p and ζ_c become positive, in conjunction with the reduction of A_d as well (see Table 7.1). All these results with the bare glass surface prove that the conventional DLVO theory can be adopted to fully describe the deposition case of the silicone oil droplets onto the hydrophilic bare glass surface in various aqueous solutions.

Figure 7.6b shows similar results of the dimensionless mass transfer rate Sh numbers for the FC725-precoated glass surface at different concentrations of CTAB (10^{-6}-10^{-3} M) and SDS (10^{-6}-10^{-2} M). As the CTAB concentration increases from 10^{-6} M to 10^{-3} M, both Sh_{exp} and Sh_{cal} increase by about 100%. In the present case, as given in Table 7.2, such a rapid increase of Sh number is caused by both gradually increased attractive vdW interaction (A_d) and the attractive EDL interaction ($DI<0$) as well. However, for the anionic surfactant SDS, as might be expected, Sh decreases slightly in the concentration range of from 10^{-6} to 10^{-2} M since the considerably increased repulsive EDL interaction ($DI>0$) is partially counteracted by the slightly increased attractive vdW interaction (A_d). In either case, the measured Sh numbers are substantially larger than the theoretical values. Especially, it is noted from Figure 7.6b that as the CTAB concentration increases, such difference becomes even larger, which is far beyond the experimental error (10%) of deposition tests. As mentioned above, the large deviations between the measured Sh numbers and the numerical data are observed for the FC725-precoated glass surface only. They are assumed to be due to the attractive hydrophobic interaction between the hydrophobic silicone oil surface and the hydrophobic FC725-precoated glass surface in the aqueous solutions. In contrast to the deposition case of the silicone oil droplets onto the hydrophilic bare glass surface in aqueous solutions, the deposition process of such oil droplets onto the hydrophobic surface in water can not be adequately described by the classical DLVO theory in which the hydrophobic interaction is not accounted for. A concise discussion of the hydrophobic interaction between two hydrophobic surfaces in aqueous solutions and its possible influence on the present deposition study will be presented in the next section.

7.4 Hydrophobic Effect

The attractive interaction between two hydrophobic surfaces in water is known to be unusually strong. This "hydrophobic interaction" (Franks, 1973) belongs to a class of important phenomena collectively referred to as the "hydrophobic effect". The hydrophobic interaction plays a central role in micelle formation, biological membrane structure, and in determining the conformations of proteins. In conjunction with the well-known vdW and the EDL interactions, it determines the stability of many suspension and emulsion systems if the dispersed colloidal particles are hydrophobic. It also accounts for the high interfacial tension of liquid hydrocarbon-water interfaces, and the large contact angles subtended by water on hydrophobic surfaces.

In the literature, there have been several experimental findings and estimates of the hydrophobic interaction. For example, Israelachvili and Pashley (1982; 1984) derived the attractive force-law between two hydrophobic (hydrocarbons) surfaces in electrolyte solutions from total force measurements on monolayer coated mica surfaces. They further showed that this hydrophobic interaction is much stronger than the expected vdW interaction at the separation distances below 8 nm and decays exponentially with distance. Their experimental results indicate that these forces may determine the magnitude of the energy barriers between interacting charged particles and hence the stability of hydrophobic colloids. Later on, Xu and Yoon (1989) conducted a series of coagulation experiments on aqueous suspensions of methylated silica. Their coagulation experiments provide evidence that non-DLVO interaction (i.e. assumed the hydrophobic interaction) is the major driving force for the coagulation of these colloidal particles with strong hydrophobicity. Furthermore, they derived the hydrophobic interaction potential from the results of coagulation experiments. The hydrophobic interaction potential is expressed in terms of the nondispersion component of deposition work of water phase and the distance between the two interacting particles. More recently, Dai and Lu (1991) showed experimentally that a non-polar oil (kerosine) emulsion can significantly intensify the hydrophobic flocculation of minerals. The non-polar oil was found to play two roles in accelerating the flocculation, one is to adhere onto the surface of hydrophobic particles to enhance their hydrophobicity and the other is to form an oil bridge among the hydrophobic particles to increase the strength of the flocs. Eventually, they also derived an explicit expression for calculation of the hydrophobic interaction potential between an oil drop and a hydrophobic particle in terms of hydrophobic interaction theory.

In the present deposition study, it has been shown in Figures 7.4, 7.5a and 7.6a that the all the experimental Sh numbers for the bare glass surface (solid symbols) are in an excellent agreement with the theoretical predictions (lines). The latter are determined by numerically solving the mass transfer equation in which only the vdW and EDL interactions are included. However, the experimental data Sh_{exp} for the FC725-precoated glass surface are found to be significantly higher than the theoretical results based on the classical DLVO theory. In comparison with the calculated values (lines) in Figures 7.4, 7.5b and 7.6b, the measured dimensionless mass transfer rates of the hydrophobic silicone oil droplets onto the hydrophobic surface (empty symbols) in these figures usually increase by approximately 30-45%, which is far beyond the deposition experimental error of approximately 10%. Therefore, the present deposition experimental results for the FC725-precoated glass surface provide proof that non-DLVO attractive interaction is also involved in deposition. This additional interaction, which may be referred to as the hydrophobic interaction, is responsible for the deviations of the experimental data of deposition tests from the theoretical predictions based on the classical DLVO theory alone.

Strictly speaking, the hydrophobic surfaces can be classified into those that are naturally hydrophobic (e.g., talc, paraffin wax, Teflon, molybdenite, some types of coal) and those made hydrophobic by surfactant adsorption (e.g., by cationic surfactant adsorption on proper solid surfaces). In this study, the FC725 coating material is naturally hydrophobic and thus the FC725-precoated glass surface belongs to the first kind of hydrophobic surface. Its strong hydrophobic effect on the deposition process has been identified and discussed above. It is also noted in Figure 7.6b that the deposition rates at the higher cationic concentration of CTAB are increasingly larger than the theoretical values. This fact suggests that the second kind of hydrophobicity may also be involved in the deposition experiments with the cationic surfactant solutions. In Chapter 5, such cationic surfactant adsorption has been verified by the variations of the ζ-potential of the FC725-precoated glass surfaces with the cationic surfactant concentration (see Table 5.4). Hence, the cationic surfactant adsorption on the FC725-precoated glass surface may further enhance its hydrophobicity and thus lead to rather higher measured deposition rates at the higher cationic surfactant concentrations as shown in Figure 7.6b.

Furthermore, a visualized insight into the hydrophobic effect can be obtained from the contact angle measurements of the silicone oil drops on these two kinds of glass surfaces. Figure 7.7a is the digital image of a silicone oil drop residing on the FC725-precoated glass slide in the pure DIUF water. The contact angle of the hydrophobic oil drop on the hydrophobic surface is measured by using the ADSA technique to be 56.6°. However, as shown in Figure 7.7b, the hydrophobic silicone oil drop forms 148.6° on the hydrophilic bare glass surface. Figure 7.7a clearly shows that there is a strong attractive hydrophobic interaction and thus an acute contact angle forms between these two hydrophobic surfaces in the aqueous phase. Conversely, the hydrophilic glass surface repulses the hydrophobic oil drop and results in an obtuse contact angle. Such strong attractive hydrophobic interaction between two hydrophobic surfaces in water can be also understood in another fashion. It is not difficult to prove that one needs to do much more work in order to detach the flat silicone oil drop from the hydrophobic surface (Figure 7.7a) than that required to remove the nearly spherical oil drop from the hydrophilic surface (Figure 7.7b).

With more experimental proof available in the literature, it is increasingly recognized that there is strong hydrophobic effect between two hydrophobic surfaces in water. Hence, determination of the hydrophobic interaction is necessary in order to understand the non-wetting properties of hydrophobic surfaces, the coagulation phenomena of hydrophobic colloidal particles, mineral separation processes using flotation techniques, the waterproofing of surfaces and fabrics, in paint technology, and in many other industrial applications. However, up to now the hydrophobic effect itself is still poorly understood, though it has long been reported in the literature. So far neither theoretical predictions nor experimental measurements of the hydrophobic interaction are consistent and satisfactory. A more general expression of the hydrophobic interaction is still not available yet. This is largely caused by the following three obvious facts related to the hydrophobic effect, which are addressed in detail by Israelachvili and Pashley (1982; 1984) and Xu and Yoon (1989).

First of all, the origin of the hydrophobic interaction still remains controversial. The hydrophobic effect is so strong that it is believed by some researchers that it is either due to phase changes in the interlayer between two surfaces in close proximity or due to anomalous polarization of water molecules near hydrophobic surfaces. In other words, they believed that there is a so-called "hydrophobic bond" associated with it. Many investigators, nevertheless, have taken the opposite view based on general theoretical considerations of the liquid state and on Monte Carlo and Molecular Dynamic simulations of liquid water. They consider the effect largely entropic in origin, arising mainly from the configurational rearrangement of water molecules in the vicinity of hydrophobic surfaces. In this approach the hydrophobic interaction would have to be of significantly longer range than any typical "bond". Another problematic aspect of the hydrophobic interaction between surfaces concerns the effect of surface hydrophilic groups (e.g., ionic groups or the polar head groups of surfactants and lipids) on this interaction. Ultimately, this study suggests that the hydrophobic interaction is nonadditive, and further implicates the involvement of water structure which is known to be delicately sensitive to the nature of dissolved solute molecules and surface groups (Israelachvili and Pashley, 1984). At this point, it is worthwhile noting that, as was shown in Section 3.2, the vdW interaction between any two bodies can be evaluated on the bases of the Hamaker approach and the pairwise additivity. Similarly, in Section 3.9, the EDL interaction between two surfaces has been derived by employing the Derjaguin's integration method, which is additive in origin. Hence, the non-additivity of the hydrophobic interaction would pose an almost intractable obstacle to its accurate determination in practice, if it should be true.

Thirdly, there is no general formula available for calculating the hydrophobic interaction. To date there has been no direct method available to measure the hydrophobic interaction. Generally, two kinds of indirect methods were endeavored in the literature. In full analogy to the excess quantities such as the surface concentration defined in surface thermodynamics, the first method considers the hydrophobic interaction as the surface equivalent of the bulk vdW and EDL interactions. This means that a subtraction step is required in order to estimate the hydrophobic interaction. For instance, one can simply subtract the measured "total" force from the theoretical DLVO forces. Then the "extra" attractive interaction obtained in this way is assumed to be the hydrophobic contribution. Depending on the specific scheme adopted, such subtraction procedure may vary from straightforward as stated above to cumbersome (Israelachvili and Pashley, 1984). In principle, it is anticipated that this method should not function well because of the non-additivity of the hydrophobic interaction, while both the vdW and EDL interactions are additive. Accordingly, a second method is used to derive the hydrophobic interaction potential in terms of hydrophobic interaction theory (Xu and Yoon, 1989; Dai and Lu, 1991). Nevertheless, their final expressions of the hydrophobic interaction potentials are quite different, in which some constants have to be found by applying a nonlinear regression curve-fitting procedure. In summary, all the existing expressions for calculating the hydrophobic interaction force or potential are empirical and thus as claimed valid for the specific case only. The precise behavior of the hydrophobic effect between two hydrophobic surfaces in various aqueous solutions remains almost unknown, and will, of course, depend on a range of properties other than the decay length and the hydrophobicity of the interacting surfaces. Only further experiments on other types of colloidal systems will determine the generality of these formulas derived for some typical cases.

Based on the current understanding and relevant research status of the hydrophobic interaction (or the hydrophobic effect), it is not attempted in this study to study quantitatively its detailed influence on the present deposition phenomena. In the full realization of the above complexities with the hydrophobic effect, it is unlikely that any empirical expression for the hydrophobic interaction derived for a specific case can be adopted to generate satisfactory predictions for rather different colloidal systems. Inevitably, much more substantial research work has to be accomplished in order to understand the hydrophobic interaction and further incorporate it into the existing DLVO theory if feasible. Only after one has achieved an adequate and fundamental understanding of the hydrophobic effect can such modified or generalized DLVO theory be generated so as to match even wider research interests and likely be accepted by the academic society. Development of the generalized DLVO theory is certainly an important and challenging research topic, which is beyond the intended scope of this thesis research.

Table 7.1 Dimensionless mass transfer rate Sh (Sherwood) numbers of silicone oil droplets onto the bare glass fiber surfaces in various aqueous solutions

Aqueous Medium	A_d [a]	Dl [b]	Da [b]	κ^{-1} (10^{-9} m) [b]	Sh_{cal} [c]	Sh_{exp} [d]
DIUF Water	5.35	+48200	+0.16	966.46	0.0153	0.0168
pH=2.68	4.07	-23400	-2.06	9.46	0.0391	0.0430
pH=3.52	4.16	-16000	-2.59	24.87	0.0332	0.0349
pH=4.20	4.04	-8700	-4.28	54.41	0.0264	0.0277
pH=6.50	5.35	+48200	+0.16	966.46	0.0153	0.0168
pH=7.20	4.99	+60900	+0.07	918.18	0.0123	0.0134
pH=8.93	5.01	+76300	+0.06	148.14	0.0109	0.0120
pH=10.32	4.87	+107200	+0.07	29.90	0.0097	0.0112
10^{-6} M NaCl	3.90	+51300	+0.07	305.62	0.0150	0.0173
10^{-5} M NaCl	4.16	+40000	+0.01	96.65	0.0169	0.0177
10^{-4} M NaCl	4.18	+16900	0.00	30.56	0.0181	0.0217
10^{-3} M NaCl	4.43	+11600	0.00	9.66	0.0195	0.0224
10^{-6} M $AlCl_3$	2.88	+43600	+0.11	124.77	0.0162	0.0177
10^{-5} M $AlCl_3$	3.88	-30700	-2.09	39.46	0.0390	0.0371
10^{-4} M $AlCl_3$	3.81	-20200	-2.26	12.48	0.0379	0.0439
10^{-3} M $AlCl_3$	4.33	-8600	-2.18	3.95	0.0406	0.0467
10^{-6} M CTAB	4.00	+33900	+0.21	305.62	0.0163	0.0179
10^{-5} M CTAB	3.54	-22200	-2.10	96.65	0.0381	0.0323
10^{-4} M CTAB	2.96	-13100	-6.69	30.56	0.0370	0.0426
10^{-3} M CTAB	1.92	+10300	+6.32	9.66	0.0361	0.0433
10^{-6} M SDS	4.62	+49100	+0.16	305.62	0.0144	0.0158
10^{-5} M SDS	4.60	+65900	+0.21	96.65	0.0101	0.0106
10^{-4} M SDS	4.26	+86000	+0.19	30.56	0.0082	0.0090
10^{-3} M SDS	3.35	+112200	+0.11	9.66	0.0056	0.0061
10^{-2} M SDS	2.84	+117300	+0.11	3.06	0.0045	0.0050

[a] Quoted from Table 4.8.

[b] Quoted from Table 5.3.

[c] Numerical predictions by solving the mass transport equation for the one-dimensional case.

[d] Experimental data of the deposition tests.

Table 7.2 Dimensionless mass transfer rate Sh (Sherwood) numbers of silicone oil droplets onto the FC725-precoated glass fiber surfaces in various aqueous solutions

Aqueous Medium	A_d [a]	Dl [b]	Da [b]	κ^{-1} (10^{-9} m) [b]	Sh_{cal} [c]	Sh_{exp} [d]
DIUF Water	0.89	+19000	+0.07	966.46	0.0192	0.0259
pH=2.68	0.98	-9200	-2.18	9.46	0.0298	0.0492
pH=3.52	0.89	-6300	-2.01	24.87	0.0263	0.0408
pH=4.20	0.88	-3500	-2.46	54.41	0.0251	0.0351
pH=6.50	0.89	+19000	+0.07	966.46	0.0192	0.0259
pH=7.20	0.72	+24000	+0.16	918.18	0.0154	0.0200
pH=8.93	0.45	+30100	+0.18	148.14	0.0147	0.0185
pH=10.32	0.16	+42300	+0.16	29.90	0.0119	0.0149
10^{-6} M NaCl	0.86	+20200	+0.16	305.62	0.0190	0.0257
10^{-5} M NaCl	0.81	+15700	+0.63	96.65	0.0188	0.0246
10^{-4} M NaCl	0.64	+6700	+0.50	30.56	0.0153	0.0205
10^{-3} M NaCl	0.33	+4600	+0.50	9.66	0.0115	0.0161
10^{-6} M $AlCl_3$	0.70	+17200	+0.11	124.77	0.0181	0.0244
10^{-5} M $AlCl_3$	0.65	-12100	-3.05	39.46	0.0194	0.0235
10^{-4} M $AlCl_3$	0.59	-8000	-3.68	12.48	0.0186	0.0193
10^{-3} M $AlCl_3$	0.34	-3500	-3.39	3.95	0.0123	0.0135
10^{-6} M CTAB	1.00	+13400	+0.04	305.62	0.0201	0.0264
10^{-5} M CTAB	1.18	-8700	-3.13	96.65	0.0317	0.0396
10^{-4} M CTAB	1.77	-5200	-15.22	30.56	0.0353	0.0494
10^{-3} M CTAB	2.74	+4000	+17.90	9.66	0.0389	0.0564
10^{-6} M SDS	0.91	+19400	+0.07	305.62	0.0194	0.0252
10^{-5} M SDS	1.00	+25900	+0.04	96.65	0.0190	0.0245
10^{-4} M SDS	1.14	+34000	+0.05	30.56	0.0183	0.0238
10^{-3} M SDS	1.43	+44300	+0.11	9.66	0.0159	0.0215
10^{-2} M SDS	2.66	+46300	+0.12	3.06	0.0152	0.0205

[a] Quoted from Table 4.9.

[b] Quoted from Table 5.4.

[c] Numerical predictions by solving the mass transport equation for the one-dimensional case.

[d] Experimental data of the deposition tests.

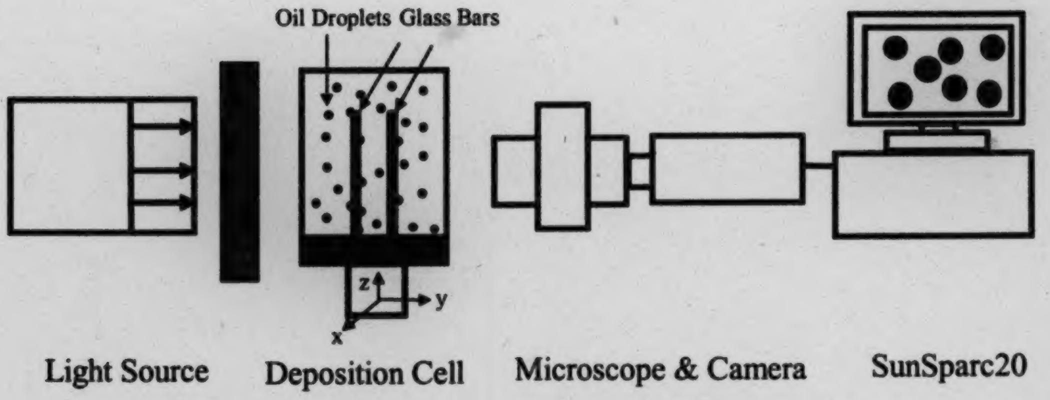
Oil Droplets
Glass Bars
z
y
x
Light Source
Deposition Cell
Microscope & Camera
SunSparc20

Figure 7.1 Experimental set-up for the deposition measurements

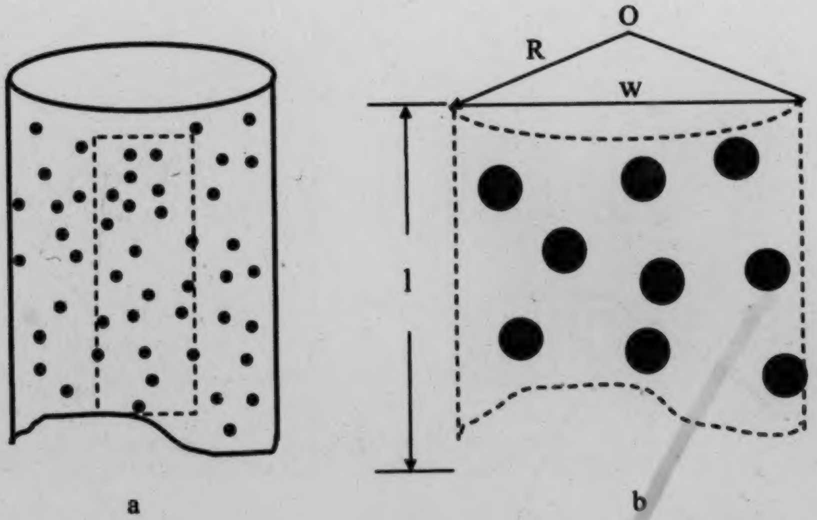

Figure 7.2a (left) The deposition area under examination on the lateral surface of glass cylinder; Figure 7.2b (right) Magnified deposition area on the cylindrical surface

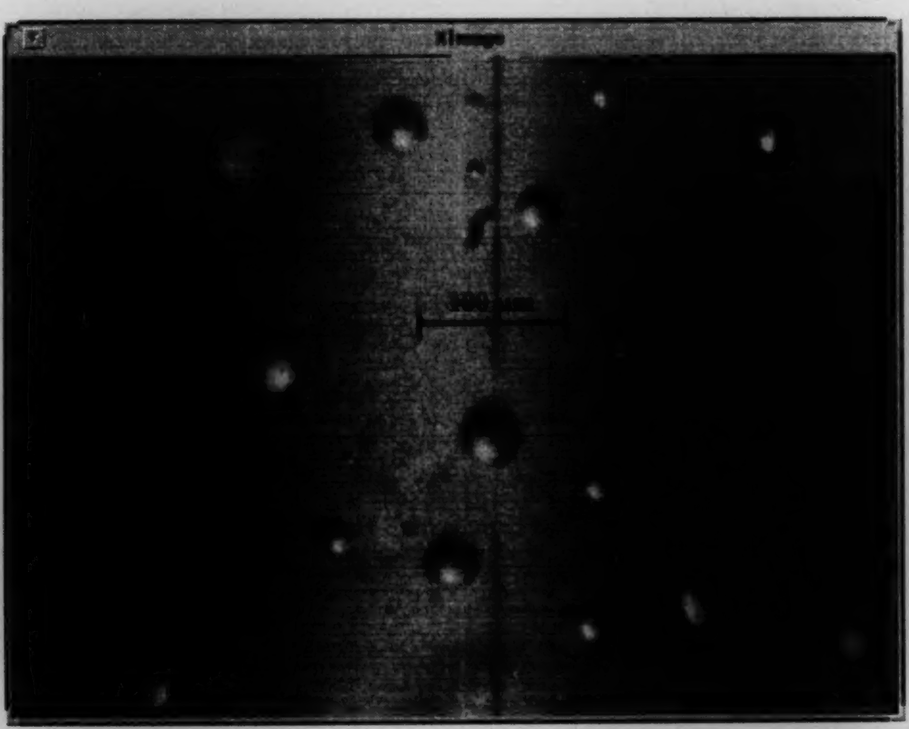

Figure 7.3 The snapshot of the attached silicone oil (No. 1) droplets on the bare glass bar in the pure DIUF water at t=15 min

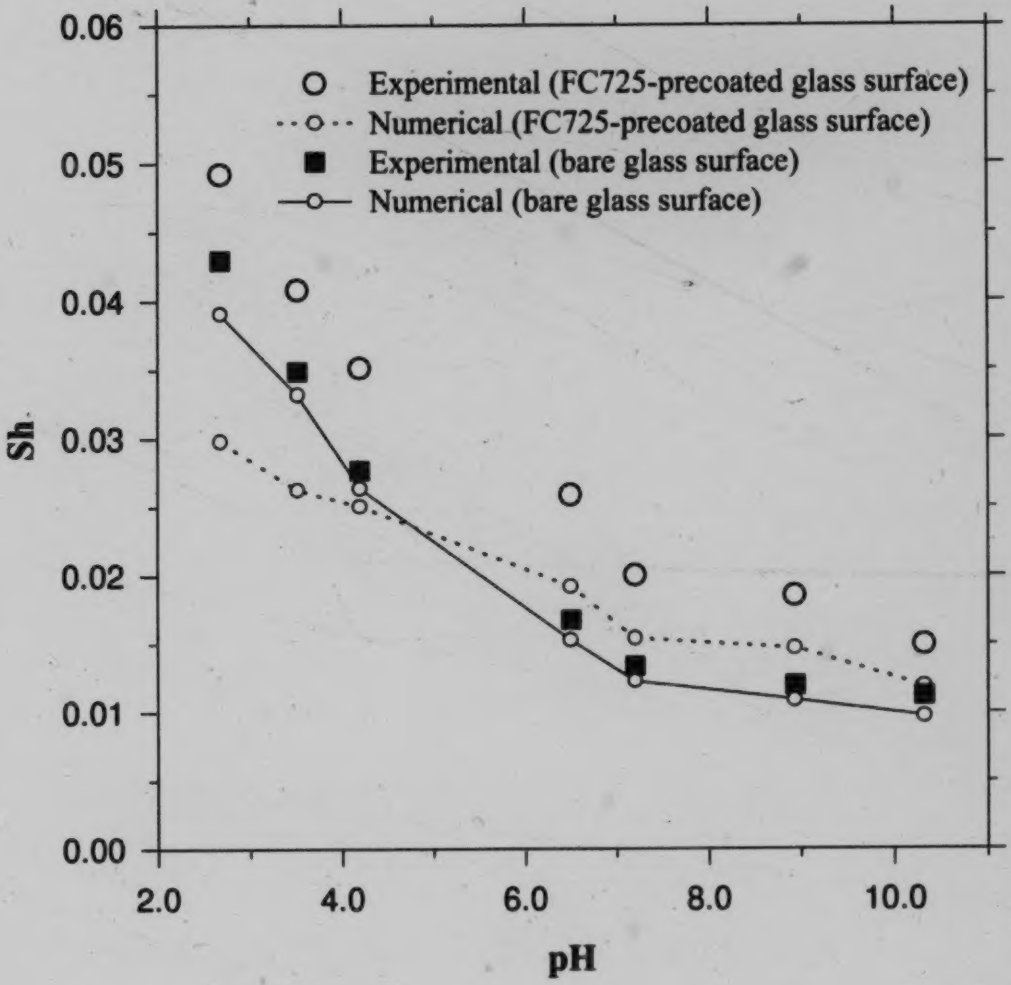

Figure 7.4a Dimensionless mass transfer rate Sh (Sherwood) number as a function of pH of the aqueous phase

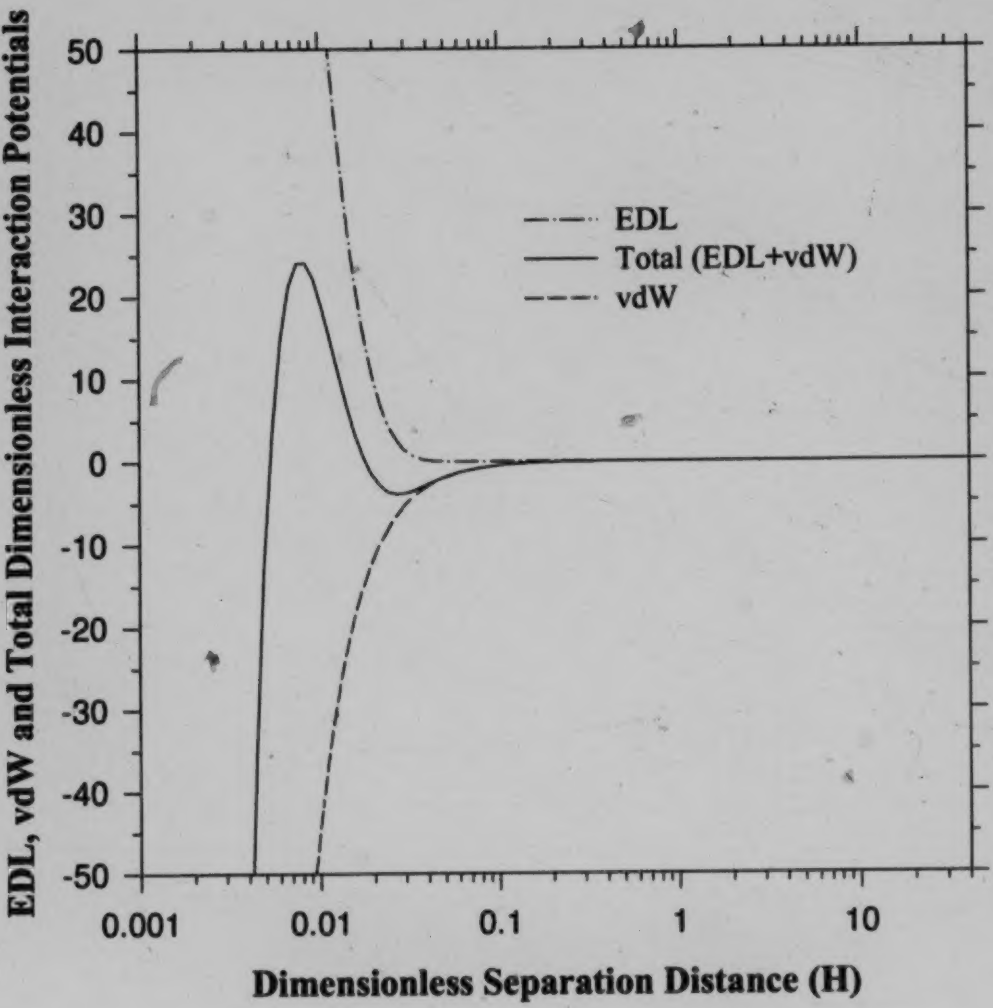

Figure 7.4b The EDL, vdW and total dimensionless interaction potentials between a silicone oil droplet and the bare glass fiber in the pure DIUF water (A_d=5.35, Dl=+48200, Da=+0.16, τ=10, Sh_{cal}=0.0153)

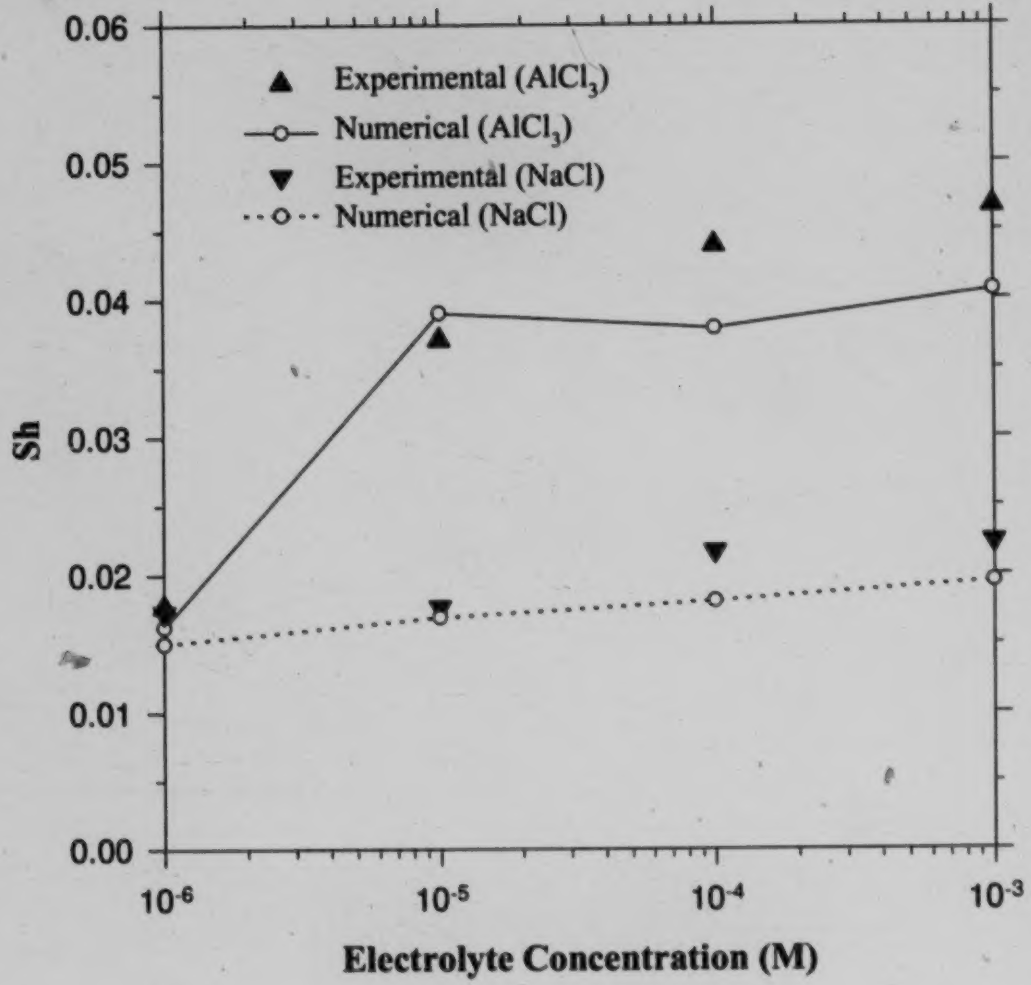

Figure 7.5a Dimensionless mass transfer rate Sh (Sherwood) number versus log concentration of two electrolytes with different valences (bare glass surface)

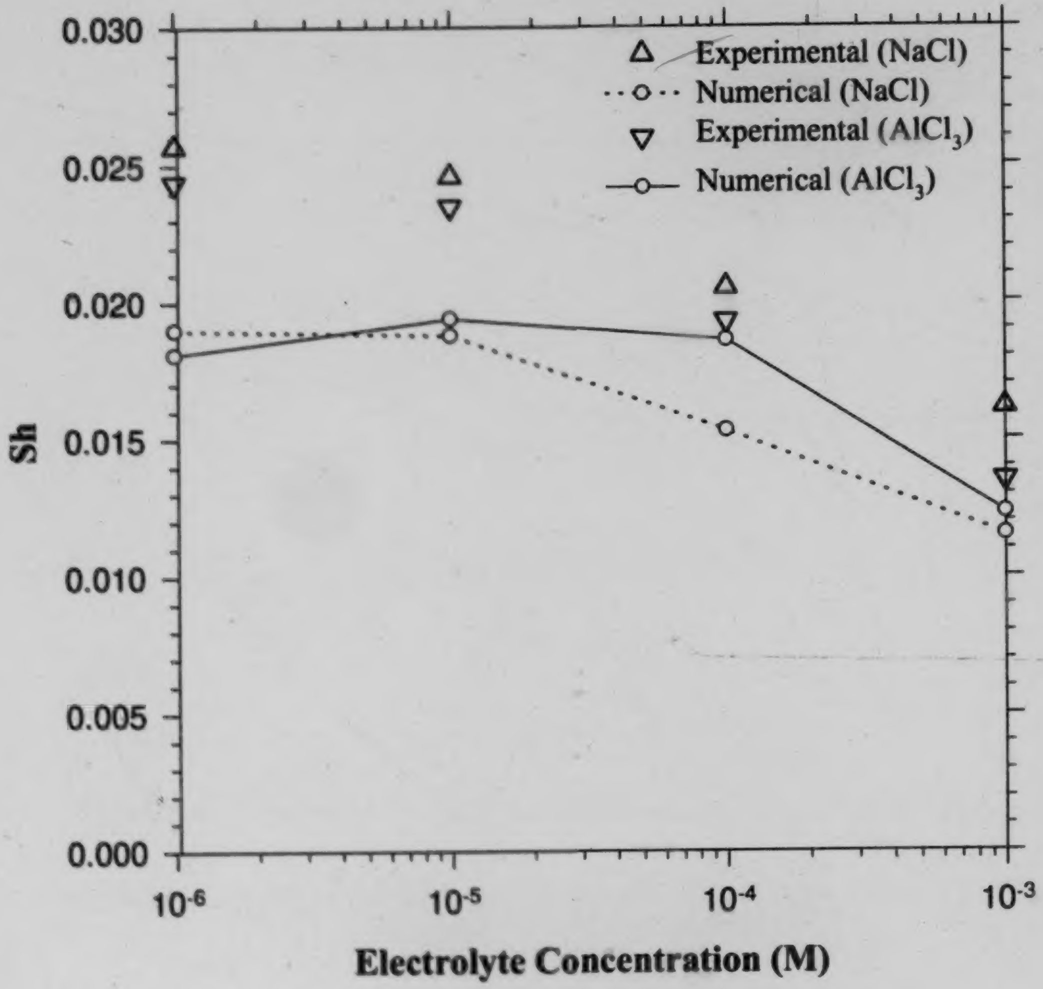

Figure 7.5b Dimensionless mass transfer rate Sh (Sherwood) number versus log concentration of two electrolytes with different valences (FC725-precoated glass surface)

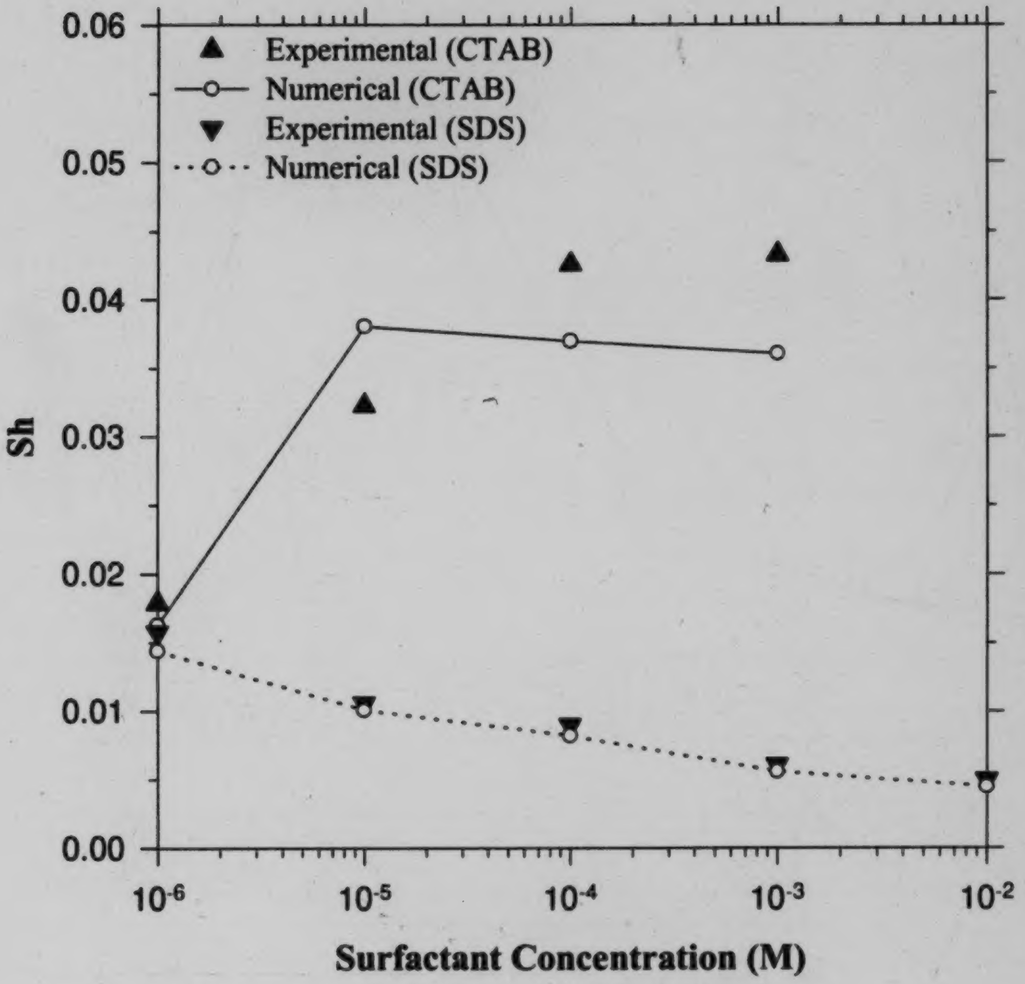

Figure 7.6a Dimensionless mass transfer rate Sh (Sherwood) number versus log surfactant concentration of CTAB or SDS (bare glass surface)

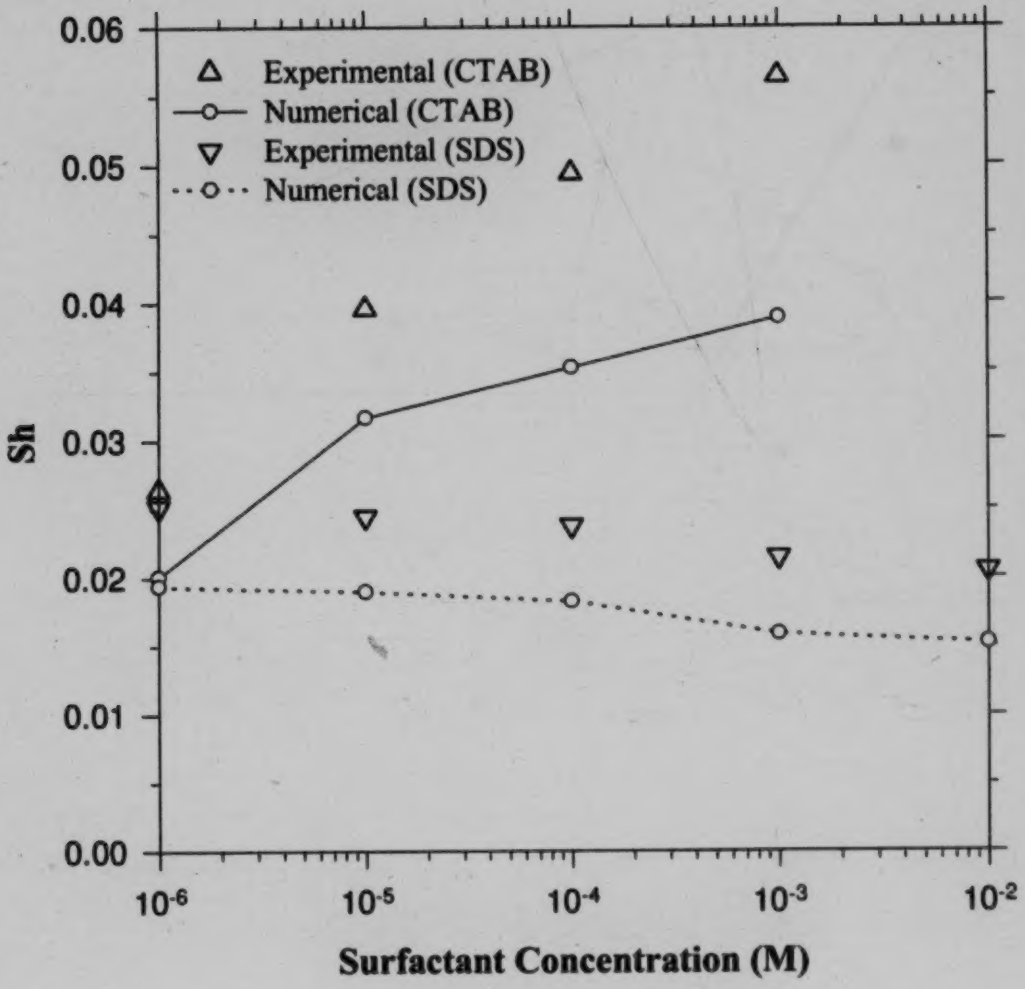

Figure 7.6b Dimensionless mass transfer rate Sh (Sherwood) number versus log surfactant concentration of CTAB or SDS (FC725-precoated glass surface)

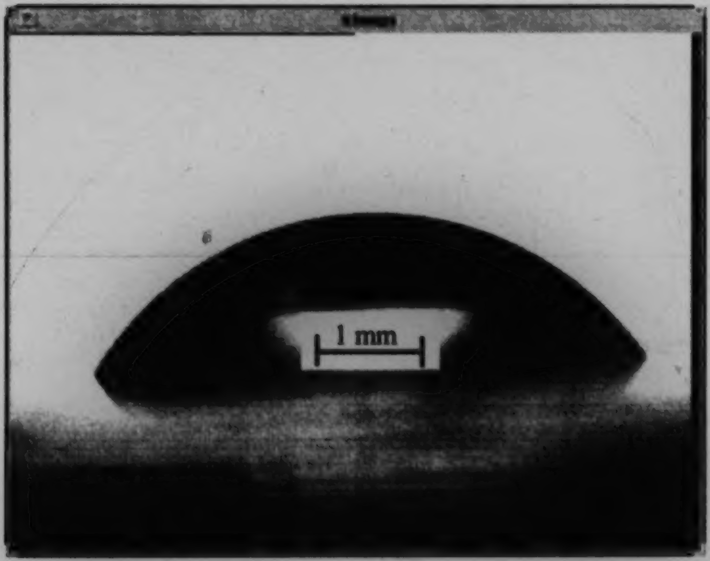

Figure 7.7a Digital image of silicone oil (No. 1) drop on the FC725-precoated glass slide in the pure DIUF water. The measured parameters are as follows: the contact angle θ=56.6°, the base radius of the sessile drop R_b=0.2729 cm and the drop volume V_o=0.0189 cm^3

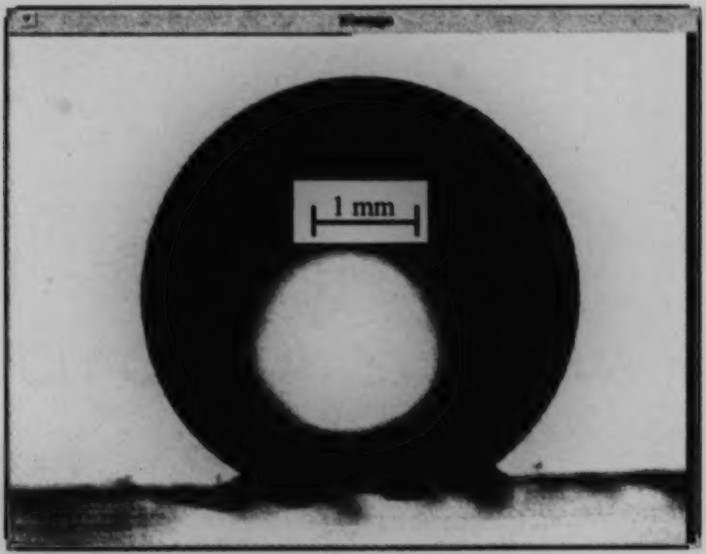

Figure 7.7b Digital image of silicone oil (No. 1) drop on the bare glass slide in the pure DIUF water. The measured parameters are as follows: the contact angle θ=148.6°, the base radius of the sessile drop R_b=0.1234 cm and the drop volume V_o=0.0404 cm^3

Chapter 8

Conclusions and Recommendations

8.1 Major Academic Contributions

In retrospect of those principal research objectives conceived in Chapter 1, a more complete and fundamental understanding is achieved for the colloidal interactions and the overall deposition processes of small oil droplets onto solid surfaces in aqueous solutions (Chapters 2-7). Some major conclusions made throughout this dissertation are summarized as below.

1. In the first part of Chapter 3, a general theoretical method was presented to determine the retarded van der Waals (vdW) interaction between a spherical particle and a cylindrical body. Based on the Hamaker approach, first, the unretarded vdW interaction between these two bodies is obtained by pairwise summation of all the relevant intermolecular interactions and evaluated by accurate numerical integration. Such obtained interaction was then modified to account for the retardation effect by incorporating a correction factor. The detailed numerical predictions indicate that the vdW interaction between a sphere and a finitely long cylinder can be approximated as the interaction between a sphere and an infinitely long cylinder only if the ratio of the cylinder length to its radius is greater than a certain lower limit. At smaller dimensionless separation distances ($H \leq 1$), the vdW interaction between a sphere and a cylinder can be approximated by that between a sphere and a flat plate. Such a commonly used flat plate approximation is found to be acceptable only if the ratio of the cylinder radius to the sphere radius is larger than 10. In all other cases, however, this approximation will seriously overestimate the vdW interaction for the sphere-cylinder system.

2. In the second part of Chapter 3, an approximate integral solution was presented to determine the electrical double layer (EDL) interaction between a spherical particle and a cylindrical surface. Based on this numerical solution, it has been found that the curvature effect of cylinder on the EDL interaction can not be neglected at smaller separation distances. In particular, when $H \leq 1$, the flat plate approximation, i.e. the well-known HHF expression for the sphere-flat plate system, will considerably overestimate the EDL interaction between a sphere and a cylinder. Above H≈1, nevertheless, the EDL interaction quickly becomes diminishing. In addition, the ratio of the radius of the particle to the EDL thickness also has strong influence on the EDL interaction. Particularly, at small separation distances (H≈0.001~0.1), the EDL interaction is nearly proportional to the ratio. It has also been estimated that the maximum separation distance between the two nearby EDLs should be around three times of the EDL thickness in order for them to interact with each other appreciably. Finally, the detailed numerical results for different values of dimensionless EDL asymmetry parameter Da show that the EDL interaction is always repulsive for the symmetric EDLs ($\zeta_p=\zeta_c$), i.e. Da=0, irrespective of the separation distance between the interacting EDLs. However, it is unexpectedly found that, at smaller separation distances, the EDL interaction can become attractive between the asymmetric EDLs (Da>0), even though their ζ-potentials have the same polarity. Only at relatively larger separations, the EDL interaction resumes its originally repulsive feature. A possible explanation of this phenomenon is also furnished.

3. In Chapter 4, a new contact angle measurement technique has been developed in order to determine the Hamaker constant involved in the vdW interaction (Chapter 3). This method can be used to accurately measure the contact angle of a liquid-fluid interface by analysis of the capillary profile around a cylinder (ACPAC). The ACPAC technique has been successfully tested to measure the contact angles by analysis of the capillary rise profiles around a constant-diameter or conic cylinder (ACRPAC). The measured contact angles agree very well with those measured by the Wilhelmy plate technique or the ADSA technique for the sessile drop case, respectively. This novel technique is also adopted to measure such a contact angle formed between an oil-water interface and a fiber surface by analysis of the capillary depression profile around a cylinder (ACDPAC). The relevant experimental data for the ACDPAC case indicate that the ACPAC technique is an appropriate experimental method to study the wetting effect of any surfactants dissolved in the aqueous solution on the liquid-fluid interface around a curved solid surface. By applying the novel contact angle measurement technique, the Hamaker constants are found to be about 10^{-19} to 10^{-20} J for the high-energy bare glass surfaces and 10^{-20}-10^{-21} J for the low-energy FC725-precoated glass fiber surfaces. Changes in the Hamaker constants (i.e. the vdW interaction) of the fiber-water-oil systems are attributed to the variations of the surface energies of the fiber-water-oil systems with the liquid properties of the aqueous media.

All these experimental results show that the ACPAC technique is a powerful tool for accurate measurements of contact angles of any liquid-liquid interfaces on fiber surfaces. It can be used to measure the contact angles between a liquid-vapour interface, or a liquid-liquid interface and a constant-diameter or conic cylinder. The ACPAC method will be particularly useful for studying the wetting phenomena associated with a liquid-vapour interface, or an oil-water interface on these fiber surfaces.

4. In Chapter 5, a new simple electrical suspension method was devised to measure the ζ-potential of small liquid droplets dispersed in another immiscible liquid. This method is then utilized to determine the ζ-potential of the silicone oil droplets dispersed in various aqueous solutions. To determine the ζ-potential measurements of glass surfaces in contact with these aqueous phases, the streaming potential technique is applied by using a parallel-plate microchannel. The effect of surface conductance is identified and ultimately its influence on the measured ζ-potential of glass surfaces is corrected. Using these two experimental methods, the effects of the following factors on the measured ζ-potential of the silicone oil droplets and the glass surfaces can be studied quantitatively: varying pH value, the valence and the concentration of electrolytes and the ionic surfactants. With the ζ-potentials of both silicone oil droplets and glass surfaces in various aqueous solutions, three important EDL interaction parameters are determined. Furthermore, in conjunction with the consideration of the curvature effect, the EDL interaction between a spherical oil droplet and a cylindrical fiber has been determined experimentally.

5. In Chapter 6, both the analytical and numerical solutions of 1-D mass transfer equation, i.e. in the presence of the vdW and EDL interactions only, have been obtained. The detailed numerical results in the 1-D case have clearly shown the specific effects of the dimensionless adhesion number A_d, the EDL interaction parameter Dl and the ratio (τ) of the radius of the particle to the EDL thickness on the droplet number concentration distribution and the mass transfer rate Sh. The 2-D numerical model is also developed in which both the external force fileds and the colloidal forces can be accounted for. In particular, the effects of the gravitational field and the externally applied electric field on the mass transfer rate Sh have been examined using the 2-D model. However, there are some intrinsic limitations in applying the present 1-D and 2-D models to simulate the practical deposition cases. These two models are established for the static steady state deposition of dilute emulsion droplets onto a cylindrical surface. They are applicable only to the region close to the solid surface where the vdW and EDL force are dominant. It can be used for low surface coverage only, i.e. small Sh number and relatively short deposition duration.

6. Finally, Chapter 7 presents a systematic deposition experiment to examine the effects of the colloidal forces on the deposition processes of the silicone oil droplets onto two kinds of glass fiber surface in a variety of aqueous solutions. The experimental results of deposition test are then compared with the theoretical predictions of the 1-D numerical model based on the classical DLVO theory. It has been found that, generally, the deposition experimental data for the bare glass surface (hydrophilic) are in an excellent agreement with the numerical results of the 1-D model. This fact indicates that the deposition process of the silicone oil droplets onto such hydrophilic solid surface can be well described by the existing DLVO theory in which the vdW and EDL interactions are included. However, the experimentally measured deposition rates for the FC725-precoated glass surface are found to be significantly higher than the theoretical predictions. This fact suggests that non-DLVO attractive interaction is present in the deposition process of the silicone oil droplets onto such hydrophobic solid surface. This additional interaction, which is referred to as the hydrophobic interaction, is responsible for the difference between the experimental deposition data and the theoretical predictions based on the classical DLVO theory alone.

8.2 Future Research

The following recommendations are made as a result of this study.

1. The 2-D model for deposition process has been developed in the presence of the gravitational field and the electric field in Chapter 2. Its numerical solutions have also been obtained and presented in Chapter 6. In comparison with the colloidal forces, these external force fields were found overwhelmingly dominant in the 2-D deposition case. Therefore, it will be interesting research work to experimentally test their effects on the practical deposition cases under the gravitational field and/or the electric field to accelerate/decelerate the deposition process at one's desire. Then the measured deposition data can be used to verify the numerical predictions presented in Chapter 6 and, if necessary, to improve the 2-D model.

2. In Chapter 7, it has been observed that the attractive hydrophobic interaction (or generally referred to as the hydrophobic effect) is involved in the deposition case of the hydrophobic silicone oil droplets onto the hydrophobic FC725-precoated glass surface in aqueous solutions. However, the hydrophobic interaction is not accounted for by the conventional (i.e., classical) DLVO theory. As has been pointed out, it is unlikely that any existing empirical expression for the hydrophobic interaction derived for a specific case can be adopted to generate satisfactory predictions for rather different colloidal systems. Hence, a substantial research work has to be accomplished in order to understand the hydrophobic interaction and further incorporate it into the existing DLVO theory, if feasible. Development of such modified/generalized DLVO theory is an exciting and demanding research work, which is probably significant enough to be another doctoral thesis topic.

3. The fluid flows are often involved in the interactions between the colloidal particles and the solid collectors in most industrial applications. Accordingly, the deposition process in the hydrodynamic case is of more concern. In particular, one desires to know the exact effects of the hydrodynamic conditions such as the Reynolds number and the Péclet number on the deposition rates. In the literature, an excellent numerical work on the hydrodynamic deposition of the Brownian particles onto cylindrical collectors has been accomplished by Adamczyk and van de Ven (1981b). Therefore, it is desired to see some experimental work on the hydrodynamic deposition case. Such experimentally measured deposition data can be utilized to verify the existing numerical predictions and, if necessary, to improve the numerical model.

4. Once deposition occurs, the deposited oil droplets start spreading on the solid surface in the aqueous solution. As reported by Jachowicz and Berthiaume (Jachowicz and Berthiaume, 1989; Berthiaume and Jachowicz, 1991), for instance, their experimental observations indicated that the spreading process plays an important role in the subsequent deposition and spreading processes of upcoming oil droplets. Therefore, it is essential to obtain a thorough understanding of such spreading phenomenon of oil droplets on solid surface in aqueous solutions. In practice, the deposition and spreading processes are coupled and thus affect each other. Such coupling effect can become substantial especially when the surface coverage of the deposited liquid droplets is high.

In this direction, a new model for an oil droplet spreading on a solid surface in air has been developed. Recently, a simple working spreading model (Gu and Li, 1998e; 1998f) has been developed using the modified overall energy balance (OEB) method (Madejski, 1976; San Marchi et al., 1993) and the widely accepted "lubrication theory approximation". This spreading model synthesizes surface physics and fluid mechanics and contains only one adjustable parameter. By employing the famous de Gennes model for the viscous force of a moving contact line (de Gennes, 1990; Brochard-Wyart and de Gennes, 1992) and the OEB method, this novel theoretical spreading model takes account of the inertial, viscous and gravitational forces, the interfacial tensions and the wettability of the solid-liquid-fluid system. The numerical predictions of this spreading model (Gu and Li, 1998e) are in an excellent accord with the experimental data of spontaneous spreading of silicone oil drops on a soda-lime glass plate measured by Chen (1988). Furthermore, a good agreement is also obtained (Gu and Li, 1998f) for water drops spreading on an anodized aluminium surface and on a glass plate measured by Thoroddsen and Sakakibara (1998) at different low impact speeds. Nonetheless, all our numerical predictions and the existing spreading data are for the case in which the liquid drops spread on a solid surface in air. At present, it is not clear whether such known spreading behaviour of the liquid drops on a solid surface in air is quite similar to that of a liquid droplet (such as an oil droplet) on a solid surface in another immiscible liquid (such as an aqueous solution). Hence, the spreading phenomenon for the latter case is to be explored probably by means of both numerical and experimental methods. Such research will further one's understanding of the possible coupling effect of the deposition and spreading, as well as the well-recognized blocking/masking effect, which is expected to become appreciable at high surface coverage.

References

Abramson, H. A., Moyer, L. S., and Gorin, M. H., 1942, "Electrophoresis of Proteins," Reinhold, New York, pp. 121.

Adamczyk, Z., Dabros, T., Czarnecki, J., and van de Ven, T. G. M., 1983, *Adv. Colloid Interface Sci.* **19**, 183.

Adamczyk, Z., Dabros, T., Czarnecki, J., and van de Ven, T. G. M., 1983, *J. Colloid Interface Sci.* **97**, 91.

Adamczyk, Z., and van de Ven, T. G. M., 1981a, *J. Colloid Interface Sci.* **80**, 340.

Adamczyk, Z., and van de Ven, T. G. M., 1981b, *J. Colloid Interface Sci.* **84**, 497.

Adamson, A. W., 1982, "Physical Chemistry of Surfaces," 4th edn, Wiley, New York.

Alince, B., 1989, *Colloids Surf.* **39**, 39.

Alince, B., Petlicki, J., and van de Ven, T. G. M., 1991, *Colloids Surf.* **59**, 265.

Alince, B., and van de Ven, T. G. M., 1993, *Colloids Surf.* **71**, 105.

Ambwani, D. S., and Fort, Jr., T., 1979, "Surface and Colloid Science," R. J. Good and R. R. Stromberg (Eds.), Vol. **11**, Plenum, New York, pp.93-119.

Avranas, A., and Stalidis, G., 1991, *J. Colloid Interface Sci.* **140**, 180.

Babchin, A. J., Chow, R. S., and Sawatzky, R. P., 1989, *Adv. Colloid Interface Sci.* **30**, 111.

Bach, N., and Gilman, A., 1938, *Acta PhysiCochim. URSS* **9(1)**, 1.

Berthiaume, M. D., and Jachowicz, J., 1991, *J. Colloid Interface Sci.* **141**, 299.

Bhattacharjee, S., and Sharma, A., 1995, *J. Colloid Interface Sci.* **171**, 288.

Bochkarev, A. A., Pukhovoy, M. V., and Kasyanova, L. N., 1995, *J. Colloid Interface Sci.* **175**, 6.

Boruvka, L., and Neumann, A. W., 1977, *J. Chem. Phys.* **66**, 5464.

Bowen, B. D., 1981, *J. Colloid Interface Sci.* **82**, 574.

Brenner, H., 1961, *Chem. Eng. Sci.* **16**, 242.

Brochard-Wyart, F., and de Gennes, P. G., 1992, *Adv. Colloid Interface Sci.* **39**, 1.

Budziak, C. J., and Neumann, A. W., 1990, *Colloids Surf.* **43**, 279.

Carroll, B. J., 1986, *Langmuir* **2**, 248.

Carroll, B. J., 1988, *Text. Res. J.* **58**, 495.

Casimir, H. B. G., and Polder, D., 1948, *Phys. Rev.* **73**, 360.

Chapman, D. L., 1913, *Phil. Mag.* **25**, pp. 475.

Chen, J. D., 1988, *J. Colloid Interface Sci.* **122**, 60.

Cheng, P., Li, D., Boruvka, L., Rotenberg, Y., and Neumann, A. W., 1990, *Colloids Surf.* **43**, 151.

Chorom, M., and Rengasamy, P., 1995, *Eur. J. Sci.* **46**, 657.

Collins, G. L., Motarjemi, M., and Jameson, G. J., 1978, *J. Colloid Interface Sci.* **63**, 69.

Czerniawski, M., 1966, *Roczn. Chem.* **40**, 1935.

Dabros, T., Adamczyk, Z., and Czarnecki, J., 1977, *J. Colloid Interface Sci.* **62**, 529.

Dabros, T., and Adamczyk, Z., 1979, *Chem. Eng. Sci.* **34**, 1041.

Dabros, T., and van de Ven, T. G. M., 1983, *Colloid Polym. Sci.* **261**, 694.

Dabros, T., and van de Ven, T. G. M., 1987, *PCH Physicochemical Hydrodynamics* **8**, 161.

Dai, Z., and Lu, S., 1991, *Colloids Surf.* **57**, 61.

de Gennes, P. G., 1990, "Dynamics of Wetting," Course 6 in Liquids at Interfaces (J. Charvolin, J. F. Joanny and J. Zinn-Justin, Eds), p.273.

Derjaguin, B. V., 1934, *Kolloid Z.* **69**, 155.

Derjaguin, B. V., 1939, *Acta Physicochim.* **10**, 333.

Derjaguin, B. V., 1954, *Disc. Faraday Soc.* **18**, 85.

Derjaguin, B. V., and Landau, L. D., 1941, *Acta Physicochim.* **14**, 633.

Deshiikan, S., and Papadopoulos, K. D., 1995a, *J. Colloid Interface Sci.* **174**, 302.

Deshiikan, S., and Papadopoulos, K. D., 1995b, *J. Colloid Interface Sci.* **174**, 313.

Dittgen, M., and Zosel, B., 1991, *Colloid Polym. Sci.* **269**, 259.

Doren, A., Lemaitre, J., and Rouxhet, P. G., 1989, *J. Colloid Interface Sci.* **130**, 146.

Drzal, L. T., Madhukar, M., and Waterbury, M. C., 1994, *Composite Structures* **27**, 65.

Duncan, D., Li, D., Gaydos, J., Neumann, A. W., 1995, *J. Colloid Interface Sci.* **169**, 256.

Dzjalosinskij, I. E., Lifshitz, E. M., and Pitaevskij, L. P., 1961, *Adv. Phys.* **10**, 165.

Elimelech, M., 1991, *J. Colloid Interface Sci.* **146**, 337.

Fisher, J. C., 1948, *J. Applied Phys.* **19**, 1062.

Fowkes, F. M., and Patrick, R. L., 1967, "Treaties on Adhesion and Adhesives," Vol. **1**, Dekker, New York.

Franks, F., 1973, "Water: A Comprehensive Treaties," F. Franks, Ed., Vol. **4**, Chapt. 1, Plenum, New York.

Gaydos, J., and Neumann, A. W., 1987, *J. Colloid Interface Sci.* **120**, 76.

Gibbs, J. W., 1961, "The Scientific Papers," Vol. **1**, Dover, New York, pp. 288.

Gilman, A., and Bach, N., 1938, *Acta PhysiCochim. URSS* **9(1)**, 27.

Goldman, A. J., Cox, R. G., and Brenner, H., 1967a, *Chem. Eng. Sci.* **22**, 637.

Goldman, A. J., Cox, R. G., and Brenner, H., 1967b, *Chem. Eng. Sci.* **22**, 651.

Good, R. J., 1992, *J. Adhesion Sci. Technol.* **6**, 1269.

Good, R. J., and Koo, M. N., 1979, *J. Colloid Interface Sci.* **71**, 283.

Gouy, G., 1910, *J. Phys. Chem.* **9**, 457.

Graciaa, A., Morel, G., Saulnier, P., Lachaise, J., and Schechter, R.S., 1995, *J. Colloid Interface Sci.* **172**, 131.

Gregory, J., 1981, *J. Colloid Interface Sci.* **83**, 138.

Gu, Y., Li, D., and Cheng, P., 1996, *J. Colloid Interface Sci.* **180**, 212.

Gu, Y., Li, D., and Cheng, P., 1997a, *Colloids Surf.* **122**, 135.

Gu, Y., and Li, D., 1997b, *J. Colloid Interface Sci.* **195**, 343.

Gu, Y., and Li, D., 1997c, A Force Balance Method for Measuring the Surface Charge and Potential of Small Oil Droplets in the Oil-in-Water (O/W) Emulsions, The 47th Canadian Chemical Engineering Conference, Edmonton, October 5-8, 1997.

Gu, Y., and Li, D., 1997d, *J. Chem. Eng. Jpn.* **30**, 302.

Gu, Y., and Li, D., 1998a, *J. Colloid Interface Sci.* **206**, 288.

Gu, Y., and Li, D., 1998b, A New Experimental Technique to Measure the Contact Angle of a Liquid-Fluid Interface on a Fiber, The 1998 AIChE Annual Conference, Miami Beach, November 20-25, 1998.

Gu, Y., and Li, D., 1998c, *J. Colloid Interface Sci.* **206**, 346.

Gu, Y., and Li, D., 1998d, *Colloids Surf.* **139**, 213.

Gu, Y., and Li, D., 1998e, *Colloids Surf.* **142**, 243.

Gu, Y., and Li, D., 1998f, Liquid Drop Spreading on Solid Surfaces at Low Impact Speeds, *Colloids Surf.*, in press.

Gu, Y., and Li, D., 1998g, *Colloids Surf.* **137**, 205.

Gu., Y., and Li, D., 1998h, The van der Waals Interaction between a Spherical Particle and a Cylinder, *J. Colloid Interface Sci.*, in press.

Gu, Y., and Li, D., 1998i, An Experimental Study on the Drop Size Dependence of Contact Angle of a Liquid-Fluid Interface on a Fiber, The 1998 AIChE Annual Conference, Miami Beach, November 20-25, 1998.

Hamaker, H. C., 1937, *Physica.* **4**, 1058.

Hamieh, T., and Siffert, B., 1994, *Colloids Surf.* **84**, 217.

Henry, D. C., 1931, *Proc. Roy. Soc. (London) Ser. A.* **133**, 106.

Hoffman, J. D., 1992, "Numerical Methods for Engineers and Scientists," McGraw-Hill, Inc., New York, pp. 543-548

Hoffmann, J. M. A., and Stein, H. N., 1992, *J. Colloid Interface Sci.* **154**, 359.

Hogg, R., Healy, T. W., and Fuerstenau, D. W., 1966, *Trans. Faraday Soc.* **62**, 1638.

Hough, D. B., and White, L. R., 1980, *Adv. Colloid Interface Sci.* **14**, 3.

Hunter, R. J., 1981, "Zeta Potential in Colloid Science, Principles and Applications," Academic Press, New York.

Israelachvili, J. N., 1972, *Proc. Roy. Soc. Lond. A* **331**, 39.

Israelachvili, J. N., 1985, "Intermolecular and Surface Forces," 2nd edn., Academic Press, London.

Israelachvili, J. N, and Pashley, R. M., 1982, *Nature* **300**, 341.

Israelachvili, J. N, and Pashley, R. M., 1984, *J. Colloid Interface Sci.* **98**, 500.

Ives, K. J., 1984, "The Scientific Bases of Flotation, Applied Sciences," Academic Press, New York, Series E, pp. 75.

Jachowicz, J., and Berthiaume, M. D., 1989, *J. Colloid Interface Sci.* **133**, 118.

Jachowicz, J., and Berthiaume, M. D., 1993, *Cosmetics Toiletries.* **108**, 65.

Kawahara, F. K., Fiutem, R. A., Silvus, H. S., Newman, F. M., Frazar, J. H., 1983, *Analytica Chimica Acta.* **151**, 315.

Lahooti, S., Yueh, H. K., Neumann, A. W., 1993, An Image Analysis Strategy to Study Cell Adhesion, The **67th** Annual Colloid and Surface Science Symposium, Toronto, June 20-23, 1993.

Li, D., 1996, *Colloids Surf.* **116**, 1.

Li, D., Cheng, P., and Neumann, A. W., 1992, *Adv. Colloid Interface Sci.* **39**, 347.

Li, D., and Neumann, A. W., 1990a, *J. Colloid Interface Sci.* **137**, 304.

Li, D., and Neumann, A. W., 1990b, *Colloids Surf.* **43**, 195.

Li, D., and Neumann, A. W., 1992a, *Adv. Colloid Interface Sci.* **39**, 299.

Li, D., and Neumann, A. W., 1992b, *Adv. Colloid Interface Sci.* **36**, 125.

Li, D., and Neumann, A. W., 1992c, *Colloid Polym. Sci.* **270**, 498.

Lifshitz, E. M., 1956, *Sov. Phys. JETP* **2**, 73.

Lin, F. Y. H., and Li, D., 1994, *Colloids Surf.* **87**, 93.

Lyklema, J., 1995, "Fundamental of Interface and Colloid Science," Vol. **II**, Academic Press.

Lykelema, J., and Minor, M., 1997, *Colloids Surf.* **140**, 33.

Madejski, J., 1976, *J. Heat Mass Transfer* **19**, 1009.

Mala, G. M., 1999, "Fluid Flows and Heat Transfer in Microchannels," Ph.D. Dissertation, Department of Mechanical Engineering, University of Alberta, Canada.

Mala, G. M., and Li, D., 1997, *Int. J. Heat and Fluid Flow* **18**, 489.

Marmur, A, 1992, *J. Colloid Interface Sci.* **148**, 541.

Masliyah, J. H., 1994, "Electrokinetic Transport Phenomena," Technical Publication Series No. **12**, Alberta Oil Sands Technology and Research Authority (AOSTRA), Canada.

Mendenhall, W., and Sincich, T., 1992, "Statistics for Engineering and the Sciences," 3rd ed., Dellen Publishing, pp.419-476.

Miklavcic, S. J., Chan, D. Y. C., White, L. R., and Healy, T. W., 1994, *J. Phys. Chem.* **98**, 9022.

Miklavcic, S. J., Horn, R. G., and Bachmann, D. J., 1995, *J. Phys. Chem.* **99**, 16357.

Neumann, A. W., 1974, *Adv. Colloid Interface Sci.* **4**, 105.

Neumann, A. W., Absolom, D. R., Zingg, W., van Oss, C. J., and Francis, D. W., 1983a, "Biocompatible Polymers, Metals and Composites," M. Szycher (Ed.), pp.53.

Neumann, A. W., Absolom, D. R., Francis, D. W., Omenyi, S. N., Spelt, J. K., Policova, Z., Thomson, C., Zingg, W., and van Oss, C. J., 1983b, *J. Ann, NY Acad, Sci,* **416**, 276.

Neumann, A. W., and Good, R. J., 1972, *J. Colloid Interface Sci.* **38**, 341.

Neumann, A. W., and Good, R. J., 1979, "Surface and Colloid Science," R. J. Good and R. R. Stromberg (Eds.), Vol. **11**, Plenum, New York, pp.31-91.

Nir, S., and Vassilieff, C. S., 1988, "Thin Liquid Films," I. B. Ivanov, Ed., Surface Science Series, Vol. **29**, Dekker, New York, pp. 207.

Noh, J. S., and Schwarz, J. A., 1989, *J. Colloid Interface Sci.* **130**, 157.

Ogawa, T., and Ikeda, M., 1993, *J. Adhesion* **43**, 69.

Okada, K., and Akagi, Y., 1987, *J. Chem Eng. Jpn.* **20**, 11.

Okada, K., and Akagi, Y., Kogure, M., and Yoshioka, N., 1990a, *Canad. J. Chem. Eng.* **68**, 393.

Okada, K., and Akagi, Y., Kogure, M., and Yoshioka, N., 1990b, *Canad. J. Chem. Eng.* **68**, 959.

Overbeek, J. Th. G., 1952, "Phenomenology of Lyophobic Systems," Chapter II in Colloid Science (H. R. Kruyt, Ed.), Elsevier, Amsterdam.

Padday, J. F., 1968, "Surface and Colloid Science," E. Matijevic (Ed.), Vol. 1, Wiley, New York, pp. 101-149.

Padday, J. F., 1992, *J. Adhesion Sci. Technol.* **6**, 1347.

Panton, R., 1984, "Incompressible Flow," Wiley, New York.

Papadopoulos, K. D., and Kuo, C., 1990, *Colloids Surf.* **46**, 115.

Parsegian, V. A., 1975, "Physical Chemistry: Enriching Topics from Colloid and Surface Science Theory," H. V. Olphen and K. J. Mysels (Eds.), pp.27-72, Theorex, La Jolla, California.

Parsegian, V. A., and Weiss, G. H., 1981, *J. Colloid Interface Sci.* **81**, 285.

Payatakes, A. C., Rajagopalan, R., and Tien, C., 1974, *Canad. J. Chem. Eng.* **52**, 722.

Penn, L. S., and Jutis, B., 1989, *J. Adhesion* **30**, 67.

Prieve, D. C., and Ruckenstein, E., 1974, *AIChE J.* **20**, 117.

Rajagopalan, R., and Tien, C., 1977, *Canad. J. Chem. Eng.* **55**, 246.

Rajagopalan, R., and Tien, C., 1979, "Progress in Filtration and Separation," R. J. Wakeman (Ed.), Vol. 1, Elsevier, Amsterdam, pp.179-269.

Rajagopalan, R., and Kim, J. S., 1981, *J. Colloid Interface Sci.* **83**, 428.

Ramsden, J. J., Li, S. Y., Prenosil, J. E., and Heinzle, E., 1994, *Biotech. Bioeng.* **43**, 939.

Rotenberg, Y., Boruvka, L., Neumann, A. W., 1983, *J. Colloid Interface Sci.* **93**, 169.

Ruardy, T. G., Schakenraad, J. M., van der Mei, H. C., Busscher, H. J., 1995, *J. Biomed. Mater. Res.* **29**, 1415.

San Marchi, C., Liu, H., Lavernia, E. J., Rangel, R. H., Sickinger, A., and Muehlberger, E., 1993, *J. Mater. Sci.* **28**, 3313.

Sanders, R. S., Chow, R. S., and Masliyah, J. H., 1995, *J. Colloid Interface Sci.* **174**, 230.

Saulnier, P., Lachaise, J., Morel, G., and Graciaa, A., 1996, *J. Colloid Interface Sci.* **182**, 395.

Sawatzky, R. P., and Babchin, A. J., 1993, *J. Fluid Mech.* **246**, 321.

Schenkel, J. M., and Kitchener, J. A., 1960, *Trans. Faraday Soc.* **56**, 161.

Shinoda, K., Nakagawa, T., Tamamushi, B. I., and Tsemura, T., 1963, "Colloidal Surfactants," Academic Press, New York/London.

Sirois, L. L., and Millar, G., 1973, *Canad. Metall. Q.* **12**, 281.

Smoluchowski, M. von, 1903, Bull. Akad. Sci. Cracovie, *Classe Sci. Math. Natur.* **1**, 182.

Stachurski, J., and Michalek, M., 1996, *J. Colloid Interface Sci.* **184**, 433.

Stalidis, G., Avranas, A., and Jannakoudakis, D., 1990, *J. Colloid Interface Sci.* **135**, 313.

Stewart, M. G., Moy, E., Chang, G., Zingg, W., and Neumann, A. W., 1989, *Colloids Surf.* **42**, 215.

Suzuki, A., Ho, N. F. H., and Higuchi, W. I., 1969, *J. Colloid Interface Sci.* **29**, 552.

Thoroddsen, S. T., and Sakakibara, J., 1998, *Physics of Fluids* **10**, 1359.

Tien, C., 1989, "Granular Filtration of Aerosols and Hydrosols," Butterworths, Waltham, Massachusetts.

Toshev, B. V., and Platikanov, D., 1992, *Adv. Colloid Interface Sci.* **40**, 157.

Truskey, G. A., and Pirone, J. S., 1990, *J. Biomed. Mater. Res.* **24**, 1333.

van de Ven, T. G. M., 1989, "Colloidal Hydrodynamics," Academic Press, London.

Verwey, E. J. W., and Overbeek, J. T. G., 1948, "Theory of the Stability of Lyophobic Colloids," Elsevier, Amsterdam.

Wallace, J. A., and Schürch, S., 1990, *Colloids Surf.* **43**, 207.

Weast, R. C., Lide, D. R., Astle, M. J., and Beyer, W. H., 1989-1990, "CRC Handbook of Chemistry and Physics," CRC Press, Inc., Boca Raton, Florida.

Wu, S., 1982, "Polymer Interface and Adhesion," Marcel Dekker, New York.

Xu, Zhenghe, and Yoon, Roe-Hoan, 1989, *J. Colloid Interface Sci.* **134**, 427.

Yekta-Fard, M., and Ponter, A. B., 1988, *J. Colloid Interface Sci.* **126**, 134.

Zeman, L., and Wales, M., 1981, "Synthetic Membranes: HF and UF Uses," A. F. Turbak (Ed.), *ACS Symp. Series* **154**, Amer. Chem. Soc., Washington, DC, pp.411.